University of Southampton

FACULTY OF MEDICINE

Academic Unit of Human Development and Health

Polymeric nanoparticles loaded with a Wnt agonist for enhancing bone fracture healing

by

Edoardo Scarpa

Thesis for the degree of Doctor of Philosophy

September 2016

UNIVERSITY OF SOUTHAMPTON

ABSTRACT

FACULTY OF MEDICINE

Stem Cell Science and Regenerative Medicine

Thesis for the degree of Doctor of Philosophy

Polymeric nanoparticles loaded with a Wnt agonist for enhancing bone fracture healing

Edoardo Scarpa

In the UK, over 2 million people suffer a bone fracture every year. 10% of bone fractures will not heal adequately and require surgical intervention and, as yet, there is no approved systemic drug that is effective in promoting and accelerating fracture healing. Wnt signalling activation is a promising therapeutic target to address this paucity of treatments. Wnt is a molecular pathway that controls bone homeostasis and repair. However, its activation can have both positive and negative effects on bone cell function depending on the timing and site of delivery. Polymersomes (PMs) are polymeric nanoparticles that allow for a spatio-temporal controlled delivery of molecules, including Wnt agonists. This study addresses the hypothesis that PMs loaded with a Wnt agonist can be used as a novel systemic treatment to accelerate bone fracture healing fracture. The aims were: to assess cellular uptake of PMs and to quantify the amount of payload released intracellularly from PMs, to determine the ability of Wnt agonist loaded PMs to promote the osteogenic differentiation of human bone marrow stromal cells (BMSCs), and to assess the distribution of PMs *in vivo* following systemic injection in a mouse model of bone fracture. Cellular uptake was demonstrated using fluorescein as a model payload. By combining microscopy and flow cytometry, it was demonstrated that PMs are internalised by different cell types, including skeletal stem cells (SSCs), and real-time intracellular release of fluorescein was quantified at a single-cell level. Activation of Wnt signalling was achieved loading PMs with the Wnt agonist 6-bromoindirubin-3'-oxime (BIO), and demonstrated using a luciferase assay and RT-qPCR. In a reporter cell line, BIO-PMs induced a significant activation of the Wnt pathway without cytotoxicity, differently from free BIO. In BMSCs, BIO-PMs induced a significant increase in the expression of the Wnt target gene *AXIN2* ($p<0.05$) and in the expression of the early osteogenic marker *RUNX2* ($p<0.05$). Biodistribution *in vivo* was assessed loading PMs with a fluorescent dye (DiR) and using IVIS and histological analysis. PMs localised in the fractured bone within 24 hours after systemic administration in mice with a femoral drill defect and reached the maximum of accumulation after 48 hours. Histological sectioning confirmed the presence of PMs in the defect area post injection. Preliminary results demonstrated that BIO-PMs injected systemically have the ability to promote bone formation after injury. This project demonstrated that PMs are internalised by SSCs, which are the ideal cellular targets for bone regenerative approaches. When loaded with Wnt agonists, PMs induce a controlled activation of the pathway, promoting osteogenic differentiation of BMSCs. Upon systemic injection *in vivo*, PMs accumulate at the fracture site and were able to promote bone formation. Overall, the novel and exciting findings presented in this project showed that PMs loaded with Wnt agonists could represent an effective pharmacological treatment to promote bone regeneration after fracture.

Contents

Contents ..... **IV**

List of Figures ..... **IX**

Declaration of Authorship ..... **XIII**

Contributors ..... **XVI**

Acknowledgments ..... **XVIII**

Abbreviations ..... **XIX**

1 Chapter 1: Introduction **1**

1.1 Bone tissue 2

1.2 Bone fracture 3

1.2.1 Definition 3

1.2.2 Epidemiology 3

1.2.3 Healing process 3

1.2.3.1 Inflammation 4

1.2.3.2 Repair 6

1.2.3.3 Remodelling 11

1.2.4 Healing failure 12

1.2.5 Current pharmacological strategies for promoting bone healing 14

1.2.5.1 Growth factors 15

1.2.5.2 Small molecules 16

1.3 The Wnt pathway 18

1.3.1 Wnt canonical pathway 18

1.4 The Wnt pathway in bone homeostasis and stem cell biology 20

1.5 Wnt signalling in bone healing 22

1.6 Drug delivery systems in regenerative medicine 24

1.7 The journey of a drug delivery system towards its target 24

1.8 Types of drug delivery system 26

1.8.1 Polymer-drug conjugates 26

1.8.2 Self-assembled nanoparticles 27

1.8.2.1 Micelles 27

1.8.3 Liposomes 28
1.9 Polymersomes 29
1.9.1 Polymersomes: self-assembly process and physical characteristics 29
1.9.2 Polymersome production 32
1.9.3 Environment responsive polymersomes 33
1.9.4 Polymersomes and the delivery of small molecules 36
1.10 Nanoparticles and Wnt 37
Hypothesis and aims 40
2 Chapter 2: Materials and Methods 42
2.1 Materials 43
2.1.1 Cells 43
2.1.2 Block copolymers 43
2.2 Methods 44
2.2.1 Bone marrow mononuclear cells (BMMNCs) isolation 44
2.2.2 Polymersomes (PMs) preparation 45
2.2.2.1 Encapsulation of hydrophilic molecules in PMs (fluorescein and BIO) 45
2.2.2.2 Encapsulation of hydrophobic molecules in PMs (BIO, DiR and DiI) 46
2.2.2.3 Encapsulation of both fluorescein and BIO in PMs 46
2.2.3 Polymersome characterisation 47
2.2.3.1 Dynamic light scattering (DLS) 47
2.2.3.2 Nanoparticle tracking analysis (NTA) 48
2.2.3.3 Fluorescein encapsulation and release *in vitro* 48
2.2.3.4 Measurements of fluorescence intensity 49
2.2.4 Cellular uptake of fluorescein-PMs 49
2.2.4.1 Live cell imaging of L929 cells 49
2.2.4.2 Live cell imaging of MG63 cells and BMSCs 50
2.2.4.3 Flow cytometry 50
2.2.4.4 Immunological staining of freshly isolated BMMNCs incubated with fluorescein-PMs 52
2.2.4.5 Image Stream cytometry 53
2.2.5 AlamarBlue assay 54
2.2.6 Quantification of the number of PMs *per* cell 54

2.2.7 Luciferase assay 54
2.2.8 BIO encapsulation and release *in vitro* 56
2.2.9 Quantitative reverse transcription-polymerase chain reaction (qRT-PCR) 57
2.2.10 PicoGreen assay for dsDNA quantification 58
2.2.11 Alkaline phosphatase (ALP) activity measurement 58
2.2.12 In vivo study 59
2.2.13 Histological analysis 61
2.2.14 Micro-computed tomography (μ-CT) analysis 62
2.2.15 Statistical analysis 63

3 Chapter 3: Cellular uptake of polymersomes and quantification of intracellular payload release 64

3.1 Introduction 65
3.2 Results 69
3.2.1 Physical characterisation of fluorescein-polymersomes 69
3.2.2 Fluorescein fluorescence is quenched within PMs 71
3.2.3 Real-time detection of intracellular delivery of fluorescein by PMs 72
3.2.4 Un-encapsulated fluorescein in PM preparations does not cause cellular fluorescence 74
3.2.5 Investigation of the kinetics of fluorescein-PM uptake, at single cell resolution, by L929 cells 75
3.2.6 Quantification of PMs releasing payload intracellularly in L929 cells 78
3.2.7 Investigation of fluorescein-PM uptake MG63 cells and human BMSCs 81
3.2.8 Quantification of the intracellular payload release in BMSCs 85
3.2.9 Effect of serum on PM uptake 88
3.2.10 Uptake of fluorescein-loaded PMs in freshly isolated BMMNCs 91
3.2.11 Investigation of fluorescein-PMs uptake using Image Stream 95
3.3 Discussion 99

4 Chapter 4: Polymersomes for intracellular delivery and activation of the Wnt signalling pathway 107

4.1 Introduction 108
4.2 Results 112
4.2.1 Efficency of BIO as Wnt signaling agonist 112

4.2.2 Loading polymersomes with BIO....113
4.2.3 Internalisation of 5k-18k polymersomes by 3T3 reporter cells....116
4.2.4 Effect of core-loaded and shell-loaded polymersomes on Wnt activity....120
4.2.5 Stability of association between polymersome and BIO....122
4.2.6 BIO-PMs *vs* free BIO. 124
4.2.7 Differences in the kinetics of activation between free BIO and BIO-PMs 127
4.2.8 BIO-PMs induce the activation of Wnt signalling in BMSCs 130
4.2.9 Effect of BIO-PMs on BMSC proliferation and metabolism. 133
4.2.10 Effects of BIO-PMs on BMSCs early osteogenic differentiation. 135
4.2.11 Effects of BIO-PMs on BMSCs late osteogenic differentiation....137
4.3 Discussion....139

5 Chapter 5: Accumulation of polymersomes in the bone fracture and controlled delivery of a Wnt agonist 148

5.1 Introduction....149
5.2 Results....153
5.2.1 Characterisation of DiR and DiI loaded PMs....153
5.2.2 PMs distribution *in vivo* following systemic injection in a healthy mouse model. 155
5.2.3 Characterisation of the bone injury. 157
5.2.4 DiR-PMs accumulate at the fracture site. 160
5.2.5 PMs localise in the liver. 163
5.2.6 Effects of BIO-PMs on bone fracture healing 169
5.3 Discussion....173

6 Chapter 6: General discussion....181

6.1 Summary of the main findings of the study 182
6.2 Relevance of the findings, limitations and future opportunities 184
6.3 Conclusions....193

References....194

7 Appendix....227

7.1 Materials and methods 228
7.2 Chapter 3: supplementary data 235
7.2.1 Characterisation of polymersomes produced using the 5k-18k copolymer.238

7.2.2 Uptake of fluorescein-loaded PMs formed by the 5k-18k block copolymer in cultured BMSCs. 239
7.2.3 Quantification of uptake of new PMs and fluorescein release in BMSCs ... 240
7.3 Chapter 4: supplementary data 243
7.4 Chapter 5: supplementary data 244
7.5 Quantification of intracellular payload release from polymersome nanoparticles. 246
7.6 Transient Canonical Wnt Stimulation Enriches Human Bone Marrow Mononuclear Cell Isolates for Osteoprogenitors 259

List of Figures

Figure 1.1: Bone tissue structure and major cellular components.....2
Figure 1.2: Suggested expression of markers of skeletal stem cell (SSC) differentiation.....9
Figure 1.3: Phases of bone fracture healing.....11
Figure 1.4: Schematics of bone fracture healing.....12
Figure 1.5: The canonical Wnt signalling pathway.....20
Figure 1.6: Amphiphilic block copolymers self-assembly into different structures.....31
Figure 2.1: Lymphoprep gradient separation of bone marrow cells.....44
Figure 2.2: Overview of the methodology used to prepare PMs loaded with various molecules.....47
Figure 2.3: Dynamic light scattering analysis.....48
Figure 2.4: Methodology used to assess the effect of serum on PM uptake.....51
Figure 2.5: Luciferase assay.....56
Figure 2.6: Creation of the bone drill defect.....60
Figure 2.7: Orientation of the sectioning.....61
Figure 3.1: Overview of the principle behind the use of fluorescein for measuring intracellular payload delivery.....68
Figure 3.2: Physical characterisation of PMs loaded with fluorescein.....69
Figure 3.3: Fluorescein is encapsulated within PMs and it is stably retained over time.....71
Figure 3.4: Fluorescein fluorescence is quenched upon encapsulation within PMs.....72
Figure 3.5: Fluorescein-PMs are quickly internalised by L929 cells.....73
Figure 3.6: Time-dependent intracellular delivery of fluorescein from loaded PMs.....74
Figure 3.7: Uptake of residual un-encapsulated fluorescein present in PM solution does not result in cellular fluorescence.....75
Figure 3.8: L929 cells internalisation of fluorescein-PMs assessed by flow cytometry.....76
Figure 3.9: Fluorescein-PMs do not induce cytotoxicity in L929 cells.....77
Figure 3.10: Estimation of the number of PMs releasing fluorescein in L929 cells.....79
Figure 3.11: Quantification of the number of PMs releasing fluorescein in L929 at single cell level.....80
Figure 3.12: MG63 and BMSCs cells internalise fluorescein-PMs.....82
Figure 3.13: Kinetics of PM uptake by MG63 cells and BMSCs.....83

Figure 3.14: MG63 cells and BMSCs reach saturation of fluorescein within a 24 hour incubation. 84
Figure 3.15: Fluorescein-PMs do not induce significant cytotoxicity in MG63 cells or BMSCs 85
Figure 3.16: Estimation of the concentration of fluorescein released in BMSCs from fluorescein-PMs. 86
Figure 3.17: Quantification of the number of PMs releasing fluorescein in BMSCs at a single cell level. 87
Figure 3.18: The concentration of serum present in solution affects PM uptake by cells. 88
Figure 3.19: The concentration of serum present in solution and the culture conditions affect fluorescein-PMs uptake by cells 90
Figure 3.20: Cell lineages in human BMMNCs. 92
Figure 3.21: Freshly isolated BMMNCs internalise fluorescein-PMs. 93
Figure 3.22: Monocytes internalise fluorescein-PMs. 94
Figure 3.23: SSCs internalise fluorescein-PMs. 94
Figure 3.24: Monocytes and SSCs positive for fluorescein analysed by Image Stream. 96
Figure 3.25: Co-localisation of fluorescein with LAMP-1 in MG63 cells. 97
Figure 3.26: Quantification of fluorescein and LAMP-1 co-localisation in MG63 cells. 98
Figure 4.1: Responsiveness of the 3T3 Wnt reporter cell line to BIO. 112
Figure 4.2: BIO concentrations up to 5 μM do not affect cell proliferation. 113
Figure 4.3: Summary of the methodology used to characterise core- and shell- BIO loaded PMs 114
Figure 4.4: Size and concentration of BIO-PMs measured by DLS and NTA 115
Figure 4.5: PMs can be loaded in either core or shell with BIO. 116
Figure 4.6: Overview of the methodology used to assess internalisation of PMs by reporter cells. 117
Figure 4.7: Fluorescein- and fluorescein and BIO-PMs are internalised by Wnt reporter cells. 118
Figure 4.8: Co-loading PMs with fluorescein and BIO reduces the ability of PMs to activate the Wnt pathway. 119
Figure 4.9: Overview of the methodology used to assess activity of PMs loaded with BIO. 120
Figure 4.10: Wnt signalling induced activation of core- or shell-loaded PMs. 121

Figure 4.11: PMs loaded with 200 or 400 μM BIO activate the Wnt signalling pathway in reporter cells. 122
Figure 4.12: BIO is stably loaded within PMs. 123
Figure 4.13: Overview of the methodology used to compare BIO-PMs and free BIO in reporter cells. 124
Figure 4.14: Comparison of BIO-PMs *vs* free BIO activity. 125
Figure 4.15: Induced cytotoxicity of BIO-PMs *vs* free BIO. 126
Figure 4.16: High volumes of PBS or empty-PMs do not affect the intensity of the luminometric readout. 126
Figure 4.17: High concentrations of PMs affect the luminometric readout. 127
Figure 4.18: BIO-PMs and free BIO present different kinetics of Wnt signalling activation. 128
Figure 4.19: Activity of BIO-PMs *vs* free BIO after a 24 or 48 hour incubation. 128
Figure 4.20: Overview of the methodology used to assess the effects of BIO-PMs on BMSCs. 130
Figure 4.21: Fluorescein and BIO-PMs are internalised by BMSCs. 131
Figure 4.22: BIO-PMs induce up-regulation of AXIN2 in BMSCs. 132
Figure 4.23: Effects of BIO-PMs on C-MYC and CCND1 expression. 133
Figure 4.24: Proliferation BMSCs after incubation with BIO-PMs, free BIO or Wnt3A. 134
Figure 4.25: Metabolism of BMSCs after incubation with BIO-PMs, free BIO or Wnt3A. 135
Figure 4.26: BIO-PMs promote up-regulation of the early osteogenic markers RUNX2 and SP7 in BMSCs. 136
Figure 4.27: ALP activity of BMSCs in complete osteogenic media after incubation with BIO-PMs, free BIO or Wnt3A. 137
Figure 4.28: ALP activity of BMSCs in osteogenic media (-dexamethasone) after incubation with BIO-PMs, free BIO or Wnt3A. 138
Figure 5.1: Physical characterisation of PMs loaded with DiR or DiI. 154
Figure 5.2: DiR-PMs injected subcutaneously are visible using IVIS. 155
Figure 5.3: DiR-PMs injected systemically accumulate in the region of the liver of healthy mice. 156
Figure 5.4: Bone drill defect. 157

Figure 5.5: Day 0 of fracture healing. 158
Figure 5.6: Day 7 of fracture healing. 159
Figure 5.7: Day 10 of fracture healing. 160
Figure 5.8: DiR-PMs accumulate at the fracture site after systemic injection. 161
Figure 5.9: Analysis of the fluorescence measured at the fracture site after systemic injection. 162
Figure 5.10: DiI-PMs are localised in the injury area 7 days following systemic administration. 163
Figure 5.11: DiR-PMs are present in the liver area of bone injury models 1 day post systemic injection. 164
Figure 5.12: DiI-PMs are present in the liver 7 days following systemic administration but do not induce hepatotoxicity. 165
Figure 5.13: Encapsulation of DiR in PMs favours accumulation at the fracture site. 166
Figure 5.14: Fluorescent signal preferentially accumulated in the skin of the sham group. 167
Figure 5.15: Encapsulation of DiR in PMs favours accumulation at the fracture site. 168
Figure 5.16: Time-line of the methodology. 169
Figure 5.17: Temporal μ-CT analysis of bone drill healing process. 170
Figure 5.18: μ-CT analysis of the type of tissue bridging the bone drill defect. 171
Figure 5.19: Histological analysis of bone femurs 21 days post treatments with BIO-PMs, free BIO or empty-PMs. 172
Figure 6.1: Quantification of intracellular payload released from PMs. 185
Figure 6.2: Polymersomes for bone regeneration. 193

Declaration of Authorship

I, Edoardo Scarpa, declare that this thesis and the work presented in it are my own and have been generated by me as the result of my own original research.

Polymeric nanoparticles loaded with a Wnt agonist for enhancing bone fracture healing

I confirm that:

1. This work was done wholly or mainly while in candidature for a research degree at this University;

2. Where any part of this thesis has previously been submitted for a degree or any other qualification at this University or any other institution, this has been clearly stated;

3. Where I have consulted the published work of others, this is always clearly attributed;

4. Where I have quoted from the work of others, the source is always given. With the exception of such quotations, this thesis is entirely my own work;

5. I have acknowledged all main sources of help;

6. Where the thesis is based on work done by myself jointly with others, I have made clear exactly what was done by others and what I have contributed myself;

Parts of this work has been published as:

Paper

- Scarpa E, Bailey J, Janeczek AA, Stumpf P, Johnston A, Oreffo ROC, Woo YL, Cheong Y, Evans ND, Newman TA. "Quantification of intracellular payload release from polymersome nanoparticles". *Scientific Reports,* 2016 (see section 7.5).

- Janeczek AA, Tare RS, Scarpa E, Moreno-Jimenez I, Rowland CA, Jenner D, Newman TA, Oreffo ROC, Evans ND. "Transient Canonical Wnt Stimulation Enriches Human Bone Marrow Mononuclear Cell Isolates for Osteoprogenitors". *Stem Cells,* 2016 (see section 7.6).

Book chapter

- Janeczek AA, Scarpa E, Newman TA, Oreffo ROC, Tare RS, Evans ND. "Skeletal Stem Cell Niche of the Bone Marrow". Published in: Tissue-Specific Stem Cell Niche. Springer International Publishing 2015. ISBN: 978-3-319-21704-8.

Abstracts

"Wnt pathway activating polymeric nanoparticles for fracture localisation", *Tissue Engineering and Regenerative Medicine International Society 2016*, Uppsala, Sweden. TERMIS abstracts are published in Tissue Engineering Part A.

"Promoting Bone Fracture Healing Using BIO-Loaded Polymersomes", *Tissue Engineering and Regenerative Medicine International Society 2015*, Boston (MA), USA. TERMIS abstracts are published in Tissue Engineering Part A.

"Polymeric nanoparticles for the delivery of small molecules during fracture repair", *Tissue and Cell Engineering Society meeting 2015*, Southampton, UK. TCES abstracts are published in eCells & Materials

"A nano solution for a big problem", *SET for BRITAIN 2015*, House of Parliament, Portcullis House, Westminster, UK.

"Wnt agonist loaded polymersomes for bone repair", *Faculty of Medicine Research Conference,* Southampton General Hospital, Southampton, UK.

"The use of polymersomes in stem cell-specific targeting for bone regeneration", *Tissue and Cell Engineering Society annual conference*, Newcastle upon Tyne, UK. TCES abstracts are published in eCells & Materials

"Stem-cell targeting of polymersomes for bone regeneration", *Second annual Conference of the Health & Pharma University-Industry Sector Team (UIST),* Garden Court, Highfield Campus, University of Southampton, Southampton, UK.

Signed:

Date:

Contributors

All experiments and data analysis were performed by the author in the Bone and Joint Group laboratory, Academic Unit of Human Development and Health, Faculty of Medicine, Southampton University Hospital, University of Southampton, with the following exceptions:

Section 3.2.1

Nanoparticle tracking analysis was performed with help of Malvern company representatives, respectively.

Section 3.2.3

Confocal imaging was performed under the supervision of Dr Joanne Bailey and Dr David Johnston, University of Southampton.

Section 3.2.10

Staining of bone marrow mononuclear cells for flow cytometry experiments and successive analysis were performed by the author with the collaboration of Dr Agnieszka Janeczeck, University of Southampton.

Section 3.2.11

Samples for Image Stream flow cytometry were prepared by the author and the sampling and analysis was performed by Dr Dominic Jenner, Biomedical Sciences Department, Defence Science and Technology Laboratory, Porton Down, Salisbury.

Section 5.2

Tail vein injections during *in vivo* experiments were performed by the staff of the Biomedical research facility, University of Southampton.

Section 5.2

Histological sectioning and staining were performed by Miss Alethia Hoad, University of Southampton, under the supervision of the author.

Section 5.2.6

μ-CT scanning and analysis have been performed by Gry Hulsart-Billström, University of Southampton.

Acknowledgments

I am grateful to my supervisors Dr Nicholas Evans, Dr Tracey Newman and Professor Richard Oreffo for their continuous support and guidance. Nick and Tracey in particular have been teaching and helping me, on a daily basis, throughout the last 4 years. They encouraged my professional and personal development, and I will treasure their advice for the rest of my career.

I am thankful to all the people within the Bone and Joint Group and the Nanoneuroscience group for creating a friendly working environment where working was just good fun.

Thank to the people who started with me Inés, Sophia, Mindy, Gaia. We have helped and supported each other during our countless meals and coffees, thanks for being great friends. Thanks to Stu, for being a good friend and an amazing gym buddy, and to May for being like a sister to me in this adventure. I also want to thank the special people who guided me and helped me over the last 4 years, Patrick, Tsiloon, Jon, Prof Wilson, Christine, Jo, Andrew, Julia, Ewa and Alethia. All of you made this journey so special.

Thanks to Janos and Gry for patiently teaching me the surgical procedures in the *in vivo* study and thanks to Dr Emre Sayan for letting me use of the whole-body imaging machine. Also thanks to Dr Dominic Jenner for the help with the Image Stream, and to Vikki, Lisa and Mel from the animal units for the help with the i.v. injections.

I am especially grateful to Agnieszka who has been a continuous inspiration and who taught me basically all the techniques that I have used in these 4 years. Thanks for being my 'other' supervisor and a very good friend.

I want to thank my Mum and Dad, Fedy and Ge; you are the most amazing family and I am the luckiest person to have you in my life.

Finally, a very special thanks goes to Mel. Thank you for patience and encouragement, thanks for your endless help and for taking care of me. I would not have made it without you.

Abbreviations

A.U.	Arbitrary units
ACTB	Actin-beta
AD	Alzheimer's disease
ALP	Alkaline phosphatase
aP2	Adipocyte protein-2
APC	Adenomatous polyposis coli
BBB	Blood brain barrier
BF	Bright field
BIO	6-bromoindirubin-3'-oxime
Bm	Bone marrow
BMMNCs	Bone marrow mononuclear cells
BMP	Bone morphogenetic protein
BMSC	Bone marrow stromal cells
BSA	Bovine serum albumin
BV	Bone volume
Cal	Callus
CB	Cortical bone
CCD	Charge-coupled device
CCL-2	C-C motif chemokine 2
CD	Cluster of differentiation
CDK	Cyclin-dependent kinases
CK	Casein kinase
CMC	Critical micelle concentration
COPD	Chronic obstructive pulmonary disease

DAPI	4',6-diamidino-2-phenylindole
DDS	Drug delivery system
DiI	DiI-DiIC18 (3) (1, 1'-Dioctadecyl-3, 3, 3', 3'-tetramethylindotricarbocyanine Iodide
DIR	DiIC18 (7) (1, 1'-dioctadecyl-3, 3, 3', 3'-tetramethylindotricarbocyanine iodide)
DKK-1	Dickkopf-1
DLS	Dynamic light scattering
DMEM	Dulbecco's modified Eagle's medium
DMF	Dimethylformamide
DMSO	Dimethyl sulphoxide
DVL	Dishevelled
EDTA	Ethylenediaminetetraacetic acid
ELVIS	Extravasation through leaky vasculature and inflammatory cell mediated sequestration
EPR	Enhanced permeability and retention
FBS	Foetal bovine serum
FDA	Food and Drug Administration
FGF	Fibroblast growth factor
FRAT	Frequently rearranged in advanced T-cell lymphomas-1 protein
FZD	Frizzled
GAPDH	Glyceraldehyde 3-phosphate dehydrogenase
GFP	Green fluorescent protein
GSK-3β	Glycogen synthase kinase 3 beta
Gt	Granulation tissue
HPLC	High performance liquid chromatography
HSC	Hematopoietic stem cells

hsCRP	High-sensitive C-reactive protein
IC_{50}	Inhibitory concentration
IL	Interleukin
INJ	Injury
ISCT	International Society for Cellular Therapy
I.V.	Intravenous
IVIS	*In vivo* imaging system
LEF	lymphoid enhancer factor
LRP	Lipoprotein receptor-related protein
MFI	Mean fluorescence intensity
MPS	Mononuclear phagocyte system
MSC	Mesenchymal stem cell
MW	Molecular weight
MWCO	Molecular weight cut-off
NO	Nitric oxide
NSAID	Non-steroidal anti-inflammatory drugs
NTA	Nanoparticles tracking analysis
OC	Osteocalcin
OCT	Optimal cutting temperature
OSE2	Osteoblast-specific cis-acting element 2
PBD	Polybutuadiene
PBS	Phosphate buffer saline
PCL	Polycaprolactone
PDGF	Platelet-derived growth factor
PdI	Poly dispersity index
PDMS	Polydimethylsiloxane

PDPA	Poly-2-(diisopropylamino)ethyl methacrylate
PEG	Polyethylene glycol
PEO	Polyethylene oxide
PFA	Paraformaldehyde
PI	Propidium iodide
PIPES	Piperazine-N,N'-bis 2-ethanesulfonic acid
PLA	Polylactic acid
PLGA	Polylactic-co-glycolic acid
PM	Polymersome
PMCP	Poly-2-methacryloyloxyethyl phosphorylcholine
PNIPAM	poly-N-isopropylacryl-amide
PNPP	P-nitrophenyl phosphate
PPAR-γ	Peroxisome proliferator-activated receptor gamma
PPS	Polypropylene sulphide
PTH	Parathyroid hormone
PTHrP	Parathyroid hormone-related protein
PVCL	Poly-*N*-vinylcaprolactam
qRT-PCR	Quantitative reverse transcription-polymerase chain reaction
RANK-L	Receptor activator of nuclear factor kappa-B ligand
RES	Reticuloendothelial system
ROI	Region of interest
RUNX-2	Runt-related transcription factor 2
SD	Standard deviation
SDF-1	Stromal cell-derived factor-1
SDS	Sodium dodecyl sulphate
SFRP	Secreted frizzled related protein

siRNA	Small interfering RNA
SOST	Sclerostin
SPM	Specialised pro-resolution lipid mediators
SSC	Skeletal stem cell
TCF	T-cell factor
TE	Tris/EDTA
TGF	Transforming growth factor
TNF	Tumour necrosis factor
TV	Tissue volume
UK	United Kingdom
UV	Ultra violet
VEGF	Vascular endothelial growth factor
VOI	Volume of interest
Wb	Woven bone
Wg	Wingless
WIF-1	Wnt inhibitory factor 1
Wnt-PCP	Wnt-planar cell polarity

Chapter 1: Introduction

1.1 Bone tissue

Bone tissue is part of the skeletal system, a major component of the human body accounting for approximately 20% of the total mass. This tissue has numerous physiological functions including providing structural support and protection, facilitating locomotion, serving as storage for minerals, and hosting bone marrow tissue.

Bone formation can be divided into two processes: primary, which either takes place during embryogenesis or following injury leading to the rapid formation of a disorganised tissue called 'woven' bone, and secondary, that results in the replacement of woven bone with a more structured bone tissue called 'lamellar'. Bones have different shapes depending on their function but their archetypal structure is recurrent across the different types. Lamellar bone comprises an outer region of solid and dense mineralised tissue called cortical bone, and an inner cavity of trabecular bone. Within these regions, three main cell types can be found: osteoblasts, which produce and release a collagenous matrix enriched with proteins (osteoid) that is then mineralised forming the final bone tissue; osteocytes, which control bone health by governing the mechanisms of bone repair and removal, while sensing mechanical stimulations; and osteoclasts, which are macrophage-derived cells tasked to reabsorb bone by producing enzymes (Figure 1.1).

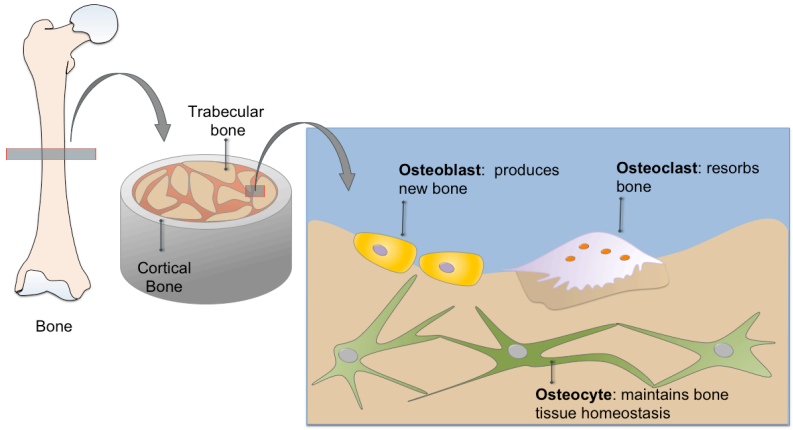

Figure 1.1: **Bone tissue structure and major cellular components.**

Pictorial representation of bone structure comprising cortical and trabecular bone. Within these, three main cellular types can be observed: osteoblast, osteoclast and osteocyte.

These cell types cooperate to maintain bone homeostasis either by increasing bone mass according to physiological needs (bone modelling), or replacing mature bone with

new bone (bone remodelling). The interaction of these cells is also fundamental during regenerative processes following injury, such as bone fracture (reviewed by Clarke 2008).

1.2 Bone fracture

1.2.1 Definition

A bone fracture is defined as a complete or incomplete discontinuity of the bone tissue (Adler 1989). This is caused by the application of a stress that exceeds the compliance of the tissue, which then cracks, dissipating the energy (Fratzl 2008).

1.2.2 Epidemiology

It is estimated that across the UK alone over 2 million people suffer a bone fracture every year (van Staa et al. 2001). A small subset of these fractures is due to osteoporosis, a skeletal disorder characterised by bone fragility, and costs the UK economy more than £1.7 billion *per* year (Holroyd et al. 2008). Bone fracture is considered among the most common causes of hospitalisation in the world, affecting the quality of life and socio-economic position of millions (Riggs & Melton. 1995; Kilgore et al. 2009). Most fractures heal without complications and the bone tissue is restored to pre-injury conditions within a relatively short time frame (Hooper et al. 1991). However, it is estimated that 10% to 50% of all the fractures diagnosed, depending on their anatomical localisation, will not heal adequately resulting in what is defined as 'non-union' (Zimmermann et al. 2009; Lack et al. 2014). In these circumstances, patients require one or multiple reparative surgeries, and the current paucity of systemic pharmacological treatments aimed to aid bone healing is a critical unmet issue.

1.2.3 Healing process

Bone tissue has a remarkable regenerative ability, and unlike many tissues in the human body, bones can heal without the formation of scar-tissue, restoring the form and the mechano-physical properties present prior to injury (Loi et al. 2016), as demonstrated by microscopy, histomorphometry and mechanical testing (Shapiro, 1988; Klein et al. 2003)Following fracture, depending on the mechanical stability of the tissue and the grade of displacement of the two fractured extremities, two types of regenerative

processes can take place: primary, also known as intramembranous, and secondary, also called endochondral.

Primary healing occurs when the bone fragments are reduced anatomically and are mechanically stable. This process closely resembles the physiological remodelling mechanism, whereby osteoclasts reabsorb dead bone, while osteoblasts fill the fracture gap by laying new bone (Einhorn & Gerstenfeld 2015). Nevertheless, this process is rare, and, due to poor mechanical stability or extreme inter fragmentary rigidity, it is often replaced by secondary healing. John Hunter was the first to characterise secondary fracture healing dividing this process into major sequential steps namely inflammation, repair (comprised of soft callus formation and hard callus formation) and remodelling (Hunter 1837).

1.2.3.1 Inflammation

The first physiological reaction to a fracture is the establishment of an acute inflammatory response that lasts, on average, 7 days (data from rats) (Claes et al. 2012). The traumatic stress causing the bone crack alters not only the microarchitecture of the bone itself, but also disrupts the vasculature network of the tissue, leading to leukocyte extravasation and the formation of a haematoma (Einhorn & Gerstenfeld 2015). The critical role played by early inflammation during fracture repair has been underlined by studies *in vivo*, where irrigation of the haematoma with saline solution (Park et al. 2002), or its total removal by surgical procedure (Grundnes & Reikerås 1993; Park et al. 2002) severely impaired fracture healing.

Neutrophils are the first leukocytes to migrate into fractured bone attracted by both the blood clot and the presence of cellular debris (Chung et al. 2006). The role of these cells during bone healing remains controversial. Neutrophils should reside in the haematoma for 24 hours (Andrew et al. 1994), where they contribute to the healing process by releasing chemotactic molecules, such as C-C motif chemokine 2 (CCL2) and interleukin-6 (IL-6) (Hurst et al. 2001; Xing et al. 2010). In addition, they produce a fibronectin scaffold that permits the infiltration of monocytes and macrophages (Bastian et al. 2016). However, earlier evidence suggests that neutrophils are not essential during healing processes (Simpson & Ross 1972) and could in fact be detrimental if they persist in the injured tissue, where they may impair bone healing (Grøgaard et al. 1990). Nevertheless, in normal conditions neutrophils are progressively replaced in the

haematoma by infiltrating macrophages and monocytes. The initial vascular damage and the subsequent secretion of pro-inflammatory molecules such as nitric oxide (NO) induce an increase in vascular permeability, allowing the bi-directional movement of cells, nutrients and macromolecules from the blood stream to the site of injury, which is a crucial mechanism for promoting bone fracture healing (Nagy et al. 2008).

Macrophages migrate into the haematoma from either the blood stream or the bone marrow, and begin the clearance of necrotic cells and fibrin matrix. In parallel, osteoclasts, which are macrophage-derived cells, remove the remaining bone fragments present in the fracture area. They produce and release a number of pro-inflammatory and chemotactic molecules, including tumour necrosis factor (TNF)-α, IL-1, IL-6 and CCL-2, which promote inflammation and serve to recruit fibroblasts, osteoprogenitor cells and skeletal stem cells (SSCs), which will be discussed further later in this chapter (see section 1.2.3.2) (Kon et al. 2001; Wu et al. 2013). Macrophages are important to bone healing as they secrete angiogenic molecules such as angiopoetin-1 (Ang-1) and vascular endothelial growth factor (VEGF) (Street et al. 2000; Street et al. 2002; Willenborg et al. 2012). These molecules encourage the migration of other cells to the injury site and promote angiogenesis in the tissue (Brighton & Krebs 1972).

Overall during bone healing, macrophages serve a number of functions and have a cardinal role in controlling the switch from the inflammatory to the reparative step. It has been recently demonstrated that depleting macrophages during fracture healing, using colodronate, severely delays the regeneration process. Conversely, treatment with IL-4 and IL-13 promote macrophage class switching from pro-inflammatory (M1) to anti-inflammatory (M2), enhancing bone healing (Schlundt et al. 2015). Furthermore, vascularisation and osteoclast function are significantly reduced when macrophage recruitment into the injury site is exogenously limited, leading to impaired bone healing (Xing et al. 2010). In physiological conditions, macrophage class switching is favoured by autocrine and paracrine secretion of anti-inflammatory molecules and specialised pro-resolution lipid mediators (SPMs) (Deng et al. 2014). These lipid mediators actively induce the resolution of acute inflammation by reducing leukocyte infiltration, counteracting the action of pro-inflammatory molecules while promoting the clearance of apoptotic neutrophils and cellular debris (Serhan et al. 2015). Although the secretion of these molecules during fracture healing has not yet been demonstrated, it is likely that

they contribute to the natural progression of the reparative process, avoiding the onset of chronic inflammation that could be detrimental for bone healing (further discussed in section 1.2.4).

As previously mentioned, macrophages promote the migration of a number of cell types in the haematoma, including fibroblasts which produce and lay a collagen matrix that forms the basis of the granulation tissue. This then functions as a scaffold for the growth of new blood vessels and the proliferation of SSCs (Claes et al. 2012; Gerstenfeld et al. 2003). Blood vessel formation and SSC migration and differentiation, mark the onset of the reparative stage.

1.2.3.2 Repair

Skeletal stem cells (SSCs) have a central role in bone homeostasis and regeneration, and will be introduced before proceeding with the description of the repairing mechanisms of fracture healing.

SSCs, also known as mesenchymal stem cells (MSCs) (Caplan 1991), are rare cells (1 in 10^4 - 10^5 cells) able to grow *in vitro* under clonogenic culture conditions (colony forming unit-fibroblast) with self-renewal and multipotent ability (Sacchetti et al. 2007; Friedenstein 1980; Friedenstein et al. 1974). *In vivo,* SSCs are located in the bone marrow in close proximity to the outer-surface of the sinusoids and are part of a complex three-dimensional architecture called the bone marrow niche (Bianco et al. 2013; Sacchetti et al. 2007: Janeczek et al. 2015). In this niche they contribute to bone development and homeostasis (Pittenger et al. 1999), as well as influencing the fate of the hematopoietic stem cells (HSCs) by cooperating with the other stromal cells (Mendez-Ferrer et al. 2010).

One of the earliest evidences of the presence of SSCs within bone marrow is dated 1968, when Tavassoli and Crosby demonstrated that fragments of bone marrow, re-implanted *in vivo*, were able to reconstitute the organ of origin (Tavassoli & Crosby 1968). Subsequently, Friedenstein and colleagues demonstrated that this skeletogenic ability was restricted to the stromal population within the bone marrow that was capable of adhering to tissue culture plastic (Friedenstein 1980). These bone marrow stromal cells (BMSCs) are a heterogeneous population that includes SSCs (Bianco et al. 2013).

The terms BMSCs and SSCs/MSCs are often and incorrectly used interchangeably in the literature; the abbreviation bone marrow stromal cell (BMSC) refers to a heterogeneous cell population that includes not only SSC/MSCs but also other cells at different stage of differentiation (Caplan 1991; Bianco et al. 2013). Therefore, this semantic distinction between BMSC and SSC will be used through the reminder of this thesis.

SSCs can be isolated from the bone marrow by using a density gradient and clonogenic culture conditions (Böyum 1968). Alternatively, they can be recovered from a fraction of bone marrow containing mononuclear cells, known as bone marrow mononuclear cells (BMMNCs), by using cellular surface markers (Bianco 2014). A single and reliable marker for sensitively selecting SSCs has not yet been recognised, therefore, a panel of them is required in order to increase selectivity and purity of the cells isolated. According to the guidelines set by the Mesenchymal and Tissue Stem Cell Committee of the International Society for Cellular Therapy (ISCT), SSCs must express the cluster of differentiation markers (CD)105 (endoglin), CD73 (membrane-bound ecto-5'-nucleotisidase) and CD90 (Thy-1), while lacking the expression of classical hematopoietic markers such as CD45 (tyrosine phosphatase), CD34 and CD14. However, the clonal and multilineage differentiation capacity following transplantation *in vivo* is the most stringent test used in order to determine the potential of an isolated single cell (Bianco et al. 2013).

An alternative marker for the selection of SSCs is represented by STRO-1, which has been shown to enrich for skeletal multipotent cells within the bone marrow (Simmons & Torok-Storb 1991; Tare et al. 2012). However, STRO-1 is also not an exclusive SSC marker since it binds 10% of the BMMNC population including erythroid progenitors and a subset of stromal cells (Simmons & Torok-Storb 1991). Despite these limitations, STRO-1 still represents a valuable marker for identifying and increasing the purity of SSCs (Gronthos et al. 2003), sometimes in combination with other markers such as glycophorin A (GPA) and CD14 (Janeczek et al. 2016).

SSCs are not only multipotent cells able to generate a miniaturised bone marrow organ (ossicle) *in vivo* following ectopic implantation (Sacchetti et al., 2007), but also have immunomodulatory abilities producing and releasing a variety of molecules that contribute to both the innate immune response and regenerative processes (reviewed by Caplan & Correa 2011; Le Blanc & Mougiakakos 2012). Nevertheless, the primary

function of the SSCs is to proliferate and differentiate into different cell types including osteoblasts.

Indication of this multilineage ability from the SSCs has been provided by Sacchetti and colleagues. The authors identified SSCs from the whole stromal population by the high expression of the surface marker CD146. The cells isolated demonstrated the self-renewal ability in a series of transplantations *in vivo,* and within 8 weeks from clonal implantation in immunocompromised mice, were able to form a hematopoietic microenvironment comprised of mineralised bone tissue as well as a sinusoidal system with functional hematopoiesis (Sacchetti et al., 2007). In a second study *in vivo*, SSCs were identified by the expression of nestin protein. Green fluorescent protein (GFP)-nestin positive cells were responsive to parathyroid hormone stimulation, which favoured the proliferation of these cells and their osteoblastic differentiation. Moreover, by crossing transgenic mice, Mendez-Ferrer and colleagues demonstrated that GFP-nestin positive cells were contributing to the physiological skeletal remodelling through differentiation into cartilage- and bone-forming cells (Mendez-Ferrer et al., 2010).

The differentiation of SSCs into osteoblasts is crucial for maintaining bone homeostasis and for facilitating the process of bone healing. Such differentiation comprises a series of molecular steps, and can arguably be divided into various commitment stages. Each of these stages are routinely identified by the expression of target genes or by the synthesis of specific molecules (Hayrapetyan et al. 2015). The first step is the expression of runt-related transcription factor 2 (*RUNX2*). Also known as 'master-gene', RUNX2 binds to osteoblast-specific cis-acting element 2 (OSE2), and controls the expression of other osteogenic marker genes including *SP7*, alkaline phosphatase (*ALP*), collagen type 1 (*COL1A1*), and osteocalcin (*OC*) (Ducy & Karsenty 1995). This osteoinductive control by RUNX2 occurs in cooperation with SP7 (Osterix in mice), which is another pivotal transcription factor during osteodifferentiation. Mice deficient in *Runx2* demonstrated a lack of *Sp7/Osterix* expression, indicating that the latter is downstream of the former (Nakashima et al. 2002). Importantly, mice lacking the expression of both *RUNX2* and Osterix do not produce osteoblasts, demonstrating the importance of these two genes for osteogenesis and bone homeostasis (Nakashima et al. 2002). A series of molecular pathways are able to influence the expression of *RUNX*2, including fibroblast growth factor (FGF) pathway, platelet derived growth factor (PDGF)

signalling, notch pathway, and WNT signalling pathway, the importance of which will be further introduced later on (see section 1.3) (reviewed by Hayrapetyan et al. 2015). Overall, the expression of *RUNX2* and Osterix/*SP7* drives SSC into proliferating osteoprogenitors, which are cells committed to the osteoblastic lineage but that still retain a degree of plasticity (Sacchetti et al. 2007). Successively, osteoprogenitors start producing collagen type I, the main collagenous protein of the bone tissue, which is subsequently mineralised by the activity of the ALP enzyme (Dimai et al. 1998). At this stage, osteoprogenitors have become immature osteoblasts, namely preosteoblasts, which terminally differentiate into osteoblasts following further cellular proliferation and production of bone proteins such as osteonectin, osteopontin and osteocalcin (Figure 1.2) (Harris et al. 2009; reviewed by Rucci 2008)

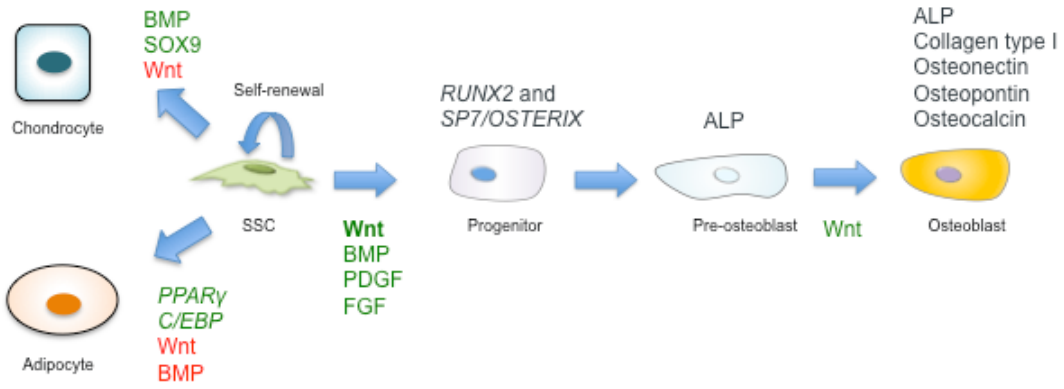

Figure 1.2: **Suggested expression of markers of skeletal stem cell (SSC) differentiation.**

Schematic illustration depicting the differentiation of a SSC into various cell types. Wnt inhibits SSC differentiation in chondrocytes and adipocytes, but favours the commitment into osteoblast progenitor. Once committed, SSC expresses *RUNX2* and *SP7*. These induce the progression toward the pre-osteoblast phenotype, which is characterised by the expression of ALP. Finally, mature osteoblast expresses ALP, Collagen type I, osteonectin, osteopontin and osteocalcin. Based on Rucci 2008.

In considering the repair stage of fracture healing, SSCs mediate a therapeutic effect through the secretion of a number of immunosuppressive molecules such as IL-6, prostaglandin E_2, NO, FGF, stromal cell–derived factor 1 (SDF-1) and VEGF (Reviewed

by Wang et al. 2014) as well as differentiating into various stromal cell type including osteoblasts and chondrocytes. An elegant demonstration *in vivo* of the SSCs role during fracture repair has been provided by Worthley and colleagues. The authors demonstrated that SSCs, identified by the expression of gremlin 1, a secreted antagonist of BMPs, contributed to the expansion and differentiation of osteoblasts and chondrocytes at the fracture site. Also, SSCs expanded *in vitro* and implanted in a fractured bone were self-renewing, differentiating into osteoblasts, and could be further isolated and expanded (Worthley et al., 2015). The phenotypic pathway of differentiation followed by the SSCs depends of the type of bone repair taking place.

In the case of primary repair, SSCs proliferate and differentiate into osteoblasts and, in conjunction with the maturating osteoprogenitors, begin the deposition of a woven bone from the periostium, which is a membrane that covers all bones, while they progressively advance towards to centre of the injury. Meanwhile, osteoclasts that have migrated from other locations, or differentiated *in situ*, are activated by the release of receptor activator of nuclear factor kappa-B ligand (RANKL) from osteoblasts and start resorbing bone creating tunnels that are subsequently filled by growing blood vessels. This process terminates with the restoration of the bone tissue continuum.

In terms of secondary repair, the residual hypoxic conditions present in the centre of the granulation tissue as well as the inter-fragmentary micro motions induce the differentiation of SSCs towards a chondrogenic phenotype (Hirao et al. 2006; Gerstenfeld et al. 2003). Chondoroblasts form a 'soft callus' by producing a cartilaginous matrix that is meshed with fibrous tissue. Such tissue provides mechanical stability, minimising the inter-fragmentary movement, and functions as platform for the successive formation of bone matrix (Marsell & Einhorn 2011; Claes et al. 2012; Gerstenfeld et al. 2003). The soft callus is then mineralised by hypertrophic chondrocytes that release calcium before undergoing apoptosis. Meanwhile the tissue is being extensively re-vascularised, leading to the accumulation of macrophages, osteoclasts and osteoprogenitors. Consequently, macrophages and osteoclasts begin to reabsorb the mineralised cartilaginous matrix leaving space to the formation of bone matrix. Osteoblasts begin the simultaneous replacement of the fibro-cartilaginous callus with woven bone in order to increase the mechanical strength of the tissue. This process leads to the formation of a 'hard callus' (Einhorn 2005; Gerstenfeld et al. 2003; Claes et al. 2012; Loi et al. 2016) (Figure 1.3).

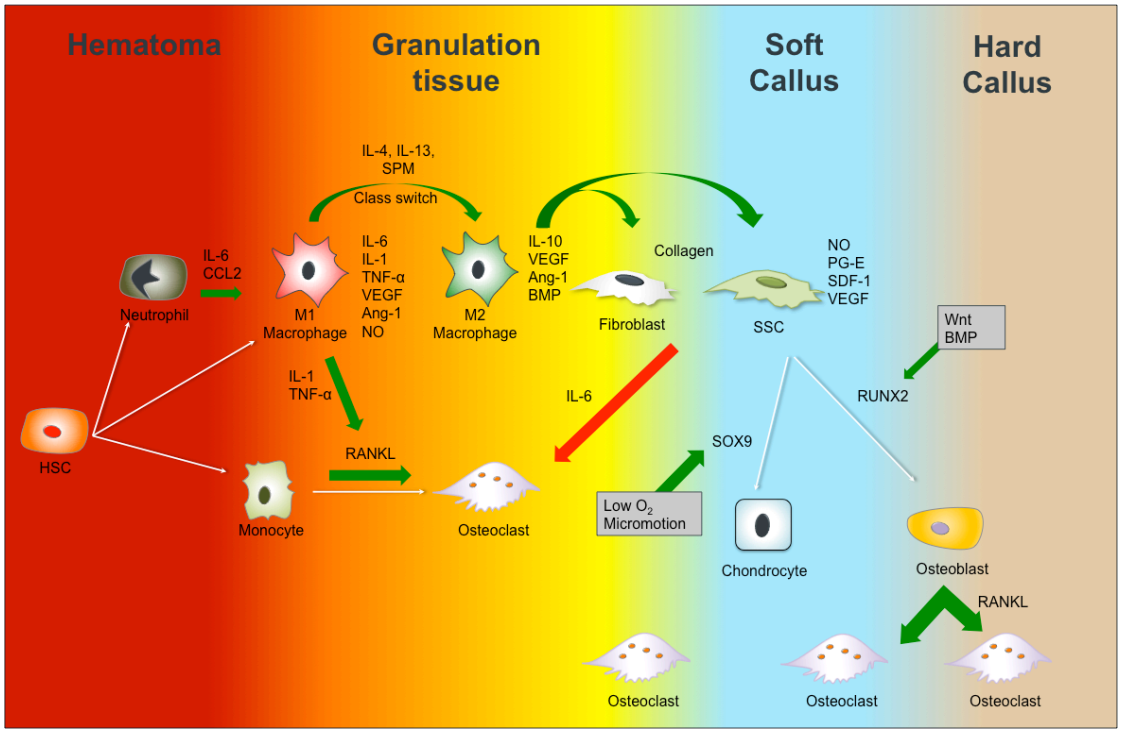

Figure 1.3: **Phases of bone fracture healing.**

The major metabolic phases during fracture healing are represented in the coloured columns. In red is the haematoma, characterised by the infiltration of neutrophils that release molecules promoting the infiltration of macrophages and monocytes. In orange/yellow is the granulation tissue, characterised by the end of the inflammation, by macrophage class switching, infiltration of fibroblasts and SSCs. In blue is the soft callus stage whereby SSCs differentiate into chondrocytes, whilst in brown is the hard callus characterised by the differentiation of SSCs into osteoblasts that produce new bone. Based on Claes et al. 2012; Kolar et al. 2010; Einhorn & Gerstenfeld 2015.

1.2.3.3 Remodelling

The hard callus that has filled the inter-fragmentary gap is progressively replaced by new bone during the remodelling phase of bone healing. The hard callus is a rigid but weak matrix of woven bone, made of collagen fibres and randomly deposited mineralised matrix. In the final step of the fracture healing, osteoclasts and osteoblasts synergistically replace the woven bone with lamellar bone, while the vasculature returns to pre-injury levels. The duration of the remodelling process depends on various factors, including patient age, type of bone involved and orientation of the fracture (Wilkins 2005), but is estimated to take 5-8 weeks in rats, whilst in humans it can be an extremely long process lasting years (Claes et al., 2012). Nevertheless, once healed, the bone is restored without

the presence of a scar, and with mechanical and functional properties identical to the original tissue (Loi et al. 2016).

Overall, fracture healing is conventionally divided into discrete stages; in reality it occurs in a series of overlapping steps in a progressive alternation of catabolic and anabolic states (Figure 1.4). Despite the complexity of this process, the bone tissue retains a remarkable ability to self-regenerate. However, such healing process can fail under adverse circumstances resulting in 'non-union' fractures.

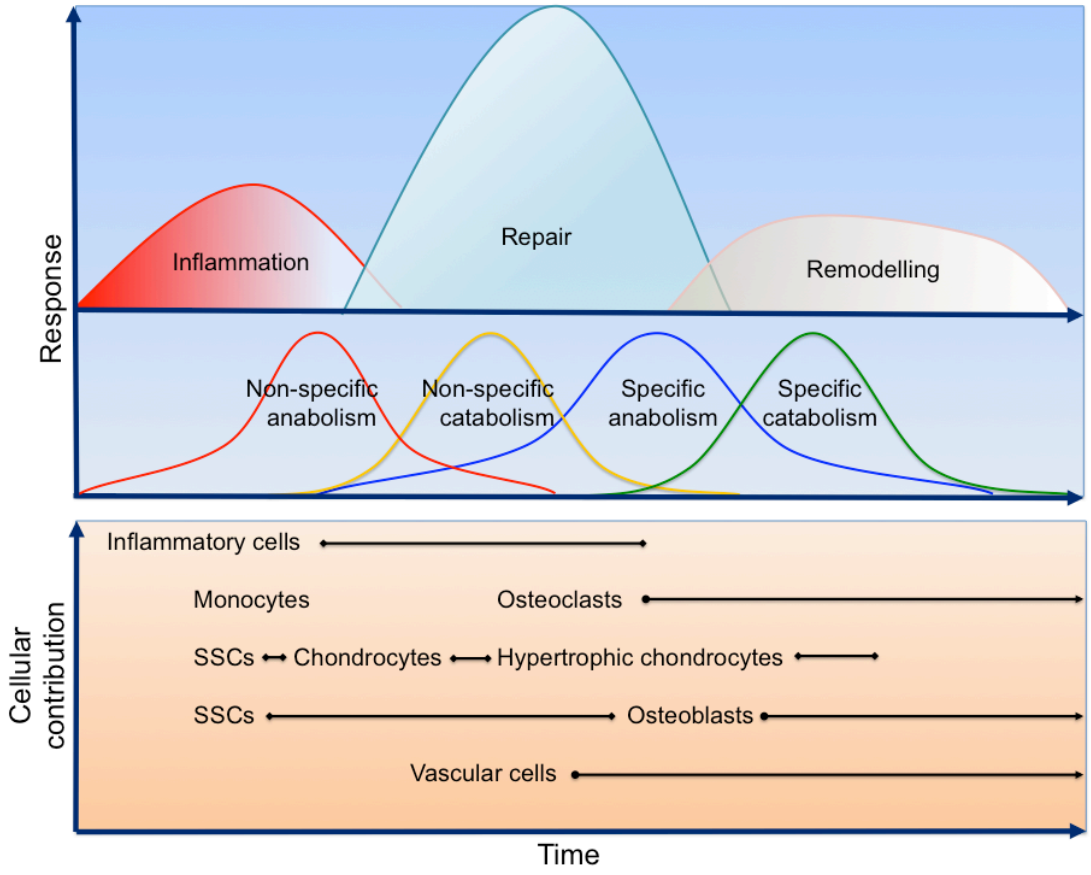

Figure 1.4: **Schematics of bone fracture healing.**

The top panel represents the canonical steps involved in fracture healing (inflammation, repair and remodelling), comprising an alternation of anabolic and catabolic stages. The bottom panel depicts the type of cells contributing to fracture healing and their persistence during the different stages of fracture healing. Based on Pivonka & Dunstan 2012.

1.2.4 Healing failure

A non-union fracture has a major impact on the socio-economic status of the patient affected (Kanakaris & Giannoudis 2007). The lack of healing in otherwise healthy

patients may be due to the trauma event itself, where the severity of the fracture, the involvement of surrounding soft-tissue (Bhandari et al. 2003), the pattern (Fong et al. 2013), the size of the gap (Mehta et al. 2012), and inadequate stabilisation (Giannoudis et al. 2000) directly affect the ability of the bone tissue to regenerate. These conditions may impair the healing process by inducing alterations to the fracture environment, at a physical and molecular level. For example, sheep with inadequate mechanical fixation displayed an increased infiltration of leukocytes in the fracture gap, indicating more pronounced inflammation (Schmidt-Bleek et al. 2012). This increased inflammation is likely to prolong the presence of pro-inflammatory M1 macrophages delaying their class switching and consequent onset of the reparative step (Grundnes & Reikeraas 2000; Schlundt et al. 2015).

Alternatively, factors independent from the traumatic injury may indirectly induce a non-union. For example, the presence of pathologies affecting the vascularisation and oxygenation of the fracture (*e.g.* peripheral vascular disease, diabetes mellitus or anaemia) have been reported to cause delayed repair (Gaston & Simpson 2007). Alteration of the overall structure of the bone is also associated with poor bone healing. Osteoporosis is a disease characterised by low bone mass and deterioration of the microarchitecture of the bone, and it is associated with a high incidence of bone fractures (Holroyd et al. 2008). Osteoarthritis and other chronic inflammatory diseases such as chronic obstructive pulmonary disease (COPD) and inflammatory bowel disease are intrinsically associated with sustained inflammation and high levels of pro-inflammatory cytokines including TNF- α and IL-1. These molecules promote the release of the receptor activator RANKL, which in turn initiates osteoclast activity leading to bone loss and secondary osteoporosis (Hardy & Cooper 2009). Having outlined the pivotal role of inflammation during fracture healing (section 1.2.3.1), it is not surprising that impaired inflammation is also associated with poor bone healing. In this context, the prolonged use of corticosteroids and non-steroidal anti-inflammatory drugs (NSAIDs), which are part of the standard treatment for chronic inflammatory diseases, has been shown to significantly impair bone healing (Aspenberg 2005). Similar effects are seen with the consumption of alcohol or the use of cigarettes (Bhandari et al. 2003; Gaston & Simpson 2007).

Although a reliable and consistent way to predict non-union fractures is not yet available, the presence of one or more of these risk factors is useful in estimating the

outcome of a fracture. Bhandari and colleagues determined that both severe open fractures and transverse fractures, together with the presence of large post-operative fracture gaps are significant predictors of non-union in tibial fractures (Bhandari et al. 2003). Recently, Meyer and colleagues demonstrated that changes in the microstructure of the bone during the first 4 weeks of the bone healing process, are predictors of the outcome of a radius fracture at 12 weeks. The authors also reported that an early increase in the serum levels of high-sensitive C-reactive protein (hsCRP), a marker of inflammation, augments the ability of the patient to actively move the injured bone 12 weeks post fracture. Therefore, it was suggested that the outcome of a bone fracture could be predicted by assessing the early levels of inflammation (Meyer et al. 2014).

Nevertheless, the ability of the bone tissue to self-regenerate following severe fractures or non-unions is limited. In these cases, a surgical intervention is required, and ideally, these procedures should be supported by pharmacological treatments to aid regeneration. Various pharmacological treatments aiming to improve and speed-up fracture healing have been investigated and demonstrated encouraging effects (see section 1.2.5). Nevertheless, all the strategies proposed present drawbacks that limit their application, so new approaches are urgently needed.

However, such treatments are still lacking, and new strategies are urgently needed.

1.2.5 Current pharmacological strategies for promoting bone healing

In cases of severe fractures, where loss of bone is significant, the first aim is to mechanically stabilise the extremities while filling the gap created by the fracture. Stabilisation is routinely achieved through the use of metal plates, rods and pins following surgical procedures, while gap filling is achieved by insertion of biomaterials or bone grafts. The gold standard in terms of bone grafts is represented by autologous bone, usually derived from the patient's iliac crest, which is source of cells and growth factors that stimulate the deposition of new matrix while allowing perfect biocompatibility. Nevertheless, autografts have inherent complications including donor site morbidity, pain, extended hospitalisation and low availability (Oryan et al. 2014). Besides the use of bone grafts, a wide range of synthetic bone substitutes derived from calcium phosphate, calcium sulphate and bioactive glass are available for clinical use in the UK, while other

biomaterials are currently under investigation. A review of such materials is beyond the scope of this thesis, but further information can be found in the following publications (Kurien et al. 2013; Dawson & Oreffo 2013; Stevens 2008).

1.2.5.1 Growth factors

In addition to the use of bone grafts, other strategies are utilised to enhance bone regeneration. Various growth factors are known to promote bone formation or aid bone healing (Gothard et al. 2014), which has led to the investigation of growth factors as a possible strategy to promote bone formation during fracture repair. Currently, bone morphogenetic proteins (BMPs) are the only growth factors approved by the food and drug administration (FDA) and the European Medicines Agency for aiding fracture healing. However, over the past 50 years, a vast number of growth factors have been tested both *in vitro* and *in vivo*, and all of them have proven ability to induce bone formation. They are briefly discussed below.

BMPs are a family of growth factors fundamental for skeletal development, bone growth and regeneration. More than 20 different isoforms have been characterised, but BMP-2 and BMP-7 are the most studied. Since 2001, these two isoforms have been approved for bone fracture treatment by the FDA and are now routinely used in different clinical conditions (Mehta et al. 2012; Dimitriou et al. 2011). Administration of BMP-7 in the early stages post-fracture accelerates both the healing process and recovery speed (Giannoudis et al. 2009), reducing the costs related to non-union fractures (Dahabreh et al. 2007). However, there are several limitations when using BMPs in clinic, including osteolysis, soft tissue swelling, ectopic bone formation due to the use of supra-physiological doses, and the high cost of the drug ($6,000 - $10,000) (Lissenberg-Thunnissen et al. 2011). Furthermore, from its initial approval for clinical use, studies investigating the application of BMP-2 after tibial fractures concluded that its use provided no significant advantages over the current standard cares (Aro et al. 2011; Lyon et al. 2013).

Local application of FGF in human tibial fractures through the use of a loaded hydrogel has been shown to promote bone union during radiographic assessments (Kawaguchi et al. 2010). PDGF, a powerful mitogen for SSCs that increases the number of immature osteoblasts while stimulating angiogenesis (Marx et al. 1998), is currently used in the clinic for the treatment of periodontal defects (Hollinger et al. 2008).

However, its efficacy in promoting bone healing following fractures is yet to be demonstrated.

Parathyroid hormone (PTH) is secreted by the parathyroid gland and regulates calcium and phosphate metabolism. Influencing the body's mineral homeostasis, PTH can indirectly affect the bone tissue and its regeneration. Intermittent administration of this hormone in humans induces an increase in bone formation and bone mineral density (Keaveny et al. 2008), and accelerates healing time (Aspenberg et al. 2008). In contrast, continuous administration of PTH or its related protein (PTHrP) has the opposite effect, inducing bone resorption and reducing bone formation. The recombinant form of the human PTH, Teriparatide (Lilly), is approved by the FDA for the treatment of osteoporosis (Tashjian & Gagel 2006) and has shown promising results in a clinical trial accelerating fracture healing in radial fractures (Aspenberg et al. 2010). Interestingly, this effect is likely due to the inhibition of Sclerostin and Dickkopf-related protein 1 (Dkk1), which are inhibitors of the Wnt signalling pathway (Guo et al. 2010).

1.2.5.2 Small molecules

Small molecules represent an attractive alternative to the use of growth factors for promoting bone repair given their vast availability and limited cost of synthesis and purification. For example, the statins are a class of hypolipidemic agents able to lower the levels of cholesterol and to induce the activation of the BMP pathway (Alam et al. 2009). Simvastatin and Lovastatin are two clinically approved small molecules with a potent bone anabolic effect. Mundy and colleagues demonstrated that following either subcutaneous injection in mice calvaria, or oral administration in rats, Simvastatin and Lovastatin were able to increase bone formation (Mundy et al. 1999). Furthermore, oral administration of Simvastatin has been shown to increase fracture healing in mice (Skoglund et al. 2002). However, these effects were only observed following continuous infusion of large doses of the small molecule, likely due to the extremely low half-life of the molecule (~2 hours), raising the issue of alternative forms of administration.

Strontium ranelate is a strontium salt of the ranelic acid, and is another anabolic molecule that reduces osteoclast activity while increasing osteoblast mineral deposition (Marie 2007). Strontium ranelate is currently prescribed in the UK for the treatment of osteoporosis (Stevenson et al. 2007), and its systemic administration has been shown to promote tibial fracture healing in rats (Li et al. 2010). Prolonged pharmacological therapy

(30/40 days) with this molecule in humans was beneficial for fracture healing in two case studies (Tarantino et al. 2010).

FTY720 is a synthetic analogue of sphingosine-1-phosphatem, which is a signalling molecule that enhances the proliferation of various cell types including endothelial cells and osteoblasts (Pederson et al. 2008). Rat models of tibial fracture treated with FTY720 demonstrated increased bone graft osseointegration, augmented mechanical stability and reduced levels of inflammation compared to control (Petrie Aronin et al. 2010).

Interesting results have been reported with the use of other small molecules such as purmorphamine (agonist of the Hedgehog pathway), and SVAK-12 and TH (agonists of the BMP pathway) which promoted bone formation following injury accelerating the healing process (Gellynck et al. 2013; Wong et al. 2013; Maeda et al. 2013).

Bisphosphonates are another class of small molecules with bone anabolic effects. These molecules are able to impair bone homeostasis towards bone formation by inducing osteoclast apoptosis (Russell et al. 2008). This ability has led to the commercialisation of various bisphosphonates for the prevention and treatment of osteoporosis (Khosla & Shane 2016). Bisphosphonates have also been shown to be efficacious for enhancing bone healing as they increase the mineral content, volume and mechanical properties of the fracture callus *in vivo* (Jørgensen & Schwarz 2011; Goodship et al. 1994; Li et al. 2000). However, concerns regarding the prolonged use of such molecules have been raised since they alter bone turnover. Therefore, and similarly to the statins, their application for fracture repair has potential but requires controlled forms of delivery.

All these growth factors and small molecules are currently under investigation for their potential role in promoting bone fracture healing. However, there is another molecular pathway fundamental in bone physiology and repair: Wnt (Marsell & Einhorn 2011). The activation of the Wnt signalling pathway through the use of proteins, small molecules or antibodies has demonstrated promising results in promoting bone fracture healing. For this reason, the modulation of the Wnt signalling pathway was the main focus of this PhD project.

1.3 The Wnt pathway

Wnt is the name of a family of proteins and their related signalling pathways (Rijsewijk et al., 1987). Its name derives from the combination of the two homologous genes, *Wingless* (*Wg*) discovered in *Drosophila* (Baker, 1987) and the proto-oncogene *Int1* discovered in mouse (Nusse et al., 1984).

The Wnt signalling pathway can be divided into the canonical and the non-canonical Wnt pathway. The latter is comprised of the planar cell polarity (Wnt-PCP) pathway, which is important for cell movement during gastrulation (Veeman et al. 2003), and the Wnt-calcium (Wnt-Ca^{2+}) pathway, which is involved in the intracellular release of calcium (Ling et al. 2009). The distinction between the canonical and non-canonical pathway is primarily ascribed to the type of Wnt receptors present on a cell membrane. However, the two signalling pathways can overlap and inhibit each other's activity (Ishitani et al., 2003). The canonical and non-canonical Wnt pathways are involved in a number of physiological processes including embryonic development, cell proliferation, cell polarity and cell fate determination (Ling et al. 2009). Therefore, it is not surprising that their impaired or unregulated activation is associated with different pathologies such as renal cell carcinoma (Hsu et al. 2012) hepatocellular carcinoma (J. Liu et al. 2011), as well as a wide spectrum of other diseases (Baron & Kneissel 2013).

1.3.1 Wnt canonical pathway

The bulk of Wnt signalling follows the canonical pathway (Reya & Clevers 2005), which is also the most investigated in the field of bone regeneration (Baron & Kneissel 2013). Activation of the canonical pathway is strictly related to the nuclear translocation of the transcriptional co-activator β-catenin. Usually, β-catenin accumulates in the cytoplasm where it is bound to a destruction complex consisting of the tumour suppressor protein axin, the scaffolding proteins dishevelled (DVL) and adenomatous polyposis coli (APC), the two constitutively active serine-threonine kinases known as glycogen synthase kinase (GSK)-3β and casein kinase (CK)-1, and the ubiquitin ligase beta-transducin repeats-containing protein (β-TrCP). In the absence of upstream stimuli, β-catenin is sequentially phosphorylated by CK1 and GSK3β, and ubiquitinated by β-TrCP, resulting in β-catenin degradation by a proteasome. When Wnt proteins bind to a heterodimeric receptor complex consisting of the seven-pass transmembrane receptor

frizzled (FZD) and the low-density lipoprotein receptor-related protein (LRP) 5/6, the pathway is activated. The creation of the receptor complex (LRP 5/6 and FZD) induces the creation of a binding site for the destruction complex, which is then sequestered. This stops the activity of β-TrCP, meaning β-catenin remains un-ubiquitinated, enabling accumulation in the cytoplasm and translocation into the nucleus. Once within the nucleus, β-catenin interacts with transcription factors such as T-cell factor (TCF) and lymphoid enhancer factor (LEF), and co-activators, promoting the expression of Wnt target genes, several of which control proliferation and differentiation of stem cells including (Clevers & Nusse 2012).

Various extracellular and intracellular molecules control Wnt signalling by interfering either with receptor-ligand binding or with intracellular signalling. Secreted FZD-related peptides (sFRPs) and Wnt inhibitory factor 1 (WIF-1) antagonise the Wnt pathway competing with Wnt proteins for binding to FZD, while Dkk and sclerostin inhibit the pathway by antagonising LRPs (Ling et al. 2009) (Figure 1.5).

Wnt signalling is involved in many physiological processes - from development to homeostasis - and its misregulation has been linked to the onset of cancer in various tissues (Reya & Clevers 2005). This is because the Wnt pathway plays a crucial role in controlling self-renewal and differentiation of embryonic stem cells (ESCs), induced pluripotent stem cells and HSCs (Ding et al. 2010; Reya et al. 2003). Moreover, there is a significant evidence for the importance of Wnt signalling in controlling SSCs fate (Ling et al. 2009), which will be reviewed in following section. Therefore, it is not surprising that the Wnt pathway has a key role in maintaining the homeostasis of the bone marrow niche (Janeczek et al. 2015), while contributing to reparative mechanism of various tissues.

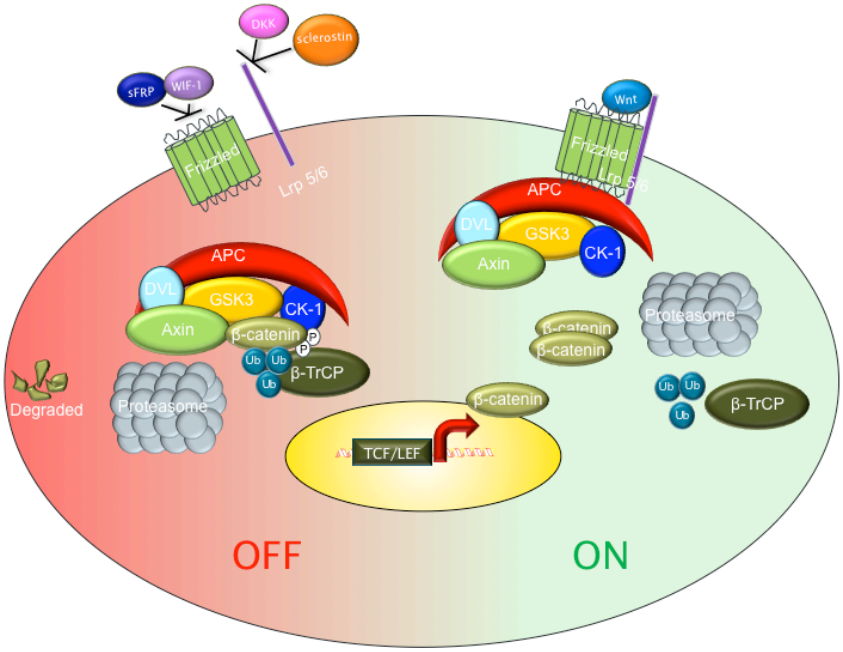

Figure 1.5: **The canonical Wnt signalling pathway**.

In the absence of Wnt proteins (OFF), β-catenin is produced and released in the cytoplasm, but sequestered by the destruction complex. Axin, APC and DVL interact with β-catenin while it is phosphorylated by the two kinases GSK3β and CK1, and then ubiquitinated by β-TrCP. Consequently, β-catenin is degraded by a proteasome and the destruction complex is recycled. On the other hand, upon activation of the pathway (ON), the destruction complex binds the receptor complex formed by LRP and Frizzled. In this way, the destruction complex is still able to bind and phosphorylate β-catenin, but ubiquitination by β-TrCP is blocked. This results in an accumulation of β-catenin in the cytoplasm and its subsequent translocation to the nucleus, where it binds the transcription factors TCF/LEF transcription factors, activating target genes. Based on: Clevers & Nusse 2012.

1.4 The Wnt pathway in bone homeostasis and stem cell biology

Investigation of Wnt-related diseases revealed the crucial role of the canonical pathway in controlling bone tissue homeostasis (Baron & Kneissel 2013). Genetic mutations altering the expression of LRP5 in mice have been shown to induce both increases and decreases in bone mass (Little et al. 2002; Gong et al. 2001), and are also the cause of a bone pathology called osteoporosis-pseudoglioma syndrome (Gong et al. 2001; Boyden et al. 2002). A disease characterised by reduced bone strength and eye abnormalities that lead to vision loss. Moreover, genetic mutations of the gene encoding for sclerostin (*SOST*) are the cause of sclerostosis and van Buchem disease, which are pathologies characterised by an excess of bone growth (Mason & Williams 2010).

Various studies carried out *in vivo* have demonstrated that activation of the Wnt canonical pathway results in increased bone formation, whereas inhibition of the pathway has the opposite effect (Babij et al. 2003; Gong et al. 2001; Kato et al. 2002; Day et al. 2005). Analysis at the cellular level has shown that the activation of β-catenin in osteoblasts increases the secretion of osteoprotegerin, a protein that inhibits osteoclast activity (Glass et al. 2005). In contrast, following bone resorption, osteoclasts are able to induce osteoblast differentiation by secreting Wnt ligands (Pederson et al. 2008). Finally, evidence from studies in rodents demonstrated that osteocytes reduce their production of the Wnt inhibitor sclerostin following mechanical loading (Robling et al. 2008). Further evidence was provided by alteration of *Wnt10* gene expression, whereby enhanced osteoblast proliferation and bone formation were observed following up-regulation, whilst mice lacking the Wnt10 protein display a severe osteoporotic phenotype (Bennett et al. 2005). Overall, these results underline how the Wnt pathway influences the activity of the three major cell types present in bone tissue. Nevertheless, Wnt plays a crucial role in determining the differentiation of SSCs.

Etheridge and colleagues demonstrated that BMSCs cultivated *in vitro* express a wide range of proteins, receptors and inhibitors of the Wnt pathway (Etheridge et al. 2004), and stimulation of the canonical pathway in SSCs has been shown to inhibit their differentiation into adipocytes or chondrocytes (Day et al. 2005; Cawthorn et al. 2012). In contrast, abolishing β-catenin expression from preosteoblasts induces their re-differentiation to adipocytes (Song et al. 2012). Nevertheless, there are considerable discrepancies in the evidence as to whether activation of Wnt signalling promotes osteogenic differentiation of SSCs. Studies *in vitro* suggested that overexpression of Wnt3A induces a significant increase in ALP activity, while reducing the expression of adipocyte protein 2 (aP2) and peroxisome proliferator-activated receptor-γ (PPARγ), which are markers expressed by adipocytes (Rawadi et al. 2003). Activation of the Wnt pathway has also been linked to increased expression of RUNX2 (Gaur et al. 2005; Bennett et al. 2005; Arioka et al. 2013), which is considered a master gene of osteogenic differentiation (see section 1.2.3.2), and is the point of convergence for the Wnt, BMP and notch pathways, whose cross-talk determines the fate of the SSCs (Chen et al. 2012). In parallel, studies *in vivo* support the notion of Wnt signalling as a controller of SSC osteogenic differentiation. Genetic inactivation of β-catenin at the early stages of

development leads to chondrocyte proliferation at the expense of osteoblasts expansion (Day et al. 2005), while stable expression of Wnt10 or administration of small molecules with GSK-3β inhibitor activity increases bone formation and drives SSC differentiation towards the osteoblast phenotype (Gambardella et al. 2011; Cawthorn et al. 2012; Bennett et al. 2005; Marsell et al. 2012; Sisask et al. 2013). In a recent study carried out in our group, the importance of the timing of Wnt signalling activation was demonstrated. A transient activation of the Wnt pathway using Wnt3A induced SSCs proliferation, reduction in cellular death and promoted osteogenic differentiation. In contrast, continuous activation of the Wnt pathway resulted in a complete abrogation of osteogenic differentiation (Janeczek et al. 2016). Overall, these studies highlight the importance of the Wnt pathway as a promoter of SSC differentiation towards the osteoblastic phenotype, and as a regulator of bone formation. However, other findings suggest that activating the canonical Wnt signalling pathway in SSCs induces their proliferation (de Boer et al. 2004; Baksh & Tuan 2007; Boland et al. 2004; Quarto et al. 2010), but inhibits both apoptosis and differentiation (Boland et al. 2004).

These contrasting results reflect a lack of consistency in experimental design, cell type, concentration, and the exposure times of the Wnt agonists used across the studies. Although a general consensus is not available, it is reasonable to speculate that canonical Wnt activation is crucial for the production of bone and its role in regulating SSC fate depends on the level (de Boer et al. 2004) and the timing (Eijken et al. 2008) of its activation.

1.5 Wnt signalling in bone healing

The activation of the Wnt signalling pathway is crucial during bone healing, as indicated by finding showing that several Wnt ligands and receptors are up-regulated during fracture repair (Chen et al. 2007). Multiple studies have evaluated the role of Wnt signalling in terms of bone regeneration following injury.

For example, a significant reduction in bone regeneration compared to control was observed in a mouse model of bone injury in which Wnt antagonist DKK-1 expression was constitutively induced (Kim et al. 2007; Chen et al. 2007). Similarly, knockout *LRP5* mice showed impaired bone fracture repair, while the constitutive expression of the same gene induced a delay in osteoblast maturation (Komatsu et al. 2010; Kim et al. 2007). Conversely, the depletion of *SOST* and sFRP-1 (molecular inhibitors of Wnt), or the

stable expression of β-catenin in mature osteoblast, promoted bone healing (Li et al. 2011; Gambardella et al. 2011; Chen et al. 2007; Gaur et al. 2009). Wnt3A aids the regeneration of bone defects in a dose-dependent manner, whereby low doses are sufficient to induce bone regeneration in young mice, whilst high doses are necessary to achieve the same effect in old mice (Quarto et al. 2010).

Monoclonal antibodies are an alternative approach to induce Wnt signalling activation. For example, antibodies antagonising the activity of the Wnt inhibitor sclerostin enhance bone healing and bone formation in both injured and non-injured bones (Suen et al. 2014; Agholme et al. 2010), and promote bone repair in mice models of non-healing femoral defects (Virk et al. 2013). Despite these encouraging results, the main application for these anti-sclerostin monoclonal antibodies is the treatment of osteoporosis. In phase II clinical trials, administration of an antiscelrostin antibody in osteoporotic women for one year increased bone density more than using teriparatide, a recombinant form of PTH (McClung et al. 2014). These findings attracted the attention of the pharmaceutical industry, who is commercialising anti-sclerostin antibodies under different names (*i.e.* romosozumab developed by Amgen, blosozumab developed by Eli Lilly, and BPS804 developed by Novartis) and their market approval as a therapy for osteoporosis is expected by 2017 (MacNabb et al. 2016).

Finally, intracellular activation of the Wnt signalling pathway through oral or local administration of small molecules which inhibit GSK-3β function has been shown to promote fracture repair (Chen et al. 2007; Sisask et al. 2013; Marsell et al. 2012), and represents an attractive alternative to modulating Wnt signalling activation in bone repair (also reviewed in Chapter 5).

Overall, Wnt/β-catenin signalling plays a fundamental role in bone development, homeostasis and fracture repair. The pharmacological activation of this pathway through systemic administration and without surgical methods represents a novel strategy for the treatment of delayed or compromised bone healing (Silkstone et al. 2008). However, because of the pleiotropy of Wnt signalling, its modulation should be carefully considered. Systemic distribution of Wnt signalling agonists may lead to a reduced therapeutic effect or to undesirable side effects such as degradation of the articular cartilage (Enochson et al. 2014). Furthermore, Wnt signalling exerts different effects on SSCs depending on the time of its activation as it could either stimulate SSCs

proliferation and osteogenic differentiation, or inhibit SSCs division and osteoblast commitment (Janeczek et al. 2015). Thus, the timing of delivery as well as the spatial localisation are crucial factors to be considered.

Given this, the use of nanoparticles such as polymersomes, may enable spatio-temporally controlled delivery of Wnt agonists to the injury site for the promotion of bone regeneration.

1.6 Drug delivery systems in regenerative medicine

The potential use of proteins, macro and small molecules as therapeutic agents for the treatment of non-healing fractures has been outlined in the previous sections. Within a given family of therapeutic agents, some molecules are more potent than others, which is an index of the amount of each molecule required to obtain the desired effect. However, the translation from bench to clinic of the most potent molecules is often limited by a number of factors such as the cost of their isolation and purification, short circulating half-life and poor solubility. Consequently, the pharmaceutical industry tends to prefer the commercialisation of less potent molecules, but with optimal pharmaceutical characteristics (Shi et al. 2010).

The continued progress in research has led to the development of nano-sized drug delivery systems (DDSs) that overcome the limitations related to the use of some molecules. In these, the therapeutic molecule of interest can be covalently linked with the carrier as well as loaded, dissolved or adsorbed into it (Gao et al. 2014). DDSs increase drug solubility and circulation half-life, permit targeted delivery and also decrease body clearance. Given such advantages, it is not surprising that the market for DDSs was estimated to be worth $121 billion in 2010 and is expanding (Almeida & Souto 2007).

The following sections will introduce some of the challenges that have to be considered when using DDSs and then some of the different types of DDSs investigated to date.

1.7 The journey of a drug delivery system towards its target

Before introducing the different types of DDSs currently under investigation in regenerative medicine, it is worth considering the barriers to transit that a DDS encounters after administration.

Each administration route presents inherent challenges that undermine the stability of a DDS, limiting its functionality and ability to reach the intended target. For example, following oral administration a carrier is transported into the low pH and enzyme rich environment which is the stomach (Ensign et al. 2012). Alternatively, DDSs can be administered *via* dermal applications or inhaled. However, dermal application requires the DDS to traverse a series of discrete cellular layers, whilst the pulmonary surface is coated with mucus and immune cells that obstruct the permeation (Prausnitz & Langer 2008; Ruge et al. 2013).

Undoubtedly, the most direct route for a DDS is *via* intravenous (i.v.) injection, leading to systemic distribution. However, DDSs in the blood stream encounter the presence of serum proteins and cellular crowding. Some of the proteins present in the serum are adsorbed on the surface of the DDS (opsonisation) resulting in clearance by either circulating or tissue resident professional phagocytic cells. The latter are often part of the reticuloendothelial system (RES), which is comprised of monocytes and macrophages present in various tissues (*i.e.* liver, spleen, lung and bone marrow) and serves a clearance system for exogenous material (Bertrand & Leroux 2012). Assuming the ability of a DDS to avoid opsonisation and clearance, accumulation in the target tissue and subsequent release of payload still need to be achieved.

The first step toward the intended target tissue is the extravasation from the blood stream. The vasculature can be classified, in order of increasing permeability to cells and macromolecules, as: continuous, which has no openings in the walls as the consequence of an uninterrupted lining of endothelial cells; fenestrated, which present some pores "fenestrae" of around 80-100 nm in diameter and allows transit of macromolecules; discontinuous, in which there are wide gaps in between endothelial cells (Majno & Joris 1978; Cleaver & Melton 2003). Vessel permeability is also dependent on the pathophysiological status of the tissue/organ. For example, solid tumours present an increased blood flow and vascular permeability that allows extravasation and accumulation of macromolecules (Matsumura & Maeda 1986) while inflamed tissues, have a damaged and highly permeable vasculature. In bone tissue, long bones receive blood through a series of arterial inlets (main nutrient arteries, periosteal, metaphyseal and epiphyseal arteries), but following fracture the vascular architecture within the bone marrow and around the fracture site is disrupted. This physical damage and the

consequent onset of inflammation increase the overall permeability of the vessels (Carano et al. 2003)(see section 1.2.3.1).

These factors promote passive targeting, which is the accumulation of macromolecules and DDSs into specific tissues. Alternatively, DDSs can be induced to actively target an organ or tissue by decorating their surface with binding motifs that are specific to receptors of ligands for a tissue or cell type (Moghimi et al. 2001; Friedman et al. 2013).

Finally, depending on whether the therapeutic molecule carried by the DDS functions extracellularly or intracellularly, the last barrier to be crossed is represented by the cell membrane. A detailed description of the possible mechanisms by which a DDS is internalised by cells is provided by Canton & Battaglia (2012). Overall, the route of internalisation greatly depends on the chemical-physical properties of the DDS used (*e.g.* size, surface charge, presence of binding motifs on the surface and shape), but generally they converge intracellularly into the endosomal pathway. In this, the DDS is initially confined into an intracellular vesicle called endosome; from there it can be recycled back towards the cellular membrane and exocytosed, transported to the trans Golgi network, or transported to lysosomes. The latter are organelles characterised by a low pH (~4/5), which induces the degradation of the DDS and the release of the payload originally incorporated (Canton & Battaglia 2012; Torchilin 2005; Sahay et al. 2010).

Despite the number of barriers and challenges present during the journey through the body, the intended target delivery can be achieved by using different types of DDS or by modulating their chemical-physical properties.

1.8 Types of drug delivery system

Several different types of DDS have been employed over the years. Below some of the most investigated will be presented, namely polymer-drug conjugates, micelles, liposomes and polymersomes (Massignani et al. 2009).

1.8.1 Polymer-drug conjugates

From a structural point of view, polymer-drug conjugates represent the simplest type of DDS. These are constituted from a polymer chain covalently linked to a molecule of

interest. Polyethylene glycol (PEG), also known as polyethylene oxide (PEO), is one of the most commonly used polymers for such DDSs. PEG is a biocompatible hydrophilic polyether and has been shown to reduce protein adsorption and aggregation in groundbreaking experiments by Frank F. Davis and Abraham Abuchowski. The authors demonstrated that both bovine albumin and bovine catalase conjugated with PEG not only lose their immunogenic properties in rabbits, but also increase their circulation-time while maintaining functional activity (Abuchowski, van Es, et al. 1977; Abuchowski, McCoy, et al. 1977). PEG is approved by the FDA for use in humans, which favoured approval in 1990 of Adagen®, a PEG-adenosine deaminase conjugate used for the treatment of severe combined immunodeficiency disease. Since then, other polymer-drug conjugates have been explored and are commercially available for various applications. Nevertheless, despite increasing the solubility and circulation half-life, polymer-drug conjugates allow for a limited spatio-temporal control of delivery, therefore, different DDSs have been proposed in order to achieve such a control.

1.8.2 Self-assembled nanoparticles

Nanoparticles represent another type of DDS comprising a wide range of subtypes that can be divided according to the material they are made of and their final supramolecular structure. Among these, self-assembled nanoparticles have been widely investigated for spatio-temporally controlled delivery of molecules. The term self-assembled refers to the process by which discrete building blocks spontaneously reorganise according to specific direct or indirect interactions (Grzybowski et al. 2009). The constituent block can be made of lipids or polymers, and following self-assembly, these will form different structures such as polymeric micelles, liposomes or polymersomes.

1.8.2.1 Micelles

A micelle is a spherical nanostructure comprising a hydrophobic core and a hydrophilic corona, which can be formed through the self-assembly of amphiphilic block copolymers or phospholipids in aqueous solution. Block copolymers are comprised of two distinct polymeric units that are linked together by a non-repeated subunit functioning as a junction between the two blocks. The final structure of a block copolymer can be simplified as $(A)_n$-b-$(B)_m$ where A and B are two different polymers, 'b'

is the junction, while *n* and *m* are the average molecular weight distribution (MW) of the polymer. Amphiphilic copolymers present a hydrophilic and a hydrophobic block, which can self-assemble in micellar structures. Micelles can be loaded with a payload of interest by either conjugating a drug with the polymer chains that form the micelle, or by loading the drug in the hydrophobic core. Such DDSs increase the solubility of water insoluble drugs and increase their circulation time (Ahmad et al. 2014). These characteristics are particularly relevant for the delivery of chemotherapeutic drugs and have led to the investigation of drug-loaded polymeric micelles for anticancer therapy in several clinical trials (Cabral & Kataoka 2014; Oerlemans et al. 2010). Nevertheless, micellar formulations present a number of limitations such as inadequate rate of drug release and loading efficiency, or the inability to deliver hydrophilic molecules (Ahmad et al. 2014).

1.8.3 Liposomes

Firstly described in the 1960s, liposomes are composed of amphiphilic phospholipids that, in aqueous solutions, self-assemble into lipidic vesicles with a structure similar to the cellular membrane (Bangham & Horne 1964). Structurally, liposomes differ from micelles as they self-assemble into one or more lipid bilayers that enclose an aqueous core.

Liposomes are widely used as pharmacological carriers given their ability to encapsulate hydrophilic molecules in their aqueous core and hydrophobic molecules within the lipid bilayer (Torchilin 2005). In 1990, the FDA approved the therapeutic use of liposomes containing amphotericin B for the treatment of fungal infections (AmBisome®). Following the commercialisation of this landmark product, other liposomal preparations have been produced. These include Doxil®, Caelyx® and Myocet® which are all trade names for liposomes loaded with the chemotherapeutic drug doxorubicin, a DNA intercalating agent approved in 1995 for the treatment of AIDS-associated Kaposi's sarcoma (Farokhzad & Langer 2009). One of the major limitations to the use of liposomes is their relatively short life-time. When systemically administered, liposomes are cleared from the blood stream within minutes by macrophages or components of the RES (Moghimi & Szebeni 2003; Moghimi et al. 2001). Although this issue has been partially overcome through the creation of synthetic lipids conjugated with PEG, which has been shown to significantly increase blood circulation time of various nanocarriers by reducing their opsonisation and clearance (Photos et al. 2003; Li &

Huang 2009), another major limitation related to the use of liposomes is the drug release profile. Liposomes are intrinsically leaky and therefore are poor at retaining payloads (Discher et al. 1999; Discher et al. 2007; Lasic & Papahadjopoulos 1998). In this context, block copolymers can self-assemble in vesicle-like structures called polymersomes, which present increased chemical-physical properties compared to liposomes.

1.9 Polymersomes

Polymersomes (PM) are composed of block copolymers that self-assemble in polymeric vesicles, creating a structural conformation similar to that of liposomes with a aqueous core and a hydrophobic shell (Discher et al. 1999; Discher & Eisenberg 2002). However, the presence of block copolymer rather than lipids confers advantages to PMs over liposomes. By measuring the rate of PM swelling as a function of external medium osmolarity, Discher and colleagues reported that PMs have a thick hydrophobic wall, ~10 times less permeable than the phospholipid bilayer that composes liposomes (Bermudez et al., 2002, Discher et al., 1999). The thick polymeric shell also underpins the enhanced mechanical properties of PMs in comparison to liposomes (Discher & Eisenberg 2002). The differences between the two types of DDSs are likely due to the arrangement of phospholipids and block copolymers into the bilayer. In fact, while phospholipids usually form an ordered structure with a well-defined spatial distribution of the hydrophobic tails, block copolymers entangle, thus creating a more interdigitated structure (Discher & Eisenberg 2002; Battaglia & Ryan 2005). This explains why liposomes have a characteristic hydrophobic shell thickness of ~3-5 nm, while in PMs this can be 4 fold thicker (Bermudez et al. 2002). Additionally, by analysing the concentration of fluorescent PMs in blood serum following systemic injection in rats, it was demonstrated that the circulation time of PMs *in vivo* is ~ 2 fold longer than liposomes (Photos et al. 2003). These attractive characteristics have led to a wider investigation of these polymeric self-assembled nanocarriers for drug delivery.

1.9.1 Polymersomes: self-assembly process and physical characteristics

Block copolymers can self-assemble into different conformational structures ranging from spherical micelles to vesicles (Mai & Eisenberg 2012). The self-assembly process is initiated when the concentration of amphiphilic molecules in solution matches

or exceeds a value defined as critical micelle concentration (CMC), leading to the aggregation and spatial re-arrangement of the molecules (Mai & Eisenberg 2012; Discher & Eisenberg 2002).

In solutions where the concentration of block copolymer is above the CMC, the transition between different structures is dictated by the molecular packing factor '*p*'. This parameter is derived from the formula

$$p = \frac{v}{a * lc} \quad (1)$$

Where '*v*' is the volume of the hydrophobic segments (which is approximately similar to the molecular weight of the hydrophobic block), '*a*' is the surface area occupied by the hydrophilic chain, and 'l_c' is the length of the hydrophobic chain. By calculating '*p*' it is possible to predict the final self-assembled structure, this can be summarised in three main groups:

I) Spherical micelles, formed when $p \leq 1/3$,

II) Cylindrical micelles (also called worms-like structures), formed when $1/3 \leq p \leq 1/2$,

III) PMs, formed when $1/2 \leq p \leq 1$ (Christian et al. 2009; Blanazs et al. 2009) (Figure 1.6).

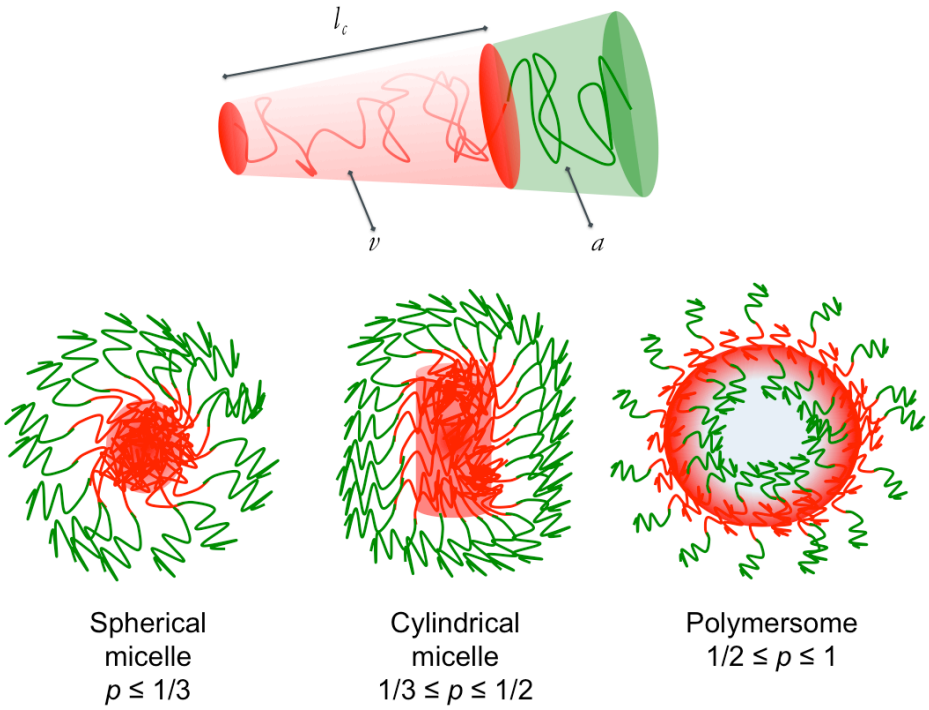

Figure 1.6: **Amphiphilic block copolymers self-assembly into different structures.**

Block copolymers re-arrange their orientation creating different structures depending on the size of the hydrophilic and hydrophobic blocks. p is the packing parameter that is defined as $p = v/(a^*lc)$, where v is the volume of the hydrophobic chains, a is the area of the hydrophilic head group, and lc is the length of the hydrophobic tail. Based on Oltra et al. 2014; Blanazs et al. 2009.

The re-arrangement of the copolymers into different morphologies influences the ability of these structures to function as DDSs. PMs possess a wide hydrophilic core that can accommodate water-soluble molecules and a thick hydrophobic shell that can be loaded with hydrophobic payloads, whereas spherical and cylindrical micelles can only be loaded with hydrophobic molecules (Oltra et al. 2014). Additionally, the final conformation and size can greatly affect the biodistribution and circulation time *in vivo* (Geng et al. 2007; René P Brinkhuis et al. 2012). The hydrodynamic diameter of micelles ranges from 2 to 20 nm, while PMs can span tens of nm to μm (Cabral & Kataoka 2014; Discher et al. 1999). This difference in size is important considering that upon systemic administration *in vivo*, nanocarriers encounter a series of physiological barriers with different size selectivity, which together determine their final distribution (Bleul et al. 2015; Bertrand & Leroux 2012). For example, the kidneys, which are responsible for blood filtration, present an endothelium with a fenestration of 60 to 80 nm, while the glomerulus within the kidneys is freely permeable to molecules smaller than ~6 nm

(Haraldsson et al. 2008). The lungs have capillaries of 2 to 13 μm and the liver has sinusoids of 5 to 10 μm, but with fenestrations of 100 to 150 nm (Bertrand & Leroux 2012; Bleul et al. 2015). These numbers underline the importance of controlling the size of the DDS employed in order to allow its distribution and accumulation in the intended target tissue.

1.9.2 Polymersome production

Several methodologies for the production of PMs have been reported in the literature, and the size of the PMs produced can be altered by the synthesis strategy. The preparation methods include electroformation (Bi et al. 2013), photolithography (Howse et al. 2009) and microfluidic approaches (Zhang et al. 2006); however, the most commonly used techniques are thin-film rehydration and solvent injection, which is also called nanoprecipitation or solvent-switch. Film rehydration is routinely used for the preparation of liposomes, and is also applicable to amphiphilic block copolymers (Discher et al. 1999; Photos et al. 2003). In brief, phospholipids or copolymers are dissolved into an organic solvent in a round-bottomed flask. The solvent is evaporated leaving a thin-film of lipids or polymer. The film is then rehydrated through addition of an aqueous buffer, and uni- and multi-lamellar vesicles are formed with the application of sonication. This process is optimal for a bulk production, but it results in the formation of nanoparticles with a broad size range, and therefore requires a successive step of filtration where nanoparticles are extruded through nanosized pores. Such filtration is practical for liposomes, given the fluidity of their lipidic membrane, but is less optimal for PMs (Guan et al. 2015). Nanoprecipitation is the alternative method, which results in the production of more uniformly sized PMs. In this technique, the block copolymer is dissolved in a water-miscible organic solvent, which is then slowly added to the aqueous buffer, leading the formation of PMs with a narrow size distribution (a detailed description of the process is provided in section 2.2.2). This methodology presents limitations, such as the need for a purification step to remove the excess of organic solvent still present in the preparation; however, it is highly reproducible and relatively quick (Kamaly et al. 2013; Oltra et al. 2014; Guan et al. 2015; Zhu 2014).

Besides the choice of preparation technique, PMs final size can be influenced by the nature of the solvent, the presence of additives during the process, and most importantly, by the concentration and composition of the block copolymer used, which

also dictates the final properties of the DDS to a much bigger extent (Bleul et al. 2015). With particular regards to the choice of polymer used, several reports demonstrate that the MW of the hydrophobic block influences the size of the final vesicle and the thickness of the shell, which in turn, affects the permeability and retention of hydrophobic molecules. For example, Photos and colleagues showed that PMs formed using PEG-b-polybutuadiene (PBD) copolymer, whose MW ranged from ~46 to 130 g/mol, displayed various thicknesses of the PM shell (9.6 – 14.8 nm) (Photos et al. 2003). These results were supported by studies from Bermudez and Battaglia (Bermudez et al. 2002; Battaglia & Ryan 2005), underlining the possibility that the DDS can be adapted according to the intended payload and target tissue.

1.9.3 Environment responsive polymersomes

The wide number of polymers available commercially offers the ability to create environmental stimuli-responsive PMs that release their payload in a controllable way. PMs can be engineered to be pH-sensitive by using block polymers whose solubility in water is dependent on the pH of the environment. One such example is PMPC-PDPA (Poly(2-methacryloyloxyethyl phosphorylcholine)-co-poly(2-(diisopropylamino)ethyl methacrylate)) block copolymer (Hannah Lomas et al. 2010). The DPA block present in this copolymer is comprised of a tertiary amine group that is un-protonated and therefore hydrophobic at pH ~6.4, whilst it becomes protonated and hydrophilic at a pH lower than 6.4 (Pearson et al. 2013). PMs produced with this block copolymer result to be structurally stable at physiological pH, whereas they disassemble at a lower pH thus releasing their payload. This strategy is useful for the intracellular delivery of molecules, considering that PMs are internalised by cells by endocytosis, that leads the entrapment of nanoparticles in specialised vesicles (*i.e.* endosomes and lysosomes) with a very acidic pH (Canton & Battaglia 2012) (see section 1.7). pH responsive PMs are able to escape from these organelles due to the high osmotic pressure created by the rapid disassembly of the PMs into numerous unimers, that induces the rupture of the cellular organelle and the diffusion of the payload in the intracellular environment (Massignani, Lomas, et al. 2010).

Temperature responsive PMs can be created using copolymers that incorporate poly-N-isopropylacryl-amide (PNIPAM). PMs formed from PEG-PNIPAM copolymer self-assemble in water at temperatures higher than 32 °C, and so disassemble when the temperature is reduced, releasing their payload (Qin et al. 2006). Alternatively,

temperature responsive PMs can be created using poly(*N*-vinylcaprolactam)-poly(dimethylsiloxane)-poly(*N*-vinylcaprolactam)(PVCL-PDMS-PVCL). These PMs are responsive to a range of physiologically relevant temperatures (37-42 °C), and were found to be able to deliver the anticancer drug, doxorubicin, in human alveolar adenocarcinoma cells (A549) (Liu et al. 2015).

Oxidative and light responsive PMs have also been created. The first type is formed using poly(propylene sulphide) (PPS) as hydrophobic block. This polymer progressively increases its hydrophilicity during its conversion from sulphide to sulphoxide and then sulphones, a process caused by oxidative stress (Napoli et al. 2004). Ultra violet (UV) and visible light responsive PMs are produced either using a photosensitive linker between the blocks of the copolymer, which undergoes cleavage following irradiation with UV light (Cabane et al. 2010; Cabane et al. 2011), or by incorporating a chromophore in the membrane of the PMs, which experiences conformational changes following exposure to light (Mabrouk et al. 2009). In both cases, the external stimuli induce a perturbation in the PM structure, which in turn leads to release of the payload.

An alternative method for controlling the release of the payload from PMs is the use of hydrolysable polymers such as polycarbonate and polyester. These polymers undergo hydrolytic degradation in the presence of water molecules, with consequent destabilisation of the PM structure and payload release (Guan et al. 2015; Ahmed & Discher 2004). A few examples of polyester structures are poly ε-caprolactone (PCL), polylactic acid (PLA) and polylactic-co-glycolic acid (PLGA). In particular, PCL is an FDA-approved hydrophobic polymer with a low melting point (59-64°C), and can be biodegraded into non-cytotoxic products by the human body (Sun et al. 2006). PCL undergoes degradation by non-enzymatic hydrolysis of the ester groups that leads to the production of 6-hydroxylcaproic acid. This is then eliminated from the body *via* the citric acid cycle (Woodruff & Hutmacher 2010). The rate of degradation of PCL depends on its MW but is generally quite slow. This affects the kinetics of release of a putative drug loaded into a scaffold or nanoparticles comprised of PCL. Peppa's group demonstrated through mathematical modelling that the release of the anticancer drug, paclitaxel, from PCL scaffolds is biphasic, with an initial burst release followed by a continuous diffusion until exhaustion (Lao et al. 2008). These characteristics have been widely investigated for

the creation of scaffolds in a variety of tissue engineering applications ranging from ligament, nerve, skin, cartilage and bone regeneration (reviewed by Ulery et al. 2011). It also led to the commercialisation of a contraceptive capsule made of PCL, which mediates the prolonged release of levonorgestrel (Darney et al. 1989).

Nevertheless, the modification of PCL with the addition of other polymers, such as PEG, leads to the formation of amphiphilic copolymers with different physical properties (Kamaly et al. 2016). For example, Ghoroghchian and colleagues demonstrated that PEG-PCL PMs display a biphasic drug release profile at physiological pH (7.4), in agreement with the mathematical modelling from the Peppa's group. However, a reduction in environmental pH (from 7.4 to 5.4) was found to accelerate the acid-catalysed hydrolysis of PCL thus inducing a single phase release (constant release) (Ghoroghchian et al. 2006). Discher and Ahmed have extensively studied the release of a payload from PEG-PCL PMs. As previously stated, polyesters undergo hydrolytic cleavage in the presence of water molecules. Such degradation occurs at the chain-end of the PCL polymer resulting in its progressive cleavage and subsequent shortening that alters the ratio between hydrophilic and hydrophobic blocks. As a consequence, PMs undergo a series of morphological changes, beginning with the initial formation of membrane pores leading to the release of any hydrophilic payload encapsulated in the aqueous core. Secondly there is a morphological transition from a vesicle to worm-like micelle, and then finally to a spherical micelle (Ahmed & Discher 2004; Ahmed et al. 2006; Geng & Discher 2006; Loverde et al. 2010). This shape transition induces a slow release of any hydrophobic cargo originally loaded, as the progressive degradation of the PCL block reduces the carrying ability of the system (Geng & Discher 2006). Gel permeation chromatography confirmed that the predominant process of PEG-PCL disassembly is hydrolysis, since the main product generated was 6-hydroxycaproic acid (Geng & Discher 2005). However, despite the fact that hydrolysis is favoured by a low pH, which is found in the endocytic organelles sequestering PMs following cellular uptake and should lead to a fast PM disassemble within cells, structurally intact PEG-PCL nanoparticles were observed within cellular bodies 24 hours after their internalisation (Chernenko et al. 2009). This gives rise to an intriguing question regarding the kinetics of payload release from PEG-PCL PMs once internalised by cells. The answer to this question depends on the type of payload encapsulated (*i.e.* hydrophilic *vs.* hydrophobic), as well as the cell type investigated, but could be extended to various DDS.

In fact, there is a paucity of information in the literature regarding the kinetics and the amount of drug released intracellularly by PMs.

PEG-PCL copolymer was chosen in this PhD project for the production of PMs. Although this does not allow for a finely controlled release such as that achievable using the copolymer previously introduced, PEG and PCL are both FDA approved polymers and PMs produced have been vastly characterised. These factors are very important in vision of a clinical translation of these PMs.

1.9.4 Polymersomes and the delivery of small molecules

This introduction has outlined how PMs represent a versatile system that can be tailored in order to obtain a controlled delivery of therapeutic molecules in both space and time. The next sections will provide some examples of encapsulation and delivery of small molecules by PMs, before focussing on the use of nanoparticles for bone regeneration and Wnt signalling activation.

Small molecules are becoming increasingly important tools not only for therapies, but also for understanding the molecular mechanisms behind important cellular processes such as stem cell proliferation and differentiation. Natural and synthetic small molecules are routinely used for the treatment of various types of cancer as they can target signalling molecular pathways, inhibit DNA replication inducing apoptosis and preventing tumour metastasis (Schugar et al. 2007). Moreover, they have also been useful in understanding the importance of the Wnt signalling pathway for the self-renewal of ESCs (Sato et al. 2004).

Encapsulation of small molecules into PMs has been the subject of several studies, most of which focused on the delivery of anticancer drugs. The possibility of increasing drug solubility while enhancing specific targeting is a very appealing feature for any chemotherapy. Doxorubicin is a common chemotherapeutic drug that intercalates in the DNA inducing cellular apoptosis, and has been one of the first small molecules to be encapsulated in PMs (Choucair et al. 2005). PMs can also be loaded with high concentrations of the hydrophobic molecule, Taxol, another anti-cancer drug (Zhang et al. 2012; Ahmed et al. 2006), and were eventually co-loaded with both molecules. Ahmed and colleagues were the first to report the successful delivery of both paclitaxel and doxorubicin using PMs. The authors demonstrated that PEG-PLA PMs, loaded with

Taxol and DOX and injected in mice, were able to induce tumour shrinkage significantly more than the unencapsulated drugs (Ahmed et al. 2006). In addition, a variety of other small molecules have been loaded within PMs, ranging from near infrared dyes for the imaging of PMs localisation into deep tissue (Christian et al. 2007; Xin et al. 2011), haemoglobin for the delivery of oxygen (Rameez et al. 2008), antibiotics (Wayakanon et al. 2013), as well as fluorescent probes (Massignani, Canton, et al. 2010). Interestingly, there are no published studies investigating the loading of PMs with small molecules targeting the Wnt pathway. This is a strategy that could be exploited for the treatment of various diseases and pathological conditions, including bone fracture healing (Nusse 2005; Xu et al. 2014).

1.10 Nanoparticles and Wnt

Despite being highly versatile and therefore suitable for multiple applications, PMs have so far been poorly employed in the orthopaedic field, likely due to the research field being focused on drug delivery for cancer therapy rather than tissue regeneration (Guan et al., 2015). Some of the challenges related to the use of nanoparticles for bone regeneration are the choice the payload that can promote bone formation, the timing of the delivery and the duration of the stimuli. In particular, there is little evidence regarding the use of nanoparticles in promoting bone fracture healing, and this is surprising given the opportunities that PMs offer, as discussed above.

Most of the research regarding the use of nanoparticles and bone has also primarily focused on the delivery of anticancer drugs for osteosarcoma and metastatic bone disease. For example, Swami and colleagues demonstrated that PEG-PLGA nanoparticles tethered with alendronate on their surface had an increased affinity for bone tissue both *in vitro* and *in vivo*. Upon loading with a model anticancer drug, bortezomib, these nanoparticles reduced the progression of metastatic cancer (Swami et al. 2014). A more detailed list of nanoparticles used for the treatment of cancer metastasis in bone and osteosarcoma is provided by Gu et al. 2013.

Some examples of bone regeneration achieved using nanoparticles have been reported with the delivery of statins and BMP. PLGA nanoparticles loaded with lovastatin and delivered locally were shown to promote bone fracture healing in fractured

mice (Garrett et al. 2007; Ho et al. 2011), while Gibbs and colleagues demonstrated the production of bone in mice following treatment with clay nanoparticle gels loaded with physiological doses of BMP (Gibbs et al. 2016). Delivery of BMP, and consequent osteogenic differentiation of BMSC was also demonstrated using polymeric nanoparticles (Mercado et al. 2009). Another strategy for promoting bone formation is the use of small interfering RNAs (siRNAs) that interfere with the expression of a specific gene, for example, a gene that inhibits the production of bone matrix from osteoblasts. The major challenge with the use of any nucleic acid based approach, including siRNA, is the need for a non-cytotoxic and cell specific intracellular delivery system (Wang & Grainger 2012). In this context, Liang and colleagues developed a liposomal preparation decorated with osteoblast specific aptamers and loaded with siRNA targeting an intracellular negative regulator of bone formation. The authors demonstrated that repeated injections of this formulation promoted bone formation in mice models of osteoporosis (Liang et al. 2015). However, the primary focus of this project was the modulation of the Wnt signalling pathway for promoting bone regeneration.

There are only a few examples in the literature where the activation of the Wnt signalling pathway has been modulated by the use of nanoparticles. PLGA nanoparticles have been efficiently loaded with curcumin, a natural agonist of canonical Wnt signalling, and shown to localise in the brain tissue of rats. Furthermore, the curcumin-loaded PLGA nanoparticles were found to induce neurogenesis and reverse cognitive deficits in mouse models of Alzheimer's disease (Tiwari et al. 2014). Another example is the functionalisation of silica nanoparticles with a short peptide (FRATide) derived from the frequently rearranged in advanced T-cell lymphomas-1 (FRAT1) protein, which has GSK-3β inhibitory functions. These nanoparticles have been shown to localise in the cytosol of human embryonic kidney cells and rat neural stem cells *in vitro* where they mediated the activation of the Wnt signalling pathway (Shah et al. 2011). In terms of bone regeneration, the only DDS used to activate the Wnt signalling pathway is the liposome.

Liposomes loaded with Wnt3A delivered locally in bone injured mice have been shown to promote bone healing by stimulating the proliferation of skeletal progenitors, and further differentiation into osteoblasts (Minear et al. 2010). The use of this preparation also promotes osseointegration of implants in murine bone defects (Popelut

et al. 2010). The enhanced bone healing as well as increased osseointegration may be mediated by the protective action that liposomes have on Wnt3A, preserving their activity, increasing their half-life and allowing for a targeted delivery, as opposite to the free formulation of the protein (Dhamdhere et al. 2014). Finally, no studies in which PMs have been employed for the delivery of Wnt agonists to induce bone regeneration are present in the literature.

These results highlight the potential of using the activation of Wnt signalling for promoting bone anabolism; however, previously outlined studies emphasised the need for spatio-temporally controlled delivery of Wnt signalling agonists (see sections 1.4 and 1.5). As such, this project focused on the investigation of PMs as a spatio-temporal controlled delivery system for the activation of Wnt signalling through the use of small molecules.

Hypothesis and aims

The overall hypothesis of this PhD project is that polymersomes loaded with a small molecule possessing Wnt agonist activity may be used as a novel systemic treatment to aid bone healing.

The project tested three different hypotheses through specific aims:

Hypothesis (I)

Polymersomes can be used to deliver a model cargo to different cell types, and the number of PMs releasing payload intracellularly can be quantified at a single-cell level.

Aims

- To produce and characterise polymersomes that incorporate quenched fluorescein that becomes fluorescent on release;
- To determine polymersome cellular uptake and induced cytotoxicity in different mammalian cell types, as well as in different culture conditions;
- To assess polymersome uptake and distribution in freshly isolated human BMMNCs;
- To quantify the number of polymersomes releasing payload intracellularly in the different cell types.

Hypothesis (II)

Polymersomes loaded with a Wnt agonist can activate the Wnt signalling pathway in a controlled manner priming the osteogenic differentiation of human BMSCs.

Aims

- To produce and characterise polymersomes that incorporate a Wnt agonist and to determine their stability over time;
- To assess the internalisation of polymersomes that incorporate a Wnt agonist in Wnt reporter cells and BMSCs;

- To measure the ability of polymersomes incorporating a Wnt agonist to induce activation of the Wnt signalling pathway in reporter cells;
- To assess differences between loaded polymersomes and free Wnt agonist in the kinetics of Wnt signalling relative to induced cytotoxicity in reporter cells;
- To measure activation of Wnt signalling in BMSCs following incubation with polymersomes incorporating a Wnt agonist;
- To quantify the effect of polymersomes incorporating a Wnt agonist on the proliferation and differentiation potential of BMSCs.

Hypothesis (III)

Polymersomes injected intravenously in a mouse model of bone injury will accumulate at the fracture site and promote bone fracture healing.

Aims

- To produce and characterise polymersomes that incorporate hydrophobic fluorescent dyes;
- To assess the distribution of polymersomes following systemic administration in healthy mice;
- To produce a unilateral bone drill defect in mice femurs, and to determine the distribution polymersomes following systemic administration;
- To quantify the effects of a systemic injection polymersomes incorporating a Wnt agonist following creation of a bone drill defect.

Chapter 2: Materials and Methods

2.1 Materials

2.1.1 Cells

Mouse L929 fibroblasts were obtained from ATCC (USA), Human MG63 cells were bought from Sigma Aldrich (UK), while the 3T3 murine fibroblast Wnt reporter cells were purchased from Enzo Life Sciences (USA). Cells were maintained in Dulbecco's Modified Eagle's medium (DMEM) (GIBCO, UK) supplemented with 10% (v/v) (foetal bovine serum (FBS) (Invitrogen, UK), 100 U/ml penicillin and 100 μg/ml streptomycin (PAA, UK). Cells were incubated at 37 °C and 5% CO_2, passaged by the addition of 1% (v/v) trypsin-EDTA (Invitrogen, UK), and seeded in T75 flasks (Fisher, UK). Note that the concentrations of penicillin and streptomycin have been kept constant regardless of the cell type or experiments carried out.

Bone marrow mononuclear cells (BMMNCs) and the stromal component, namely bone marrow stromal cells (BMSCs), were isolated from bone marrow samples obtained, with informed consent (Local Research Ethics Committee, 194/99/1), from haematologically normal patients undergoing hip arthroplasty at the Southampton General Hospital due to degenerative disease or fracture.

2.1.2 Block copolymers

α-amino-ω-hydroxy terminated NH_2-PEG (5.8k)-b-PCL (19k) and PEG (5k)-b-PCL (18k) were purchased from Polymer Source Inc. (Canada). Note that the value expressed in brackets indicates the average molar mass (M_n) of the amphiphilic copolymer used and is represented in g/mol. NH_2-PEG (5.8k)-b-PCL (19k) was in use within the group and it was used both to compare results from previous experiments and in order to complete unfinished work.

A complete list of all the reagents used can be found in the Appendix (see section 7.1).

2.2 Methods

2.2.1 Bone marrow mononuclear cells (BMMNCs) isolation

Following resection of the femoral neck with a bone saw, bone marrow material is removed from the medulla of the proximal femur and transferred to a universal container with aseptic technique by the designed surgeon. The bone marrow collected, which contains small bone fragments and fat tissue, is washed several times with minimum essential medium α (α-MEM) (Gibco, UK) supplemented with penicillin and streptomycin (PAA, UK). α-MEM is added to the tube containing the bone marrow, this is then vigorously shacked, and the content is transferred to a new collection Falcon tube. This operation is repeated several times until the bone fragments originally present in the sample appear of a white colour, indicating cells deprivation, whilst the rest of the sample is discarded into Virkon (USA). At the end of this process, the sample is filtered through a cell strainer (40 μm filter) in order to remove eventual small pieces of trabecular bone present, and is divided into 2 samples. Then, the cell suspension is carefully layered onto a density gradient separation solution (Lymphoprep, Axis-Shield, UK) in a 1:1 ratio (v/v) by the use of a plastic Pasteur. The solutions are centrifuged at 800x *g* for 40 minutes at 18 °C. Using Lymphoprep it is possible to separate erythrocytes, granulocytes and mononuclear cells. BMMNCs are present at the interface between the α-MEM and the Lymphoprep, and are manually collected by the use a plastic Pasteur. During this process, aggregates of erythrocytes and granulocytes are often collected.

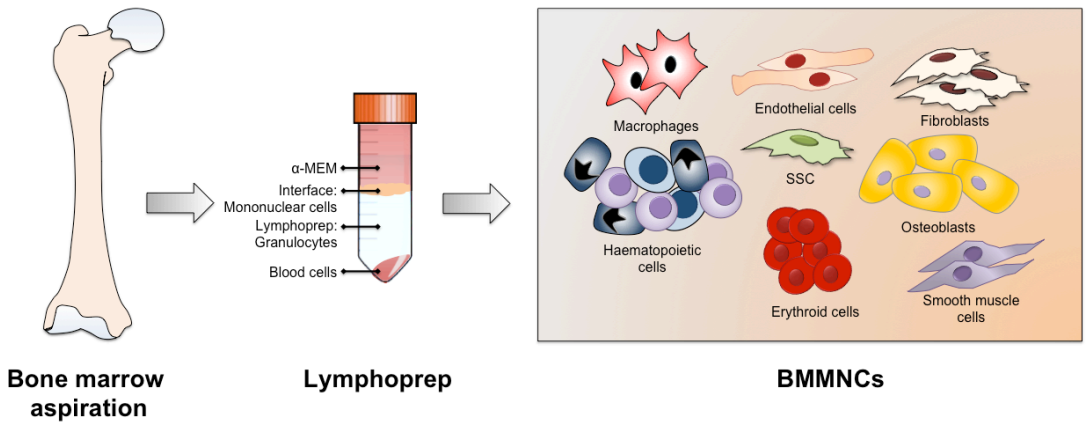

Figure 2.1: **Lymphoprep gradient separation of bone marrow cells.**

BMMNCs are then washed using α-MEM supplemented with penicillin and streptomycin by sequential centrifugation at 240x *g* for 5 minutes at 18 °C. Cells are then resuspended in α-MEM supplemented with 10 % (v/v) FBS, penicillin and streptomycin. In order to eliminate remaining red blood cells, Easy Lyse Erythrocyte Lysing Reagent (Dako, Denmark) is used. Cells are incubated for 5 minutes at room temperature with a solution of lysing reagent diluted 20x in PBS, next cells are counted using trypan-blue dye (Sigma Aldrich, UK). Finally, BMMNCs are seeded in T175 flasks and maintained in the same media for 5 days, this process aids the selection of BMSCs, which are the cells with the ability to adhere to tissue culture plastic. From day 6 onwards, cells are washed with phosphate buffered saline (PBS) and then cultured in α-MEM supplemented with 10 % (v/v) FBS, penicillin and streptomycin up to passage 5. Cells are incubated at 37 ºC and 5% CO_2 and passaged by the addition of 1% (v/v) trypsin-ethylenediaminetetracetic (EDTA). Note that all the experiments presented in this thesis were carried out using BMSCs that were passaged a maximum of three times.

2.2.2 Polymersomes (PMs) preparation

2.2.2.1 Encapsulation of hydrophilic molecules in PMs (fluorescein and BIO)

PMs loaded with hydrophilic molecules were prepared by dissolving 6 mg of either PEG5.8k-b-PCL19k or PEG5k-b-PCL18k in 0.4 ml of dimethylformamide (DMF) (Sigma, UK). The solution was placed in an ultrasonic bath to aid dissolution. Meanwhile, 0.332 g of sodium fluorescein (fluorescein) (Sigma Aldrich, UK) were dissolved in 1 ml of DMF and 9 ml of PBS creating a 100 mM solution, and placed in an ultrasonic bath to aid dissolution. For encapsulation of 6-bromoindirubin-3'-oxime (BIO), this was dissolved in PBS at the desired concentration (note that BIO is soluble in PBS up to a concentration of ~200 μM). The polymer solution was then added drop wise (~1 drop every 8 seconds) to 1.6 ml of either fluorescein or BIO under rapid stirring (Figure 2.2). Alternatively, empty-PMs, which are loaded with PBS, were produced by adding the polymer solution drop wise to 1.6 ml of PBS under rapid stirring. The sample was then dialysed against excess of PBS (300 ml) using regenerated cellulose (10,000 MWCO) (Sigma Aldrich, UK) for at least 24 hours, and with at least 3 changes of PBS in the 'sink'

compartment. Finally, the sample produced (fluorescein-PMs or core-loaded PMs) was collected, filtered through a Sephadex column (G-25, Sigma Aldrich, UK) and stored at +4 °C until used.

2.2.2.2 Encapsulation of hydrophobic molecules in PMs (BIO, DiR and DiI)

PMs loaded with hydrophobic molecules were prepared by dissolving 6 mg of PEG5k-b-PCL18k in 0.4 ml of defined concentrations of BIO, or a solution of 58 μM of DiR-DiIC$_{18}$ (7) (1, 1'-Dioctadecyl-3, 3, 3', 3'-tetramethylindotricarbocyanine Iodide) (DIR, Perkin Elmer, USA) or 49 μM of DiI-DiIC$_{18}$ (3) (1, 1'-Dioctadecyl-3, 3, 3', 3'-tetramethylindotricarbocyanine Iodide) (DiI, Sigma Aldrich, UK), and placed in an ultrasonic bath to aid dissolution. The polymer solution containing the dissolved hydrophobic molecule was then added drop wise (~1 drop every 8 seconds) to 1.6 ml of PBS solution under rapid stirring (Figure 2.2). The sample was then dialysed against excess of PBS (300 ml) using regenerated cellulose (10,000 MWCO) for at least 24 hours and with at least 3 changes of PBS in the 'sink' compartment. Finally, the sample (shell-loaded PMs, DiR-PMs or DiI-PMs) was collected and stored at 4° C until used.

2.2.2.3 Encapsulation of both fluorescein and BIO in PMs

In order to co-load PMs with fluorescein and BIO, the block copolymer was dissolved together with BIO as previously described (see section 2.2.2.2), and then added drop wise to a solution of fluorescein, prepared as previously described (see section 2.2.2.1). Co-loaded PMs were then dialysed and filtered as previously described (see section 2.2.2.1), and then stored at 4° C until used.

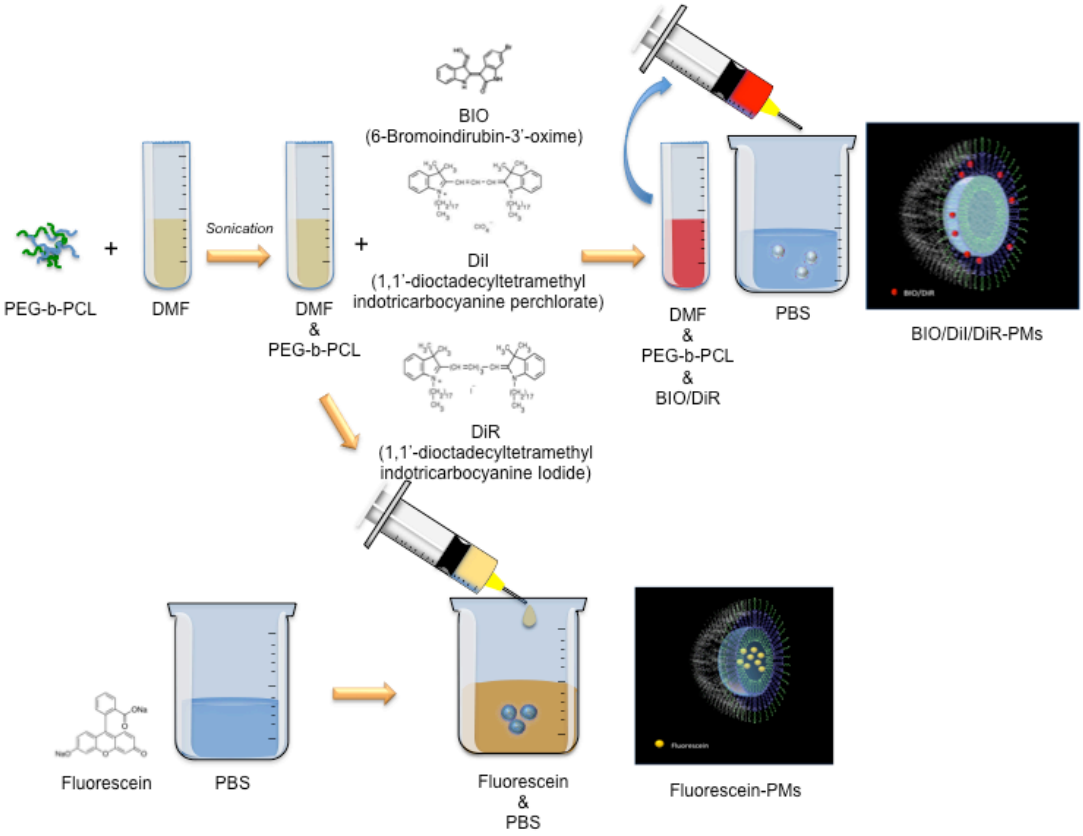

Figure 2.2: **Overview of the methodology used to prepare PMs loaded with various molecules.**

2.2.3 Polymersome characterisation

2.2.3.1 Dynamic light scattering (DLS)

DLS analysis (Zetasizer Nano ZS ZEN3600, Malvern, UK) was used to measure PM hydrodynamic diameter and polydispersity index (PdI). PM solution was diluted 100 times in PBS. Prior to analysis, samples were filtered into a plastic cuvette through a cellulose acetate syringe filter (0.22 μm, Minisart, Sigma Aldrich, UK) in order to remove particulate and dust residuals. Measurements were carried out at 20 °C with the light detected at a scattering angle of 173°. Data was collected 13 times/sample. Acquisition was for 5 seconds and each measurement was carried out in triplicate (Figure 2.3).

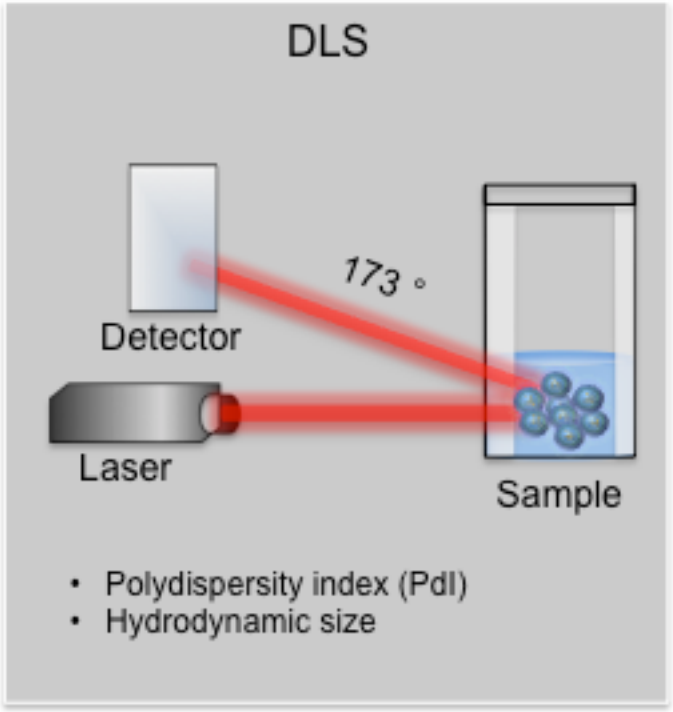

Figure 2.3: **Dynamic light scattering analysis.**

2.2.3.2 Nanoparticle tracking analysis (NTA)

NTA measurements were performed using a NanoSight LM10 (NanoSight, Malvern, UK). PMs samples were diluted 100,000 times in PBS, ~0.5 ml of which were introduced into the sample chamber by the use of a disposable 1 ml syringe. Measurements were performed at room temperature by recording videos of 30 seconds (25 frames/second) and then analysed using the NTA 3.0 software (Malvern, UK), obtaining measurements regarding PMs hydrodynamic size and concentration.

2.2.3.3 Fluorescein encapsulation and release *in vitro*

The concentration of fluorescein present in the fluorescein-PMs solution was calculated by measuring the UV absorbance at 494 nm using Nanodrop 2000c (Thermo Fisher Scientific, UK), and then comparing the results to stock solutions. The mass of fluorescein loaded *per* PM was calculated as the ratio between the mass of fluorescein present in solution and the concentration of PMs ml^{-1} measured by NTA (section 2.2.3.2).

Fluorescein release over time was measured by storing PM samples at room temperature (20 °C) under constant dialysis (regenerated cellulose, 10,000 MWCO, Sigma Aldrich, UK) against PBS. At various intervals over a total of 7 days, PM samples were collected, filtered through a Sephadex size separation column (G-25, Sigma Aldrich, UK), before measurement of UV absorbance (Nanodrop 2000c, Thermo Fisher Scientific, UK).

2.2.3.4 Measurements of fluorescence intensity

The intensity of fluorescence of fluorescein-PMs or solutions of free fluorescein at equivalent concentration to that in the fluorescein-PMs preparation (274 μM) were analysed over a range of wavelengths (increment of 1 nm from 485 nm to 600 nm) using a FluoroMax-4 (Horiba Scientific, UK). Release of fluorescein from PMs was also measured using a FluoroMax-4.

The release of residual unencapsulated fluorescein present in the fluorescein-PMs preparation was measured following ultracentrifugation of fluorescein-PMs at 100,000x *g* for 1 hour at 20 °C using an OPTIMA MAX – XP ultracentrifuge (Beckman Coulter, USA). The supernatant was collected and fluorescence was measured using a FluoroMax-4 (Horiba Scientific, UK).

2.2.4 Cellular uptake of fluorescein-PMs

2.2.4.1 Live cell imaging of L929 cells

Uptake of fluorescein-PMs by L929 cells was investigated by the use of confocal microscopy. L929 cells were seeded at a density of 50,000 cells/cm^2 and the medium was replaced with DMEM supplemented with low FBS concentrations (0.5%, v/v) 24 hours before the experimental assay. Cells were incubated in an environmental chamber set at 37 °C and 5% CO_2, and 2 hours before addition of fluorescein-PMs, the media was replaced with piperazine-N,N'-bis (2-ethanesulfonic acid) (PIPES) buffer supplemented with 0.5% (v/v) FBS. Fluorescein-PMs were filtered through a 0.22 μm cellulose acetate filter (Minisart, Sigma Aldrich, UK) and incubated with cells at a concentration of 5 x 10^{12} PMs ml^{-1}. Images were taken every 60 seconds over 60 minutes using a TCS SP5 laser scanning confocal microscope (Leica, Germany) with a 63X 1.30 glycerol immersion

objective. Cell nuclei were stained with Hoechest 33342 (Life Technologies, UK). Negative controls were, empty-PMs (5 x 10^{12} PMs ml^{-1}) and a 10 mM solution of fluorescein. Image analysis was performed by randomly selecting 20 cells of interest and measuring the mean fluorescence intensity (MFI) at each time point using Leica application suite X software (Leica, Germany).

2.2.4.2 Live cell imaging of MG63 cells and BMSCs

Uptake of fluorescein-PMs by MG63 cells or BMSCs was investigated by the use of inverted fluorescence microscopy. MG63 cells and BMSCs were seeded at a density of 50,000 cells/cm^2 and were transferred to low FBS medium 0.5% (v/v) 24 hours prior to incubation with PMs. Fluorescein-PMs were filtered through a 0.22 μm cellulose acetate filter (Minisart, Sigma Aldrich, UK) and, depending on the type of PMs used, were added to cells at a concentration of 5 x 10^{12} (PMs formed from 5.8k-19k copolymer) or 1.5 x 10^{12} PMs ml^{-1} (PMs formed from 5k-18k copolymer). Images were acquired after 1 hour incubation using an Axiovert 200 inverted microscope (Zeiss, Germany). The nucleus was labelled using a solution of 4',6-diamidino-2-phenylindole (DAPI, Invitrogen, UK) diluted 1 in 100 in PBS. Staining was performed for 10 minutes after which cells were washed two times with PBS and imaged. Negative controls were untreated cells.

2.2.4.3 Flow cytometry

Uptake of fluorescein-PMs by adherent L929 cells, MG63 cells or BMSCs, as well as BMMNCs was assessed by flow cytometry. All cells were considered positive when showed a fluorescence intensity greater than that detected in 99 % of the untreated cells.

For cells cultured in adhesion, cells were seeded at a density of 50,000 cells/cm^2 and allowed to adhere overnight, then the media was changed to low FBS (0.5% v/v) for 24 hours. PMs were added to each well at the following concentrations: 5 x 10^{12} (PMs formed from 5.8k-19k copolymer) or 1.5 x 10^{12} PMs ml^{-1} (PMs formed from 5k-18k copolymer). After defined time intervals, cells were washed twice with PBS, detached using trypsin, centrifuged at 220x *g* for 4 minutes at 4 °C, and resuspended in PBS (500 μl). Then, 1 μl of propidium iodide (PI, Sigma Aldrich), at a concentration of 3 mM, was

added prior to flow cytometry analysis with Guava Easycyte Mini Flow Cytometer (Merck Millipore, USA). Negative controls were untreated cells.

In a different experiment, aimed to assess the effects of the serum concentration on the internalisation of fluorescein-PMs, BMSCs were seeded at a density of 50,000 cells/cm^2 and cultured in either 0.5% or 10% (v/v) FBS for 24 hours. Then cells were incubated with 5 x 10^{12} fluorescein-PMs ml^{-1} either in media supplemented with the same % of FBS or switching between the two (Figure 2.4). At the end of 1, 3 or 24 hour incubation, cells were detached with trypsin, centrifuged at 220x *g* for 4 minutes at 4 °C, resuspended in PBS (500 µl) and analysed using Guava Easycyte Mini Flow Cytometer (Merck Millipore, USA). Negative controls were untreated cells.

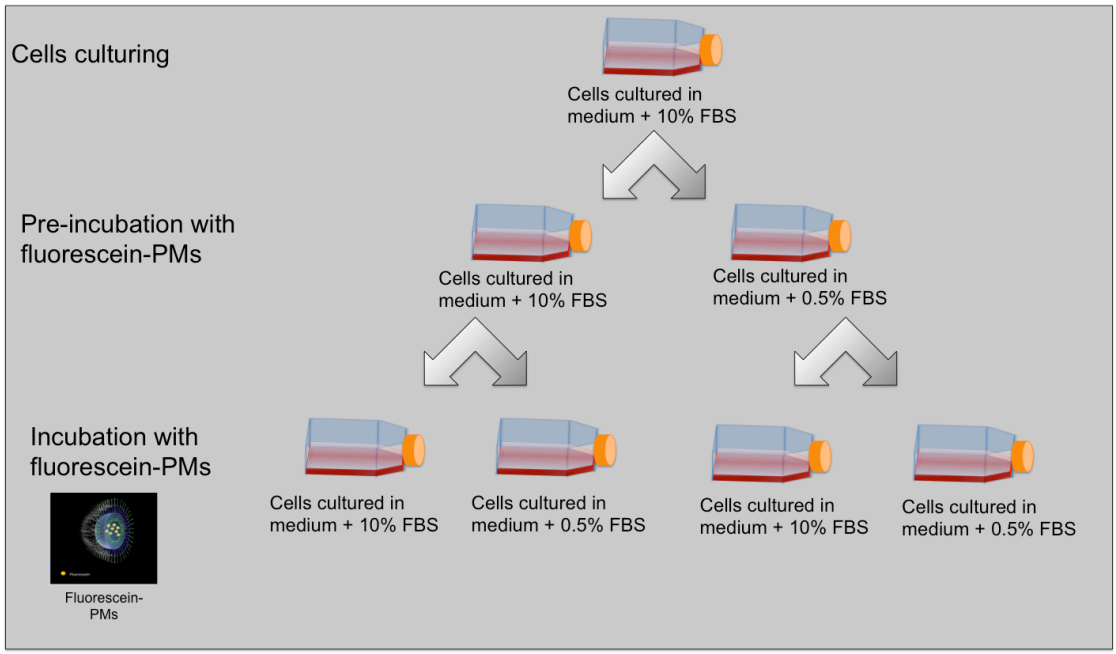

Figure 2.4: **Methodology used to assess the effect of serum on PM uptake.**

Graphic representation of the culture conditions used to assess the effect of serum concentration on fluorescein-PMs uptake by BMSCs.

In another experiment, aimed to assess the effects of both serum concentration and culture conditions (adhesion *versus* suspension) on the internalisation of fluorescein-PMs, BMSCs were seeded at 50,000 cells/cm^2 for 24 hours. Cells were either left in adhesion or detached using trypsin, and incubated for 24 hours with 5 x 10^{12} fluorescein-PMs ml^{-1} formed using the 5k-18k block-copolymer, in the presence of increasing concentrations of serum in the media (0%, 0.5%, 1%, 2.5%, 5%, 10% v/v). At the end of

the 24 hour incubation, when needed, cells were detached with trypsin, then centrifuged at 220x *g* for 4 minutes, resuspended in PBS and analysed using Guava Easycyte Mini Flow Cytometer (Merck Millipore, USA). Negative controls were untreated cells.

2.2.4.4 Immunological staining of freshly isolated BMMNCs incubated with fluorescein-PMs

Freshly isolated BMMNCs were divided in different Falcon tubes and kept in suspension cultures using a MACS rotator (Miltenyi Biotec, Germany). Cells were suspended in ~10 ml of α-MEM supplemented with 10 % (v/v) FBS, penicillin and streptomycin, and were incubated for 3 hours with 1.5 x 10^{12} fluorescein-PMs or empty-PMs (formed using the 5k-18k block copolymer).

In order to identify cellular subtypes, ~10^6 - 10^7 cells were stained with monoclonal antibodies or matched isotypes controls. The list of antibodies and suppliers is provided in the appendix section 7.1. The staining protocol was as follow: at the end of the 3 hour incubation, cells were washed twice in MACS buffer comprising 0.5% (v/v) bovine serum albumin (BSA) and 2 mM EDTA. Next, cells were incubated for 30 minutes at room temperature with blocking buffer composed of PBS, 1% (v/v) BSA, 2 mM EDTA and 3% (v/v) goat serum. Cells were then washed twice in MACS buffer, resuspended in 100 µl of the same buffer and stained with the relevant monoclonal antibodies, at the concentration indicated by the manufacturer, for 30 minutes at 4 °C. Subsequently, cells were washed twice with MACS buffer and, when required, the secondary antibody was added, at the concentration indicated by the manufacturer, in 100 µl of MACS for 30 minutes at 4 °C. Finally, after two washes with MACS buffer, cells were fixed with 2% paraformaldehyde (PFA) for 20 minutes at 4 °C, washed twice with MACS buffer and resuspended in the desired volume of MACS buffer. When possible, compensation controls for fluorescence spectral overlap were prepared using OneComp eBeads (eBioscience, UK). 5 µl of antibody were added to a drop of beads, vortexed, and incubated for 30 minutes at 4 °C. Next, the beads were washed with MACS buffer, and then centrifuged at 400 x *g* for 5 minutes. Alternatively, compensation controls were obtained by staining ~1 x 10^6 cells with one antibody. Samples were assayed on a FACS

Calibur/Canto II cytometer (BD Biosciences, USA) and analysed using FlowJo v10 software (Ashland, USA).

2.2.4.5 Image Stream cytometry

Internalisation of fluorescein-PMs in freshly isolated BMMNCs was also studied by imaging flow cytometry. Samples were stained as described in the previous section (see section 2.2.4.4) and data was acquired using an ImageStream X MkII (Merck Millipore, USA). Cells were imaged using a 60x lens objective with an image resolution of ~0.33 μm/pixel. Data was then analysed using IDEAS software v.2 (Merck Millipore, USA). In particular, following acquisition, only cells that were in-focus were considered from the raw data. These were then divided according to their aspect ratio in order to analyse only single cells. Single stained controls were imaged for each fluorophores and used to create a compensation matrix in order to calculate the fluorescent spectral overlap.

In another experiment, aimed at the use Image Stream for investigating the mechanism of PMs internalisation by cells, ~1 x 10^6 MG63 were cultured in DMEM supplemented with 5 % (v/v) FBS, penicillin and streptomycin, and incubated for 24 hours with 1.5 x 10^{12} fluorescein-PMs or empty-PMs. At the end of the 24 hours, cells were washed twice with PBS, detached using trypsin, fixed for 20 minutes in 2% PFA at room temperature, and then washed again with PBS. Subsequently, cells were permeabilised for 15 minutes at room temperature using a solution of 0.1% (v/v) triton X-100 (Sigma Aldrich, UK) in PBS. This was followed by incubation in PBS supplemented with 0.5% (v/v) BSA and 3% (v/v) goat serum for 20 minutes at 4 °C. Subsequently, cells were resuspended in 100 μl of MACS buffer and with a mouse anti human LAMP-1 antibody or relative isotype control incubated (Biolegend, USA) for 30 minutes at 4 °C. Following two washes with MACS buffer, cells were incubated with secondary antibody goat anti mouse AF647 for 30 minutes at 4 °C. Finally, cells were washed twice with MACS buffer, resuspended in the desired volume and analysed by Image Stream as previously described. Co-localisation of fluorescein staining with LAMP-1 staining was assessed by image analysis using the co-localisation function within the IDEAS software v.2 (Merck Millipore, USA).

2.2.5 AlamarBlue assay

The alamarBlue® reduction assay was used to assess metabolic activity following incubation of L929 cells with empty-PMs, and after incubation of 3T3 reporter cells with either BIO-PM or free BIO. Regardless cell type, 20,000 cells/well were seeded into a 96-well plate in DMEM supplemented with 5% (v/v) FBS, penicillin and streptomycin. After 24 hours, cells were incubated for further 24 hours with increasing concentration of empty-PMs in the L929 cells experiment. Whilst, in the experiment with 3T3 reporter cells these were incubated with increasing concentrations of BIO-PMs or free BIO. The media was removed, cells were washed twice with PBS, and a 1 in 10 dilution of alamarBlue reagent (Thermo Fisher, UK) was added. Cells, were incubated in the dark for 4 hours at 37 °C, after which fluorescence emission was recorded (0.1s/well) at 610 nm (background) using a Varioscan Flash microplate reader (Thermo Scientific, UK).

2.2.6 Quantification of the number of PMs *per* cell

In order to quantify the number of PMs internalised *per* cell, L929 or BMSCs were seeded in a 6 well plate at a density of 100,000 cells/well in conditions described previously (section 2.2.4.3), and incubated with increasing concentrations of fluorescein-PMs for 24 hours. At the end of the incubation period, cells were washed twice with PBS in order to remove the excess of PMs that were not internalised, and lysed using a solution of HEPES (20 mM), NaCl (125 mM) and sodium dodecyl sulphate (SDS) (2% v/v) for 1 hour at room temperature. The relative fluorescence was then measured at 521 nm using a Varioscan Flash microplate reader (Thermo Fisher Scientific, UK). The mass of fluorescein released *per* cell was calculated by comparing the cellular fluorescence measured against a calibration curve that was produced by diluting of a stock solution of fluorescein (100 mM) (Sigma-Aldrich, UK) in PBS supplemented with cell lysate. For quantification at the single cell level, raw data was extracted from FCS files using Matlab (Mathworks, Cambridge, UK) and analysed using Microsoft Excel.

2.2.7 Luciferase assay

In order to determine the Wnt signalling pathway activation, a luciferase assay was performed using 3T3 murine fibroblast Wnt reporter cells (Enzo Life Sciences, USA). These cells express the firefly luciferase gene under the control of Wnt-responsive

promoters (TCF/LEF). The level of pathway activation is directly related to the amount of light produced following the addition of a D-luciferin substrate, which is converted oxyluciferin by the luciferase enzyme with concurrent release of light. Cells were seeded at a density of 15,000 cells/well into 96 well plates in 50 µl of DMEM supplemented with 5% (v/v) FBS and 25 mM HEPES, and incubated overnight at 37 °C. After 24 hours, BIO-PMs, free BIO or empty-PMs were filtered through a 0.22 µm cellulose acetate filter (Minisart, Sigma Aldrich) and then added to the cells in plain DMEM at the desired concentrations. As a positive control 5 µM of free BIO (not loaded in PMs) diluted in DMEM was used in each assay. Plates were incubated for 16-18 hours at 37 °C and then 100 µl/well of luciferase substrate diluted in luciferase buffer (Promega, USA) were added (Figure 2.5). The chemiluminescent signal was read (0.1 s/well) on a Varioscan Flash microplate reader (Thermo Scientific, UK) 10 minutes after the addition of the buffer/substrate solution. Data was analysed using Microsoft Excel and values were normalised against untreated cells and also to cells incubated with 5 µM BIO. To control for cell count, cell lysates were analysed for dsDNA content, as described in section 2.2.10.

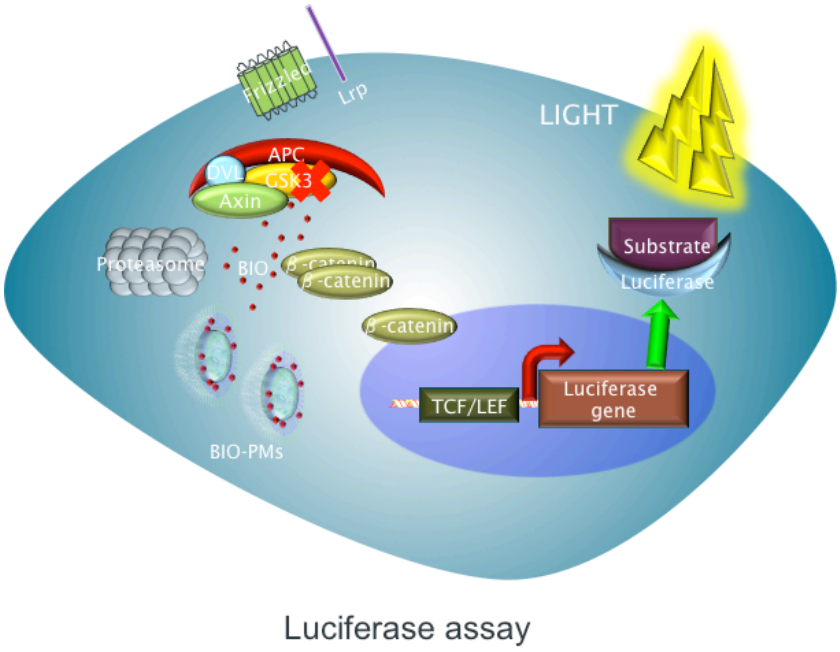

Figure 2.5: **Luciferase assay.**

3T3 mouse fibroblast cells expresses the firefly luciferase reporter gene under the control of Wnt-responsive promoters (TCF/LEF). The luciferase activity from the luciferase gene is regulated in a dose-dependent manner by the activation of the Wnt pathway. BIO can activate the Wnt pathway by inhibiting GSK-3β and inducting the nuclear translocation of β-catenin. Following Wnt activation, the reporter gene is expressed and the luciferase enzyme is synthesised. D-luciferin is then added to the cells and it is transformed into oxyluciferin and light by the enzyme activity.

2.2.8 BIO encapsulation and release *in vitro*

The concentration of BIO encapsulated within PMs was calculated by measuring the UV absorbance at 518 nm using Nanodrop 2000c (Thermo Fisher Scientific, UK) and comparing it to stock solutions. To determine the kinetics of BIO release, PM samples were kept at room temperature (20 °C) under constant dialysis (regenerated cellulose, 10,000 MWCO, Sigma-Aldrich, UK) against PBS. At various intervals over a total of 7 days, PM samples were collected and UV absorbance was measured. Release of BIO over time was also measured following ultracentrifugation. BIO-PMs were ultracentrifuged at 100,000 x *g* for 1 hour at 20 °C using an OPTIMA MAX – XP ultracentrifuge (Beckman Coulter, USA). Supernatant and pellet were collected and assessed using luciferase assay as previously described (section 2.2.7).

2.2.9 Quantitative reverse transcription-polymerase chain reaction (qRT-PCR)

qRT-PCR was performed in order to assess gene expression following incubation with BIO-PMs. BMSCs were seeded at a density of 15,000 cells/cm^2 in 24 well plates in α-MEM supplemented with 0.5 % (v/v) FBS, penicillin and streptomycin, and incubated for 24 or 96 hours with: 6 x 10^{11} or 15 x 10^{11} BIO-PMs ml^{-1}, 2 μM BIO, 15 x 10^{11} empty-PMs ml^{-1}, 100 ng ml^{-1} Wnt3A (R&D systems, UK), or dimethyl sulphoxide (DMSO, Sigma Aldrich, UK). At the end of the incubation, cells were washed 3 times with PBS and lysed in 300 μl of buffer RLT (Qiagen, Netherlands). Then, total RNA was extracted using an RNeasy Mini Kit (Qiagen, Netherlands). Ethanol 70% (v/v) was added to cell lysate in a 1:1 ratio (v/v), solutions were mixed, transferred into spin columns and centrifuged at 8000x *g* for 1 minute. Flow-through was discarded, the columns were firstly washed with 700 μl of buffer RW1 and, after centrifugation at 8000x *g* for 1 minute, cell lysate was washed 2 times with 500 μl of RPE. Following centrifugation at 8000x *g* for 2 minutes, RNA was released into a new collection column by addition of 30 μl of RNAse-free water and subsequent centrifugation at 8000x *g* for 1 minute. The concentration and purity of the RNA extracted were determined by NanoDrop ND-1000 spectrophotometer (Thermo Fisher, UK). RNA was reverse transcribed with SuperScript VILO cDNA Synthesis Kit (Life Technologies, UK) using manufacturer's recommendations.

Relative quantification of gene expression was assessed with an ABI Prism 7500 detection system (Applied Biosystems, USA). Reaction mixtures were prepared in triplicate and contained 250 nM of each defined primer, 1 μl of complementary DNA and 50 % (v/v) of power SYBR Green PCR Master Mix (Applied Biosystems, USA). Thermal cycler conditions were set as follow: activation step at 95 °C for 10 min, followed by 40 cycles of 95 °C for 15 seconds and 60 °C for 60 seconds. The ΔΔCt method was used for relative quantification of gene expression. Two house-keeping genes, *GAPDH* and *ACTB*, were initially used, but for analysis only *GAPDH* gene was used as an internal control. All the primers used in this project (see Appendix section 7.1) were previously validated for the use in qRT-PCR experiments by Dr Agnieszka Janeczek and Dr Maria Carmen de Andres, Bone and Joint Research Group, University of Southampton.

2.2.10 PicoGreen assay for dsDNA quantification

Double stranded DNA was quantified using Quant-iT™ PicoGreen® dsDNA reagent (Thermo Fisher, USA). Cell lysates were recovered either from luciferase assay (see section 2.2.7), or following a 24 hour incubation with increasing concentrations of BIO-PMs, free BIO or Wnt3A. These were diluted 1 in 10 in Tris/EDTA (TE) buffer and transferred into a black 96 well plate. PicoGreen, 0.5% (v/v) in TE buffer was added to the wells, and incubated in the dark for 5 minutes prior measurement of fluorescence at 520 nm using a FLx800 fluorescence microplate reader (Biotek, UK). DNA concentration was calculated against a standard curve of DNA prepared using Lambda DNA standard (Thermo Fisher, UK).

2.2.11 Alkaline phosphatase (ALP) activity measurement

ALP activity was measured on BMSCs following incubation with BIO-PMs. Cells were seeded at a density of 15,000 cells/cm^2 in 24 well plates, in osteogenic media comprising α-MEM supplemented with 0.5 % (v/v) FBS, penicillin, streptomycin, 100 μM sodium 2-ascorbate, 5 mM β-glycerophosphate and 10 nM dexamethasone. Alternatively, cells were incubated basal media comprising in α-MEM supplemented with 0.5 % (v/v) FBS, penicillin and streptomycin, which constituted a control for the experiment. Cells were exposed for 24 hours to 6 x 10^{11} or 15 x 10^{11} BIO-PMs ml^{-1}, 2 μM BIO, 15 x 10^{11} empty-PMs ml^{-1}, 100 ng ml^{-1} Wnt3A (R&D systems, UK), or DMSO (Sigma Aldrich, UK). At the end of the 24 hours, cells were washed twice with PBS and then cultured in either basal or osteogenic media for further 13 days. Next, cells were detached using trypsin and lysed using CelLytic (Sigma Aldrich, UK) for 30 minutes at room temperature. Cell lysates were diluted 1 in 10 in a substrate solution composed of 0.04 g p-nitrophenyl phosphate, PNPP, Sigma Aldrich, UK), 10 ml of 1.5 M alkaline buffer solution (Sigma Aldrich, UK) and 20 ml of distilled water. Plates were incubated in the dark for 30 minutes at 37 °C, after which the colorimetric reaction was stopped by addition of 100 μl/well of 1 M NaOH. Absorbance was measured at 415 nm using an ELx800 microplate reader (Biotek, USA). ALP activity was calculated against a standard curve of known concentrations p-nitrophenol (final product of ALP enzymatic reaction)

and adjusted according the final DNA content calculated by PicoGreen assay (section 2.2.10).

2.2.12 In vivo study

MF1 male mice 3 months old (Biomedical research facility, University of Southampton) were used in all the experiments described. This strain represents a robust model of an outbred mouse, therefore with a degree of genetic variability, with docile disposition. Experiments were carried out under the procedure project license 30/2880 and using the personal licence I1211ECA0. Before and after the experimental use, the animals were fed *ad libitum* in cages which compiled with Home Office Licensing requirements.

Biodistribution of PMs in healthy mice was assessed following tail vein injection of 200 μl of either DiR-PMs or empty-PMs. Biodistribution of PMs in models of bone injury was analysed following the creation of a bone drill defect. The femur was selected as site of injury. Its thickness and mechanical strength allow for the bearing of a 1 mm wide drill hole without the need of internal fixators and/or mechanical supports, therefore avoiding impairment of the mobility, and align with the ARRIVE guidelines.

In order to create the bone injury, mice were anaesthetised by intraperitoneal injection of approximately 0.1 ml/10 mg body weight of 1:1 Hypnorm (Fentanyl)/Hypnovel (Benzodiazepine). Then, mice fur was shaved by the use of a trimmer and the animals were gently placed on a warmed surface in order to maintain the body temperature at physiological conditions. The skin was firstly sterilised using cotton wool sprayed with 70% (v/v) ethanol, and then incised using a scalpel on the lateral side, approximately over the quadriceps muscle and along the longitudinal orientation of the femur.

The femur was gently exposed by carefully separating the muscles from the connective tissue, and then a drill hole defect was created using a 1 mm wide drill. The femur was drilled until the bone marrow cavity was exposed (Figure 2.6A & B), then the muscles were placed back on their original position and the skin was stitched.

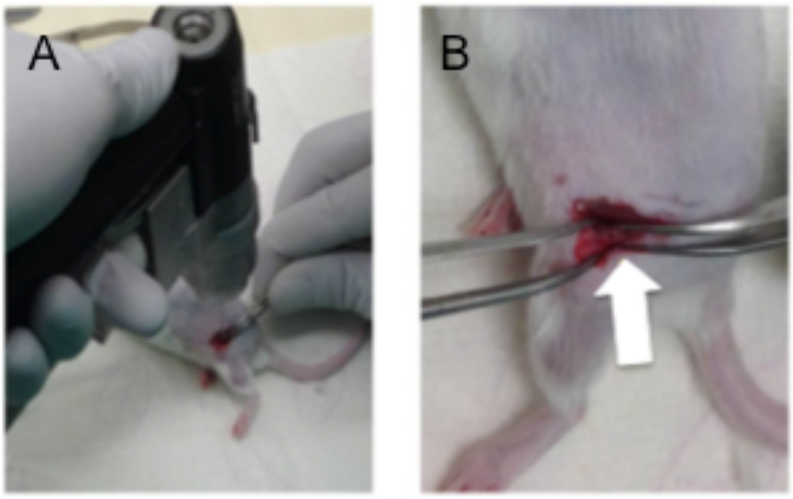

Figure 2.6: **Creation of the bone drill defect.**

A: Image showing the drilling of the femur. **B:** Image showing the bone drill defect created in the femur (white arrow).

Within 1 hour from the creation of the injury, mice were injected *via* tail-vein with either: 100 µl of DiR-PMs (~100 µM) and 100 µl of DiI-PMs (~100 µM), 200 µl of empty-PMs or 58 µM DiR (Perkin Elmer, USA) in 5% (v/v) ethanol in sterile water. Mice undergoing the same surgical procedure, but in which the femur was not injured represented the sham control. These mice were injected *via* tail-vein with 100 µl of DiR-PMs and 100 µl of DiI-PMs. For imaging, animals were anesthetised using isoflurane and imaged at 0.5 seconds exposure using an IVIS Lumina series III (Perkin Elmer, USA). During longitudinal studies, mice were maintained under standard housing conditions and imaged at defined time points as described. At the end of the experiments, mice were culled by neck dislocation; organs were explanted, imaged as previously described, and fixed in 0.4% (v/v) PFA over-night. Images were analysed using Living Image Software 4.3.1 (Perkin Elmer, USA). The fluorescence intensity measured is expressed in radiant efficiency ([p/sec/cm^2/str]/[mW/cm^2]) as recommended by the manufacturer. For the quantification of the fluorescent signal, a region of interest (ROI) was manually drawn, keeping the size of the region drawn constant across images, time points and experimental groups, and then fluorescence within the selected region was automatically quantified using the Living Image Software 4.3.1 (Perkin Elmer, USA).

2.2.13 Histological analysis

Following fixation in 0.4% PFA, samples were washed twice in PBS and embedded in the appropriate mounting media, while femurs were first decalcified in a solution of EDTA for 12 days, changing the solution every 5 days. Samples destined for cryosectioning, were first cryoprotected by placing them in a solution of 30% (v/v) sucrose in water at 4 °C over-night, then embedded in optimal cutting temperature compound (OCT, Thermo Fisher, UK), and sectioned at 7 µM thickness using Microm H500 cryostat (Thermo Fisher, UK). The temperature was set between -27 °C and -24 °C, subject to room conditions and the tissue type. Femurs were cut along the coronal plane, while livers along the sagittal plane (Figure 2.7). Sections were mounted onto charged glass slides and were allowed to air-dry for 15 minutes before being stored at -40 °C. Samples destined to paraffin embedding and sectioning were dehydrated through a series of ethanol washes (50 %, 90 % and 100 % (v/v) in dH_2O), incubated for 1 hour in Histo-Clear (National Diagnostics, USA), then 1 hour in paraffin wax (Leica, Germany), before final embedding in wax blocks. 7 µM sections were obtained cutting the femurs along the coronal plane using a HM355-S microtome (Microm International GmbH, Germany), and were then mounted on glass slide, which were allowed to air-dry for 15 minutes before being stored at 4 °C.

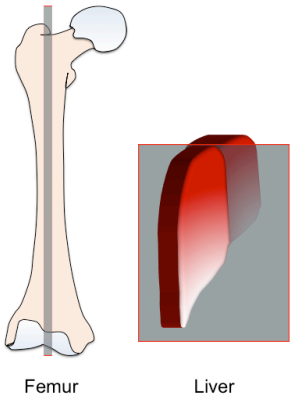

Figure 2.7: **Orientation of the sectioning.**

Femurs were cut along the coronal plane, whilst livers were sectioned along the sagittal plane.

In order to detect DiI fluorescence, selected cryosectioned slides of either femurs or livers were washed in PBS for ten minutes, and then stained with a solution of DAPI diluted 1 in 100 in PBS in the dark for 5 minutes at room temperature. Slides were washed twice with PBS, a coverslip was mounted with hydromount (National Diagnostics, USA), and then images were taken using a Nikon Eclipse Ti inverted microscope (Nikon, Japan). The sections of tissue embedded in paraffin were rehydrated through a series of ethanol washes, before staining with either Hematoxylin and Eosin (H&E) or tetrachrome staining (see appendix 7.1), dehydrated through a series of ethanol washes and mounted as previously described. Sections were finally imaged using a Zeiss Axiovert 200 (Zeiss, Germany).

2.2.14 Micro-computed tomography (μ-CT) analysis

In order to quantitatively determine bone healing following the creation of the bone drill defect and subsequent tail-vein injection of BIO-PMs, free BIO or empty PMs, mice were analysed using μ-CT. Briefly, at all the time points investigated mice were anesthetised using isoflurane and scanned using a SkyScan 1179 (Bruker, Belgium) with the following settings: X-ray source 50 kV, 500 μA, exposure time 116 ms, rotation step 0.7° and average voxel size of 18 μM. During the study, mice were maintained under standard housing conditions and imaged at defined time points as described. After scanning, raw data was reconstructed using NRecon software (Bruker, Belgium), while correcting for misalignment, ring artefacts and beam hardening (30%), then reconstructed images were oriented in the desired 3D orientation using DataViewer (Bruker, Belgium). In order to binarise the data and segment bone from the tissue according to their density a global threshold was set, and these settings were kept constant throughout all the samples and time points. Finally, using CTAn software (Bruker, Belgium), bone volume, tissue volume and percentage of bone tissue were calculated within standardised a volume of interest (VOI).

2.2.15 Statistical analysis

Statistical analysis was performed using GraphPad Prism 6 software (GraphPad, USA). Differences in the data were assessed by investigating the distribution of the entries by Shapiro-Wilk's test and then either parametric or nonparametric tests were used. Statistical significance was defined as $*p<0.05$, $**p<0.01$, $***p<0.001$, $****p<0.0001$ and non significant (n.s.) $p>0.05$. The *n* number reported in the figure legends represents independent replicates of the experiment performed in analogous conditions. Details of the statistical tests used, and how the data is represented in each graph, can be found in the figure legends.

Chapter 3: Cellular uptake of polymersomes and quantification of intracellular payload release.

3.1 Introduction

As discussed in Chapter 1, PMs can incorporate both hydrophilic and hydrophobic compounds and represent a promising system for spatio-temporally controlled delivery of these molecules. Several studies have shown that PMs can be efficiently loaded with a number of different payloads, and following uptake, these molecules and compounds are released in an active form inside cells (see section 1.9.4). The incorporation of payloads into PMs offers a series of advantages including increased drug solubility, enhanced circulation time, and improved targeting. The exquisite control that PMs can provide has resulted in significant interest in the potential of PMs as DDS, especially in oncology where a targeted localisation and release of chemotherapeutic drugs is of primary interest, and led to the investigation of various PM preparations for the delivery of a range of anti-cancer drugs (reviewed by Guan et al. 2015).

Nevertheless, considering the variety of block copolymers commercially available, as well as the numerous different types of PMs that can be created from them, it is essential to determine whether the PMs employed in a given study are internalised by the cells of interest, and then to assess the kinetics of uptake. Furthermore, it is important to quantify the payload released intracellularly following uptake. The clinical translation of PMs is undermined by the current lack of safety assessments *in vivo* and by the paucity of information regarding the effective dose of therapeutic agent delivered to the target tissue and cell type. This information is essential for determining the effect mediated by PM delivery, starting from biodistribution and pharmacokinetics in the organs and tissues, and finishing on the biological effects at the cellular and sub-cellular level (Cheng et al. 2015).

Studies investigating the use of nanoparticles for drug delivery routinely report the quantification of the total exposure dose, rather than assessing the number of discrete entities that induced the biological effect observed (Summers et al. 2013). Several methods aimed to qualitatively and quantitatively determine cellular uptake of nanoparticles have been reported. However, most of these have relied on the use of nanoparticles inherently fluorescent (directly labelled with fluorescent molecules). This strategy has been very important for providing basic information regarding the mechanism of nanoparticle uptake. For example, Xin and colleagues created PEG-PCL nanoparticles conjugated with rhodamine and, by using a cocktail of inhibitors specific

for various endocytic pathways in combination with fluorescent imaging, demonstrated preferential uptake of nanoparticles by caveolae-mediated endocytosis (Xin et al. 2011)

Despite being very useful, quantification experiments with directly labelled PMs are limited by a number of drawbacks, the most important of which is the lack of ability to distinguish between nanoparticles internalised by cells from those associated with the external leaflet of the cellular membrane. Alternative methods able to overcome these limitations have been suggested. For example, Gottstein and colleagues proposed a workflow integrating data from three different analytical techniques (fluorimetry, flow cytometry and confocal microscopy) into a mathematical model, which then derives the average number of nanoparticles internalised by cells (Gottstein et al. 2013). Sorrell and colleagues assessed cellular internalisation of rhodamine conjugated PMs by flow cytometry, and then created a mathematical model by fitting *in vitro* data. This model took into consideration both concentration and size of the PMs used, as well as biological parameters such as the number of receptors binding to PMs and their recycle rate. In this way the authors were able to estimate of the number of PMs internalised by various cell types (Sorrell et al. 2014). These approaches are complex, but useful; however, they do not address another fundamental question as to when and how much of the payload has been released intracellularly by the nanoparticles.

Real-time intracellular delivery from PMs has been demonstrated in various cell types, ranging from human dermal fibroblasts to monocytes, by loading PMs with a number of hydrophilic and hydrophobic fluorescent molecules including rhodamine and PI (Massignani et al. 2009). Liu and colleagues utilised an alternative approach whereby the release of doxorubicin, a light adsorbing drug, from hollow nanoparticles emitting UV or visible light results in a shift of emission that is detectable using upoconversion luminescence (Liu et al. 2014). Furthermore, Semmling and colleagues demonstrated real-time drug release by loading polyelectrolyte capsules with fluorophores that alter their excitation profile upon change in pH. Using this system, the authors were able to assess drug release and determine its spatial localisation (Semmling et al. 2008).

Real-time delivery can be assessed using fluorescent molecules that are self-quenched while encapsulated in a nanoparticle, or that are able to quench the fluorescence of a specific nanoparticle. Doxorubicin is one example of a molecule with such characteristics. Qui and colleagues have shown that following loading in micelles

formed from star-conjugated copolymers, both polymeric micelles and doxorubicin fluorescence were quenched; however, upon intracellular release, the fluorescence of both drug and carrier was recovered (Qiu et al. 2014). Nevertheless, doxorubicin is a chemotherapeutic drug that slows down cellular growth, and is therefore not the ideal payload for studies focused on the kinetics of nanoparticle uptake.

An alternative to doxorubicin is represented by disodium salt of fluorescein (hereafter referred to as fluorescein). This is a hydrophilic fluorescent molecule with limited ability to cross the cellular phospholipid bilayer. Fluorescein is excited at λ 496 nm and emits at λ 521 nm, but most importantly its fluorescence is quenched when the fluorophore is highly concentrated in aqueous solutions (Weinstein, 1977 and Weinstein 1978). These characteristics make fluorescein an ideal candidate for real-time investigation of drug delivery from nanoparticles. Weinstein and colleagues exploited these features loading liposomes with 6-carboxyfluorescein, a more hydrophilic version of fluorescein, and were able to demonstrate liposome uptake and payload release in human lymphocytes using flow cytometry (Weinstein et al. 1977). This preparation was further used to investigate how changes in the external surface of liposomes affect their ability to deliver payload intracellularly (Weinstein et al. 1978; Straubinger et al. 1983). This system has not been reported thus far for analysing PM cellular uptake and payload release, and could also be useful for determining differences of uptake in various cell types and culture conditions.

Taking this into consideration, the hypothesis underlying the experiments presented in this chapter is that PMs can be used to deliver a model cargo to different cell types, and that the number of PMs releasing payload intracellularly can be quantified at a single-cell level (Figure 3.1).

The aims of the work reported in this chapter are:

- To produce and characterise PMs that incorporate fluorescein;
- To determine PM cellular uptake and induced cytotoxicity in different mammalian cell types, as well as in different culture conditions;
- To assess PM uptake and distribution in freshly isolated human BMMNCs;
- To quantify the number of PMs releasing payload intracellularly in the different cell types.

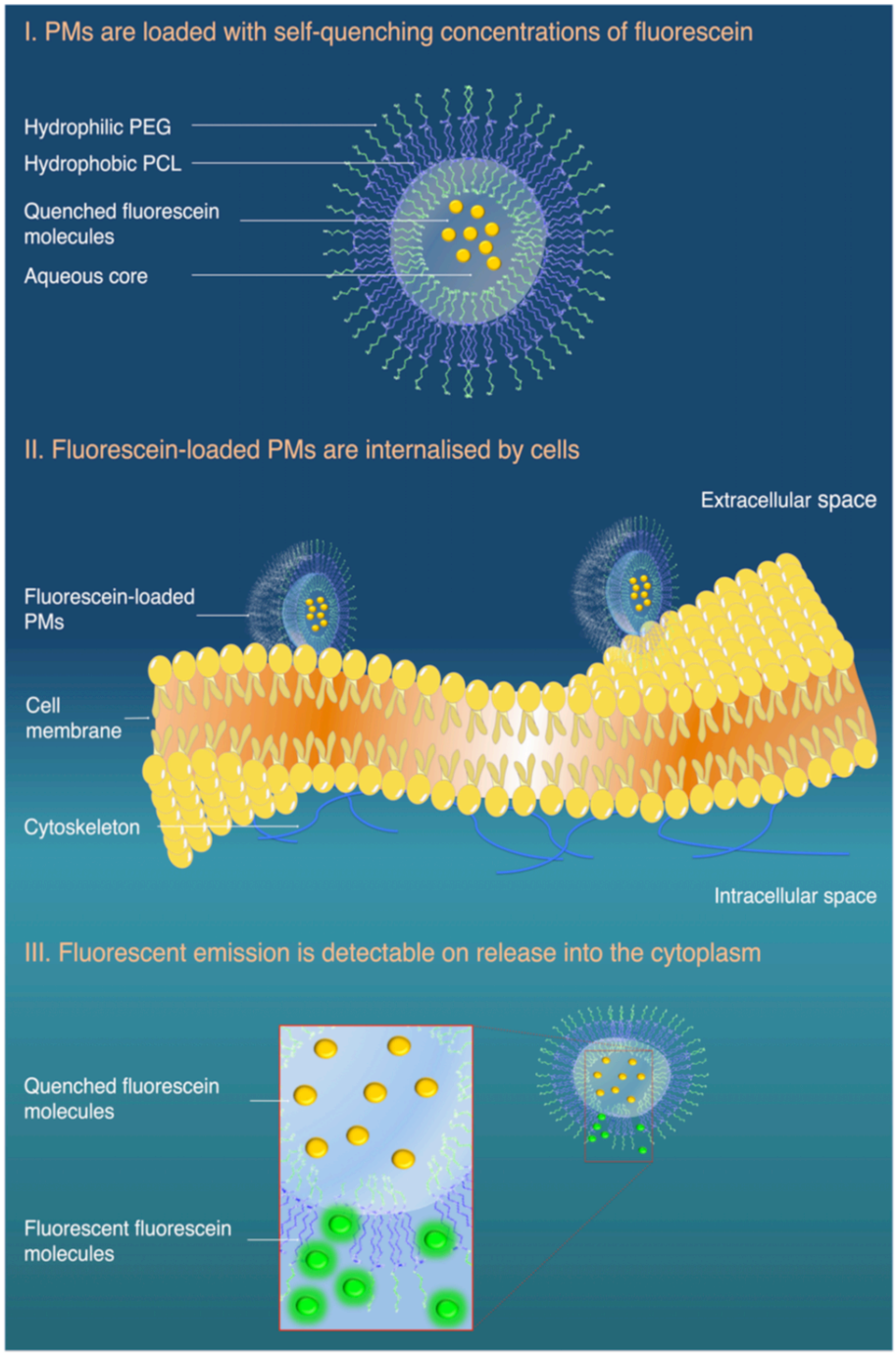

Figure 3.1: **Overview of the principle behind the use of fluorescein for measuring intracellular payload delivery.**

(I) PEG-b-PCL block copolymers self-assemble in an aqueous environment to form polymersome structures. The PCL units of the polymer form a hydrophobic membrane, the PEG units form a hydrophilic corona and line the interior cavity of the polymersome. (II) When carrying a payload of sodium fluorescein above the quenching concentration the polymersome is non-fluorescent. Upon cellular internalisation (III) payload release can be visualized as the fluorescein disperses and falls below the quenching concentration.

3.2 Results

3.2.1 Physical characterisation of fluorescein-polymersomes

PMs loaded with fluorescein (fluorescein-PMs) were produced by nanoprecipitation of NH_2–PEG 5.8k-PCL 19k block copolymer into a solution of 0.1 M fluorescein. Then, both fluorescein-PMs and empty-PMs (PMs loaded with PBS) were characterised by DLS and NTA. The loading of fluorescein inside the PMs did not affect the hydrodynamic size or polydispersity index (PdI) of the nanoparticles (Figure 3.2 A & B). These parameters were stable over a period of 7 days for fluorescein-PMs stored at room temperature (Figure 3.2 C). The hydrodynamic size of fluorescein-PMs determined by DLS (86 nm with PdI of 0.103) was in close agreement with measures from NTA (85 ± 33.6 nm), which also provided information regarding the final concentration of fluorescein-PMs, 5.0 x 10^{13} PMs ml-1 (Figure 3.2D).

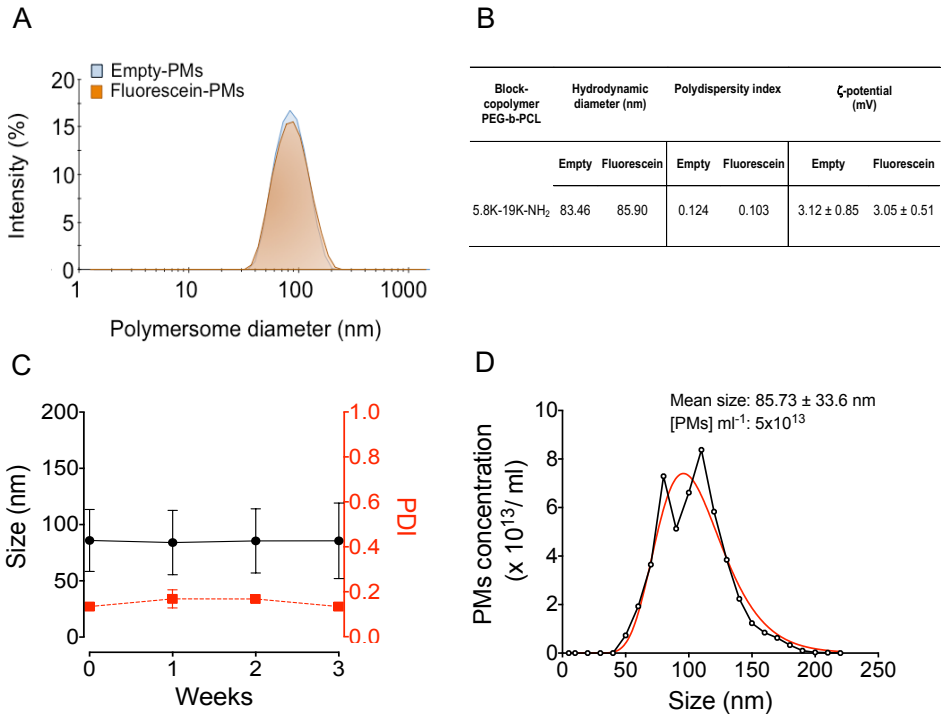

Block-copolymer PEG-b-PCL	Hydrodynamic diameter (nm)		Polydispersity index		ζ-potential (mV)	
	Empty	Fluorescein	Empty	Fluorescein	Empty	Fluorescein
5.8K-19K-NH_2	83.46	85.90	0.124	0.103	3.12 ± 0.85	3.05 ± 0.51

Figure 3.2: **Physical characterisation of PMs loaded with fluorescein.**

A: Representative histogram from DLS measurements showing the narrow distribution of the hydrodynamic diameter of both empty- and fluorescein-PMs formed from 5.8k-19k block copolymer. **B:** Summary of size and polydispersity index (PDI) of empty and fluorescein-PMs. **C:** Graph showing size (black) and PDI (red) stability of fluorescein-PMs over the course of 3 weeks. Data presented as mean ± SD, *n*=3 independent experiments. **D:** Histogram derived from NTA depicting size and concentration *per* ml of fluorescein-PMs. Black line is connecting different experimental values, while red line a Gaussian distribution curve fitted to the data.

Having demonstrated that encapsulation of fluorescein in PMs does not affect the hydrodynamic size of PMs formed, further experiments were performed in order to assess the concentration of fluorescein loaded within the PMs, and also to test whether fluorescein fluorescence is quenched when this is encapsulated within PMs.

Using absorbance spectroscopy, a linear relationship between increasing concentrations of both fluorescein-PMs and un-encapsulated fluorescein (free fluorescein), at concentrations < 50 μM, was found (Figure 3.3A). Next, by fitting absorbance measurements from fluorescein-PMs to a standard curve for free fluorescein, it was determined that a concentration of 274 ± 7.4 μM fluorescein is present in 1 ml of PM preparation (Figure 3.3B). With the use of absorbance, it was also demonstrated that fluorescein is stably encapsulated within PMs, as its concentration in solution is constant over time (Figure 3.3B).

Finally, by dividing the concentration of fluorescein measured to be loaded in the nanoparticle preparation (274 μM) by the number of PMs present in 1 ml of solution (5 x 10^{13} PMs ml^{-1}, Figure 3.2D), a mass of 5.48 x 10^{-21} moles of fluorescein was estimated to be encapsulated *per* PM. This number was subsequently used for the quantification of PMs releasing payload intracellularly reported in section 3.2.6.

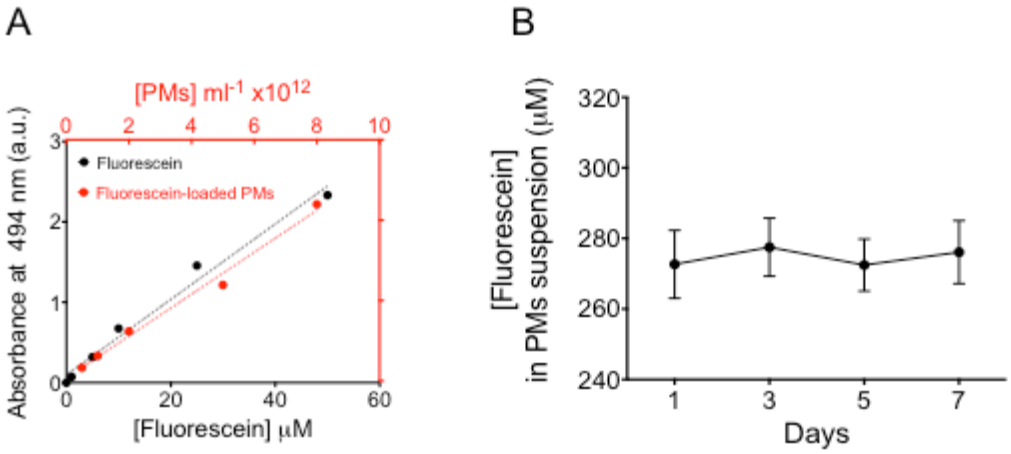

Figure 3.3: **Fluorescein is encapsulated within PMs and it is stably retained over time.**

A: Graph showing that to increasing concentrations of either free fluorescein (black) or Fluorescein-PMs (red) correspond increasing values of light absorbance (at λ = 494 nm). **B:** Graph showing the concentration of fluorescein present in the solution of fluorescein-PMs after production (274 ± 7.4 µM) and at different time intervals over the course of one week measured by light absorbance (at λ = 494 nm) Data presented as mean ± SD, *n*=3 independent experiments.

3.2.2 Fluorescein fluorescence is quenched within PMs

Next, it was tested whether the fluorescence emission of the payload was quenched inside PMs. Following dialysis and size exclusion chromatography, fluorescein-PMs displayed a dark orange colour, in contrast with the bright yellow appearance of equivalent concentrations of free fluorescein solutions (274 µM, Figure 3.4A). By using spectrophotometry, it was demonstrated that no fluorescence was detectable in PM preparations in contrast to equivalent concentrations of free fluorescein (Figure 3.4B). However, upon partial disruption of PM structure by addition of triton X-100 (5%, v/v) (Figure 3.4 C & D), an increase of fluorescence of ~2-fold was observed (Figure 3.4E). These results showed that fluorescein can be loaded within PMs and at the concentrations used its fluorescence is quenched.

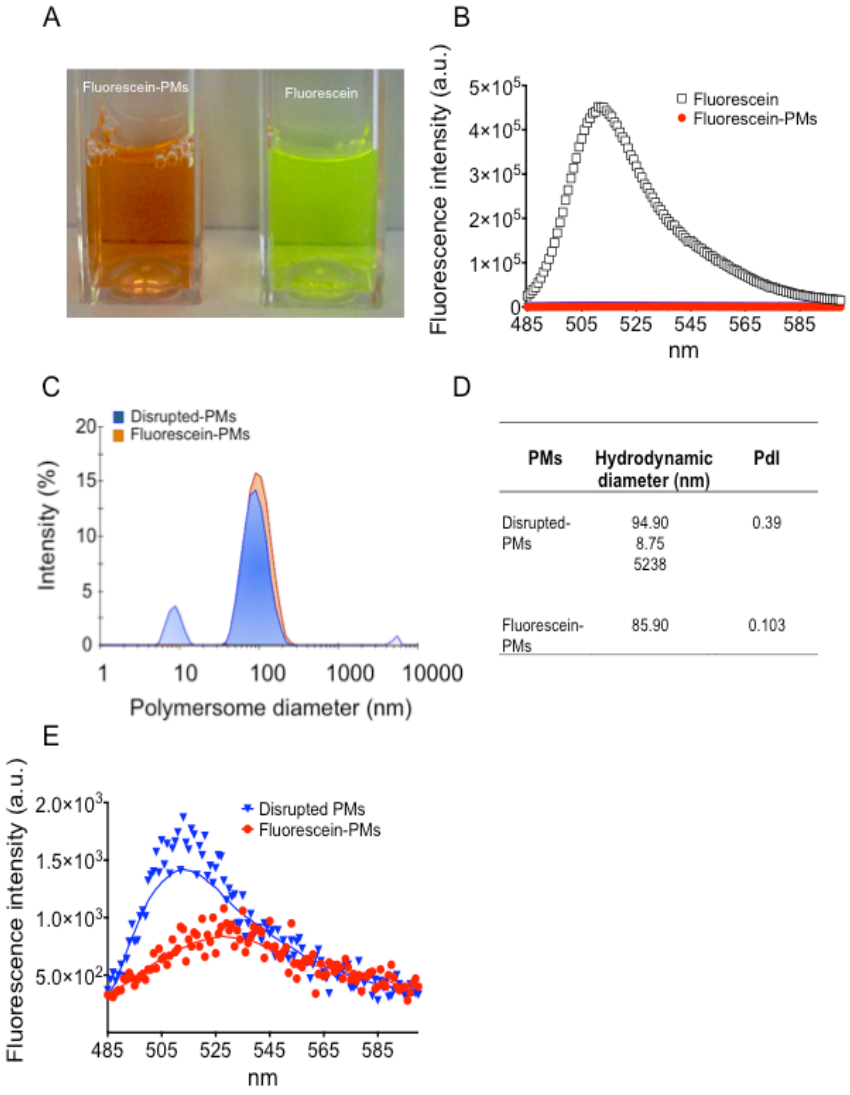

PMs	Hydrodynamic diameter (nm)	PdI
Disrupted-PMs	94.90 8.75 5238	0.39
Fluorescein-PMs	85.90	0.103

Figure 3.4: **Fluorescein fluorescence is quenched upon encapsulation within PMs.**

A: Picture showing the difference in colour of fluorescein-PMs and fluorescein at equal concentrations. **B:** Graph showing the absence of fluorescence emission from fluorescein-PMs (red) compared to equivalent concentrations (274 μM) (black) of free fluorescein measured by spectrophotometry. **C:** Representative histogram showing the difference in hydrodynamic diameter of fluorescein-PMs treated with Triton-X *vs.* untreated PMs. **D:** Table summarising both size and PdI of fluorescein-PMs disrupted with Triton-X and control untreated fluorescein-PMs. **E:** Graph showing the different intensity of fluorescence of fluorescein-PMs (red) compared to disrupted fluorescein-PMs (blue) measured by spectrophotometry.

3.2.3 Real-time detection of intracellular delivery of fluorescein by PMs

The previous results demonstrated that fluorescein can be used for determining real-time release of payload from PMs. Next, it was investigated whether fluorescein-PMs are internalised by cells and whether real-time intracellular delivery could be determined.

In order to do so, murine L929 fibroblasts were incubated with fluorescein-PMs and analysed by confocal microscopy. A time dependent increase in cellular fluorescence, associated with the release of fluorescein, was observed approximately 15 minutes from the start of the incubation (white arrows Figure 3.5). Note that incubation with empty-PMs did not produce cellular fluorescence, while treatment with high concentrations of free fluorescein (100 μM) resulted in a weak, but detectable fluorescence (Figure 3.5).

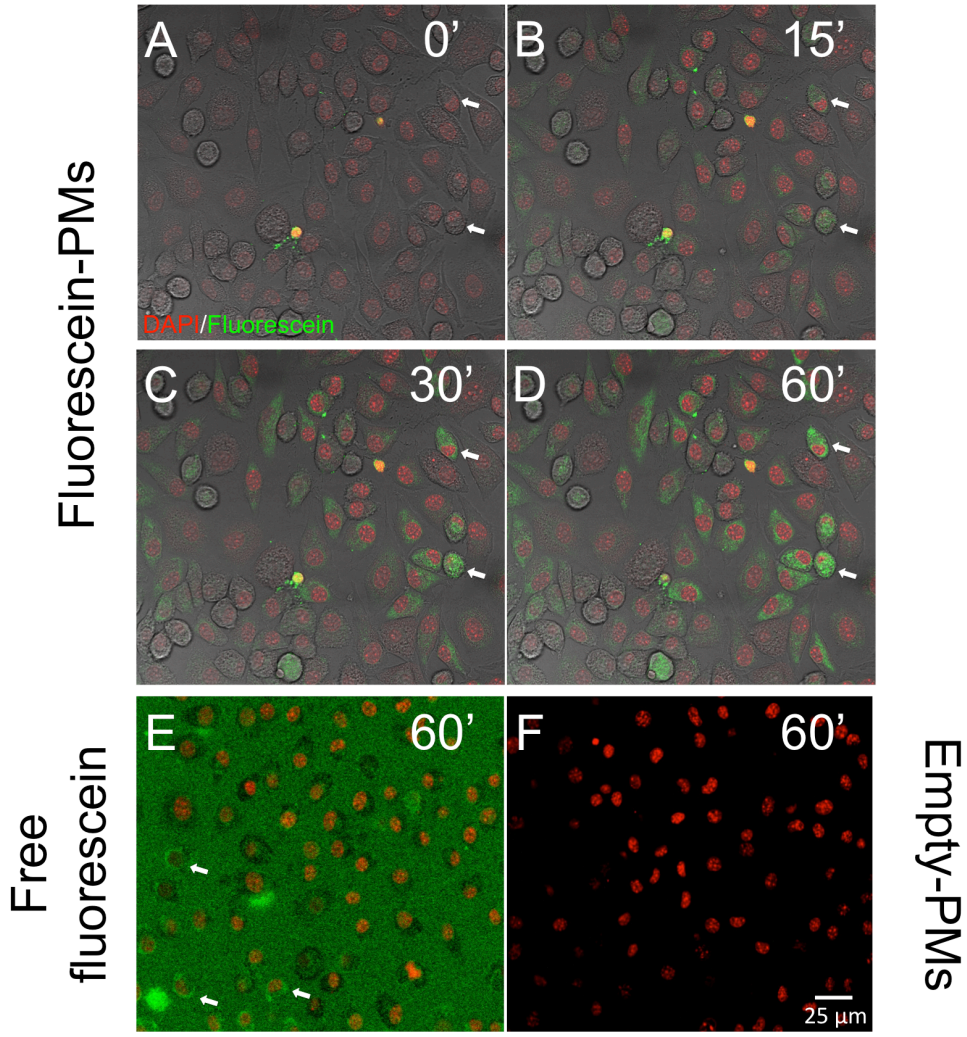

Figure 3.5: **Fluorescein-PMs are quickly internalised by L929 cells.**

Time-lapse imaging showing time-dependent intracellular release of fluorescein in L929 cells incubated with 5 x 10^{12} fluorescein-PMs/ml. Images were taken up to 1 hour after the addition of fluorescein-PMs and are representative of one z-stack. Green: cells positive for fluorescein. Red: nuclear staining. White arrows indicate examples of cells with a progressive increase in fluorescence over-time. Controls were: 5 x 10^{12} empty-PMs or 100 μM fluorescein. *n*=2 independent experiments.

Quantification of mean cellular fluorescence after incubation with fluorescein-PMs demonstrated a gradual increase over a period of one hour, with a significant difference in terms of intracellular fluorescence compared to the control (100 μM free fluorescein), which was evident within 15 minutes from the start of the incubation (p<0.05) (Figure 3.6).

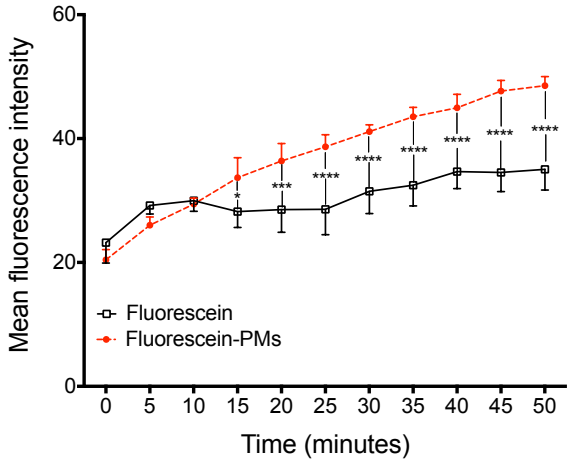

Figure 3.6: **Time-dependent intracellular delivery of fluorescein from loaded PMs.**

Graph showing the image analysis of the time-lapse experiment in Fig 3.5 and depicting the progressive and significant increase in mean fluorescence intensity of L929 cells exposed to fluorescein-PMs (red dots) compared to un-encapsulated fluorescein (100 μM) (black squares). Data presented as mean ± SD, statistical significance assessed by two-way ANOVA, with Sidak's post-hoc correction. Multiple comparison: *p<0.05, ***p<0.001 and ****p<0.0001.

3.2.4 Un-encapsulated fluorescein in PM preparations does not cause cellular fluorescence

Having demonstrated real-time delivery of fluorescein by PMs, it was then investigated whether the intracellular presence of fluorescein could also be due to unspecific cellular uptake of residual un-encapsulated fluorescein that could be present in the fluorescein-PMs solution. Following ultracentrifugation of fluorescein-PMs, only very low concentrations of free fluorescein were found in the supernatant (1 ± 0.1 μM, Figure 3.7A), and L929 cells incubated for 24 hours with these concentrations did not display levels of fluorescence greater than the control (Figure 3.7B). These results indicate that the intracellular fluorescence observed following incubation with fluorescein-PMs is due to the cellular uptake of PMs and consequent release of fluorescein.

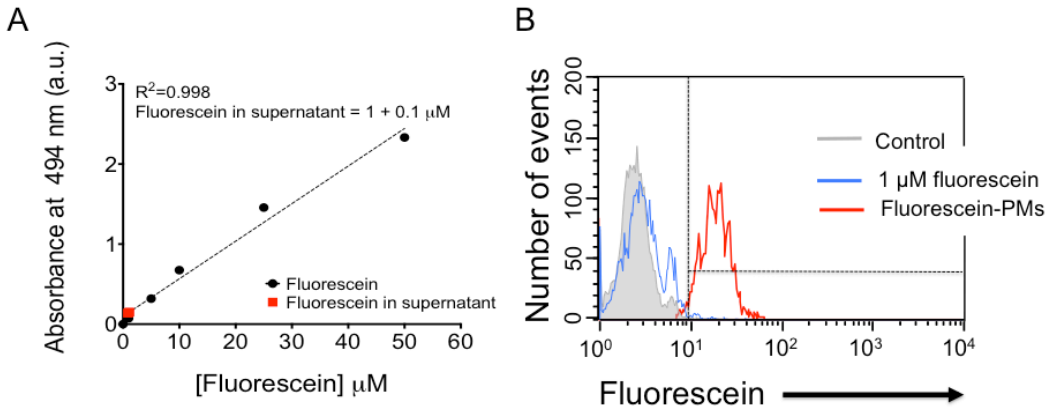

Figure 3.7: **Uptake of residual un-encapsulated fluorescein present in PM solution does not result in cellular fluorescence.**

A: Standard curve for fluorescein absorbance (at λ = 494 nm) showing the concentration of residual fluorescein present in the supernatant of fluorescein-PMs after ultracentrifugation for 1 hour at 100,000 g (~1 µM) Data presented as mean ± SD, *n*=3 independent experiments. **B:** Representative flow cytometry histogram showing negligible fluorescence over control (grey) of L929 cells incubated with 1 µM (blue) fluorescein for 24 hours, whilst 24 hour incubation with fluorescein-PMs (red) induced a marked increase in cellular fluorescence. Note that fluorescein-PMs are included in the plot to facilitate the comparison between the conditions.

3.2.5 Investigation of the kinetics of fluorescein-PM uptake, at single cell resolution, by L929 cells

Thus far it has been shown that PMs release fluorescein intracellularly within 1 hour of incubation. However, a degree of heterogeneity in the cellular fluorescence intensity was measured in the confocal experiments, indicating different rates of uptake among cells. Therefore, a further investigation of these differences at a single-cell level was carried out using flow cytometry.

Following exposure to fluorescein-PMs, cells were gated according to size and granularity in order to eliminate cellular debris within samples (Figure 3.8A). Cells were considered positive for fluorescein when their fluorescence intensity was higher than in 99% of the control cells (dotted lines, Figure 3.8B). Note that this gating strategy was used in all the experiments presented in this chapter, unless stated otherwise.

A progressive increase in cellular fluorescence as a function of time was observed following incubation with fluorescein-PMs, while incubation with empty-PMs did not result in any difference in fluorescence over the control levels (Figure 3.8 B & C). It was determined that 95.5 ± 0.6% of cells were positive for fluorescein after 24 hours from the

initial incubation and the mean fluorescence intensity (MFI) relative to the control also reached saturation at this time point (Figure 3.8 D & E). These results confirm that fluorescein-PMs are internalised by cells, but the variability in fluorescence observed, at any time point, in the flow cytometry plot indicates heterogeneity of uptake.

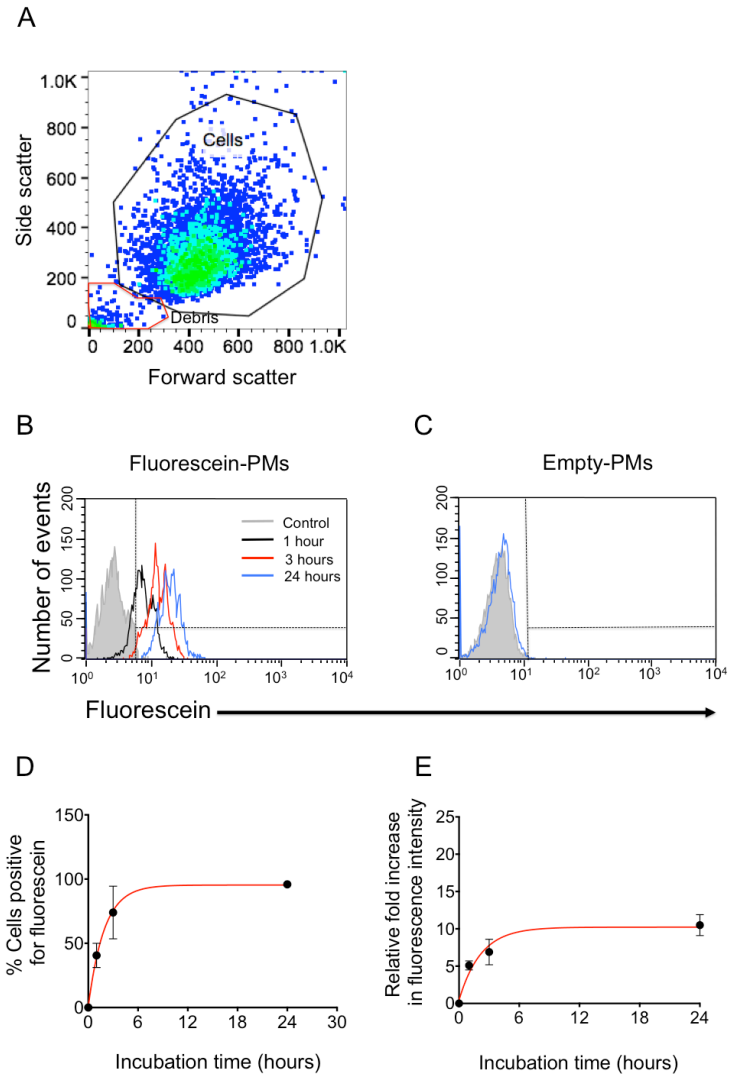

Figure 3.8: **L929 cells internalisation of fluorescein-PMs assessed by flow cytometry.**

A: Representative dot plot showing side scatter *vs.* forward scatter of L929 cells and consequent gating strategy adopted to analyse only cells (Cells), while gating out cell debris (red gate). **B:** Representative histogram of L929 cells incubated for 1 (black), 3 (red) or 24 hours (blue) with fluorescein-PMs. The graph shows the progressive increase in fluorescence intensity of cells treated with fluorescein-PMs compared to 99% of the control untreated cells (grey). Dotted lines indicate the markers set to discriminate between positive and negative cells. **C:** Representative histogram of L929 cells incubated for 24 hours (blue) with empty-PMs showing negligible difference in terms of fluorescence intensity between treated cells and untreated control (grey). **D:** Graph depicting the progressive increase in the percentage of cells positive for fluorescein over-time. Data presented as mean ± SD, *n*=3 independent experiments. **E:** Graph depicting the progressive relative increase in mean fluorescence intensity of cells incubated with fluorescein-PMs for 1, 3 or 24 hours Data presented as mean ± SD, *n*=3 independent experiments.

In parallel to the investigation of the cellular uptake, cell viability was assessed through PI staining. PI is a cell impermeable dye that stains nucleic acids in dead cells. Exclusion of PI from L929 was observed irrespective of the range of PM concentrations used (Appendix Figure 1), the duration of the incubation or the presence of fluorescein within PMs (Figure 3.9A-D).

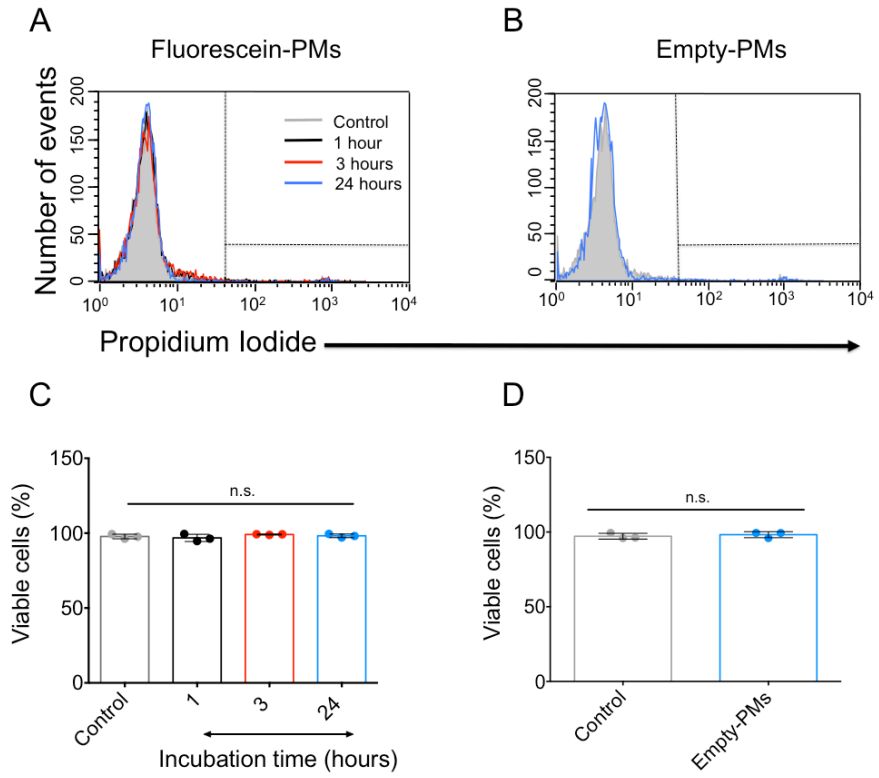

Figure 3.9: **Fluorescein-PMs do not induce cytotoxicity in L929 cells.**

A: Representative flow cytometry histogram of L929 cells incubated for 1 (black), 3 (red) or 24 hours (blue) with fluorescein-PMs and stained with PI (1 mg/ml). The graph shows the lack of difference in fluorescence intensity between cells treated with fluorescein-PMs and 99% of the control untreated cells (grey). **B:** Representative flow cytometry histogram plot of L929 cells incubated for 24 hours (blue) with empty-PMs and stained with PI (1 mg/ml). The graph shows the negligible difference in terms of fluorescence intensity between treated cells and untreated control (grey). **C:** Histogram showing the percentage of viable cells after 1, 3 or 24 hours incubation with fluorescein- PMs. The percentage is calculated as the difference in cells positive for PI between untreated cells *vs* cells exposed to fluorescein- or empty-PMs. Data presented as mean ± SD, one-way ANOVA, with Dunn's post-hoc correction, n=3 independent experiments. Multiple comparison: ns = non significant. **D:** Histogram showing the percentage of viable cells after 24 hours incubation with empty-PMs. Data presented as mean ± SD, one-way ANOVA, with Dunn's post-hoc correction, n=3 independent experiments. Multiple comparison: ns = non significant.

3.2.6 Quantification of PMs releasing payload intracellularly in L929 cells

After demonstrating that fluorescein-PMs are internalised by L929 without affecting their viability, the PM uptake was next quantified by exploiting the properties of fluorescein. Cells were incubated for 24 hours with increasing concentrations of fluorescein-PMs and then lysed. The intracellular concentration of fluorescein was determined by comparing the intensity of fluorescence measured against a standard curve of fluorescein diluted in PBS and cell lysate (Appendix Figure 2). Note that following incubation with fluorescein-PMs negligible differences in cell fluorescence intensity were observed before and after cell lysis, excluding possible limitations of the measurement due to cellular lysis (Appendix Figure 3). Cells incubated with a concentration of 5×10^{12} fluorescein-PMs ml^{-1} contained 7.85×10^{-10} nanomoles of fluorescein *per* cell (Figure 3.10A). It was previously calculated that each PM contained 5.48×10^{-21} moles of fluorescein (Figure 3.3 and section 3.2.1). Therefore, dividing the number of moles of fluorescein *per* cell (N_{cell}) by the number of moles of fluorescein *per* nanoparticle (N_{PM}) the average number of PMs releasing their payload *per* cell (Q_{cell}) was estimated (Figure 3.10B).

$$Q_{\mathbf{cell}} = \frac{N_{\mathbf{cell}}}{N_{\mathbf{PM}}} \quad (1)$$

A

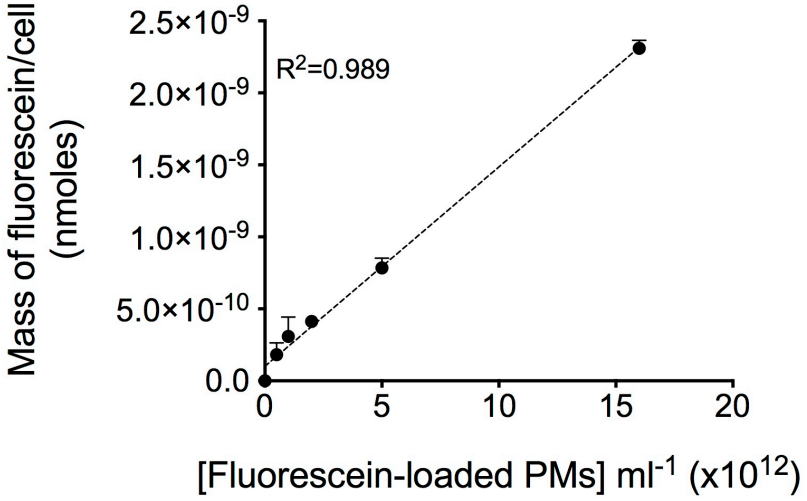

B

[Fluorescein-loaded PMs] ml^{-1} ($x10^{12}$)	Mass of fluorescein (nanomoles)		Estimated number of PMs $cell^{-1}$
	In well	Per cell ($x10^{-9}$)	
0.5	0.18 ± 0.05	0.181	33 ± 15
1	0.3 ± 0.1	0.308	56 ± 24
2	0.41 ± 0.03	0.413	75 ± 4
5	0.78 ± 0.09	0.784	143 ± 12
16	2.30 ± 0.05	2.308	421 ± 10

Figure 3.10: **Estimation of the number of PMs releasing fluorescein in L929 cells.**

A: Graph showing the linear relationship between the mass of fluorescein *per* cell and the concentration of fluorescein-PMs incubated with the cells. $R^2 = 0.989$. Data presented as mean ± SD. **B**: Table summarising the mass of fluorescein *per* well and *per* cell, as well as estimated number of PMs *per* cell following 24 hour incubation with increasing concentrations of fluorescein-PMs. Data presented as mean ± SD.

This estimation was validated by investigating the number of PMs releasing payload intracellularly at a single-cell level in a population of L929 cells. The cellular fluorescence intensity measured by flow cytometry following incubation with fluorescein-PMs (Figure 3.8) was normalised to the measurements of intracellular PM release obtained by fluorescence spectroscopy (Figure 3.10A), allowing for the number of PM releasing payload intracellularly to be calculated for every cell after 1, 3 and 24 hours

incubation (Figure 3.11A). Overall, a time-dependent increase in the maximum number of PMs releasing their contents intracellularly *per* cell was observed (217 ± 53, 243 ± 68 and 329 ± 97 PMs *per* cell after 1, 3 and 24 hour incubations, respectively). Also, a median value of 172 PMs had released the payload *per* cell after 24 hours incubation, in close similarity to the values calculated from the fluorescence spectroscopy quantification (~143 ± 12) (Figure 3.11B).

A

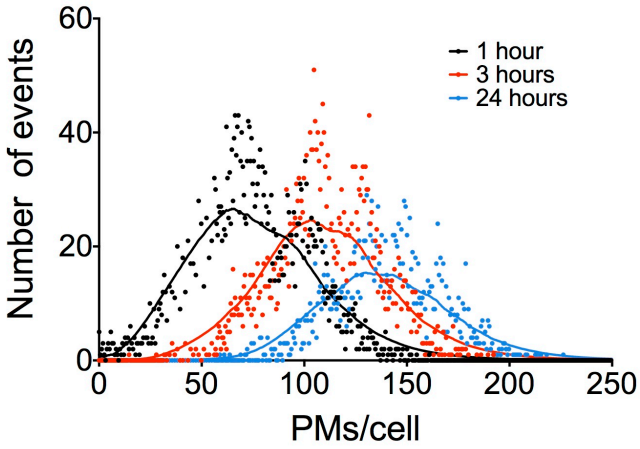

B

Estimated number of PMs releasing fluorescein *per* cell				
Hours	**Min**	**Max**	**Range**	**Median**
1	7 ± 13	216 ± 53	209 ± 54	127
3	5 ± 8	243 ± 68	238 ± 74	141
24	41 ± 35	329 ± 97	288 ± 126	172

Figure 3.11: **Quantification of the number of PMs releasing fluorescein in L929 at single cell level.**

A: Representative graph depicting the number of PMs releasing fluorescein intracellularly *per* cell after 1 (black), 3 (red) or 24 hour (blue) incubation with fluorescein-PMs. **B:** Table summarising the minimum (Min), maximum (Max), range (Max-Min) and median number of PMs *per* cell after 1, 3 or 24 hours incubation with fluorescein-PMs.

3.2.7 Investigation of fluorescein-PM uptake MG63 cells and human BMSCs

Previous data presented in this chapter demonstrated that murine fibroblast internalise fluorescein-PMs. To investigate the intracellular delivery of fluorescein from PMs in cell types more relevant to bone tissue and fracture repair, it was next tested whether MG63 cells or BMSCs internalise fluorescein-PMs. MG63 cells are human cells with features commonly associated with both mature and immature osteoblasts (Pautke et al. 2004), whilst human BMSCs are a heterogeneous population containing stromal cells and SSCs (see section 1.2.3.2).

Using fluorescence microscopy it was found that both MG63 cells and BMSCs internalise fluorescein-PMs following a 1 hour incubation. Fluorescein appears to be localised in the cytosol, whilst excluded from the nucleus since no overlap between fluorescein and DAPI fluorescence was observed (Figure 3.12A & B).

These results were further confirmed by flow cytometry analysis, as 94 ± 5% of MG63 cells (Figure 3.13A & C) and 91 ± 12 % of BMSCs (Figure 3.13B & D) were positive for fluorescein after 1 hour incubation, which represent an increase of almost 2-fold compared to L929 cells (41 ± 9%,Figure 3.8). By 3 hour incubation, more than 98% of the cells stained positive for fluorescein, irrespective of the cell type investigated (Figure 3.13C & D). Note that incubation with empty-PMs did not result in any difference in fluorescence over the control levels (untreated cells), as previously shown with L929 cells (Appendix Figure 4). Overall, the data presented indicates that fluorescein-PMs are quickly internalised by both cell types, and such uptake occurs with different kinetics compared to L929 cells.

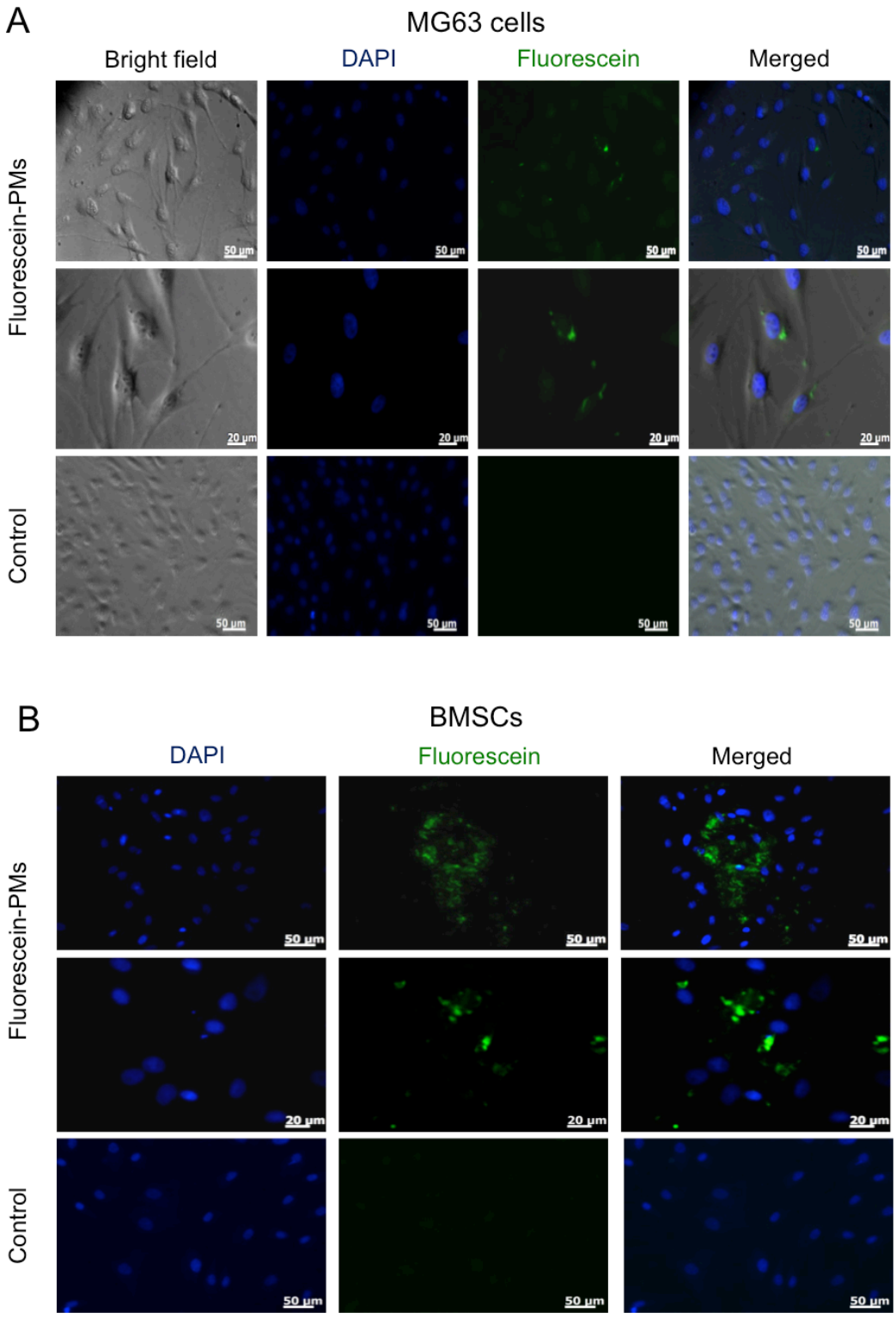

Figure 3.12: **MG63 and BMSCs cells internalise fluorescein-PMs.**

A: Fluorescence imaging showing intracellular release of fluorescein in MG63 cells incubated with fluorescein-PMs for 1 hour. Green: cells positive for fluorescein. Blue: nuclear staining. Cells not incubated with fluorescein-PMs served as negative control. **B:** Fluorescence imaging showing intracellular release of fluorescein in BMSCs incubated with fluorescein-PMs for 1 hour. Green: cells positive for fluorescein. Blue: nuclear staining. Cells not incubated with fluorescein-PMs served as negative control.

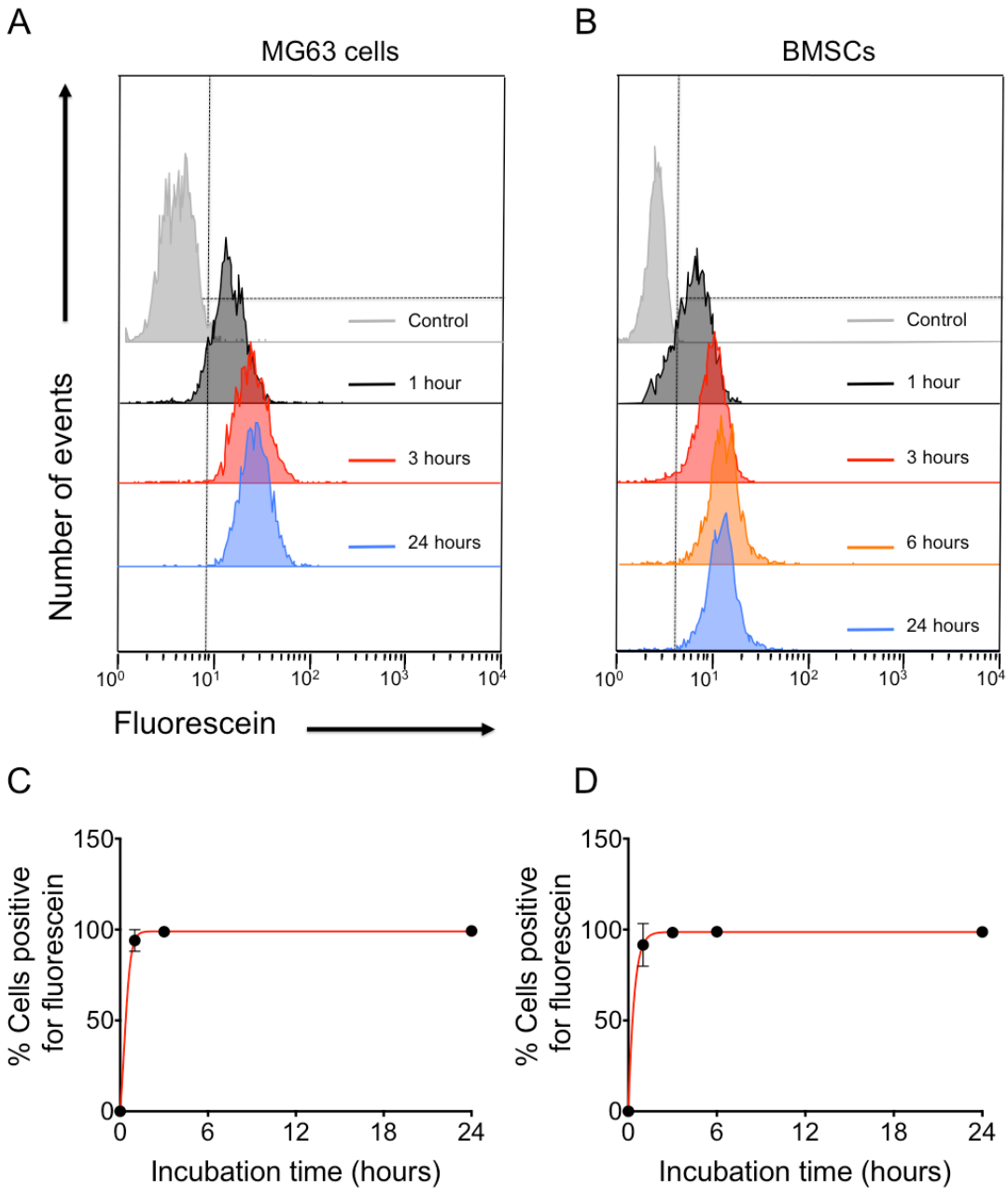

Figure 3.13: **Kinetics of PM uptake by MG63 cells and BMSCs.**

A: Representative flow cytometry histogram of MG63 cells incubated for 1 (black), 3 (red) or 24 hours (blue) with fluorescein-PMs. **B:** Representative histogram of BMSCs incubated for 1 (black), 3 (red), 6 (orange) or 24 hours (blue) with fluorescein-PMs. Both graphs show the progressive increase in fluorescence intensity of cells treated with fluorescein-PMs compared to 99% of the control untreated cells (grey). Dotted lines indicate the markers set to discriminate between positive and negative cells. **C:** Graph depicting the progressive increase in the percentage of MG63 cells positive for fluorescein over-time. **D:** Graph depicting the progressive increase in the percentage of BMSCs positive for fluorescein over-time. Data presented as mean ± SD, *n*=3 independent experiments.

The kinetics of fluorescein-PM uptake were further investigated analysing cellular MFI intensity at various end-points following incubation. In MG63 cells, a time-dependent increase in the relative MFI was measured between 1 and 3 hour incubation (4 ± 1 and 12 ± 2 fold increase compared to control, respectively), but it reached its maximum at 24 hours (Figure 3.13A). BMSCs displayed comparable trend, as the relative MFI increased by 11 ± 3 fold compared to control after a 3 hour incubation (Figure 3.13B). Additionally, it was demonstrated that cells reached saturation following a 6 hour exposure to fluorescein-PMs (14 ± 2.4 and 14 ± 3.2 fold increase compared to control at 6 and 24 hours, respectively, Figure 3.13B), and no further increments were observed over time (13 ± 1.1 and 14 ± 1.5 fold increase compared to control at 48 and 72 hours, respectively, Appendix Figure 5).

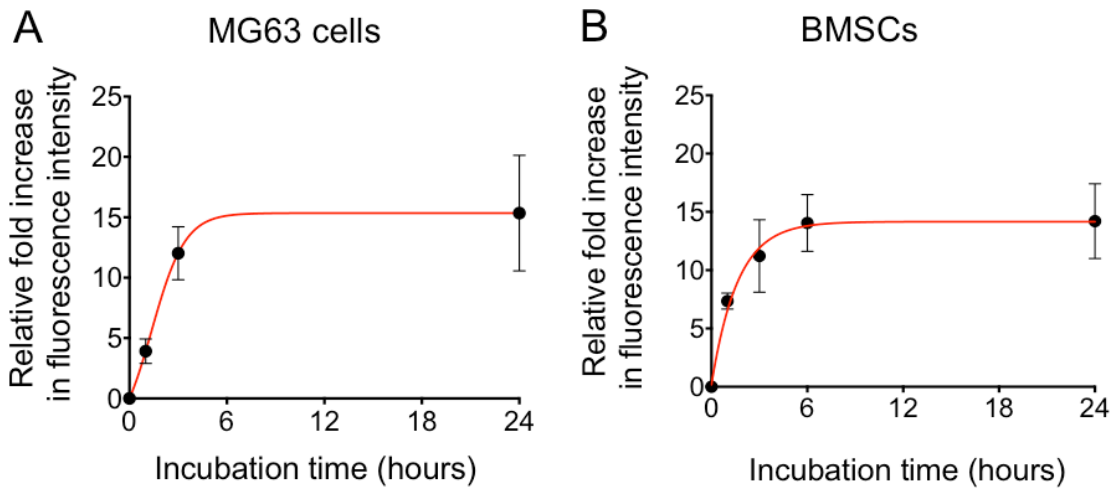

Figure 3.14: **MG63 cells and BMSCs reach saturation of fluorescein within a 24 hour incubation.**

A: Graph depicting the progressive relative increase in MFI of MG63 cells incubated with fluorescein-PMs for 1, 3, 24 hours. **B:** Graph depicting the progressive relative increase in MFI of BMSCs incubated with fluorescein-PMs for 1, 3, 6 or 24 hours. Data presented as mean ± SD, *n*=3 independent experiments.

It was also demonstrated that fluorescein-PMs did not induce a significant cytotoxicity in either MG63 cells (Figure 3.15A & C) or BMSCs (Figure 3.15B & D) as measured by PI. Note that absence of induced cytotoxicity was confirmed incubating the two cell types with empty-PMs for 24 hours (Appendix Figure 6). Overall, these results indicated that PMs are internalised by cell types with relevance in bone biology and regeneration; their uptake is time-dependent, but saturation in fluorescein release is

observed after 6 hour incubation. Finally, the internalisation of PMs by cells does not induce cytotoxic effects.

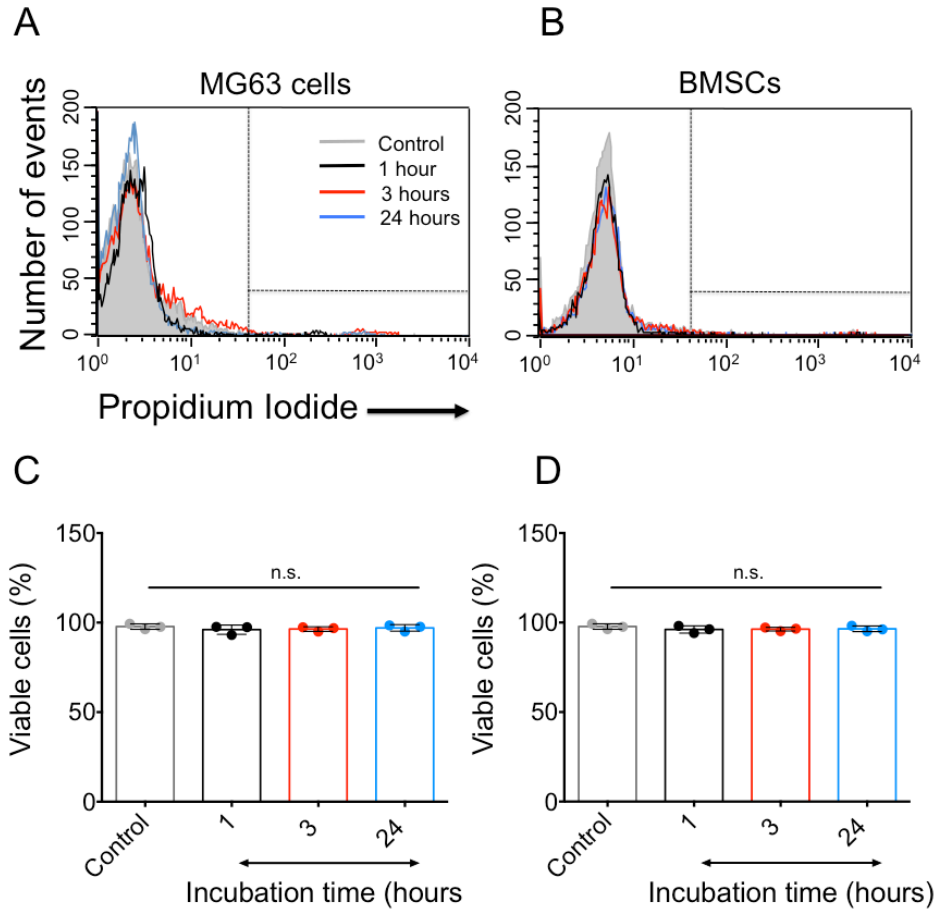

Figure 3.15: **Fluorescein-PMs do not induce significant cytotoxicity in MG63 cells or BMSCs**

A: Representative histogram of MG63 cells incubated for 1 (black), 3 (red) or 24 hours (blue) with fluorescein-PMs and stained with propidium iodide (1 mg/ml). **B:** Representative histogram of BMSCs incubated for 1 (black), 3 (red) or 24 hours (blue) with fluorescein-PMs and stained with propidium iodide (1 mg/ml). Both graphs show the lack of difference in fluorescence intensity between cells treated with fluorescein-PMs and 99% of the control untreated cells (grey). **C:** Histogram showing the percentage of viable MG63 cells after 1, 3 or 24 hour incubation with fluorescein-PMs. **D:** Histogram showing the percentage of viable BMSCs after 1, 3 or 24 hour incubation with fluorescein-PMs. The percentage is calculated as the difference in cells positive for PI between untreated cells *vs* cells exposed to fluorescein- or empty-PMs. Data presented as mean ± SD, one-way ANOVA, with Dunn's post-hoc correction, n=3 independent experiments. Multiple comparison: ns = non significant.

3.2.8 Quantification of the intracellular payload release in BMSCs

Having validated the methodology for quantifying payload release on murine L929 cells, it was next decided to determine the number of PMs releasing payload intracellularly in BMSCs using the same technique. After a 24 hour incubation with 5 x

10^{12} fluorescein-PMs, the intracellular concentration of fluorescein in BMSCs was 4.57 x 10^{-10} nanomoles *per* cell (Figure 3.16). Having previously calculated the concentration of fluorescein *per* PM (5.48 x 10^{-21} moles, Figure 3.3), it was estimated that a mean of 83 PMs release fluorescein intracellularly.

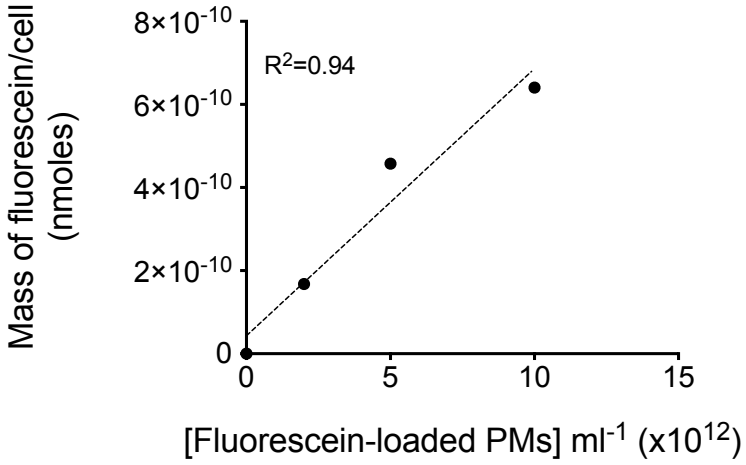

Figure 3.16: **Estimation of the concentration of fluorescein released in BMSCs from fluorescein-PMs.**

Graph showing the linear relationship between the mass of fluorescein *per* cell and the concentration of fluorescein-PMs incubated with BMSCs. $R^2 = 0.94$.

Then, the number of PMs releasing fluorescein intracellularly was calculated, at single-cell level, using the intensity of fluorescence measured on a cell-by-cell basis by flow-cytometry. Figure 3.17 shows that after a 24 hour incubation, a median of 93 and a maximum of 107 ± 2 PMs had released fluorescein *per* BMSC (Figure 3.17A & B). These values are lower than those calculated for L929 cells (median 172, max 329 ± 97) indicating cell type variability in PM cellular uptake.

A

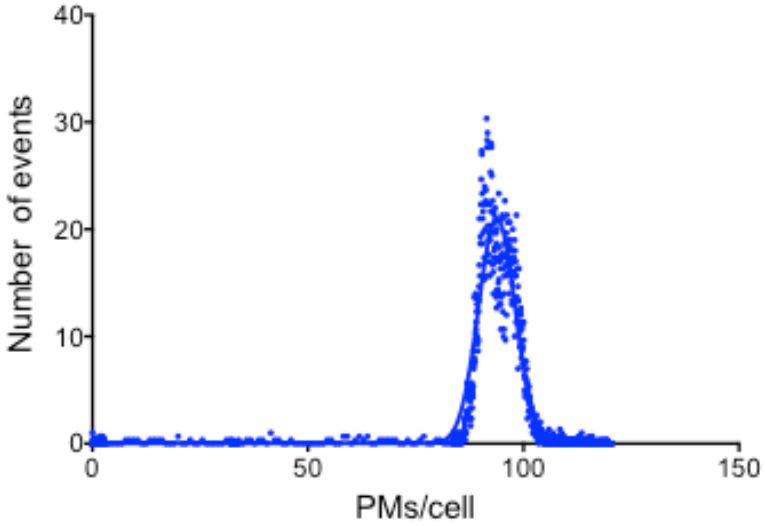

B

Estimated number of PMs releasing fluorescein *per* cell			
Min	**Max**	**Range**	**Median**
10 ± 12	107 ± 2	106 ± 2	93

Figure 3.17: **Quantification of the number of PMs releasing fluorescein in BMSCs at a single cell level.**

A: Representative graph depicting the number of PMs releasing fluorescein intracellularly *per* cell after incubation with fluorescein-PMs. **B:** Table summarising the minimum (Min), maximum (Max), range (Max-Min) and median number of PMs *per* cell after incubation with fluorescein-PMs.

3.2.9 Effect of serum on PM uptake

The results presented previously in this Chapter demonstrated that BMSCs reach saturation of fluorescein-PMs within 6 hours from the initial incubation. However, in all the experiments presented thus far, the concentration of serum in the culture media was switched from 10% to 0.5% (v/v) 24 hours prior, and during, the exposure to fluorescein-PMs. This was conducted to obtain a homogeneous population with all cells at the same stage of the cell cycle (G0/G1) (Kim et al. 2012), therefore allowing for a more robust assessment of the kinetics of PM uptake. Investigating the effect of serum-starvation on PM uptake, it was demonstrated that cell cycle synchronisation partially affects PM internalisation (1 to 2.4 fold-increase in PMs uptake following synchronisation). However, the presence of high serum (10%, v/v) during incubation with PMs significantly inhibits their uptake by BMSCs, irrespective of the cell cycle stage (p<0.0001, Figure 3.18A & B).

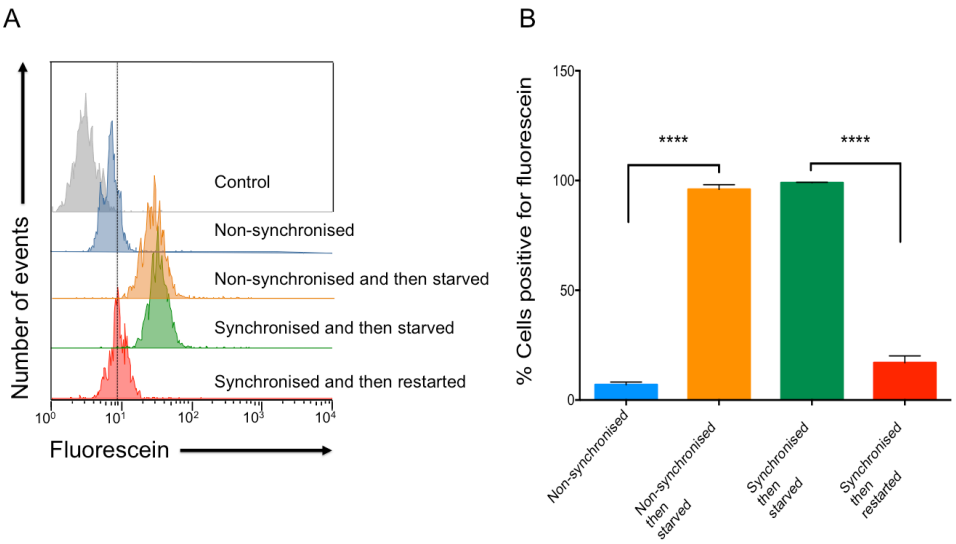

Figure 3.18: **The concentration of serum present in solution affects PM uptake by cells.**

A: Flow cytometry histograms showing the differences in fluorescence intensity measured in BMSCs incubated for 24 hours with fluorescein-PMs in different conditions: '**Non-synchronised**' are cells cultured and incubated in 10% serum, **'Non-synchronised and then starved**' are cells cultured in 10% and then incubated in 0.5% serum, **'Synchronised and then starved**' are cells cultured and incubated in 0.5% serum, **'Synchronised and then restarted**' are cells cultured in 0.5% and then incubated in 10% serum. Untreated cells (grey) served as control. Cells were considered positive when their fluorescence was greater than 99% of the control cells. Dotted lines indicate the markers set to discriminate between positive and negative cells **B:** Bar chart showing the significant difference in percentage of cells positive for fluorescein after 24 hours incubation with fluorescein-PMs in 0.5% serum. Data presented as mean ± SD, student t-test n=3 independent experiments. ****=p<0.0001.

Having demonstrated that PMs are internalised by BMSCs cultured on tissue culture plastic, it was then decided to investigate uptake of fluorescein-PMs by cells in suspension cultures. This was carried out in order to mimic the 3D environment in which cells reside in physiological conditions.

However, before determining uptake of fluorescein-PMs in a 3D setting, due to cessation of NH_2–PEG 5.8k-PCL 19k polymer manufacturing, PMs were produced using another polymer (PEG5k-PCL18k). Fluorescein-PMs produced using the new copolymer were characterised (Appendix Figure 7), their uptake by BMSCs was assessed (Appendix Figure 8), and the number of PMs releasing fluorescein intracellularly was quantified (Appendix Figure 9 & 10). Overall, fluorescein-PMs produced using the 5k-18k block copolymer were smaller and encapsulated less fluorescein, but were internalised by BMSCs with comparable kinetics compared to the other formulation.

BMSCs were incubated with the new PMs preparation either in adhesion or suspension, in the presence of increasing concentrations of serum. Note that the theoretical number of PMs available *per* cell was kept constant in both adhesion and suspension incubations.

Following 24 hour incubation more than 90% of the BMSCs have internalised fluorescein-PMs, regardless of the concentration of serum used and the culture conditions (Figure 3.19A). Overall, the percentage of cells positive for fluorescein was similar across the conditions tested, but adhesion and suspension were statistically different when BMSCs were cultured in 5% serum ($p<0.01$) (Figure 3.19B). Nevertheless, at concentrations of serum below 1% the cellular MFI was reduced in cells incubated in suspension compared to adhesion ($p<0.0001$ at 0% serum). Given these results, it was decided to use 5% serum in the media for all the experiments involving incubation of PMs with cells in suspension (Figure 3.19C).

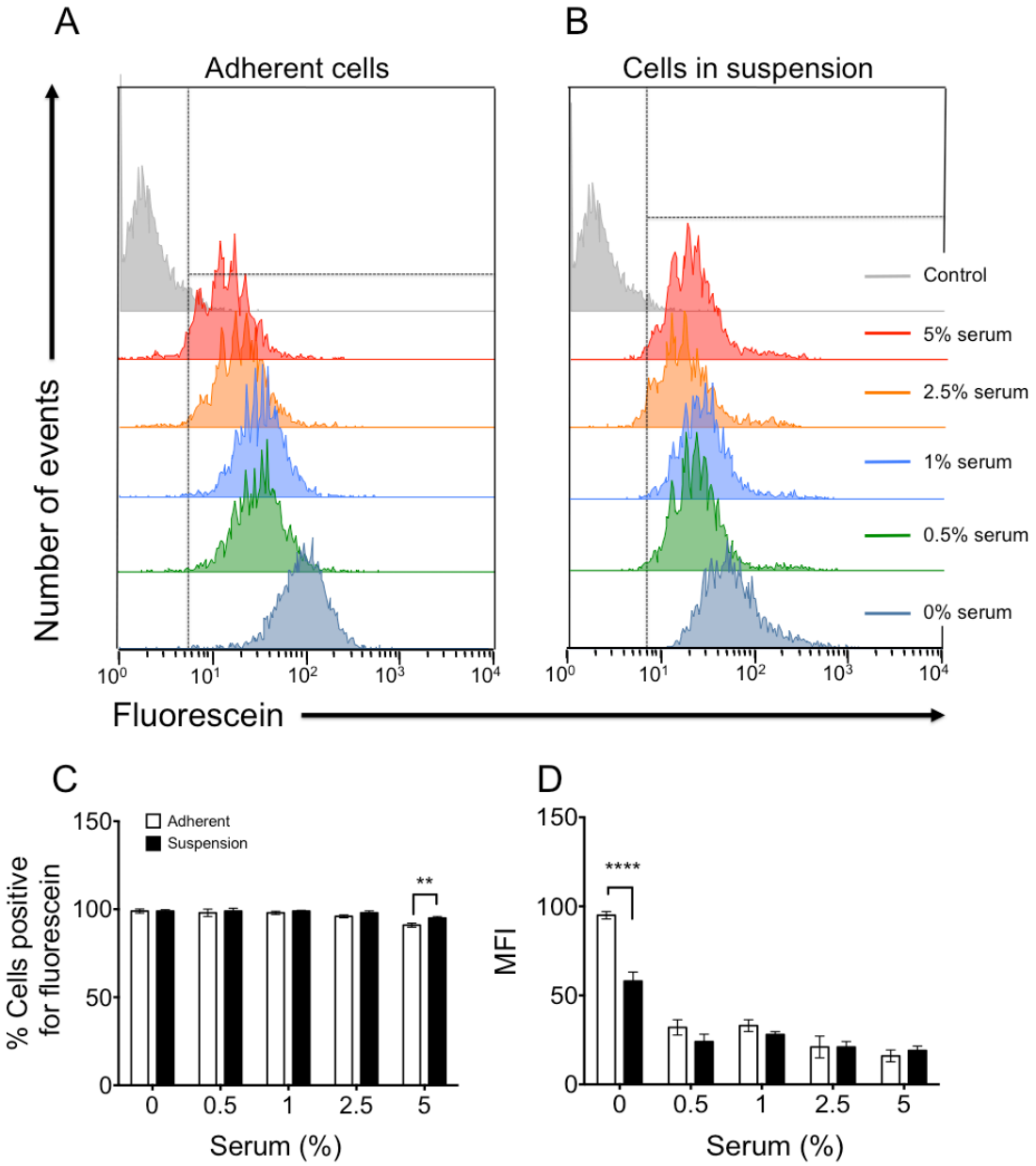

Figure 3.19: **The concentration of serum present in solution and the culture conditions affect fluorescein-PMs uptake by cells.**

A: Histograms showing the differences in fluorescence intensity measured in adherent BMSCs incubated for 24 hours with fluorescein-PMs in the presence of 5% (red), 2.5% (orange), 1% (blue), 0.5% (green) or 0% (grey) serum in the media. **B:** Histograms showing the differences in fluorescence intensity measured in BMSCs incubated for 24 hours in suspension with fluorescein-PMs in the presence of 5% (red), 2.5% (orange), 1% (blue), 0.5% (green) or 0% (grey) serum in the media. **C:** Bar chart showing the percentage of BMSCs positive for fluorescein following incubation with fluorescein-PMs either in adhesion of suspension. Statistical difference was observed when cells were incubated in 5% serum (v/v) (p<0.01). **D:** Bar chart showing the MFI of BMSCs following incubation with fluorescein-PMs either in adhesion of suspension. Statistical difference was observed when cells were incubated in 0% serum (v/v) (p<0.0001). Data presented as mean ± SD, n=3 independent experiments, statistical significance assessed by two-way ANOVA, with Sidak's post-hoc correction. Multiple comparison: **p<0.01, and ****p<0.0001.

3.2.10 Uptake of fluorescein-loaded PMs in freshly isolated BMMNCs

The bone fracture site is characterised by the presence of a plethora of cell types, most of which can be found in the bone marrow tissue (see section 1.2.3). Having demonstrated that suspension conditions support cellular uptake of PMs, it was decided to investigate how PMs partition when incubated with a mixed cellular population. In particular, following gradient separation of human bone marrow samples, numerous cell types can be identified, ranging from granulocytes to lymphocytes and SSCs. It was hypothesised that the investigation of PMs uptake in freshly isolated BMMNCs would more closely mimic the bone fracture environment, providing valuable information in support of the main aim of this project.

After lymphoprep™ separation (see section 2.2.1), and among the cells gated excluding cellular debris (Figure 3.20A), it is possible to distinguish three groups of cells according to their physical parameters (size and granularity): granulocytes, monocytes and lymphocytes (Figure 3.20B). Then, in order to distinguish cellular subtypes, three different monoclonal antibodies were used: CD14 (expressed by monocytes, Figure 3.20C & D), GPA (expressed by erythroid cells, Figure 3.20E & F) and STRO-1 (expressed by SSCs, but also by monocytes and erythroid cells, Figure 3.20G & H).

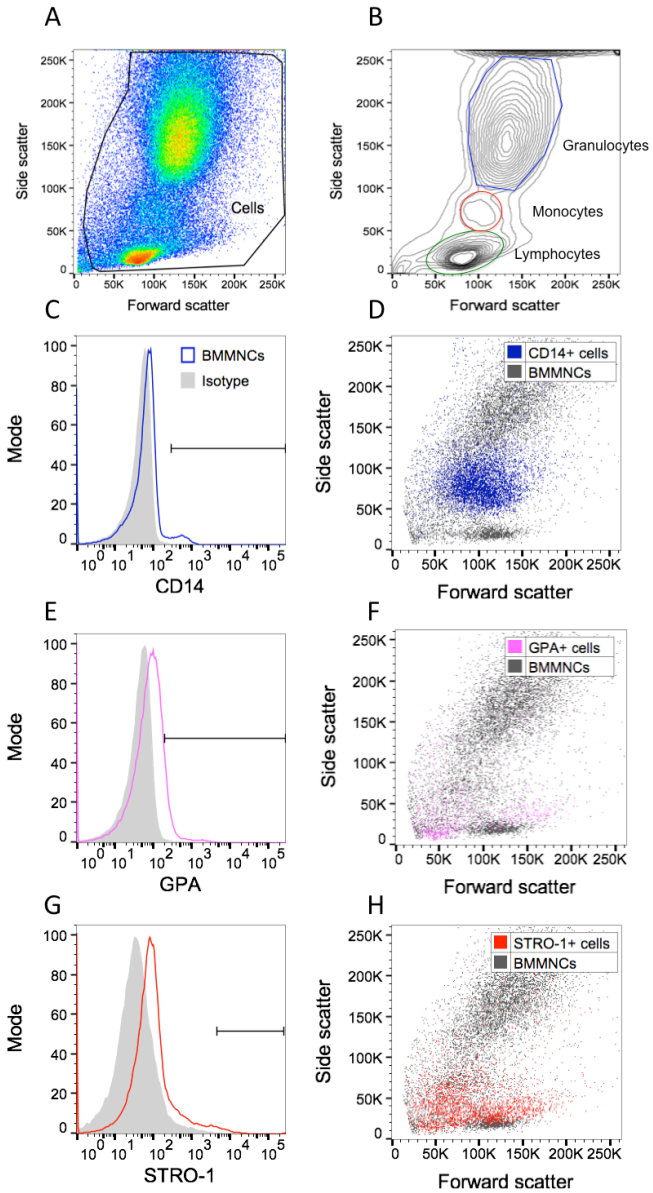

Figure 3.20: **Cell lineages in human BMMNCs.**

A: Representative dot plot showing side scatter *vs.* forward scatter of freshly isolated BMMNCs and consequent gating strategy adopted to analyse only living cells (Cells). **B:** Representative density plot depicting the gating strategy based on forward and side scatter used to distinguish between granulocytes (blue), monocytes (red) and lymphocytes (green). **C:** Histogram showing CD14 expression in freshly isolated BMMNCs (blue) compared to isotype control (grey). **D:** Representative side *vs.* forward scatter dot plot showing the overlay of CD14+ cells (blue) present in the whole freshly isolated BMMNCs (grey). **E:** Histogram showing STRO-1 expression in freshly isolated BMMNCs (blue) compared to isotype control (grey). **F:** Representative side *vs.* forward scatter dot plot showing the overlay of STRO-1+ cells (blue) present in the whole freshly isolated BMMNCs (grey). **G:** Histogram showing GPA expression in freshly isolated BMMNCs (blue) compared to isotype control (grey). **H:** Representative side *vs.* forward scatter dot plot showing the overlay of GPA+ cells (blue) present in the whole freshly isolated BMMNCs (grey). Cells were considered positive for a marker when they expressed a greater fluorescence intensity than 99% of the cells labelled with the isotype matched control.

Overall, after 3 hours incubation in suspension, fluorescein-PMs were internalised in 77 ± 4.4% of the population (Figure 3.21A), with most of the fluorescein positive cells being localised in the cellular fraction containing granulocytes. In particular 86 ± 15.6% of these cells were fluorescein positive (Figure 3.21B).

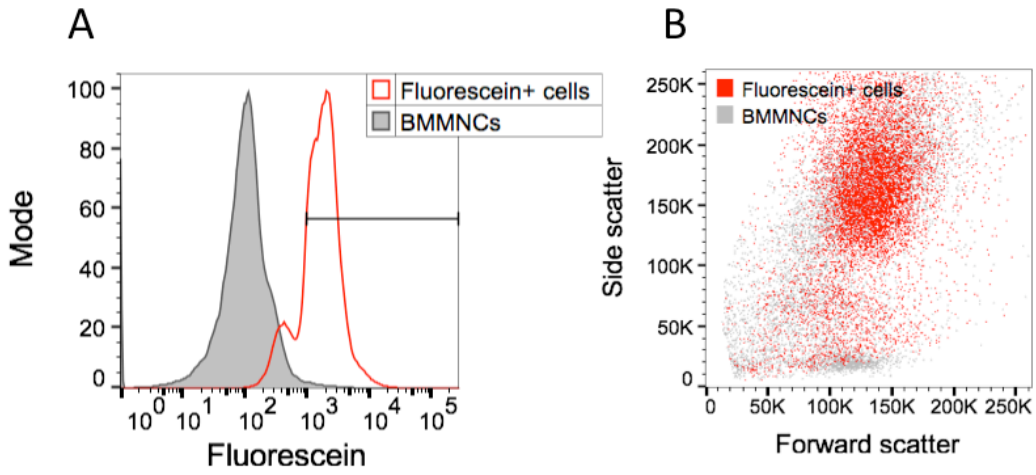

Figure 3.21: **Freshly isolated BMMNCs internalise fluorescein-PMs.**

A: Representative flow cytometry dot plot of freshly isolated BMMNCs incubated for 3 hours in suspension with 5k-18k fluorescein-PMs. The graph shows the overlay of fluorescein+ cells (red) over the whole BMMNCs (grey) **B:** Histogram showing fluorescein expression in freshly isolated BMMNCs incubated for 3 hours with fluorescein-PMs (red) compared to un-treated control BMMNCs (grey).

Monocytes, which are CD14+ cells and represented 7 ± 4.4 % of the whole bone marrow population (Q2 and Q3 in Figure 3.22A), were also internalising fluorescein-PMs (red square in Figure 3.23A) as demonstrated by the fact that 95 ± 3.1 % of them were fluorescein positive after 3 hours incubation (Figure 3.22B).

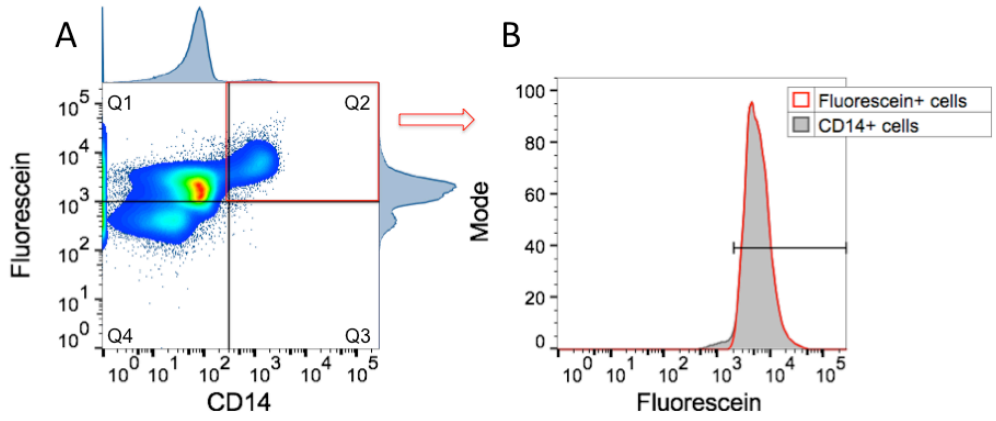

Figure 3.22: **Monocytes internalise fluorescein-PMs.**

A: Representative quadrant dot plot depicting the distribution of the BMMNCs according to their positivity or negativity for both CD14 and fluorescein. Q1 is fluorescein+/CD14- (71.9%), Q2 (red square) is fluorescein+/CD14+ (4.93%), Q3 is fluorescein-/CD14+ (0.0046%), Q4 is fluorescein-/CD14- (23.1%). The gating lines in the graph were set according to the intensity of fluorescence of BMMNCs not treated with fluorescein-PMs (black gate present in Figure 3.20B) and to the intensity of fluorescence of CD14 isotype matched control for CD14. **B:** Histogram showing fluorescein expression (red) in CD14+ cells (grey) incubated for 3 hours with fluorescein-PMs.

Finally, internalisation of fluorescein-PMs in SSCs was assessed. Firstly, SSCs were recognised by their specific surface marker profile (STRO-1+/CD14- and GPA-, red square in Figure 3.23A) and represented 2 ± 1.5% of the whole bone marrow sample (Figure 3.23B). Of these cells, 60 ± 26% were positive for fluorescein, Figure 3.23C).

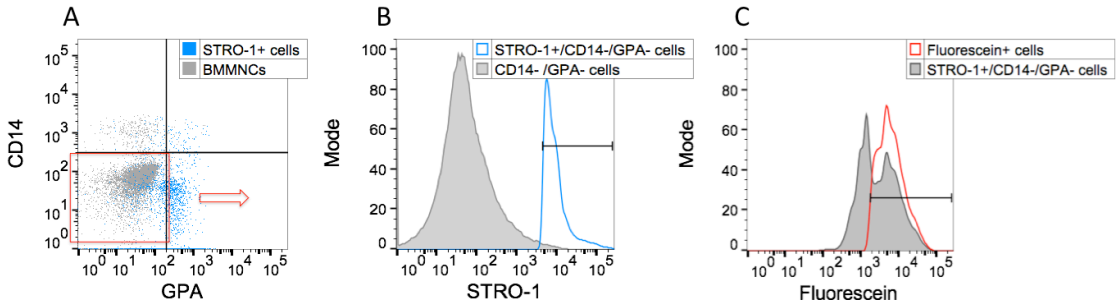

Figure 3.23: **SSCs internalise fluorescein-PMs.**

A: Representative quadrant dot plot depicting the localisation of STRO-1 positive cells (blue) among CD14- and GPA- cells (grey). The gating lines in the graph were set according to the intensity of fluorescence of CD14 and GPA isotype matched controls (black marker present in Fig3.20C & E), red square. **B:** Representative quadrant dot plot showing the overlay of STRO-1+ cells (red) over BMMNCs (blue) according to CD14 *vs.* GPA intensity of fluorescence. **C:** Histogram showing fluorescein expression (red) in STRO-1+/CD14-/GPA- cells (grey) incubated for 3 hours with fluorescein-PMs.

3.2.11 Investigation of fluorescein-PMs uptake using Image Stream

The previous results have demonstrated uptake of fluorescein-PMs by various cellular populations within the BMMNCs, including SSCs. Next, it was decided to use Image Stream to confirm these observations, whilst investigating the spatial localisation of the fluorescein within the cells and the route of PMs uptake. Image Stream is equipped with two high-resolution CCD cameras, which allow for the visualisation of an intracellular slice of every cell present in the flow stream. Therefore, this high-throughput technique enables imaging and quantification of fluorescent molecule on a cell-by-cell basis, as well as its intracellular localisation at a single organelle level.

In Figure 3.24 are reported representative images showing monocytes (STRO-1-/CD14+/GPA-, Figure 3.24A) and SSCs (Figure 3.24B) positive for fluorescein, which confirm the results previously obtained using flow cytometry. Moreover, using Image Stream it was observed that, regardless of the cell type investigated, the intracellular distribution of fluorescein was observed to be diffused (white arrow) or punctated (red arrow).

In particular, the presence of a punctate signal observed in Figure 3.24 suggests compartmentalisation of PMs in cellular organelles following cellular internalisation. This possibility was further investigated in preliminary data using Image Stream. However, this experiment was performed only one-time due time constrictions, and was carried out on MG63 cells cultivated in adhesion rather than freshly isolated BMMNCs, due to high cell death during sample preparation.

Following a 24 hour incubation with fluorescein-PMs, MG63 cells were stained for LAMP-1, which is a marker specific of late endosomes and lysosomes, and the co-localisation between fluorescein and LAMP was assessed. Of all the MG63 cells analysed, 29% were double positive for fluorescein and LAMP-1. In 66% of these, fluorescein and LAMP-1 fluorescence were co-localised (white arrow in Figure 3.25A & A1, Figure 3.26), whilst the remaining 34% of the cells showed the presence of two distinct fluorescent signals (Figure 3.25B & B1, Figure 3.26).

Overall, this preliminary data supported the hypothesis that PMs are compartmentalised in endocytic organelles following cellular uptake, and also demonstrated the potential of Image Stream technology for nanoparticles and drug delivery investigations.

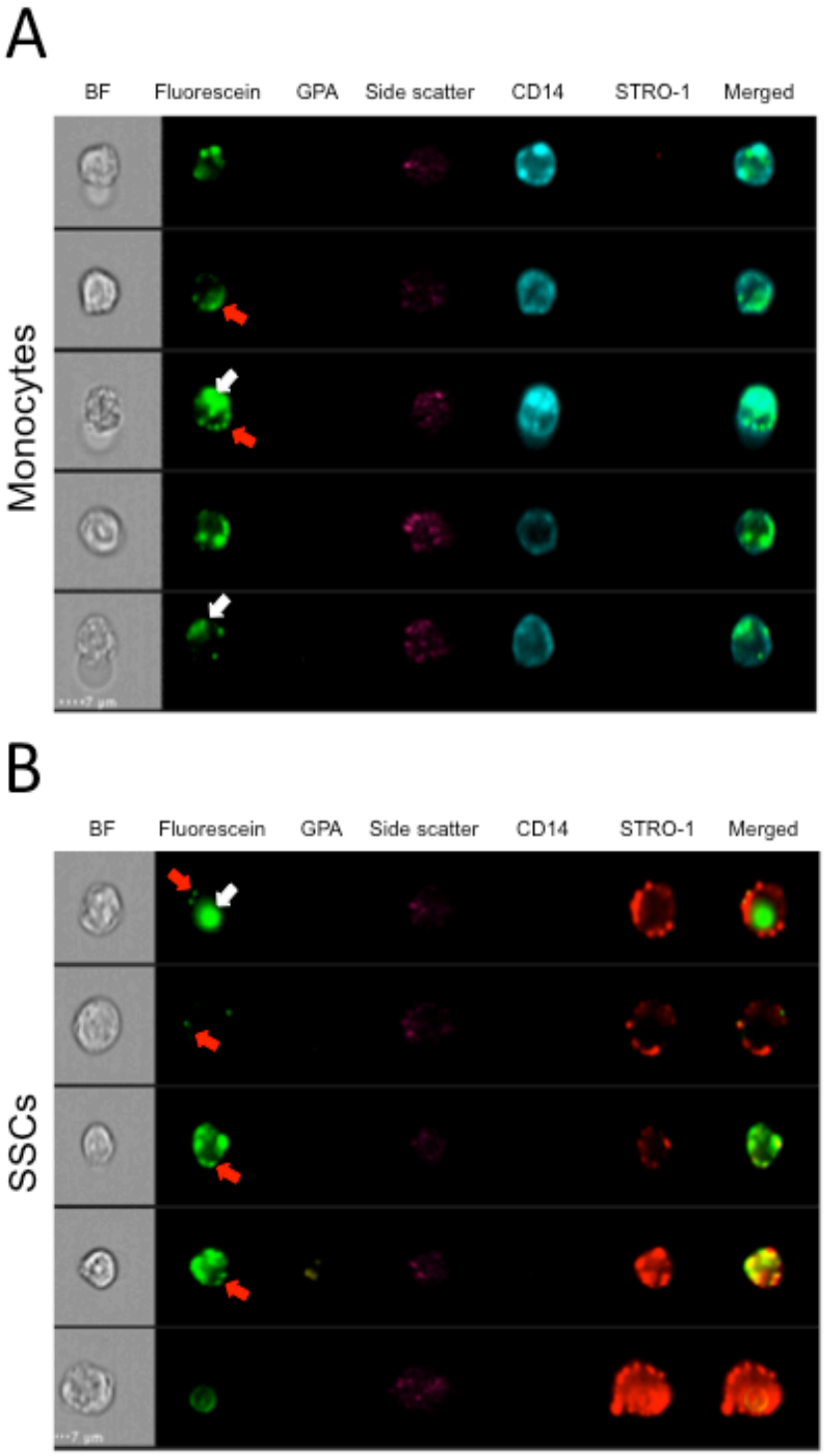

Figure 3.24: **Monocytes and SSCs positive for fluorescein analysed by Image Stream.**

A: Representative images of monocytes positive for both fluorescein and CD14 whilst negative for GPA and STRO-1. **B:** Representative images of SSCs positive for both fluorescein and STRO-1 whilst negative for CD14 and GPA. BF, bright-field. White arrow indicates diffused intracellular distribution of fluorescein. Red arrow indicates punctate intracellular distribution of fluorescein. Scale bars = 7 μm.

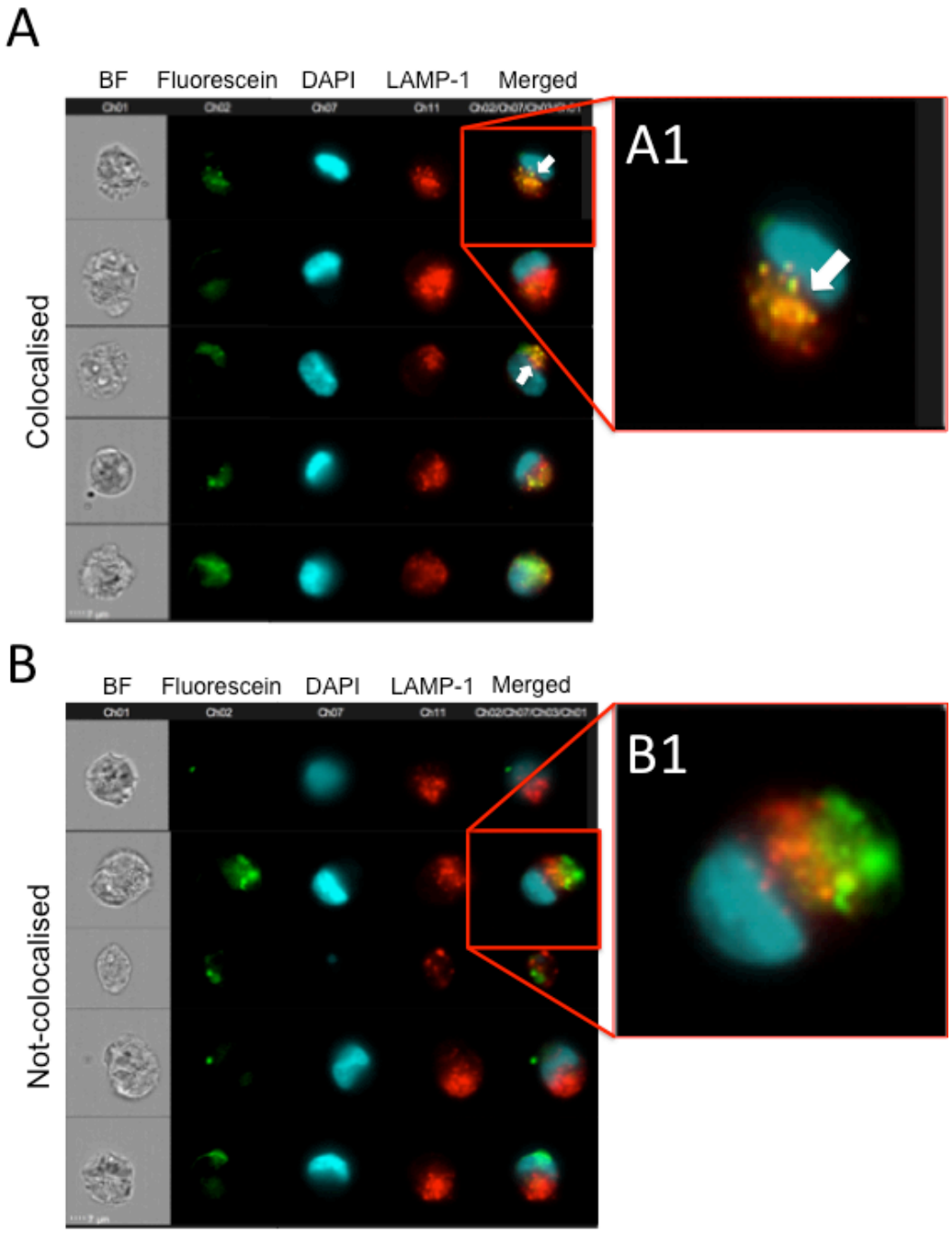

Figure 3.25: **Co-localisation of fluorescein with LAMP-1 in MG63 cells.**

A: Representative images of MG63 cells treated with fluorescein-PMs in which the intracellular fluorescence of fluorescein (green) is co-localised with LAMP-1 staining (red). **B:** Representative images of MG63 cells treated with fluorescein-PMs in which the intracellular fluorescence of fluorescein (green) is not colocalised with LAMP-1 staining (red). White arrow indicates co-localisation of fluorescein and LAMP-1. **A1 and B1:** Enlarged pictures of the correspondent red inserts. Scale bar = 7 µm. (*n*=1 independent experiment).

Region	Cell count	% of total events	% of gated cells (region)
All	3013	100	/
In focus	2886	95.8	95.8 (II)
Single cells	2456	81.5	85.1 (In focus)
Fluorescein and LAMP-1+ cells	872	28.9	35.5 (Single cells)
Co-localised	574	19.1	65.8 (Fluorescein and LAMP-1 + cells)
Non co-localised	296	9.82	33.9 (Fluorescein and LAMP-1 + cells)

Figure 3.26: **Quantification of fluorescein and LAMP-1 co-localisation in MG63 cells.**

Table summarising cell count, % of total events and % of gated cells in all the different gated sub-groups of MG63 cells. (*n*=1 independent experiment).

3.3 Discussion

PMs represent a promising system for the spatio-temporally controlled delivery of hydrophilic and hydrophobic molecules for therapeutic purposes. However, the ability of PMs to function as drug carriers is dependent on their cellular uptake and consequent release of payload. Calculations regarding the number of PMs releasing a given payload intracellularly are also of pivotal importance in determining the efficacy of delivery.

The experiments presented in this chapter addressed these topics by demonstrating that:

- PEG-PCL PMs can be loaded with fluorescein, and are functional for determining the delivery of payload in real-time;
- Fluorescein-PMs are internalised by different mammalian and do not induce cytotoxicity;
- The percentage of serum present in the culture media affects the rate of PMs uptake by cells;
- PMs are internalised by cells even when the incubation occurs in suspension conditions;
- Following incubation with freshly isolated BMMNCs, fluorescein-PMs are internalised by various cellular populations including SSCs;
- The number of PMs releasing fluorescein intracellularly can be quantified at a single-cell resolution.

PMs are formed from block copolymers that self-assemble in solution creating a vesicular structure able to carry both hydrophilic and hydrophobic molecules (Discher et al. 1999; Ahmed et al. 2006). In this project, the block copolymer used for producing PMs was PEG-PCL as it comprises two polymers approved by the FDA for clinical use, which facilitates and eventual clinical translation of the product. Also, PEG-PCL PMs were among the first to be produced and their physical-chemical properties have been widely characterised (Ahmed & Discher 2004). Nonetheless, PEG-PCL remains a 'simple' copolymer that does not allow for a more exquisite control of payload release. In this context, future experiments could investigate the use of different copolymers for producing PMs, such as those sensitive to pH alterations (Lomas et al. 2010; Massignani

et al. 2009) or temperature changes (Liu et al. 2015), which allow for a finely controlled delivery of molecules. However, PEG-PCL PMs constituted a robust model for preliminary experiments, and their functionality as DDS has been repeatedly demonstrated *in vivo* (Ahmed et al. 2006; Buckiova et al. 2012). Two PEG-PCL block copolymers with different molecular weights were used in this project, NH_2-PEG 5.8k-PCL 19k and PEG 5k-PCL18k. PMs produced with either of the two copolymers were less than 100 nm in size (hydrodynamic diameter), which is a suitable size for facilitating systemic delivery *in vivo* (Brinkhuis et al. 2012) and cellular uptake (Canton & Battaglia 2012).

In order to detect cellular uptake of PMs, sodium fluorescein (fluorescein) was encapsulated at high concentrations within PMs (274 μM). Other dyes such as rhodamine B and propidium iodide have been successfully encapsulated in PMs, and used to demonstrate intracellular release following uptake in a similar fashion (Massignani, Canton, et al. 2010). The hydrodynamic size of the PMs was not altered by fluorescein encapsulation and the carriers were stable for up to one week at room temperature (Figure 3.2). It was also demonstrated that fluorescein fluorescence was quenched within PMs and it was detectable only after release, allowing for real-time payload delivery to be measured. Weinstein and colleagues adopted a similar strategy to demonstrate liposomal-mediated delivery, but rather than using fluorescein, the authors encapsulated the more hydrophilic derivative carboxyfluorescein (Weinstein et al. 1977). The two molecules differ by the presence of two functional carboxyl groups in position 5 and 6, but such modifications are essential in order to overcome the poor ability of liposomes to retain fluorescein (Weinstein et al. 1977). In contrast, PMs are less permeable than liposomes (Bermudez et al. 2002) and as demonstrate by the encapsulation and retention of fluorescein over a period of several days (Figure 3.3).

Using time-lapse microscopy it was shown that the intracellular release of payload from PMs occurs relatively quickly, since fluorescein was visible inside the cells 15 minutes after initial incubation (Figure 3.5). This result was somewhat surprising as PEG-PCL copolymer undergoes intracellular degradation over rather long time-frames (Ahmed & Discher 2004; Geng & Discher 2006; Oltra et al. 2014); thus, these fast kinetics of release were not expected. However, previous work from our group demonstrated that the PMs used in this project are internalised by cells *via* an active process (Scarpa et al.

2016), and this was further confirmed using Image Stream which showed co-localisation of fluorescein and LAMP-1 (Figure 3.25). Therefore, as a consequence of internalisation, PMs are sequestered and compartmentalised in vesicular structures typical of the endocytic pathway (*i.e.* endosomes and lysosomes). In here, PMs are exposed to a low environmental pH and to the action lysosomal acid hydrolases, which induce the degradation of the highly hydrolase-sensitive polyester PCL (Li et al. 2002). In addition, the enzymatic destabilisation of the nanoparticles' structure may also be facilitated by the exposure to physiological temperature (~37°C) (Ahmed et al. 2006). All these factors are likely to be the cause of the quick intracellular release of fluorescein observed. It would be useful to confirm these speculations in future experiments assessing the stability of the PMs preparations to higher temperatures, different types of culture medium and the presence of hydrolytic enzymes.

Analysing the kinetics of PM uptake it was demonstrated that PMs are internalised by cells in a time-dependent fashion, but saturation of the fluorescence signal is reached within 6 hours of incubation (Figure 3.14). Although the mechanisms by which fluorescein saturation was reached were not investigated, it can be speculated this this may be due to a series of factors. For example, in a recent study using PEG-polystyrene nanoparticles, Unciti-Broceta and colleagues found that a ratio of 1000 to 4000 nanoparticles *per* cell was saturating, whilst the nanoparticle concentration was rate limiting only below a ratio of 2000 nanoparticles *per* cell (Unciti-Broceta et al. 2015). In all the experiments described in this chapter a ratio of more than 1 x 10^6 PMs *per* cell was calculated, therefore it is unlikely that the depletion of nanoparticles from the medium has any significant effect on the rate of uptake, but PMs could become less available for uptake as consequence of aggregation following exposure to medium with serum. This possibility could be investigated by analysing PMs size and PdI after incubation in media supplemented with increasing serum concentrations. Alternatively it can be hypothesised that either the cells reached an equilibrium between PMs internalisation on the one hand and fluorescein catabolism and/or exocytosis on the other, or that PM uptake was no longer occurring after 6 hours incubation. Both scenarios are plausible, but it is worth mentioning that, in these experiments, cells were cultured in a regime of serum-starvation. This decreases the variability due to the presence of cells in different phases of the cell cycle, but it is also a limitation of the study since it may reduce the possibility to 'dilute' the intracellular concentration of fluorescein across cellular generations. This

hypothesis is supported by work from by Kim and colleagues who demonstrated that following nanoparticle uptake, the cellular fluorescence intensity was decayed as a consequence of cell division (Kim et al. 2012). Future experiments aiming to assess the mechanisms behind saturation in PMs uptake should consider the limitations of the experiments presented (*i.e.* serum-starvation), whilst introducing new variables. For example, cells could be incubated with a range of PM concentrations or the exposed to PMs for different periods of time. Overall, further investigations regarding cell saturation in PMs uptake and generational inheritance are needed in order to expand the knowledge in nano-pharmacology, while reducing safety concerns about clinical application of PMs (Summers et al. 2013).

Furthermore, it was observed that PMs uptake from cells is largely independent from cell cycle synchronisation, in agreement with Kim and colleagues (Kim et al. 2012). However, the concentration of serum present in the media during incubation has a profound effect on PMs uptake, as demonstrated by the significant enhancement in the number of fluorescein positive cells when incubation with PMs occurred in 0.5% (v/v) serum. The interaction and adsorption of plasma proteins on the surface of the nanoparticles is one of the factors affecting cellular uptake and circulation-time *in vivo* (Lynch & Dawson 2008). This can be limited by covering the surface of the nanoparticles with polymers that generate steric forces which repel the interactions with proteins dissolved in the media (Leckband & Israelachvili 2001). PEG represents the gold standard in nanomedicine for reducing protein adsorption; however, PEG is not able to completely abolish such adsorption, irrespective of its density on the surface of the nanocarrier (Walkey et al. 2012). Electrostatic and hydrophobic interactions between proteins and nanoparticles surface contribute to create a layer of proteins around nanoparticles. The composition of the protein layer varies according to the intensity of the interactions and the concentration of the over 3700 proteins present in the plasma, and will result in the formation of "different" nanoparticles within a same preparation (Lynch & Dawson 2008). Considering that cells "see" what is displayed on the nanoparticle surface, it is likely that the variability in the protein layer composition will affect cellular uptake (Lynch et al. 2009). The block copolymer used in the initial experiments was amino terminated (NH_2), this would likely increase the electrostatic interactions between PEG brush and plasma proteins altering the affinities of these proteins for the nanoparticle surface and resulting in a prolonged interaction with certain

proteins. This can be considered as a strength and a limitation of the system, as it is likely that the PMs present in solution were homogeneously displaying a similar layer of proteins, but this may have also affected the rate of cellular uptake. Nevertheless, it was demonstrated that PMs produced using a 'plain' PEG-PCL copolymer (5k-18k), are also internalised by BMSCs regardless of the serum concentration used (Figure 3.19). This result, somehow, reduces the limitations related to the use of the amino-terminated copolymer.

Using fluorescein it was demonstrated that PMs are internalised by different mammalian cell types in both adhesion and suspension culture conditions (Figure 3.19). In this context, Cho and colleagues reported that the rate of uptake of gold nanoparticles depends on the culture conditions, whereby cells positioned in an 'inverted' setting internalised less nanoparticles compared to a canonical upright configuration. The authors reasoned that uptake of nanoparticles in adherent cells is deeply influenced by the gravity, which induces nanoparticles sedimentation on the cell surface facilitating the internalisation (Cho et al. 2011). In the experiments presented in this chapter, the percentage of cells positive for fluorescein after a 24 hour incubation was always exceeding 90%, regardless of the incubation setting used. However, the MFI was overall increased in adherent cells compared to suspension cells at low serum concentrations; therefore, it cannot be ruled out that the gravity is favouring PMs uptake. In future experiments it would be interesting to confirm this hypothesis by comparing kinetics of PMs internalisation in inverted and up-right culture conditions as well as measuring the kinetics of PMs sedimentation in culture media.

Next it was demonstrated that PMs are internalised by various cell types within a mixed population, including the rare population of SSCs (Figure 3.23). This result shows that SSCs, which are the cells differentiating into osteoblasts, are internalising PMs, and underpins the hypothesis that PMs can be used as DDS for promoting bone regeneration following fracture.

Finally, a new methodology for estimating and then quantifying the number of PMs releasing payload *per* cell, at a single-cell resolution, was introduced in this chapter. Figure 3.16 shows that a linear relationship between the concentration of intracellular fluorescein and concentration of fluorescein-PMs incubated with cells was found, and this was used to quantify the number of PMs *per* cell. The quantum yield of fluorescein is

affected by its molecular nanoenvironment (*e.g.* pH, charge, protein binding) (Sjöback et al. 1995), so the first limitation of the methodology proposed is that likely not all the PMs have released payload in that time frame investigated. In order to partially control for this factor, the intracellular concentration of fluorescein was determined by a standard curve of fluorescein absorbance in a solution containing cell lysate. Also, no difference in the total fluorescence intensity of aliquots of cells before and after cell lysis was found (Appendix Figure 3). However, these measurements were performed on whole cellular populations and PMs may have been at different stages of the endocytic pathway. This would result in a variation of fluorescein release on a cell-to-cell basis and would introduce errors in the estimation of intracellular concentration of fluorescein measured. Furthermore, it is likely that the intracellular fluorescence observed was originated from only a portion of all the PMs internalised, since fluorescein fluorescence remains quenched in intact PMs, resulting in an underestimation of the PMs internalised.

In future experiments, these limitations can be addressed by using high performance liquid chromatography in order to provide an additional layer of certainty of the absolute intracellular concentration of the dye, and this could be coupled with time resolved fluorescence to discern between relative concentrations of a fluorophore in different molecular microenvironments (Evans et al. 2005; Schneckenburger et al. 2004). Alternatively, pH sensitive dyes such as the one employed by Semmling and colleagues could be used for the same purpose (Semmling et al. 2008). Moreover, in order to entirely release fluorescein from PMs, these could be fabricated using a pH sensitive copolymer PDPA that undergoes complete dissociation at lysosomal pH (~6.5) (Massignani et al. 2009; Lomas et al. 2010).

Nevertheless, the number of PMs releasing fluorescein *per* cell was quantified (Figure 3.11) and as expected, a time-dependent increase was observed, and this was also associated with cell-to-cell variability of the intracellular concentration of fluorescein. Such variability was present despite the attempt to control for possible *inter* cellular variation by cell cycle synchronisation through serum-starvation (Kim et al. 2012). This cell-to-cell variability in fluorescein release from PM may be attributed to the stochastic nature of cell-PM interactions during the internalisation process, due to a combination of factors including PM agglomeration and clustering, and variable cellular surface receptor dynamics (Summers et al. 2011; Ehrlich et al. 2004). Moreover, the analysis presented

assumes that PMs formed using a single type of block copolymer (5.8k-19k or 5k-18k) have an equal chance of being taken up and releasing their contents *per* cell, regardless of the size, which is inherently not uniform. This may be an over simplification, as size is known to affect the rate and efficiency of uptake, and it was indeed demonstrated by the difference in the number of PMs releasing fluorescein in BMSCs depending on the copolymer used for production (Figure 3.17 and Appendix Figure 10). Also, the variability in PM size affects the mass of fluorescein entrapped *per* nanoparticle as it is proportional to the volume of the carrier, and the measurements of uptake reported may be particularly sensitive to variations in the uptake of PMs at the large end of the dispersion profile.

Overall, the number of PMs releasing payload *per* cell quantified in these sets of experiments fall in the same order of magnitude of what Unciti-Broceta and colleagues estimated to be the number of nanoparticles needed *per* cell in order to achieve nanoparticle uptake in 50% of a cell population, and it is similar to previously reported findings (Unciti-Broceta et al. 2015). However, in another study, Massignani and colleagues encapsulated, or conjugated, rhodamine to diblock polymers composed of PMPC25–PDPA70 and PEG23–PDPA15 and reported values of 10^6-10^7 PMs internalised/cell (Massignani et al. 2009). This marked difference between studies could be partially explained by the differences in PM concentration used, PM chemistry, encapsulation efficiency of the dye molecules, and by differences in the degradability of the PMs used. This underlines the difficulties in comparing the number of nanoparticles internalised *per* cell quantified in different studies, given the diversity of cells, nanoparticles and cell culture conditions used. Another factor limiting the kinetics of cellular internalisation of PMs and consequent release of payload is the depletion of nanoparticles from the culture medium, particularly when PM uptake for a determined time interval is equivalent to the number of PMs available *per* cell. However, using PEG-polystyrene nanoparticles it has been demonstrated that this is a limiting factor only when less than 2000 nanoparticles *per* cell were available in the extracellular compartment (Unciti-Broceta et al. 2015). In the experiments reported in this chapter, it was calculated that more than 1×10^6 and 1×10^4 PMs *per* cell were theoretically available when incubation with cells happened in adhesion or suspension, respectively, and so it is unlikely that the depletion of nanoparticles from the medium has any significant effect on the rate of uptake. Considering all the limitations of the quantification methodology here

described, it still remains a valid system by which the number of nanocarriers releasing payload inside the cells can be evaluated in real-time and on a single cell level. It could be potentially extended not only to the investigation of different PMs preparations but also to evaluate the release of a given molecule in whole tissues.

In summary the results presented in this chapter demonstrated that PEG-PCL PMs are effective in delivering a putative payload in a range of mammalian cells, including rare populations, and in a variety of culture conditions. PM uptake by cells is time-dependent, but initial internalisation of nanoparticles can be observed within 15 minutes from the start of the incubation. Finally, it was possible to establish a novel methodology for the quantification of intracellular payload release from PMs. These aspects are of fundamental importance when a spatio-temporal controlled delivery is needed, including, but not limited, to the therapeutic activation of the Wnt pathway for bone regeneration (discussed in the next chapter), and also when the payload released by PMs may have stimulatory, but also cytotoxic effects depending on its intracellular concentration.

Chapter 4: Polymersomes for intracellular delivery and activation of the Wnt signalling pathway

4.1 Introduction

The canonical Wnt signalling pathway is central to bone homeostasis and repair. Its activation increases bone mass and strength, while its inhibition has the opposite effect (Baron & Kneissel 2013). The pharmacological modulation of Wnt signalling has been widely investigated in order to generate strategies to promote bone formation - positive results have been demonstrated in preclinical *in vivo* models and in clinical trials (reviewed in section 1.5).

Nevertheless, activation of the Wnt pathway in order to promote bone formation requires careful control to achieve optimal outcomes. Dysregulation of Wnt is associated with renal cell carcinoma (Hsu et al. 2012) and hepatocellular carcinoma (J. Liu et al. 2011), as well as bone diseases such as osteoporosis-pseudoglioma syndrome, sclerosteosis and Van Buchem disease (Baron & Kneissel 2013). Wnt signalling is crucial in controlling the differentiation and proliferation of SSC towards the osteoblastic phenotype (reviewed in section 1.4). However, such osteogenic induction depends on the stage of differentiation of the target cells (Cook et al. 2014; Liu et al. 2009; Quarto et al. 2010), and on the time of activation. Recent findings from our group demonstrate that transient activation of the Wnt signalling pathway promotes the proliferation and favours the osteogenic commitment of human SSCs, whilst prolonged stimulation inhibits the differentiation (Janeczek et al. 2016). These studies emphasise the therapeutic potential of modulating Wnt signalling, but underline the need for a fine spatio-temporal controlled activation of the pathway.

PMs are an attractive DDS, as they can be loaded with a number of therapeutic molecules and enable spatially and temporally controlled delivery. The encapsulation of therapeutic molecules within PMs provides protection from degradation increasing circulation half-life and reducing off-site accumulation *in vivo*. PM encapsulation also greatly improves the solubility of a drug allowing not only for the delivery of high concentrations, but also for the use of more potent molecules that are often discarded due to their poor pharmacological characteristics (reviewed in section 1.6).

Given these considerations, PMs appear to be an optimal candidate for the delivery of Wnt agonists in order to promote bone regeneration. However, what Wnt agonist would be suitable for encapsulation within PMs?

Due to the importance of Wnt signalling in homeostasis and disease, a plethora of agonists have been developed and are available commercially, a few of which are currently being investigated in clinical trials for diverse applications (Rey & Ellies 2010). These agonists can be broadly divided into extracellular and intracellular acting molecules. The family of extracellular agonists is comprised of all the Wnt proteins, sFRPs, R-spondins and the inhibitors of the Wnt antagonists (*i.e.* Wif-1, Sost, DKK) (see section 1.3.1). The latter are of particular interest in bone biology as monoclonal antibodies, from example Romosozumab, have been developed to inhibit these molecules. The use of this anti-scelrostin antibody has shown promising results during phase III clinical trials for the treatment of osteoporosis, and is currently listed for FDA approval (reviewed in section 1.5). The most widely investigated intracellular target for the activation of the Wnt pathway is GSK-3β.

GSK-3β is part of the 'destruction complex' and has a key role within the Wnt pathway phosphorylating β-catenin, with subsequent inhibition of the pathway (reviewed in section 1.3.1). Therefore, inhibition of GSK-3β's function results in Wnt signalling up-regulation. The first inhibitor of GSK-3β to be identified was the lithium ion (Li^{2+}) (Klein & Melton 1996), which is routinely used for the treatment of bipolar disorder. Treatments with lithium have been shown to increase bone mass in mice and in humans (Clement-Lacroix et al. 2005; Zamani et al. 2009), and to promote bone healing following fracture in mice (Chen et al. 2007). However, the augmented bone regeneration was observed when lithium was administered 4 days following fracture, emphasising the need for a controlled activation of the pathway (Chen et al. 2007). Nevertheless, lithium has a half maximal inhibitory concentration (IC50) in the millimolar range, an index of a poor specificity.

Other synthetic molecules with proven GSK-3β inhibitory effects and a biological function in bone tissue are:

- AZD 2858, a pyrazine analogue, which has been shown to enhance bone mass (Marsell et al. 2012) and enhance fracture repair in rats (Sisask et al. 2013);

- CHIR99021, which promoted osteoblastogensis and inhibited adipogenesis of bone marrow-derived murine stromal cells following transient treatment (Bennett et al. 2005);
- AR-28, and amino thiazole, in studies *in vitro* promoted osteogenic commitment and proliferation of bone marrow-derived murine cells (Gambardella et al. 2011), and human BMSCs, although in the absence of dexamethasone in the osteogenic media (Cook et al. 2014). *In vivo,* 14 days treatment with AR-28 *via* subcutaneous injection enhanced bone mass in BALB/c mice (Gambardella et al. 2011).

Many other inhibitors of GSK-3β have also been shown to have biological functions, but no reports regarding their effect on bone biology are available (reviewed by Eldar-Finkelman & Martinez 2011). Among the products of natural origin able to inhibit GSK-3β, a class of molecules called indirubins stands out. These are bis-indole molecules, which constitute the main ingredient of a traditional Chinese medicine used against myelocytic leukaemia (Xiao et al. 2002). Originally investigated for their selectivity on cyclin dependent kinases (CDKs), indirubins were then found to have a strong affinity for GSK-3β (Hoessel et al. 1999; Leclerc et al. 2001). A synthetic analogue of indirubins is 6-bromoindirubin-3'-oxime (BIO), which is a specific inhibitor of GSK-3β. BIO specificity is conferred through its structural conformation that matches the ATP binding pocket of the kinase (Meijer et al. 2003). *In vitro* BIO has been shown to maintain the pluripotency of both mice and human ESCs (Sato et al. 2004), and inhibit tau phosphorylation in neurons, which is linked to the onset of Alzheimer's disease (Martin et al. 2009), while *in vivo* it promotes neovascularization following administration in a mouse model of hind limb ischemia (Kohler et al. 2014).

In bone tissue, the use of BIO *in vitro* has been shown to enhance proliferation (Hoffman & Benoit 2013) and osteogenic differentiation of human SSCs (Krause et al. 2010). *In vivo*, continuous intraperitoneal injections of BIO significantly increased bone trabecular number and thickness in healthy mice as assessed by μ-CT analysis, and improved bone quality in a mouse model of myeloma (Gunn et al. 2011). Recently indirubin-3'-oxime, a structural homologue of BIO that lacks a bromide ion, has been shown to increase mass and restore structural strength in mice models of osteoporosis

(Zahoor et al. 2014). However, BIO delivered locally in a mouse calvarial defect failed to promote regeneration more than the controls (Krause et al. 2010), possibly due to the low concentration of BIO used (200 and 800 nM). In fact, the clinical use of BIO or other indirubins is limited by their reduced solubility and bioavailability (Leclerc et al. 2001). Nevertheless, the ability of BIO to modulate the Wnt signaling pathway and bone homeostasis is evident. Given these considerations, the challenges presented by the solubility characteristics of BIO could be resolved by encapsulation in PMs, allowing for its investigation as a therapeutic molecule for promoting bone regeneration.

The studies presented in this chapter were performed to test the hypothesis that PMs loaded with the Wnt agonist BIO (BIO-PMs) can activate the Wnt pathway in a controlled manner priming the osteogenic differentiation of human BMSCs.

The aims of the experiments are:

- To produce and characterise polymersomes that incorporate a Wnt agonist and to determine their stability as a function of time;
- To assess the internalisation of BIO-PMs in reporter cells and human BMSCs;
- To measure the ability of BIO-PMs to induce activation of the Wnt signalling pathway in reporter cells;
- To assess differences between BIO-PMs and free BIO in the kinetics of Wnt signalling activation and relative induced cytotoxicity in reporter cells;
- To measure activation of Wnt signalling in human BMSCs following incubation with BIO-PMs;
- To quantify the effect of BIO-PMs on the proliferation and differentiation potential of human BMSCs.

4.2 Results

4.2.1 Efficency of BIO as Wnt signaling agonist

To validate the activity of 6-bromoindirubin-3′-oxime (BIO) as a Wnt signalling agonist, a murine 3T3 cell line expressing a luciferase reporter gene under the control of Wnt-responsive promoters (TCF/LEF) was exposed to a range of BIO concentrations. In response to increasing concentrations of BIO, 3T3 cell luciferase activity increased to a maximum before declining with increasing concentrations (Figure 4.1). The maximal activation of the Wnt pathway was observed following incubation at an extracellular concentration of 5 μM BIO (93.8 ± 19.2 fold increase in luciferase activity),

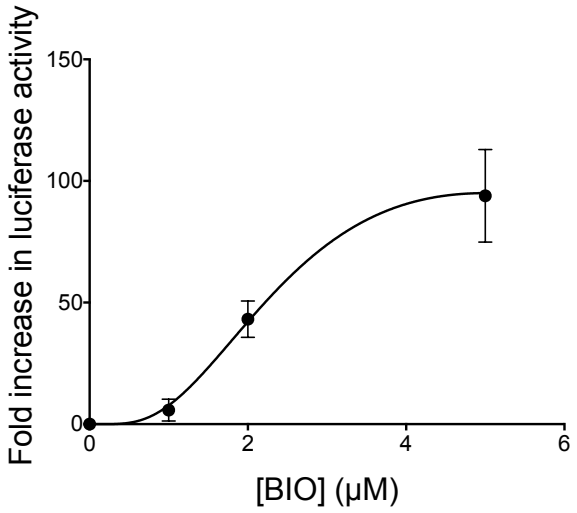

Figure 4.1: **Responsiveness of the 3T3 Wnt reporter cell line to BIO.**
Dot plot graph depicting the fold increase in luciferase activity of 3T3 luciferase reporter cells incubated for ~24 hours with increasing concentrations of BIO (0,1, 2 and 5 μM BIO). An extracellular concentration of 5 μM was found to induce the highest response and was therefore used for every future assays as an internal control. Data presented as mean ± SD, *n*=3 independent experiments. Values are normalised against untreated cells.

The intensity of the luminometric readout can be influenced by cellular density. To test this, double stranded DNA (dsDNA) content (using the PicoGreen assay) was measured as a function of BIO concentration. No significant reduction was observed in dsDNA between 2 μM or 5 μM BIO in comparison to control cells (Figure 4.2). Note that in all further luminometric assays using 3T3 reporter cells, the values are expressed as relative to cells incubated with 5 μM BIO, which was consistently the highest value measured.

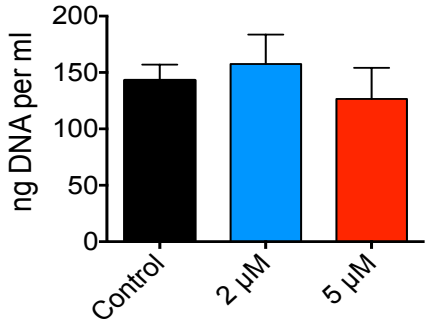

Figure 4.2: **BIO concentrations up to 5 μM do not affect cell proliferation.**

Histogram plot showing the total amount of dsDNA in 3T3 luciferase reporter cells incubated for ~24 hours with either 2 μM or 5 μM quantified using the PicoGreen assay. No statistically significant difference was found among the groups investigated. Untreated cells represent the internal control. Data presented as mean ± SD, *n*=3 independent experiments.

4.2.2 Loading polymersomes with BIO

PMs produced with the 5k-18k block copolymer were loaded with BIO by two separate methods and the physical characteristics of the preparations were analysed by DLS. In the first method, BIO was dissolved to a final concentration of 1 mM in the DMF solution together with the block copolymer (hereafter referred to as 'shell-loaded' PMs). Using this methodology and assuming complete incorporation, the theoretical concentration of BIO present in the bulk solution of PMs is 200 μM BIO (for further details see section 2.2.2.2) In the second method, BIO was directly dissolved in the PBS solution to a final concentration of 200 μM (hereafter referred to as 'core-loaded' PMs) (see section 2.2.2.1). Despite the reported solubility of BIO in water as 5 mg ml^{-1} (~14 mM) (Vougogiannopoulou et al. 2008), it was highly unstable at concentrations higher than 200 μM and precipitation out of solution was observed. Therefore, 200 μM was considered the highest concentration possible for encapsulation in the core of PMs. Core- and shell-loaded PMs were characterised by DLS to investigate their size, PdI and ζ-potential (Figure 4.3).

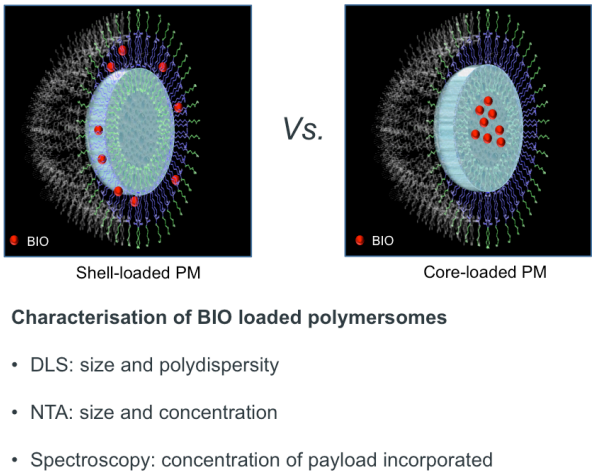

Figure 4.3: **Summary of the methodology used to characterise core- and shell- BIO loaded PMs.** PMs were loaded with BIO in either the core or the shell and then characterised using DLS, NTA and spectroscopy.

Loading BIO into PMs resulted in a small but non-significant increase of the hydrodynamic diameter compared to the unloaded counterpart (empty-PMs) (Figure 4.4A-D). The number of PMs formed per ml of solution, determined by NTA, was also not affected by the loading as the same final concentration (1.5×10^{13} PMs ml^{-1}) was achieved in both preparations (Figure 4.4B). However, core-loaded PMs displayed both a higher ζ-potential and PdI after production compared to the other preparations (Figure 4.4D). This disparity indicated poor hydrodynamic stability over time, which resulted in the aggregation of the core-PMs after 21 days in solution. In contrast, shell-loaded PMs displayed higher hydrodynamic stability, similar to empty-PMs, with only minor changes over the course of time (less than 10% increase from the original size) (Figure 4.4C).

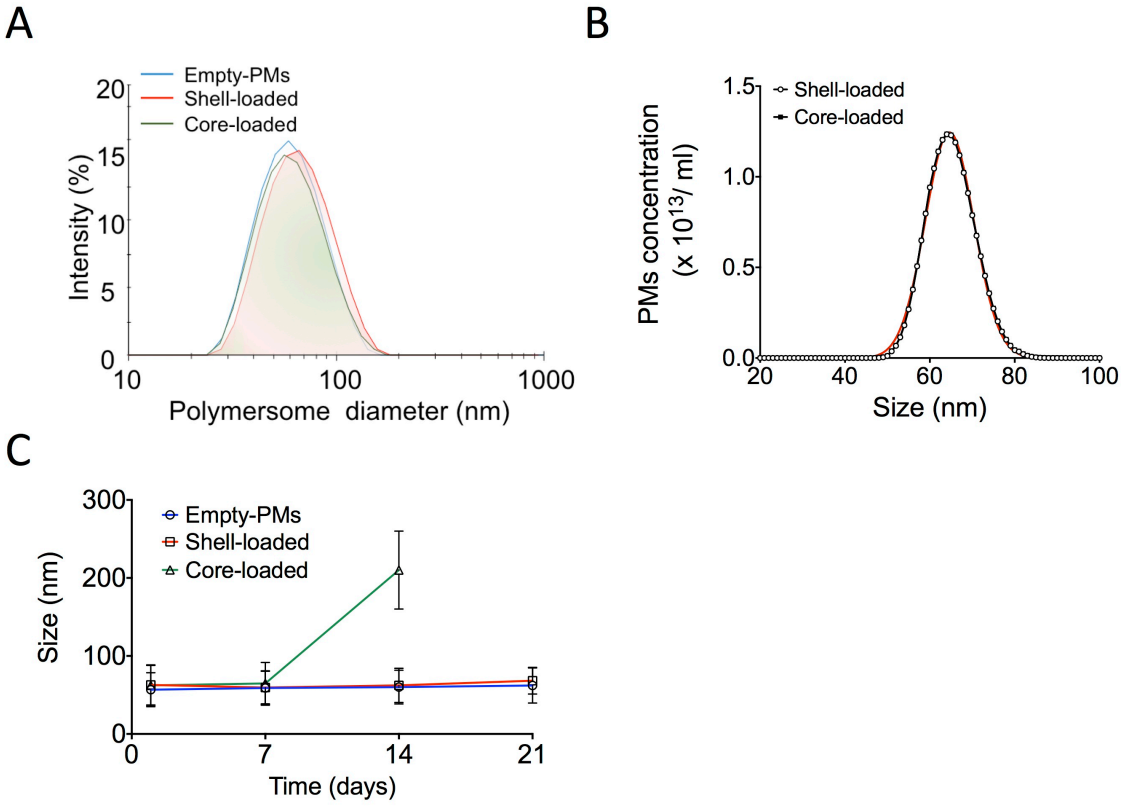

D

	PMs								
	Empty-PMs			Core-BIO loaded PMs			Shell-BIO loaded PMs		
	Size	PdI	ζ-potential	Size	PdI	ζ-potential	Size	PdI	ζ-potential
Day									
1	56.72 ± 21.88	0.113	-5.69 ± 2.16	62.35 ± 25.26	0.191	-4.31 ± 2.75	62.89 ± 25.73	0.115	-6.48 ± 0.96
7	58.95 ± 22.01	0.112		64.9 ± 26.87	0.19		59.59 ± 20.94	0.148	
14	60.10 ± 21.55	0.113		210.1 ± 50.02	0.31		62.27 ± 21.92	0.156	
21	62.15 ± 22.5	0.223		n.a	n.a	n.a	68.34 ± 17.09	0.233	

Figure 4.4: **Size and concentration of BIO-PMs measured by DLS and NTA.**

A: Representative histogram from DLS, showing the hydrodynamic distribution in diameter of core- and shell-loaded PMs, and empty PMs. **B**: Concentration and size measurement histogram from NTA. **C**: Graph showing the PM size stability in solution over the course of 21 days. **D**: Summary of size, polydispersity index (PI) and ζ-potential of core- and shell-loaded PMs and empty-PMs over 21 days. Data presented as mean ± SD, *n*=3 independent experiments.

The concentration of BIO present in the bulk solution after production was measured by light absorbance and found to be 187 ± 36 μM and 198 μM ± 38 μM for core- and shell-loaded PMs, respectively (Figure 4.5).

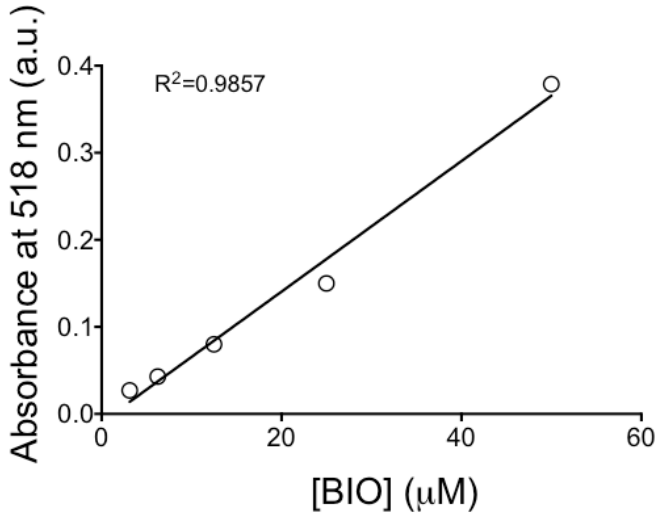

PMs	[BIO] (μM)
Core-loaded	187 ± 36
Shell-loaded	198 ± 32

Figure 4.5: **PMs can be loaded in either core or shell with BIO.**

Graph depicting the levels of light absorption (at λ = 518 nm) of core- or shell-loaded PMs after dilution 1in 10. These values were compared to increasing concentrations of free BIO and used to calculate the final concentration of BIO loaded in the two preparations.

Having previously measured the concentration of PMs (Figure 4.4B) it was possible to determine an average mass of BIO *per* PM equal to 1.25 x 10^{-21} and 1.32 x 10^{-21} moles for core- and shell-loaded, respectively. These measurements were then used to determine the amount of BIO released intracellularly (Section 4.2.6).

4.2.3 Internalisation of 5k-18k polymersomes by 3T3 reporter cells.

In Chapter 3 it was demonstrated that PMs formed from the 5k-18k block copolymer are internalised by BMSCs (Figure 3.19 and Appendix Figure 8). In the

experiments described hereafter, it was decided to verify whether PMs are also internalised by 3T3 Wnt reporter cells, which were used to assess the ability of BIO-PMs to induce the activation of the Wnt pathway. PMs were loaded with fluorescein or co-loaded with fluorescein and BIO and were incubated with reporter cells for 24 hours (Figure 4.6).

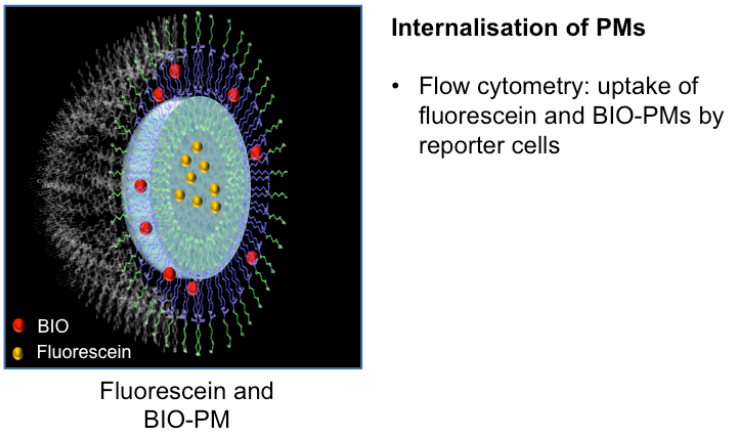

Figure 4.6: **Overview of the methodology used to assess internalisation of PMs by reporter cells.** PMs were loaded with fluorescein or co-loaded with fluorescein and BIO and internalisation by reporter cells was assessed by flow cytometry.

Figure 4.7, graphs A and B show that 99.43 ± 0.24% of the reporter cells stained positively for fluorescein. Also, co-loading PMs with fluorescein and BIO (fluorescein and BIO-PMs) did not affect the cellular internalisation rate (Figure 4.7C & D). However, fluorescein-PMs induced a small but significantly greater increase in MFI than fluorescein and BIO-PMs (1.1 fold difference, $p<0.05$) (Figure 4.7E). The luciferase activity measured following incubation fluorescein and BIO-PMs, and referred to as "relative fold increase in Wnt signalling activation", was reduced by 1.9 fold in comparison to BIO-PMs ($p<0.01$, Figure 4.8). These results emphasise that co-loading PMs with fluorescein and BIO could potentially reduce the efficiency of entrapment of either fluorescein or BIO, and more generally reduce efficiency of loading of any molecule.

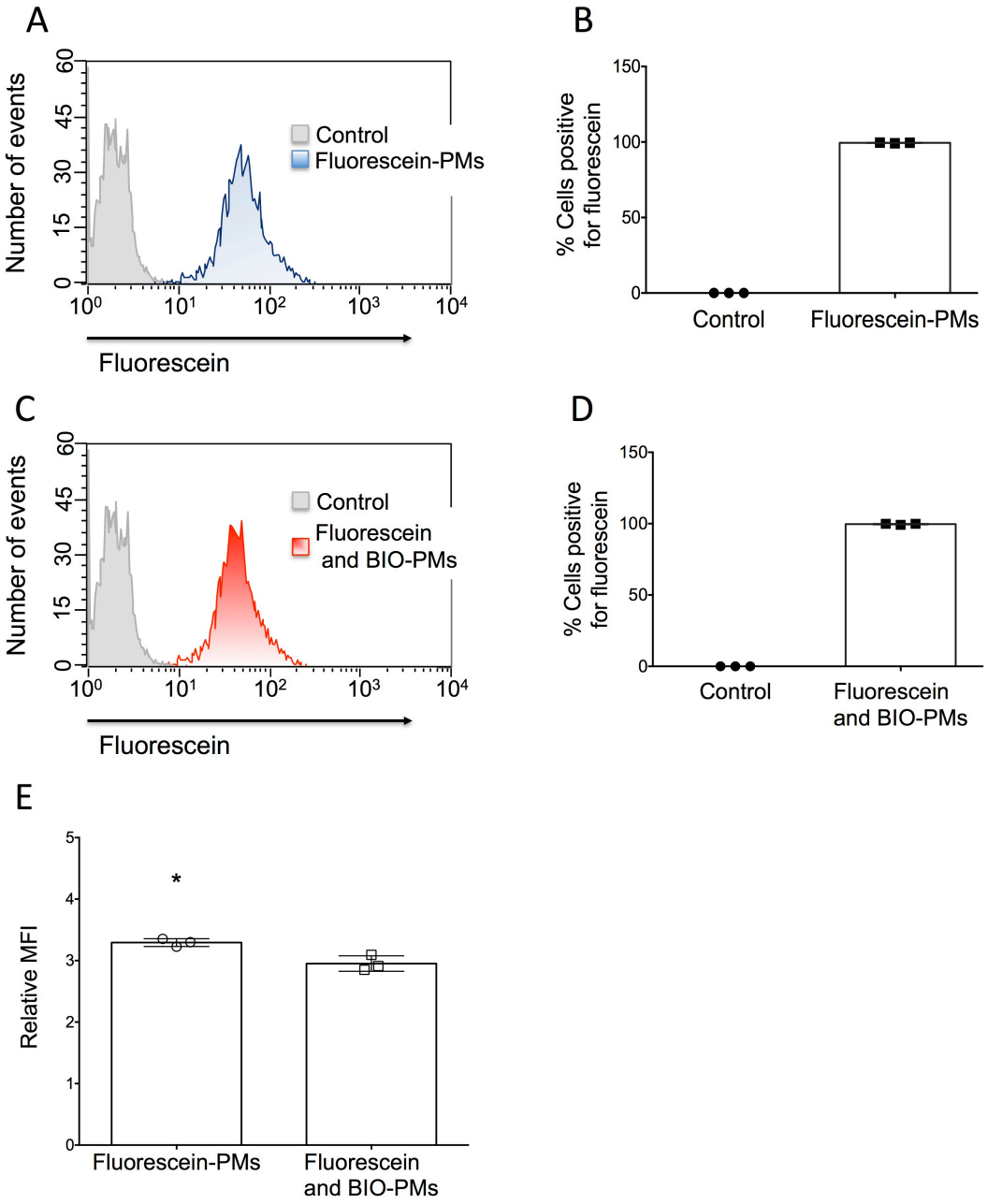

Figure 4.7: **Fluorescein- and fluorescein and BIO-PMs are internalised by Wnt reporter cells.**

A: Representative flow cytometry histogram showing a clear shift in the peak of cells incubated for 24 hours with 15 x 10^{11} fluorescein-PMs ml^{-1} (blue) *vs* control cells (grey). **B**: Bar chart showing the percentage of cells stained for fluorescein after 24 hours incubation with 15 x 10^{11} fluorescein-PMs ml^{-1} *vs* control cells. **C**: Representative flow cytometry histogram showing a shift in the peak of cells incubated for 24 hours with 15 x 10^{11} fluorescein and BIO-PMs ml^{-1} (red) *vs* control cells (grey). **D**: Bar chart showing the percentage of cells stained for fluorescein after 24 hours incubation with 15x10^{11} fluorescein and BIO-PMs ml^{-1} *vs* control cells. **E**: Bar chart showing the relative MFI of cells exposed to equal concentration of fluorescein-PMs or fluorescein and BIO-PMs. Data presented as mean ± SD, student *t*-test n=3 independent experiments. *=p<0.05.

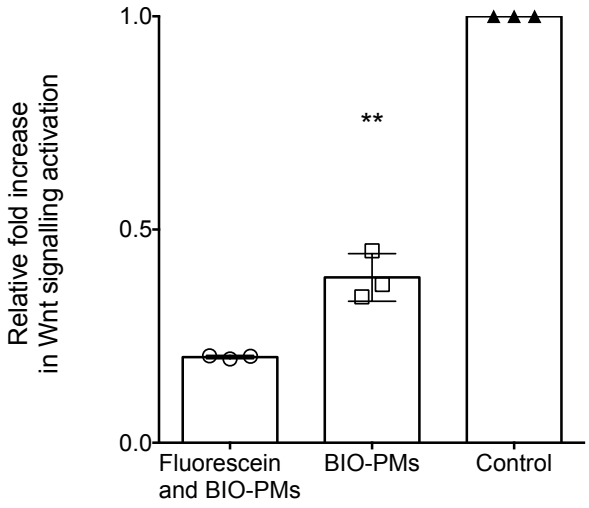

Figure 4.8: **Co-loading PMs with fluorescein and BIO reduces the ability of PMs to activate the Wnt pathway.**

Bar chart showing the differences in relative fold increase in Wnt signalling activation between BIO-PMs and fluorescein and BIO-PMs following incubation for 24 hours of 3T3 luciferase reporter cells. Data presented as mean ± SD, student t-test, n=3 independent experiments, **=p<0.01. Values are normalised against untreated cells, and are expressed as relative activation of cells treated with 5 μM BIO for 24 hours (control).

4.2.4 Effect of core-loaded and shell-loaded polymersomes on Wnt activity

Having demonstrated that PMs are internalised by reporter cells, experiments were performed to investigate the activation of Wnt signalling induced by core- or shell-loaded PMs (Figure 4.9). Whereby, the intensity activation of the pathway was measured as relative luciferase activity.

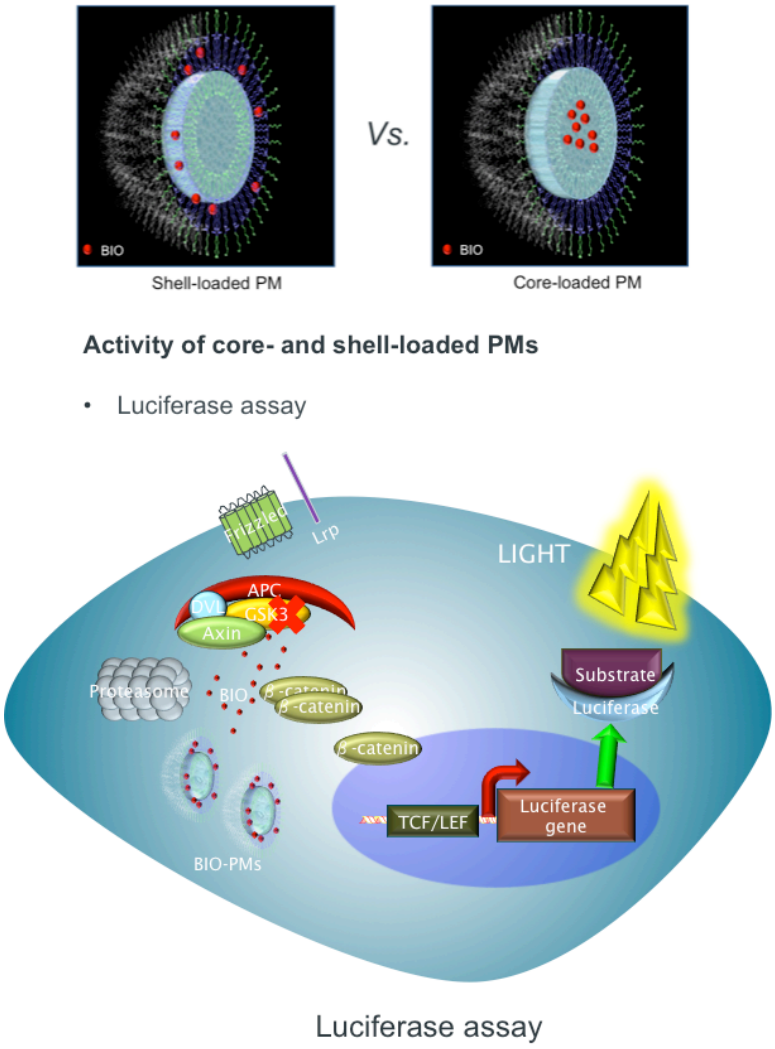

Figure 4.9: **Overview of the methodology used to assess activity of PMs loaded with BIO.**
Activity of PMs loaded with BIO was assessed using the luciferase assay whereby PMs internalised by reporter cells release BIO. This inhibits GSK-3β (red cross) allowing for the accumulation of β-catenin and, following translocation in the nucleus, activation of the Wnt pathway. As consequence of the activation of the pathway, the luciferase enzyme is synthesised. Luciferase transforms into light a substrate that is added to the culture media, and the amount of light produced is proportional to the level of activation of the pathway.

Overall, shell-loaded PMs were observed to be consistently more active than their core-loaded counterparts, particularly at a concentration of 15 x 10^{11} PMs ml^{-1} (p<0.0001). Empty PMs were also analysed in order to take into account potential activation of the Wnt pathway mediated by unspecific binding of PMs to GSK-3β, or possible interference of PMs with the luminometric readout; however, this induced a response not significantly different from control (Figure 4.10).

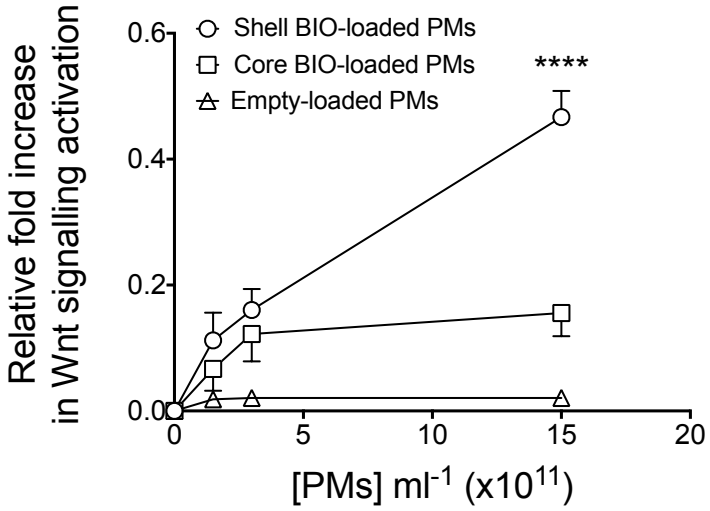

Figure 4.10: **Wnt signalling induced activation of core- or shell-loaded PMs.**

Dot plot graph showing the fold increase in Wnt signalling activation of 3T3 luciferase reporter cells incubated for 24 hours with increasing concentrations of core- or shell-loaded PMs. A significant difference between the two preparations was observed at a concentration of 15 x 10^{11} PMs ml^{-1}. Data presented as mean ± SD, one-way ANOVA, with Sidak's post-hoc correction, n=9 wells. ****p<0.0001. Values are normalised against untreated cells, and are expressed as relative to cells treated with 5 μM BIO for 24 hours.

Considering physical stability over time, as well as the enhanced activity compared to the core-loaded PMs, the rest of the studies presented in this thesis were focused on shell-loaded PMs will be referred to as 'BIO-PMs'.

As mentioned, BIO is loaded into the PM shell by dissolution in the organic solvent phase. This methodology allowed the poor solubility of BIO in water to be overcome. A range of concentrations was loaded into PMs, and the activity of the preparations produced was then tested on reporter cells. Of all the concentrations

originally loaded in the PMs, 200 μM was the minimal concentration required in order to significantly promote the activation of the Wnt pathway (p<0.0001, Figure 4.11).

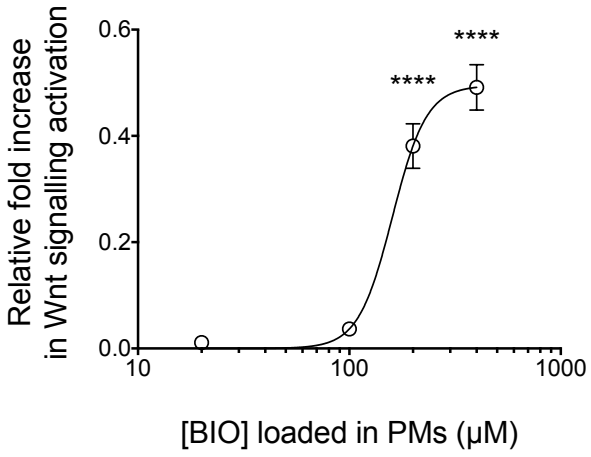

Figure 4.11: **PMs loaded with 200 or 400 μM BIO activate the Wnt signalling pathway in reporter cells.**

Dot plot graph showing the fold increase in Wnt signalling activation of 3T3 luciferase reporter cells incubated for 24 hours with BIO-PMs loaded with increasing concentrations of BIO (20, 100, 200 or 400 μM). A significant activation of the Wnt pathway was observed when PMs were loaded with initial concentrations of either 200 or 400 μM BIO. Data presented as mean ± SD, one-way ANOVA, with Sidak's post-hoc correction, n=6 wells. ****p<0.0001. Values are normalised against untreated cells, and are expressed as relative activation of cells treated with 5 μM BIO for 24 hours.

An initial concentration of 400 μM BIO induced a significant increase in Wnt signalling activity compared to 200 μM (p<0.0001, Figure 4.11); however, considering the cost-efficiency of production, the characterisation and functional activity analysis was carried out on PMs loaded with an initial concentration of 200 μM.

4.2.5 Stability of association between polymersome and BIO.

In order to use PMs as a vehicle for controlled drug delivery, it is critical to assess the stability of the association between payload and carrier, with particular attention to the rate of drug release over time.

Using light absorbance it was observed that BIO release from PMs followed a sigmoidal relationship with a biphasic rate of release. During the first 48 hours post-production BIO was almost totally retained in the PMs, as confirmed by the unaltered

levels of Wnt signalling activation induced by BIO-PMs kept in continuous dialysis over this time frame (Figure 4.12A & B). Subsequently, a fast-release rate was observed between day 3 and day 5 post-production (56.68 ± 2.5% release), followed by a slow but constant release from day 5 onwards that culminated with 12.3 ± 6.7 % residual BIO present at day 14 (Figure 4.12A).

Ultracentrifugation was used to test the stability of the association between BIO and PMs. Figure 4.12C shows that the activity of the preparation was retained in the pellet fraction consisting of PMs (~90% of the total activity measured), whilst free BIO released in the supernatant contributed for ~10% of the total activity measured.

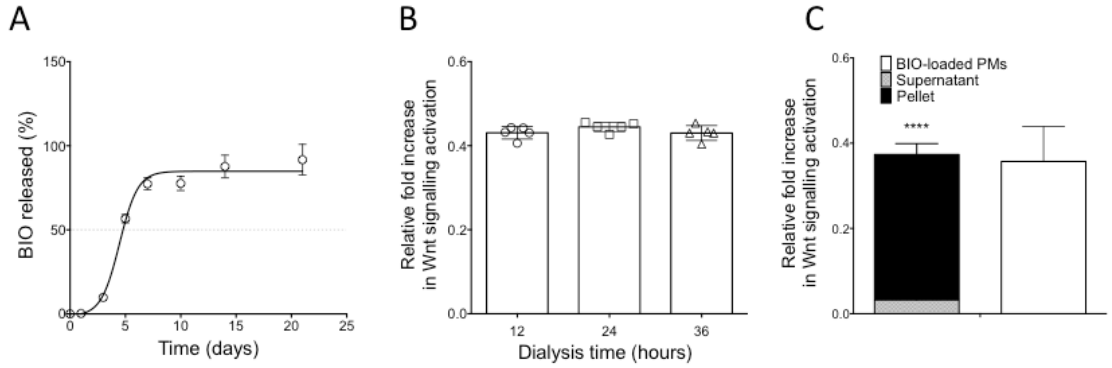

Figure 4.12: **BIO is stably loaded within PMs.**

A: Following production BIO-PMs were kept under dialysis and at defined intervals the concentration of BIO present in the solution was measured by light absorbance and compared to the concentration at time 0. *n*=3 independent experiments. **B**: Bar chart showing the unaltered relative activity of 3T3 luciferase reporter cells incubated for 24 hours with BIO-PMs dialysed for either 12, 24 or 36 hours. Data presented as mean ± SD, one-way ANOVA, with Sidak's post-hoc correction, *n*=5 independent experiments. **C:** Bar chart showing the level of activity of BIO PMs and either pellet or supernatant following ultracentrifugation. Data presented as mean ± SD, student t-test, *n*=4 independent experiments, ****$p<0.0001$. In B & C values are normalised against untreated cells, and are expressed as relative activation of cells treated with 5 μM BIO for 24 hours.

4.2.6 BIO-PMs *vs* free BIO.

The next section of this chapter will be focused on the direct comparison between BIO-PMs and BIO in its 'free' form (*i.e.* added directly to the culture media) (Figure 4.13).

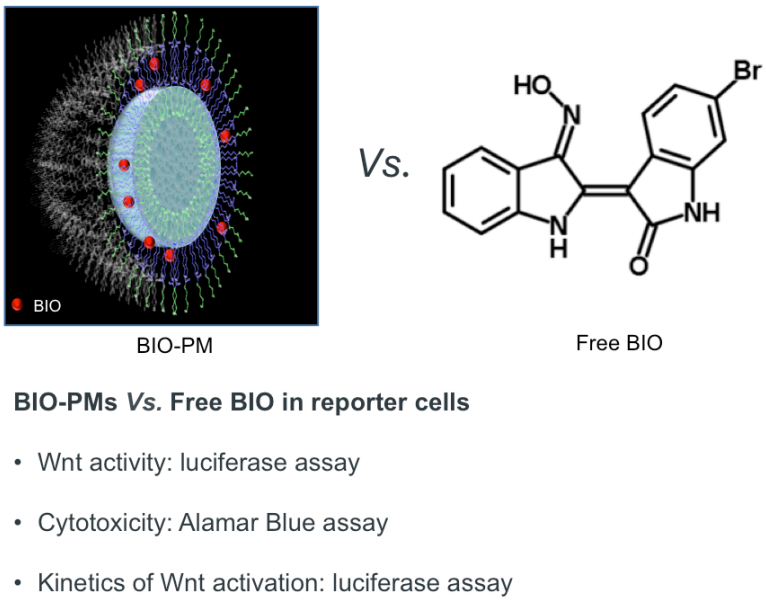

Figure 4.13: **Overview of the methodology used to compare BIO-PMs and free BIO in reporter cells.**

BIO-PMs were compared with free BIOPMs for their ability to activate the Wnt pathway and the kinetics of activation using the luciferase assay, for the levels of induced cytotoxicity using the alamarBlue assay.

Figure 4.14 shows that the maximal relative activation of the pathway following incubation with BIO-PMs was achieved at a concentration of ~15 x 10^{11} PMs ml^{-1}. This was 43.75 ± 0.54% of the activity measured following treatment with 5 μM BIO and was approximately equivalent to the activation recorded after incubation with 2 μM BIO (Figure 4.14). Having previously calculated that the concentration of BIO *per* PMs is ~1.32 x 10^{-21} moles (see section 4.2.2), and having was measured that ~172 PMs release their contents *per* cell after 24 hour incubation (Figure 3.11), it was estimated that the level of activity measured in Figure 4.14 is the result of an intracellular release of 2.32 x 10^{-19} moles of BIO *per* cell, equal to an intracellular concentration of 6.92 nM, assuming a cell diameter to be 20 μm.

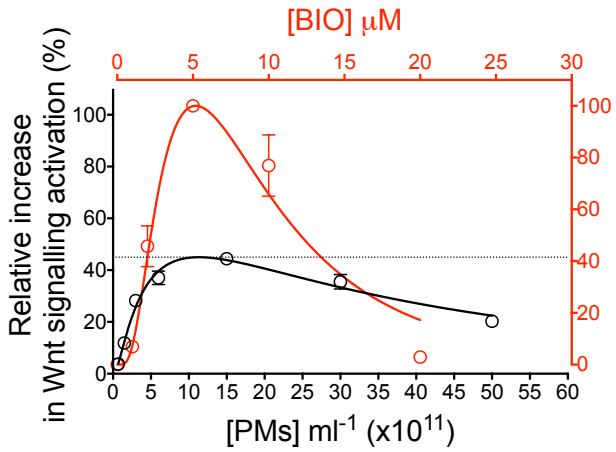

Figure 4.14: **Comparison of BIO-PMs *vs* free BIO activity.**

Dot plot graph depicting the activity of 3T3 luciferase reporter cells incubated for 24 hours with increasing concentrations of either BIO-PMs (black) or free BIO (red). Data presented as mean ± SD, Both conditions follow a positively skewed distribution with a drop in relative activity at concentrations higher than 5 μM BIO and 15 x 10^{11} BIO-PMs ml^{-1}. *n*=3 independent experiments. Values are normalised against untreated cells, and are expressed as relative activation of cells treated with 5 μM BIO for 24 hours.

Figure 4.14 demonstrates that regardless of the treatment, the activity measured followed a biphasic distribution with a drop in the intensity of the readout at concentrations above 15 x 10^{11} PMs ml^{-1} and 5 μM. This decline was not due to a reduced cell number at the time of the readout, as the total amount of DNA (measured using PicoGreen assay) after 24 hours incubation with increasing concentrations of either free BIO (Figure 4.2) or BIO-PMs (Appendix Figure 12) was not altered. Nevertheless, the alamarBlue assay showed that free BIO induced a dose-dependent increase in cell death, especially above 2.5 μM, while no cytotoxic effects were observed when cells were exposed to increasing concentrations of BIO-PMs within the range tested (Figure 4.15).

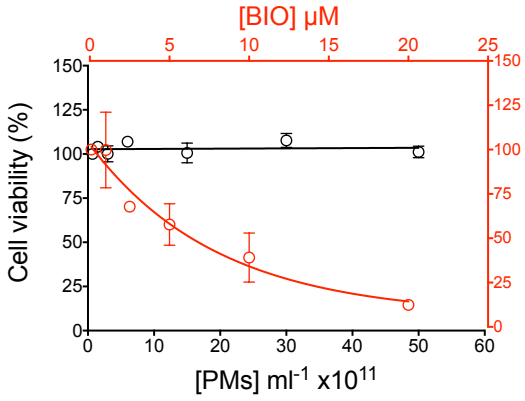

Figure 4.15: **Induced cytotoxicity of BIO-PMs *vs* free BIO.**

Dot plot graph depicting the progressive reduction in viability of 3T3 luciferase reporter cells incubated for 24 hours with increasing concentrations free BIO (red), whilst cells exposed to BIO-PMs (black) were unaffected. Data presented as mean ± SD, *n*=3 independent experiments. Values are normalised against untreated cells.

The reduction of Wnt signalling activity observed at higher concentrations of BIO-PMs (30 x 10^{11} and 50 x 10^{11} BIO-PMs ml^{-1}, Figure 4.14) could not be attributed to either high concentrations of PBS (vehicle for BIO-PMs) that might affect the responsiveness of the reporter cells, or high concentrations of non-internalised PMs still present in the media (Figure 4.16A & B).

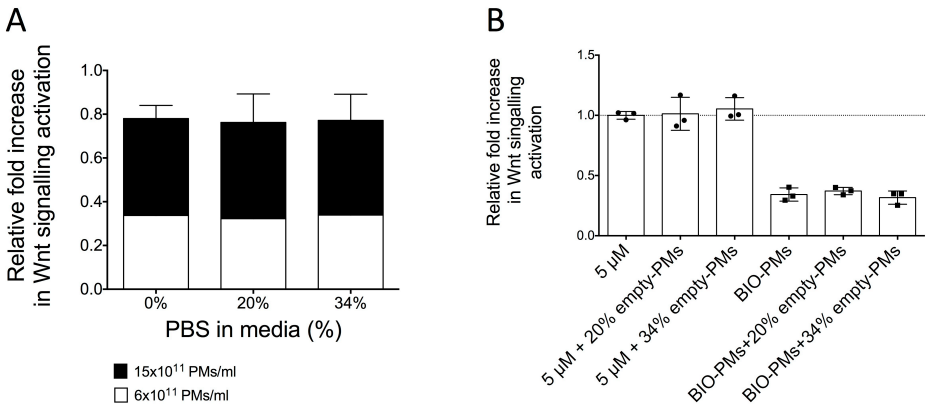

Figure 4.16: **High volumes of PBS or empty-PMs do not affect the intensity of the luminometric readout.**

A: bar chart showing the lack of differences in activity when 3T3 luciferase reporter cells were incubated with 2 concentrations of BIO-PMs in the presence of high volumes of PBS (20%, 34% v/v). Data presented as mean ± SD, one-way ANOVA, with Sidak's post-hoc correction, *n*=3 independent experiments. **B**: bar chart showing the lack of differences in activity when 3T3 luciferase reporter cells were incubated with either 5 µM BIO or BIO-PMs in the presence of high volumes of PBS (20%, 34% v/v). Data presented as mean ± SD, one-way ANOVA, with Sidak's post-hoc correction, *n*=3 independent experiments. Values are normalised against untreated cells, and are expressed as relative activation of cells treated with 5 µM BIO for 24 hours.

However, incubating cells with either free BIO or BIO-PMs in the presence of increasing concentrations of empty-PMs resulted in a significant reduction of the luminometric readout (Figure 4.17). Therefore, the reduced activity measured at high concentrations of BIO-PMs may have been due to an excess of PMs in the intracellular compartment that inhibited the intensity of the luminometric readout.

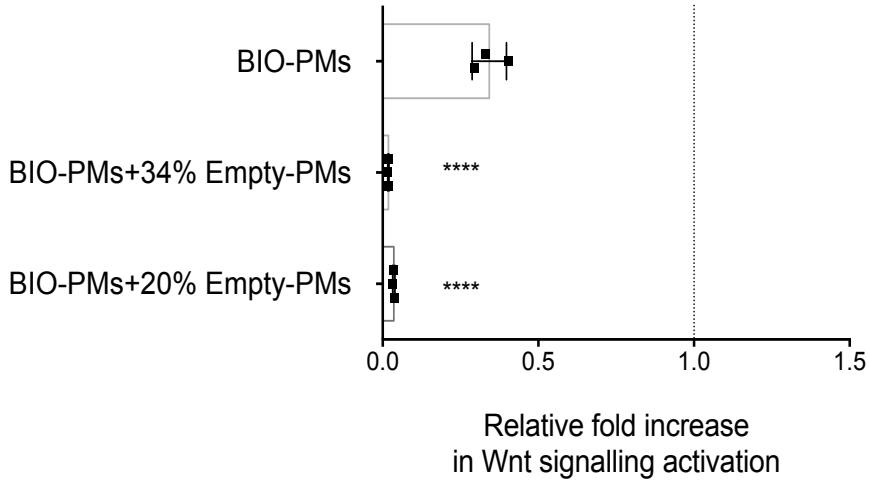

Figure 4.17: **High concentrations of PMs affect the luminometric readout.**

Bar chart showing the intensity of Wnt signalling activation of 3T3 luciferase reporter cells incubated with BIO-PMs in the presence of high volumes (20% or 34%, v/v) of empty-PMs. Data presented as mean ± SD, one-way ANOVA, with Dunnett's post-hoc correction, n=3. A significant reduction in activity was observed after addition of high volumes of empty-PMs. Multiple comparisons: ****p<0.0001. Values are normalised against untreated cells, and are expressed as relative activation of cells treated with 5 μM BIO for 24 hours.

4.2.7 Differences in the kinetics of activation between free BIO and BIO-PMs

Following the data demonstrating a clear difference in induced cytotoxicity between BIO-PMs and free BIO conditions, investigations into potential dissimilarities in the kinetics of Wnt signalling activation were conducted through pulse-chase experiments.

Cells were exposed for increasing time intervals to either BIO-PMs or 2 μM BIO and assayed after 24 hours. Following short exposure times (1 to 6 hours) free BIO induced a greater activation of the Wnt pathway compared to BIO-PMs, while after 24 hours exposure no difference between the conditions was observed. In addition, whilst

the response to free BIO approached its maximum with respect to exposure time, the rate of response to BIO-PM did not, resulting in a progressive increase (Figure 4.18).

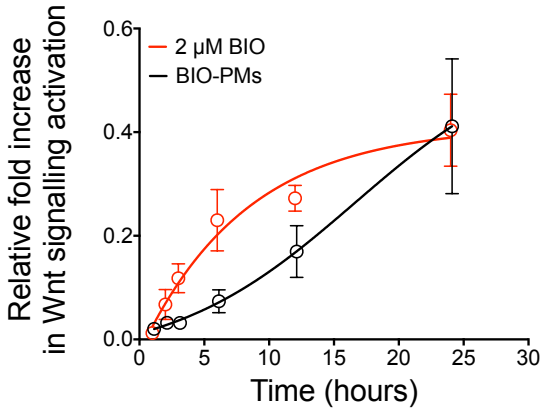

Figure 4.18: **BIO-PMs and free BIO present different kinetics of Wnt signalling activation.**
Dot plot graph of 3T3 reporter cells activity after incubation with either BIO-PMs ($15x10^{11}$ PMs ml^{-1}, black) or 2 µM BIO (red) increasing time periods (1, 2, 3, 6, 12 or 24 hours). 2 µM BIO promoted a higher activity compared to BIO-PMs up to 24 hours incubation. Data presented as mean ± SD, n=3 independent experiments. Values are normalised against untreated cells, and are expressed as relative activation of cells treated with 5 µM BIO for 24 hours.

The increased responsiveness to BIO-PMs with respect to time was further confirmed by the significantly higher activity of the loaded PMs after 48 hours incubation (p<0.05, Figure 4.19).

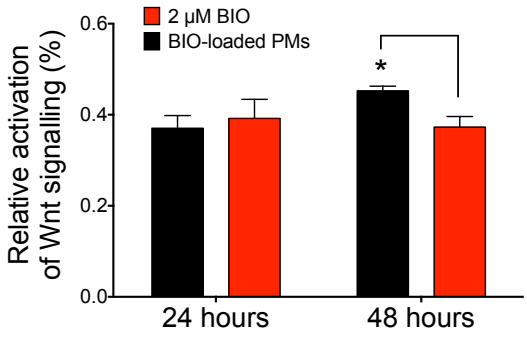

Figure 4.19: **Activity of BIO-PMs *vs* free BIO after a 24 or 48 hour incubation.**
Bar chart showing the increased activity of 3T3 reporter cells incubated with BIO-PMs ($15x10^{11}$ PMs ml^{-1}, black) compared to 2 µM BIO (red) following 48 hours incubation. Data presented as mean ± SD, two-way ANOVA, n=3. Values are normalised against untreated cells, and are expressed as relative activation of cells treated with 5 µM BIO for either 24 or 48 hours.

However, these results should be interpreted cautiously for two main reasons. First, according to the manufacturer's instructions, the readout of the luminotmetric assay is optimal only within 24 hours from the initial incubation. Second, the luminometric values are expressed as relative to cells treated with 5 μM BIO. At this concentration, BIO promotes activation of Wnt signalling after a 48 hour incubation (Appendix Figure 13), but it is highly cytotoxic (Figure 4.15).

4.2.8 BIO-PMs induce the activation of Wnt signalling in BMSCs

The previous results confirmed that BIO-PMs are able to induce the activation of the Wnt pathway in murine reporter cells. However, it was important to establish whether BIO-PMs activity would also be confirmed in BMSCs (Figure 4.20)

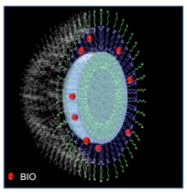

BIO-PM

BMSC

BIO-PMs in BMSCs

Investigation	Methodology
• Internalisation	Flow cytometry using fluorescein and BIO-PMs
• Activation of the Wnt pathway	qRT-PCR assessing expression of *AXIN2, C-MYC* and *CCND1*
• Metabolism	AlamarBlue
• Proliferation	PicoGreen Assay
• Osteogenic differentiation ➢ Early commitment	qRT-PCR assessing expression of *RUNX2* and *SP7*
➢ Terminal diffentiation	ALP activity assay

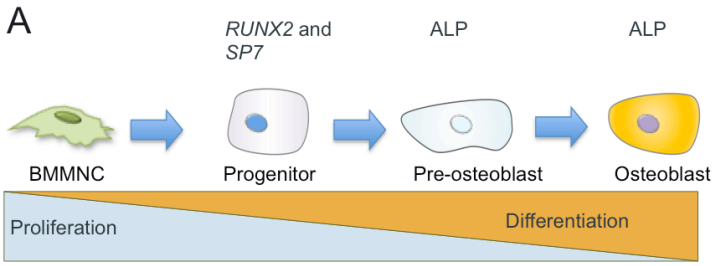

Figure 4.20: **Overview of the methodology used to assess the effects of BIO-PMs on BMSCs.**
Internalisation of BIO-PMs by BMSCs was assessed using flow cytometry and by co-loading PMs with fluorescein and BIO. Activation of the Wnt pathway was determined using RT-qPCR and investigating the expression of *AXIN2, C-MYC* and *CCND1*. Effects on cellular metabolism and proliferation were assessed by alamarBlue and PicoGreen assays. Finally, early osteogenic differentiation was determined using RT-qPCR for the expression of *RUNX2* and *SP7*, while terminal differentiation was assessed using the ALP activity assay. **A:** pictorial representation of the osteogenic differentiation of a BMSC into an osteoblast, with indication of the markers commonly used to distinguish intermediate phenotypes.

First it was confirmed that fluorescein and BIO-PMs are internalised by BMSCs after 24 hours incubation (Figure 4.21A&B).

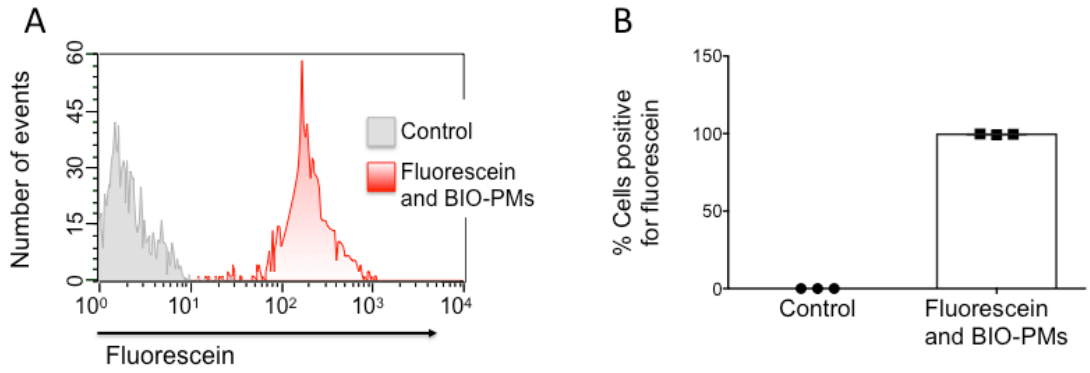

Figure 4.21: **Fluorescein and BIO-PMs are internalised by BMSCs.**

A: Representative histogram showing a clear shift in the peak of BMSCs incubated for 24 hours with 15 x 10^{11} fluorescein and BIO-PMs ml^{-1} (red) *vs* control cells (grey). **B**: Bar chart showing that 99.64 ± 0.42% of cells stained positive for fluorescein after 24 hours incubation with 15 x 10^{11} fluorescein and BIO-PMs ml^{-1}. Data presented as mean ± SD, n=3 independent experiments.

An investigation into the BIO-PMs induced modulation of Wnt signalling pathway activation in these cells was then carried out. BMSCs were incubated with either BIO-PMs or free BIO, together with relative controls, and relative gene expression levels of *AXIN2, C-MYC, CCND1,* were calculated following normalisation to *GAPDH* housekeeping gene and to 1 for cDNA from control conditions.

Exposing BMSCs to BIO-PMs caused a significant up-regulation in the expression of *AXIN2,* similar to that seen after 2 μM BIO and Wnt3A protein exposure. Consistent with what observed in the reporter cell line (Figure 4.19), BIO-PMs were able to promote sustained activation of Wnt signalling. After 48 hours incubation with BIO-PMs, *AXIN2* expression was significantly up-regulated (p<0.0001) with a greater fold-increase compared to a 24 hour exposure (the two concentration tested showed 2 ± 0.75 and 2.1 ± 1.2 fold increase *vs* 24 hours exposure; Figure 4.22A). Whereas, incubation with either 2 μM BIO or Wnt3A for 48 hours resulted in a reduction to the fold-increase compared to a 24 hour exposure time (3 ± 1 and 1.1 ± 0.3 fold increase *vs* 24 hours exposure respectively; Figure 4.22B). Nevertheless, gene expression was no longer increased at 96 hours post-incubation (Figure 4.22C).

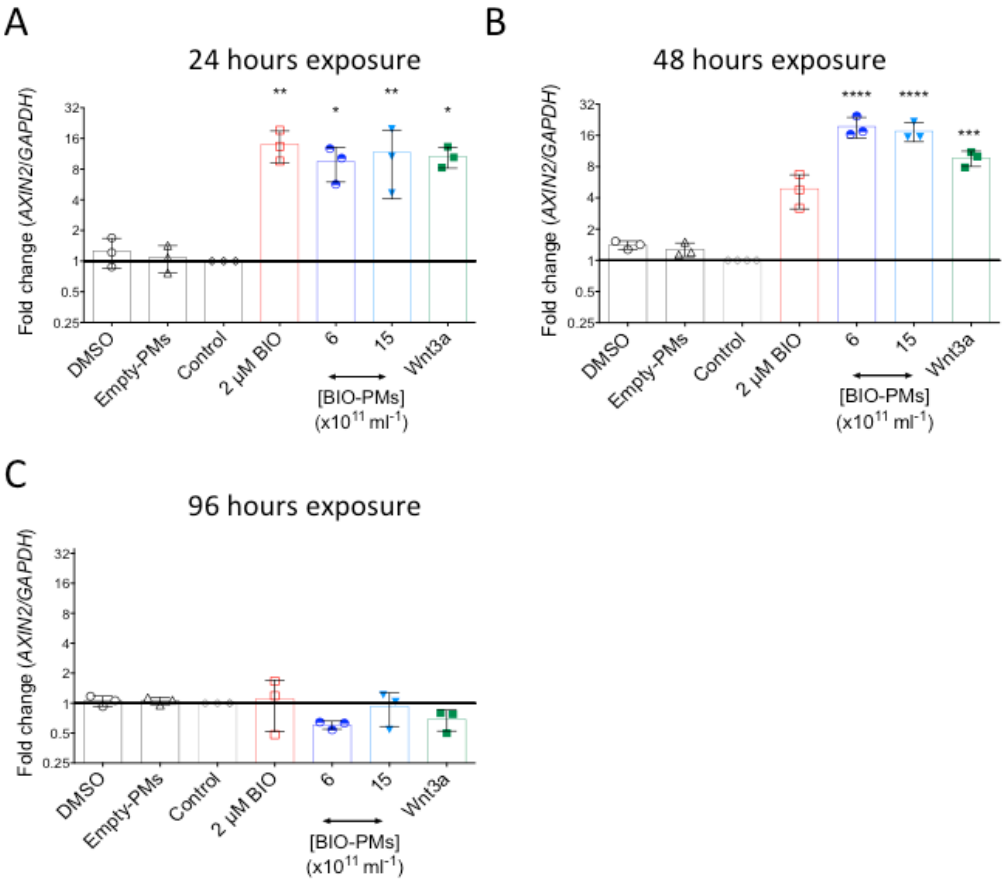

Figure 4.22: **BIO-PMs induce up-regulation of AXIN2 in BMSCs.**

Bar charts showing the relative fold expression of Wnt target genes in BMSCs incubated either with BIO-PMs, free BIO, Wnt3A, DMSO or Empty PMs. **A**: mRNA expression of *AXIN2* is significantly increased after 24 hour exposure to 6 x 10^{11} BIO PMs ml^{-1} (p<0.05), 15 x 10^{11} BIO-PMs ml^{-1} (p<0.01), 2 μM BIO (p<0.01), 100 ng ml^{-1} Wnt3A (p<0.05). **B**: mRNA expression of AXIN2 is significantly increased after 48 hour exposure to 6 x 10^{11} BIO PMs ml^{-1} (p<0.001, 2.1 ± 1.2 fold increase *vs* 24 hours exposure), 15 x 10^{11} BIO-PMs ml^{-1} (p<0.001, 2 ± 0.75 fold increase *vs* 24 hour exposure)(n=3). **C**: mRNA expression of AXIN2 after 96 hour exposure (n=3 independent experiments). Data presented as mean ± SD, one-way ANOVA, with Dunnett's post-hoc correction, n=3 independent experiments. Multiple comparisons: *p<0.05, **p<0.01, ***p<0.001, ****p<0.0001 *vs* Control. Values are normalised against housekeeping gene *GAPDH* and are expressed as fold difference compared to untreated cells.

The effects of BIO-PMs on other target genes within the Wnt pathway were also investigated. Figure 4.23A & B show that after only 24 hour incubation in BMSCs, both BIO and BIO-PMs (at both concentrations) induced a down-regulation of both *C-MYC* and *CCND1* expression, which was statistically significant in the latter (p<0.05 and p<0.001 for 6 x 10^{11} and 15 x 10^{11} BIO-PMs ml^{-1}, respectively).

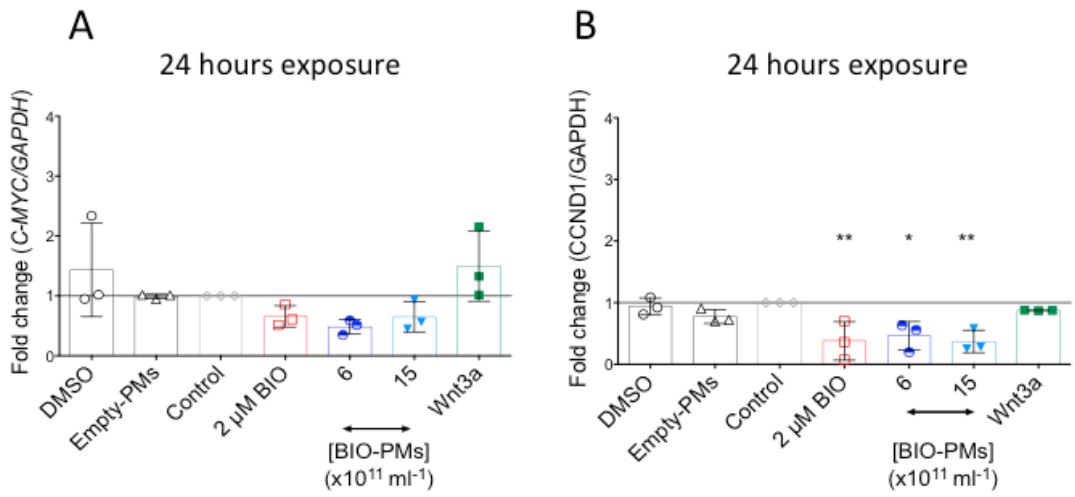

Figure 4.23: **Effects of BIO-PMs on C-MYC and CCND1 expression.**

A: mRNA expression of *C-MYC* after 24 hours exposure (n=3 independent experiments). **B**: mRNA expression of *CCND1* is significantly down-regulated after 24 hour exposure to 6 x 10^{11} BIO PMs ml^{-1} (p<0.05), 15 x 10^{11} BIO-PMs ml^{-1} (p<0.01) and 2 μM BIO (p<0.01)(n=3 independent experiments). Data presented as mean ± SD, one-way ANOVA, with Dunnett's post-hoc correction. Multiple comparisons: *p<0.05, **p<0.01 vs Control. Values are normalised against housekeeping gene *GAPDH* and are expressed as fold difference compared to untreated cells.

4.2.9 Effect of BIO-PMs on BMSC proliferation and metabolism.

Having shown that treatment with BIO either in its free form or encapsulated within PMs promotes the down-regulation of a gene involved in the cell-cycle progression, the proliferation and metabolism of BMSCs were subsequently investigated. In order to control for results mediated by the activation of Wnt signalling, but not ascribable to the off target effects of BIO, a range of Wnt3A protein concentrations was used as an internal control.

The data in Figure 4.24 shows that treatment with increasing concentrations of free BIO over a 24 hour period results in a reduction of cellular proliferation compared to that seen under control conditions, with statistical significance observed at a concentration of 5 μM (p<0.05). Incubating BMSCs with BIO-PMs for 24 hours also resulted in lower cell proliferation particularly at 3 days post incubation, which persisted by day 7. No significant differences in cellular proliferation were seen when cells were cultured with a range of Wnt3A concentrations. These results mirrored the gene expression previously reported (Figure 4.23B), with BIO treatment affecting cell proliferation probably due to off targets inhibition of cyclin proteins.

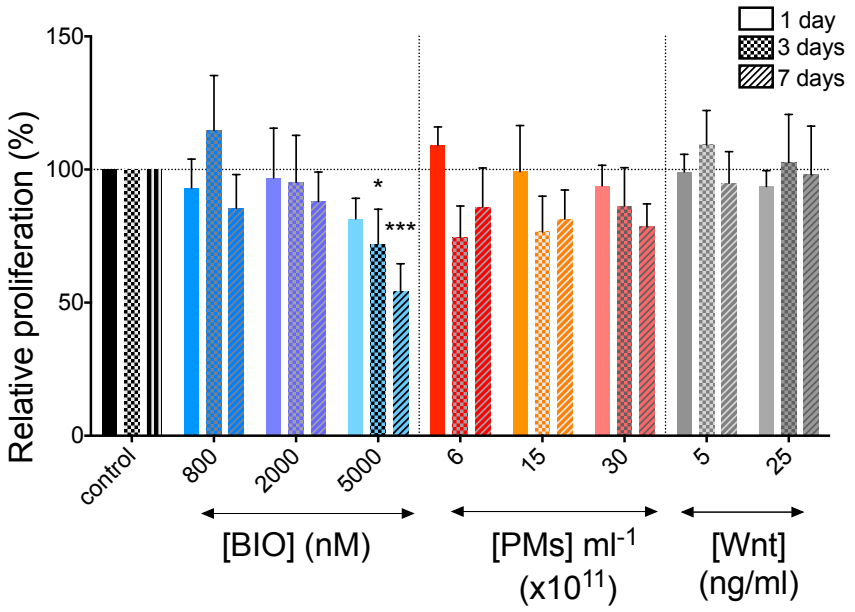

Figure 4.24: **Proliferation BMSCs after incubation with BIO-PMs, free BIO or Wnt3A.**

BMSCs were cultured in monolayer for 1, 3 or 7 days in basal media and assessed for cellular proliferation by PicoGreen assay following a 24 hours treatment with increasing concentrations of either free BIO, BIO-PMs or Wnt3A. Increased cellular proliferation was observed by day 3 with concentrations up to 800 nM, while a reduction was measured at all time points using 5 μM BIO ($p<0.05$ at 3 days *vs* control, and $p<0.001$ at 7 days *vs* control); increasing concentrations of BIO-PMs reduced cellular proliferation by day 3, while increasing concentrations of Wnt3A did not induce significant differences. Data presented as mean ± SD, $n=3$ independent experiments, two-way ANOVA, with Dunnett's post-hoc correction. Multiple comparisons: $*p<0.05$, $***p<0.001$, *vs* Control. Values are normalised against untreated cells.

The metabolic profile of the cells was also influenced by treatment with BIO. Cells had a significant peak in metabolic activity 3 days following a short incubation with 800 nM free BIO ($p<0.01$), whereas higher concentrations (2 and 5 μM) induced a time-dependent decrease in metabolic activity. BIO-PMs at a concentration of 6 x 10^{11} BIO-PMs ml^{-1} induced first a decrease in metabolic activity at 24 hours and then a time dependent increase, while at a concentration of 15 x 10^{11} BIO-PMs ml^{-1} resulted first in a peak of metabolic activity at 24 hours and then in a time-dependent decrease. Higher concentrations of BIO-PMs did not induce statistically significant differences. Finally, treatment with Wnt3A, at 5 and 25 ng ml^{-1}, resulted in a statistically significant increase in cellular metabolism by day 3 post incubation, which returned to basal levels by day 7 ($p<0.05$, Figure 4.25).

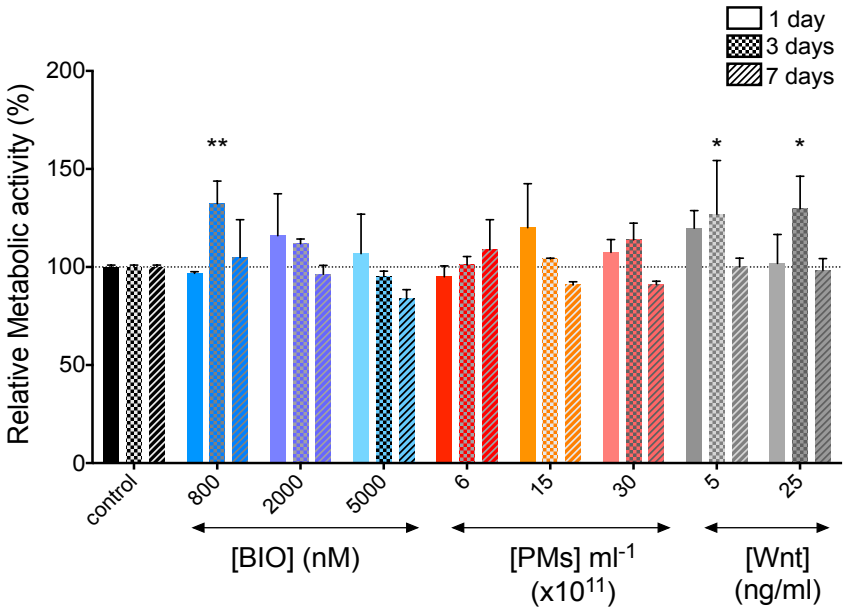

Figure 4.25: **Metabolism of BMSCs after incubation with BIO-PMs, free BIO or Wnt3A.**

BMSCs were cultured in monolayer for 1, 3 or 7 days in basal media and assessed for cellular metabolism by alamarBlue assay. Incubation with 800 nM BIO induced a significant up-regulation of the cellular metabolism at day 3 (p<0.01 *vs* control). Wnt3A up-regulated the metabolism (p<0.01 for 5 ng ml^{-1} and for 25 ng ml^{-1} *vs* control at day 3). Data presented as mean ± SD, n=3 independent experiments, two-way ANOVA, with Dunnett's post-hoc correction. Multiple comparisons: *p<0.05, **p<0.01, ***p<0.001, *vs* Control. Values are normalised against untreated cells.

4.2.10 Effects of BIO-PMs on BMSCs early osteogenic differentiation.

After the demonstration that BIO-PMs activate the Wnt signalling pathway in BMSCs, up-regulation of the expression of early markers of osteogenic differentiation such as the transcription factors *RUNX2* and *SP7* was exploited after BIO-PMs delivery.

Following 24 hour treatment with either BIO-PMs or Wnt3A, *RUNX2* was markedly up-regulated and significantly increased after incubation with 2 μM BIO (p<0.001, Figure 4.26A). Also, 96 hours post incubation with BIO-PMs and BIO, *RUNX2* expression was still up-regulated compared to control (Figure 4.26B).

Similarly, after 24 hour incubation free BIO and BIO-PMs promoted increased expression of *SP7* (3.40 ± 1.48, 1.89 ± 1.07 and 2.47 ± 0.96 fold higher than control for 2 μM BIO, 3 x 10^{11} and 15 x 10^{11} BIO-PMs ml^{-1}, respectively; Figure 4.26C), whilst up-regulation of *SP7* reached statistical significance after incubation with Wnt3A (7.03 ± 3.73 fold higher vs control, p<0.05; Figure 4.26D).

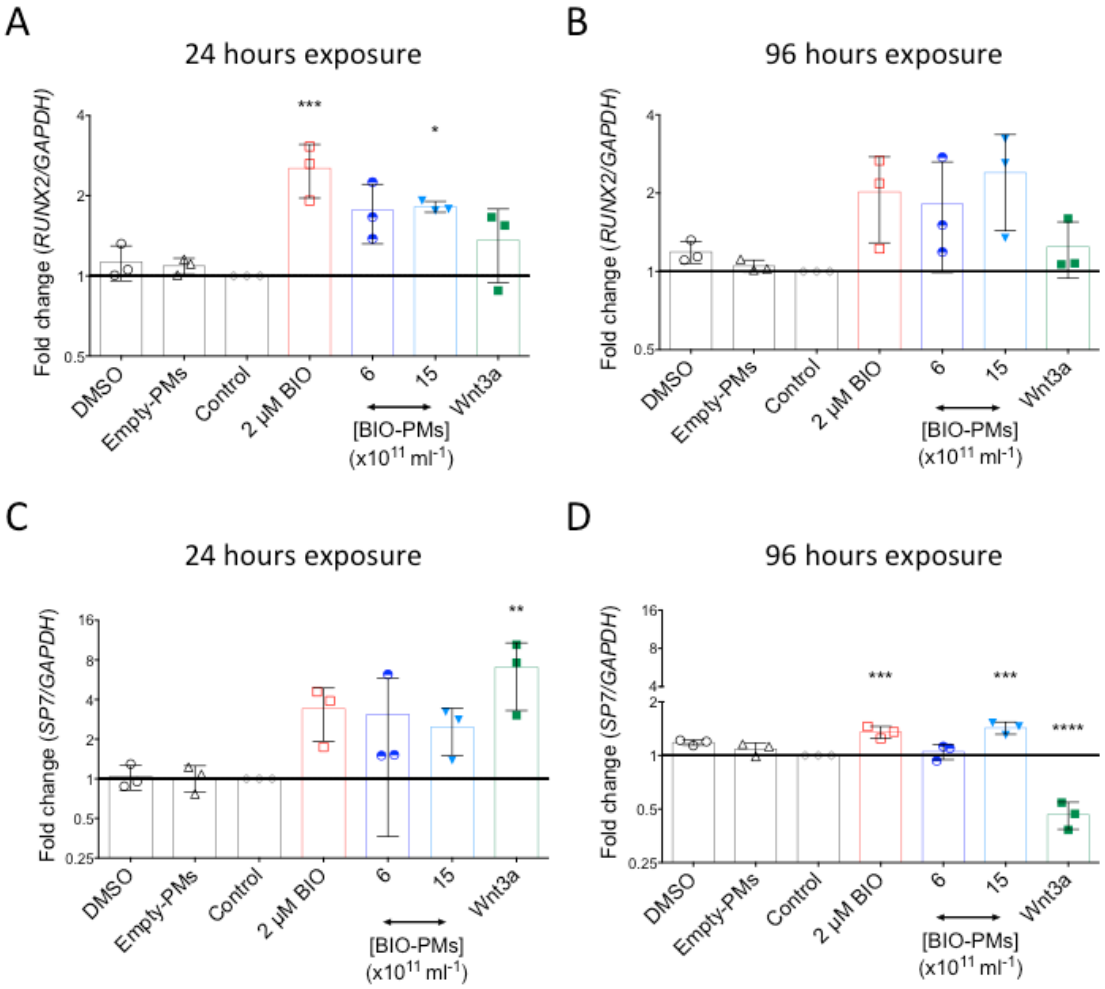

Figure 4.26: **BIO-PMs promote up-regulation of the early osteogenic markers RUNX2 and SP7 in BMSCs.**

Bar charts showing the relative fold expression of early osteogenic marker genes in BMSCs incubated with either BIO-PMs, free BIO, Wnt3A, DMSO or Empty PMs. **A**: mRNA expression of *RUNX2* is up-regulated after 24 hour exposure to 6 x 10^{11} BIO PMs ml^{-1}, 15 x 10^{11} BIO PMs ml^{-1} (p<0.05), 2 µM BIO (p<0.001) and 100 ng ml^{-1} Wnt3A (n=3 independent experiments). **B**: mRNA expression of *RUNX2* is up-regulated after 96 hour exposure to 6 x 10^{11} BIO PMs ml^{-1}, 15 x 10^{11} BIO PMs ml^{-1}, 2 µM BIO and 100 ng ml^{-1} Wnt3A (n=3). **C**: mRNA expression of *SP7* is up-regulated after 24 hours exposure to 6 x 10^{11} BIO PMs ml^{-1}, 15 x 10^{11} BIO PMs ml^{-1}, 2 µM BIO, and 100 ng ml^{-1} Wnt3A (p<0.01)(n=3). **D**: mRNA expression of *SP7* is up-regulated after 96 hour exposure to 15 x 10^{11} BIO PMs ml^{-1} (p<0.001) and 2 µM BIO (p<0.001), whilst it was significantly down-regulated after incubation with 100 ng ml^{-1} Wnt3A (p<0.0001)(n=3 independent experiments). Data presented as mean ± SD, one-way ANOVA, with Dunnett's post-hoc correction. Multiple comparisons: *p<0.05, **p<0.01, ***p<0.001, ****p<0.0001 *vs* Control. Values are normalised against housekeeping gene *GAPDH* and are expressed as fold difference compared to untreated cells.

4.2.11 Effects of BIO-PMs on BMSCs late osteogenic differentiation.

Having shown that BIO-PMs activate Wnt signalling in BMSCs and induce up-regulation of early markers of osteogenic differentiation, terminal osteogenic differentiation of BMSCs following incubation with BIO-PMs was investigated.

BMSCs were cultured in basal media for 24 hours and exposed to two concentrations of BIO-PMs (6 and 15 x 10^{11} PM ml^{-1}), two concentrations of free BIO (2000 and 5000 nM) or relative controls. Subsequently a 24 hour incubation with the various conditions, cells were cultured for 14 days in full osteogenic media. The results shown in Figure 4.27 demonstrate that treatment with free BIO significantly inhibits ALP enzyme activity (p<0.0001), while BIO-PMs preserve enzyme levels to similar to control, incubation of BMSCs with Wnt3A significantly promotes ALP activity (p<0.0001).

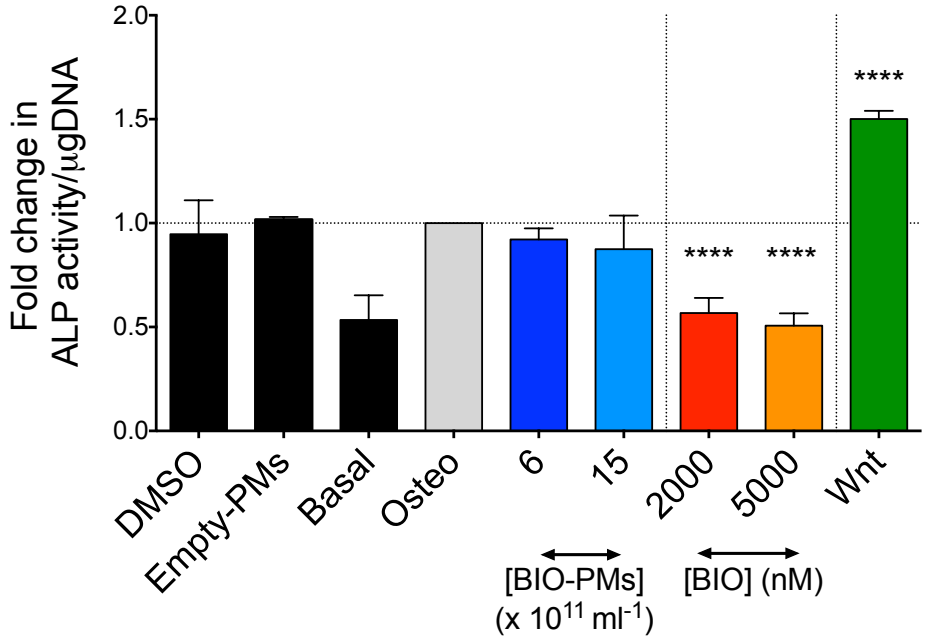

Figure 4.27: **ALP activity of BMSCs in complete osteogenic media after incubation with BIO-PMs, free BIO or Wnt3A.**

Histogram showing ALP activity of BMSCs cultured in monolayer for 14 days in basal or osteogenic media following a 24 hours treatment with different conditions. ALP activity was reduced after incubation with free BIO (p<0.0001 for both 2000 and 5000 nM BIO *vs* control) and up-regulated following incubation with Wnt3A (p<0.0001 *vs* control). Data presented as mean ± SD, one-way ANOVA, with Dunnett's post-hoc correction, n=3 independent experiments. Multiple comparisons: ****p<0.0001 *vs* Control. Values are expressed as fold difference compared to cells cultured in complete osteogenic media.

Consequently, given previous data indicating the potential inhibitory effects of dexamethasone on Wnt signalling activation, a repeat of these experiments were carried out to include a wider range of BIO-PMs and free BIO, but, more importantly, osteogenic media without dexamethasone was used. In these conditions, treatment with BIO-PMs still resulted in a reduction of the ALP activity, while incubation with a range of free BIO concentrations, up to 800 nM, induced a marginal increase. The levels of activity measured following treatment with Wnt3A were still increased compared to controls (Figure 4.28).

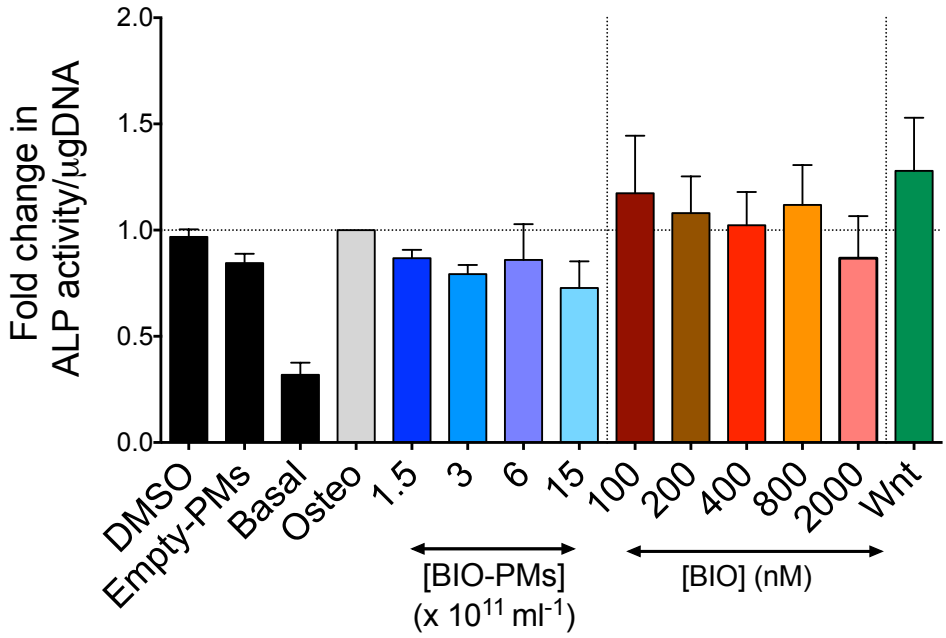

Figure 4.28: **ALP activity of BMSCs in osteogenic media (-dexamethasone) after incubation with BIO-PMs, free BIO or Wnt3A.**

Histogram chart showing ALP activity of BMSCs cultured in monolayer for 14 days in basal or osteogenic media following a 24 hours treatment with different conditions. Decreased activity compared to control was observed after incubation with BIO-PMs, while it was increased for free BIO (up to 800 nM) and Wnt3A. Data presented as mean ± SD, one-way ANOVA, with Dunnett's post-hoc correction n=3 independent experiments. Values are expressed as fold difference compared to cells cultured in osteogenic media (-dexamethasone).

4.3 Discussion

Results reported in the previous chapter demonstrated that the PMs used in this project are not only rapidly internalised by different cell types, but they can also deliver a putative payload in the intracellular compartment. Considering these features, PMs were used as drug delivery system for a known Wnt signalling agonist, which could be exploited for bone regenerative purposes.

The aims of this chapter were to characterise BIO-PMs preparations while exploring their potential to activate the Wnt signalling pathway in both 3T3 murine reporter fibroblasts and human BMSCs. It was also investigated whether, upon successful activation of the Wnt pathway, BIO-PMs could promote the osteogenic differentiation of BMSCs.

The experiments presented in this chapter addressed these aims by demonstrating that:

- PEG-PCL PMs can be loaded with BIO either in the shell or in the core; however, shell-loaded PMs are the most stable preparations.
- BIO-PMs are internalised by Wnt signalling reporter cells;
- BIO-PMs activate the Wnt signalling with different kinetics compared to free BIO;
- In the range of concentrations tested, BIO-PMs do not induce cytotoxicity, whilst free BIO does;
- BIO-PMs induce the activation of the Wnt pathway in BMSCs and do not significantly affect the proliferation or metabolism of BMSCs;
- Following incubation with BIO-PMs, the osteogenic marker genes *RUNX2* and *SP7* are up-regulated in BMSCs;
- In the conditions tested, BIO-PMs are not able to increase the expression of the marker of terminal osteogenic differentiation ALP.

PMs were loaded with BIO by two different methodologies: either dissolving BIO in the PBS solution in which the block copolymer is then dropped, or by dissolving it in the organic phase, represented by DMF (Figure 4.4). These two preparations were named as 'core-loaded' and 'shell-loaded' PMs, as it is hypothesised that the payload is

sequestered into two distinct compartments of the final PM structure: the hydrophilic core and the hydrophobic shell. However, no experiments aimed to assess the final spatial localisation of the payload within a PM were performed. Future assessment of the partitioning of BIO within the PMs, for example using molecular dynamic analysis, would allow for a better understanding of the dynamics of drug release. Nevertheless, physical analysis showed no differences in terms of hydrodynamic size between the two preparations loaded with BIO compared to empty-PMs, indicating that the presence of the payload does not affect the final size of the carrier (Sood et al. 2013). Also, no differences between core- and shell-loaded PMs, in terms of final nanoparticle concentration and moles of BIO loaded *per* PM were observed. However, core-loaded PMs were found to be physically unstable with drastic changes in size 14 days post-production (Figure 4.4). This result was surprising considering that PMs loaded with fluorescein, another hydrophilic molecule, and stored in identical conditions, were physically stable over the course of 4 weeks (Figure 3.2). A possible explanation for this difference resides in the properties of the cargo encapsulated. Vougogiannopoulou and colleagues found that BIO is soluble in water up to 5 mg/ml, equivalent to 14.04 mM (Vougogiannopoulou et al. 2008), but in these studies BIO dissolved at concentrations greater than 200 μM precipitation was observed. Therefore, it is likely that upon dissolution in PBS at a concentration of 200 μM, and subsequent the encapsulation in the PM core, BIO precipitates within the PM. This in turn may induce perturbations to the PM structure that result in its premature collapse. Future experiments aimed to predict the molecular interactions between BIO and PM could be conducted by computer modelling. In particular, two scenarios could be hypothesised, one where BIO is confined in the PM core and one where it is present in the PM shell. These experiments may confirm or reverse the speculations regarding BIO precipitation within the PM core.

Reporter cells were used to investigate the ability of the two preparations to activate the Wnt pathway. First it was demonstrated that PMs are internalised by the reporter cells and that the presence of BIO does not affect cellular uptake, which was observed in 100% of cells after 24 hours incubation (Figure 4.7). Then using a luciferase assay it was shown that shell-loaded PMs were significantly more active than core-loaded PMs, likely due to a different final concentration of BIO loaded (Figure 4.10). All

considered, shell-loaded preparations resulted to be more suitable for the delivery of BIO and were investigated further.

PMs used in this project were made of PEG and PCL providing the advantages previously described (see section 1.9.3). Nevertheless, employing PCL as hydrophobic block may have been beneficial for loading and retention of BIO. The 6 carbon atoms present in its backbone structure make PCL highly hydrophobic allowing for the encapsulation of hydrophobic molecules (Xin et al. 2011; Patel et al. 2010), which is driven by the hydrophobic interactions between the molecule and the polymer itself (Shuai et al. 2004). Using molecular dynamic interactions Patel and colleagues demonstrated that the solubility of two hydrophobic drugs within a PM preparation was determined by the number of hydrogen-bonds between payload and polymer, and given a constant concentration of drug, these bonds are directly proportional to the number of PCL monomers present (Patel et al. 2010). Using dynamic dialysis and ultracentrifugation a high level of association between BIO molecules and PMs was demonstrated in this chapter (Figure 4.12). This result is not surprising considering that BIO is a lipophilic molecule (distribution coefficient (logD) of 2.59, Vougogiannopoulou et al. 2008), and is able to create hydrogen-bonds given the presence of a hydroxylamine group and a cyclic nitrogen atom in both the pyrole ring and the lactam ring (Meijer et al. 2003). Therefore, it can be speculated that BIO and PCL form a series of weak interactions that could cause the retention of the payload during the first 48 hours post-production.

However, BIO is subsequently released from PM with a mechanism that was not investigated in details. As previously discussed (see section 1.9.3), chain-end cleavage at the interface between the hydrophobic and hydrophilic block is the predominant mechanism driving self-poration and consequent payload release form PM made from polyesters. (Ahmed & Discher 2004; Oltra et al. 2014). Interestingly, DLS analysis demonstrated that BIO-PMs size is stable over time, indicating a slow hydrolytic degradation rate (Figure 4.4C); therefore, it is unlikely that the release of BIO is occurring after PM self-poration. It can be hypothesised that hydrolytic processes taking place at the interface between PEG and PCL would promote the progressive exposure of BIO molecules to the extra-vesicular environment, which may result in an increased gradient pressure with subsequent release through a diffusion process (Lao et al. 2008; Shaikh et al. 2009). Nonetheless, the release profile showed in Figure 4.12A is in agreement with

data from Pang and colleagues who demonstrated slow release of coumarin from PEG-PCL PMs (Pang et al. 2012), but it is in contrast with previous works showing a quick drug release *in vitro* from other polyester based PMs (Ahmed et al. 2006; Shaikh et al. 2009). These discrepancies are likely due to the different chemical-physical properties of the payloads encapsulated, resulting in disparities in diffusivity coefficients, as well as differences in the blends and molecular weights of the copolymer used.

There are several limitations in this set of experiments. Firstly the release kinetics were investigated using absorbance spectroscopy, which is a conventional technique (Sanson et al. 2010; Buckiova et al. 2012), but has inherent limitations including poor quantitative sensitivity compared to other techniques (*e.g.* mass spectrometry or high performance liquid chromatography), as well as the possible cross interference of molecules absorbing light at the same wavelength (*i.e.* fluorescein and BIO). Secondly, the separation between 'retained' and 'released' drug was achieved through dynamic dialysis, which is a well-documented methodology for assessing rate of drug release from nanocarriers (Xin et al. 2011; Modi & Anderson 2013; Wallace et al. 2012), but may be misleading. Using model simulations of liposomal preparations Modi and colleagues investigated the limitations of dynamic dialysis. The authors postulated that the diffusion of a given drug from a nanoparticle to the 'sink' compartment is determined by two diffusion stages: (I) diffusion from the nanoparticle to the extravesicular environment, (II) diffusion from the extravesicular environment to the sink compartment through the dialysis membrane. Therefore, the quantification of payload release using this technique should be carefully interpreted as it could be influenced by the intrinsic permeability of both the nanoparticle barrier and the dialysis membrane, as well as by the diffusion coefficient of the payload (Modi & Anderson 2013).

After a 24 hour incubation with BIO-PMs activation of the Wnt signalling was observed in reporter cells (Figure 4.14), this demonstrated that BIO is released intracellularly where it activates the Wnt pathway. The duration of the incubation was chosen according to the instructions provided by the manufacturer (Enzo Life Sciences, USA) and because the experiments in chapter 4 demonstrated that within 24 hours, internalisation of PMs by cells occurs in almost 100% of cells. Moreover, the luciferase assay data showed that a concentration of 15 x 10^{11} BIO-PMs ml^{-1} and an extracellular concentration of 2 μM induce similar levels of Wnt signalling activation, which was

approximately ~40% of the maximal activation measured following incubation with an extracellular concentration of 5 μM BIO. BIO is a reversible ATP-competitive inhibitor of GSK-3β with a cell-free IC50 of 5 nM (Meijer et al. 2003), and despite this low IC50, maximal responses for GSK-3β measured by transgene activation required extracellular concentrations of 1000 fold this value (5 μM BIO, Figure 4.14). In this chapter, 6.92 nM BIO were estimated to be released intracellularly after a 24 hour incubation with 15 x 10^{11} BIO-PMs ml^{-1}. Therefore, assuming that incubation with 5 μM BIO results in 100% inhibition of GSK-3β, the concentration of BIO released intracellularly after PM incubation is very close to the reported value of IC50. These results indicate not only that the relative levels of Wnt signalling activation observed Figure 4.18 (43.75 ± 0.54% of the maximal) are plausible, but also that the quantification of the number of PMs releasing payload *per* cell might be correct.

The relationship between concentration of BIO-PMs used and intensity of Wnt signalling measured did not follow a linear trend, but resulted in a biphasic distribution, similar to that observed with free BIO. However, the two conditions had the opposite effect on cellular health. In fact, high concentrations of free BIO were cytotoxic for the reporter cells (Figure 4.15), in line with previous observations on several cancer cells. These effects are likely due to unspecific inhibitions of both the JAK-STAT pathway and different CDKs (Gaboriaud-Kolar et al. 2015; L. Liu et al. 2011; Vougogiannopoulou et al. 2008). On the contrary, incubation with BIO-PMs did not induce cellular toxicity indicating that intracellular delivery using PMs bypasses the activation of molecular pathways that are switched on when BIO is delivered in its free form, or PMs may mediate a protective action that inhibits BIO cytotoxic effects. One possible mechanism determining this protective effect may be due to the slow release of the payload in the cytoplasm. Pulse-chase experiments suggested that maximal activation of the Wnt pathway following incubation with BIO-PMs is delayed compared to free BIO (Figure 4.18). Using Raman spectroscopy Chernenko and colleagues demonstrated that intact PEG-PCL nanoparticles are still present intracellularly 24 hours after their initial cellular internalisation (Chernenko et al. 2009). These data suggest the possibility that PMs could function as intracellular depot of payloads (Ahmed & Discher 2004) and could explain the protective mechanism mediated by PMs. It could be speculated that high extracellular concentrations of BIO may bind ion channels present on the cellular membrane

precluding their function and inducing cell death, while the use of PMs prevent such unspecific activity. Alternatively, if it is assumed that BIO cytotoxicity is induced by the total inhibition of one of the CDK, for simplicity this will be called 'CDK*x*', then at least two scenarios are possible:

A) After incubation with free BIO, CDKx is inhibited by the high concentration of BIO at both time 0 (t_0) and time 1 (t_1) resulting in cell death. Where t_0 is the time at which BIO is available at the kinase, and t_1 represents a hypothetical time following physiological turnover of CDK*x*.
B) Incubation with BIO-PMs results in a lower but constant release of BIO that inhibits CDK*x* at t_0, but is not sufficient to inhibit the substrate at t_1, resulting in the absence of cytotoxicity.

Furthermore, the depot effect mediated by PMs is protective against induced cytotoxicity and induces a sustained activation of the Wnt signalling pathway over the course of 48 hours (Figure 4.19). A limitation of these finding is that the level of activity recorded using the reporter cells is a reflection of the amount of functional luciferase enzyme produced, and the luciferase readout can be significantly affected by a number of factors (*i.e.* the number of empty-PMs present in solution, Figure 4.17). Also, the heterogeneity of PM uptake by cells (Figure 3.8) is lost in the luminometric assay, resulting in an underestimation of the effects mediated by BIO-PMs. Therefore, results obtained with this type of assay should be carefully interpreted. In order to overcome these limitations it would be important to quantify the intracellular concentration of BIO at different time points following incubation with either free BIO or BIO-PMs, for example using Raman spectroscopy (Chernenko et al. 2013), or following cell lysis by using HPLC or mass spectrometry. Analysis at a single cell level for example using Image Stream, would be recommended in order to normalise the effects mediated by BIO depending on the number of PMs internalised *per* cell.

One of the aims of this chapter was to demonstrate that BIO-PMs are able to induce Wnt signalling activation in human BMSCs. It was shown that BMSCs internalise BIO-PMs, which results in the increased expression of *AXIN2* (Figure 4.22). Importantly, the results obtained with BMSCs corroborated what observed in the reporter cells, whereby BIO-PMs induce the maximal activation of the Wnt pathway after

a 48 hour incubation, reinforcing the hypothesis that PMs function as intracellular depot for BIO. Furthermore, treatment with either free or encapsulated BIO had inhibitory effects on the expression of *C-MYC* and *CCND1*, which are genes included in the cell cycle progression (Figure 4.23). This was in agreement with previous findings on embryonic stem cells (Sineva & Pospelov 2010; Wu et al. 2015), but in contrast with results from Hoffman and colleagues who demonstrated a significant up-regulation of *CCND1* in human BMSCs incubated for 24 hours with 2 μM BIO (Hoffman & Benoit 2013). Even more striking is the increased cellular proliferation reported by the authors 20 days following a 24 hour treatment with BIO (Hoffman & Benoit 2013). These results are in marked contrast with those observed in this work (Figure 4.24) and with finding from Krause and colleagues (Krause et al. 2010), where incubation with BIO resulted in a transient attenuation of the proliferation. These discrepancies regarding the effects of BIO on BMSC proliferation might be due to the initial seeding density of the cells (300 fold difference), as well as the human donor variability (Hoffman reported values from a single patient), or the different methodology used for analysing cell replication (manual cell counting in Hoffman and Benoit's work, and nucleic acid incorporation in Krause's paper). Nevertheless, such differences should be further investigated in order to better understand the effects that BIO has on BMSCs cellular replication.

It is not surprising that BMSCs exhibited a higher metabolic activity following BIO exposure (Figure 4.25). Using gene ontology, Krause and colleagues have shown that following treatment with BIO the expression of genes involved in the processing of both cellular proteins and metabolic macromolecules was more than 10 fold increased (Krause et al. 2010). Although the mechanism by which BIO alters the cellular metabolic activity is not clear, it can be speculated that the inhibition of GSK-3β may be involved. For example, it is known that insulin inhibits GSK-3β promoting the down-stream activation of glycogen synthase, which results in an increased cellular metabolism (Cohen & Frame 2001) that can be monitored by alamarBlue assay (Guilbault et al. 1969). However, the cellular metabolic response varied according to the concentrations of free BIO, BIO-PMs or Wnt3A used, it would be therefore overly simplistic to believe that the entire cellular metabolic activity is governed by the intracellular levels of GSK3-β. Nonetheless, this set of experiments revealed interesting results about the activation of the Wnt signalling and the cellular metabolic status in BMSCs.

The final aim of the experiments presented in this chapter was to assess whether BIO-PMs could promote the osteogenic differentiation of human BMSCs. A 24 hour treatment with either free BIO or BIO-PMs increased the relative expression of *RUNX2* and *SP7* measured at 24 and 96 hours post-incubation (Figure 4.26). These two genes were investigated because they are involved in the early osteogenic differentiation of BMSCs (Bruderer et al. 2014; Nakashima et al. 2002). Similar results are reported in the literature, showing increased expression of *RUNX2* and *SP7*, as well as increased osteogenic differentiation of SSCs after treatment with BIO (Watanabe et al. 2012; Krause et al. 2010; Zahoor et al. 2014). Nonetheless, priming the early differentiation of SSCs using BIO-PMs did not result in the terminal differentiation of BMSCs cultured in osteogenic media, as the ALP activity measured was constantly reduced compared to control levels (Figure 4.27, Figure 4.28). Cook and colleagues reported a dose-dependent reduction of ALP activity in SSCs after incubation with AR-28 (GSK-3β inhibitor) in complete osteogenic media (Cook et al. 2014). However, the authors also measured a significant increase in ALP activity following withdrawal of dexamethasone from the osteogenic supplementations. These results demonstrated that dexamethasone inhibits the late osteogenic differentiation mediated by Wnt signalling activation (Cook et al. 2014; Boland et al. 2004; Liu et al. 2009). Nevertheless, incubation of BMSC with BIO-PMs in media without dexamethasone did not increase ALP activity above control levels (Figure 4.27), while incubation with free BIO resulted in a slight increase of the enzyme functions (Figure 4.28). These results are in agreement with findings from Krause and colleagues who observed higher ALP activity following continuous incubation with low concentrations of BIO (100 and 200 nM), and emphasise the difference in the kinetics of Wnt signalling activation between free BIO and BIO-PMs (Krause et al. 2010).

A clear limitation of the experiments presented in this chapter is the use of a candidate gene approach where only a restricted number of genes associated with osteogenic differentiation was investigated. *RUNX2* and *SP7* were selected as previous studies have reported their increased expression following BIO stimulation (Watanabe et al. 2012; Krause et al. 2010; Zahoor et al. 2014). However, the major limitation of this approach is the assumption of a *priori* knowledge. Given the novelty of the study and the negative results obtained analysing the ALP activity, future work should also consider the investigation of other markers of osteogenic commitment (*i.e. ALP, osteocalcin* and *osteonectin*) as well as genes involved in adipogenic or chondrogenic differentiation such as:

Twist-1 or *PPAR-γ* and *SOX9* or collagen type II (*COL2A1*). Another limitation of the experiments reported in this chapter is the investigation of ALP activity at a single time point. Based on previous work performed in our group it was decided to analyse ALP activity following 14 days in osteogenic media (Janeczek et al., 2016). However, it cannot be ruled out that the activation of Wnt signalling using BIO-PMs may result in in different kinetics of ALP activity. Moreover, the experiments undertaken in this chapter were focused on the effects induced by a short activation of the Wnt pathway (24 hours treatment), as the osteogenic effects of a transient activation of the pathway have been previously demonstrated (Janeczek et al. 2016). However, other authors demonstrated the positive effects of a prolonged activation by the use of BIO (Krause et al. 2010; Cook et al. 2014). Therefore, future experiments may investigate ALP expression and activity at more frequent time points possibly using a wider range of concentrations of BIO-PMs, as well as the effects of a more frequent stimulation of BMSCs with BIO-PMs. Another limitation of the study is the number of assay used to assess osteogenic differentiation. Mineral deposition *in vitro*, using Alizarin and von Kossa staining, may be used to assess whether fully differentiated osteoblast are actively producing mineralised extracellular matrix. Raman spectroscopy demonstrated to able to discriminate early assessment of early adipogenic differentiation of MSCs (Smus et al. 2015), and may also be used in parallel to determine osteogenic differentiation. These possible assay do not discern from the need of an *in vivo* readout in order to fully establish the therapeutic potential of BIO-PMs, also considering the lack of congruency between *in vitro* and *in vivo* studies (Hulsart-Billström et al. 2016). Finally, it is worth to remind that most of the assays presented in this chapter do not allow for an analysis at a single cell level. It was already emphasised the ultimate need for this type of resolution when the effects mediated by PM drug delivery are investigated.

In summary, the results presented in this chapter demonstrated that PMs can be loaded with BIO and can induce the activation of the Wnt signalling pathway. Also, encapsulating the small molecule into PMs results in reduced cytotoxicity and in sustained Wnt signalling activation that promotes the early osteogenic differentiation of human BMSCs. Therefore, BIO-PMs may represent a good candidate for a therapeutic approach focused on promoting bone regeneration following injury, provided that PMs localise at the intended target.

Chapter 5: Accumulation of polymersomes in the bone fracture and controlled delivery of a Wnt agonist

5.1 Introduction

The results presented in the previous chapters demonstrated that PMs are internalised by different cell types, including rare cellular populations such as SSCs. Also, PMs loaded with BIO are able to activate the Wnt signalling pathway in BMSCs: therefore, they could be used for enhancing bone regeneration after fracture. Delayed or impaired bone healing following injury is still an unmet clinical issue, for which modulation of the Wnt signalling pathway is a promising approach. Very recently, the use of monoclonal antibodies able to antagonise the activity of Wnt signalling inhibitors, including sclerostin (McClung et al. 2014) and DKK-1 (Florio et al. 2016), have been shown to augment bone mass and reduce fracture risk in people with osteoporosis. Small molecules able to activate Wnt signalling are commercially available and represent an alternative to the use of Wnt proteins or antibodies. Oral administration of lithium, an inhibitor of GSK-3β, has been shown to increase bone mass and bone formation in rodents (Clement-Lacroix et al. 2005), or the use of small molecules able to inhibit the Wnt antagonist SFRP-1 have been shown to promote bone growth in organ culture (Bodine et al. 2009) (reviewed in section 1.5 and 4.1). However, the systemic administration of monoclonal antibodies, proteins and small molecules for Wnt signalling activation is often associated to limitations. For example, the use of monoclonal antibodies rises safety concern as they have a prolonged half-life (about 4 weeks), poor target specificity and it is often associated with adverse effects for the patient. Administration of OMP18R5 antibody, which targets FZD receptors, has been shown to cause vomiting, nausea and diarrhoea in some cases (Kahn 2014). Furthermore, the spatio-temporal activity of monoclonal antibodies can not be controlled resulting in the over activation of the Wnt pathway in different tissues, which is associated with various diseases ranging from type II diabetes to colon cancer, and could also impair bone formation (reviewed by Clevers & Nusse 2012). The use of Wnt proteins or synthetic agonists is often limited by the poor solubility of the compounds (reviewed in section 4.1) and it still linked to off-target effects following systemic administration. The latest is often minimised by injecting the therapeutic molecules directly at the site of injury, such in the case of recombinant BMP2 for the treatment of persistent non-unions fractures (Zimmermann et al. 2009; Lissenberg-Thunnissen et al. 2011). However, the local administration of these anabolic molecules has not only been linked with heterotopic

ossification, which is the formation of bone in soft tissues surrounding the actual bone injury (Axelrad et al. 2008), but is also complicated to achieve with high precision when the bone fractures occur in deep tissues with poor accessibility. For these reasons, nanoparticles offer an attractive alternative, as they are able to improve the solubility of the molecules of interest, while enhancing their spatial distribution.

A number of different nanoparticles carrying Wnt agonists have been reported for a variety of applications ranging from the activation of natural killer cells in the liver (Deng et al. 2013) to the reversal of cognitive reduction in models of Alzheimer's disease (Tiwari et al. 2014). However, only very few examples of nanoparticles loaded with Wnt agonists for bone regeneration are available (reviewed section 1.10). The packaging of Wnt3A proteins within liposomal formulations represents the most successful example so far. Local administration of these preparations *in vivo* has been shown to induce the osteogenic commitment of SSCs while promoting bone regeneration following fracture (Minear et al. 2010). Furthermore, their use also resulted in a higher implant osteointegration (Popelut et al. 2010) and augmented the regeneration of dentin, which is a component of the teeth (Hunter et al. 2015). However, the major concern regarding the efficacious translation of these products is related to the local administration of the preparations (see preceding paragraph). There is a needed to investigate alternative solutions that overcome the local injection of nanoparticles and take advantage of the systemic circulation.

Following systemic injection, nanoparticles are firstly transported to the heart by the venous circulatory system, and from there they enter the pulmonary circulation, where they face the filtration operated by the lung capillaries. Subsequently, PMs arrive in the left side of the heart, and are then pumped in the systemic circulation reaching distribution to the whole body (Bertrand & Leroux 2012). Most of the PMs injected systemically are sequestered in kidneys, liver and spleen that are part of the mononuclear phagocyte system (MPS). However, PMs have also been shown to accumulate in various organs following systemic injection in healthy animals (Gao et al. 2012; Brinkhuis et al. 2012), and the establishment of a bone injury induces vascular damage and promotes the inflammation process that could be exploited for inducing passive accumulation of PMs in the fracture site. In fact, due to the trauma the vasculature is leaky and damaged, and the consequent vasodilation and vascular fenestration could potentially favour the

extravasation and accumulation of PMs, circulating in the blood stream, into the injured bone tissue. This belief is based on observations made by Matsumara and Maeda, who reported the passive accumulation of macromolecules in solid tumours, due to increased blood flow and vascular permeability, which was then termed the enhanced permeability and retention (EPR) effect (Matsumura & Maeda 1986; Maeda et al. 2000). Nonetheless, vascular permeability is also observed in damaged and inflamed tissue where it helps the extravasation of leukocytes, plasma proteins and macromolecules (Maeda et al. 2000). In this context, seminal work form Dong and colleagues demonstrated the accumulation of polymeric-prodrug in various inflamed tissues including models of rheumatoid arthritis and bone fracture (Yuan et al. 2012; Jia et al. 2015). Accumulation in the fracture tissue was shown despite the polymeric-prodrug where lacking of specific bone tissue binding motifs (*e.g.* bisphosphonates or sialoproteins), which have high affinity for mineralised tissue and can increase bone tissue targeting by more than 9-fold compared to 'plain' nanoparticles (Swami et al. 2014). In this context, systemic administration of micelles decorated with aspartic acid, which has strong affinity for hydroxyapatite, was shown to induce accumulation of radiolabelled BIO into a fractured bone compared to unencapsulated BIO that was mainly detected in the lungs and the spleen. However, the authors also reported the presence of micelles in other organs such as the kidneys and the liver (Low et al. 2015). Prodrugs represent an interesting system for increasing the solubility of certain molecules that otherwise could not be used, but a major limitation is related to the pre-systemic metabolism of prodrugs, which prevents their accumulation at the intended target (Rautio et al. 2008).

PMs have the potential to circumvent this issue, protecting the payload from metabolism and degradation and therefore represent an intriguing alternative to the use of prodrugs. However, to the best of our knowledge, the preferential accumulation of PMs to the site of bone fracture injury after systemic injection has not been demonstrated.

The two-fold hypothesis of the experiments presented in this chapter is that PMs injected *via* tail-vein in a mouse model of bone injury will accumulate at the fracture site, and subsequently, BIO-PMs administered systemically will promote bone fracture healing.

The aims of the experiments presented in this chapter are:

- To produce and characterise polymersomes that incorporate either DiR or DiI dye.
- To assess the distribution of DiR- or DiI-PMs following systemic administration in healthy mice
- To produce a unilateral bone drill defect in mice femur, and to determine the distribution of DiR- or DiI-PMs following systemic administration.
- To quantify the effects of a systemic injection of BIO-PMs on bone healing following creation of a bone drill defect.

5.2 Results

5.2.1 Characterisation of DiR and DiI loaded PMs.

The distribution *in vivo* of PMs injected *via* tail-vein was assessed by IVIS and subsequently confirmed by histological analysis of explanted organs. In order to do this, PMs formed using the 5k-18k block copolymer were loaded with two different fluorescent molecules, DiR or DiI. These were chosen as DiR is a near infrared dye that is particularly indicated for *in vivo* experiments (Xin et al. 2011), whilst DiI is commonly used as long-time tracer for cells (Gao et al. 2013).

Consistent with what has been observed with all previous PM preparations, the hydrodynamic size of both was both DiR- and DiI-PMs was homogeneous and narrowly distributed (Figure 5.1A). No significant differences were observed in terms of size and PdI between loaded PMs compared to empty controls. However, a small increase in hydrodynamic size was measured for DiR- and DiI-PMs compared to empty-PMs (Figure 5.1B). The final concentration of dye present in the bulk solution was similar between the two preparations (58 ± 11 μM of DiR and 49 ± 13 μM of DiI; Figure 5.1C & D). Having measured that the concentration of PMs produced with the same block copolymer is 1.5 x 10^{13} PMs ml^{-1} (Appendix Figure 7), it was estimated that 3.87 x 10^{-21} and 3.27 x 10^{-21} moles of DiR and DiI were loaded *per* PM, respectively.

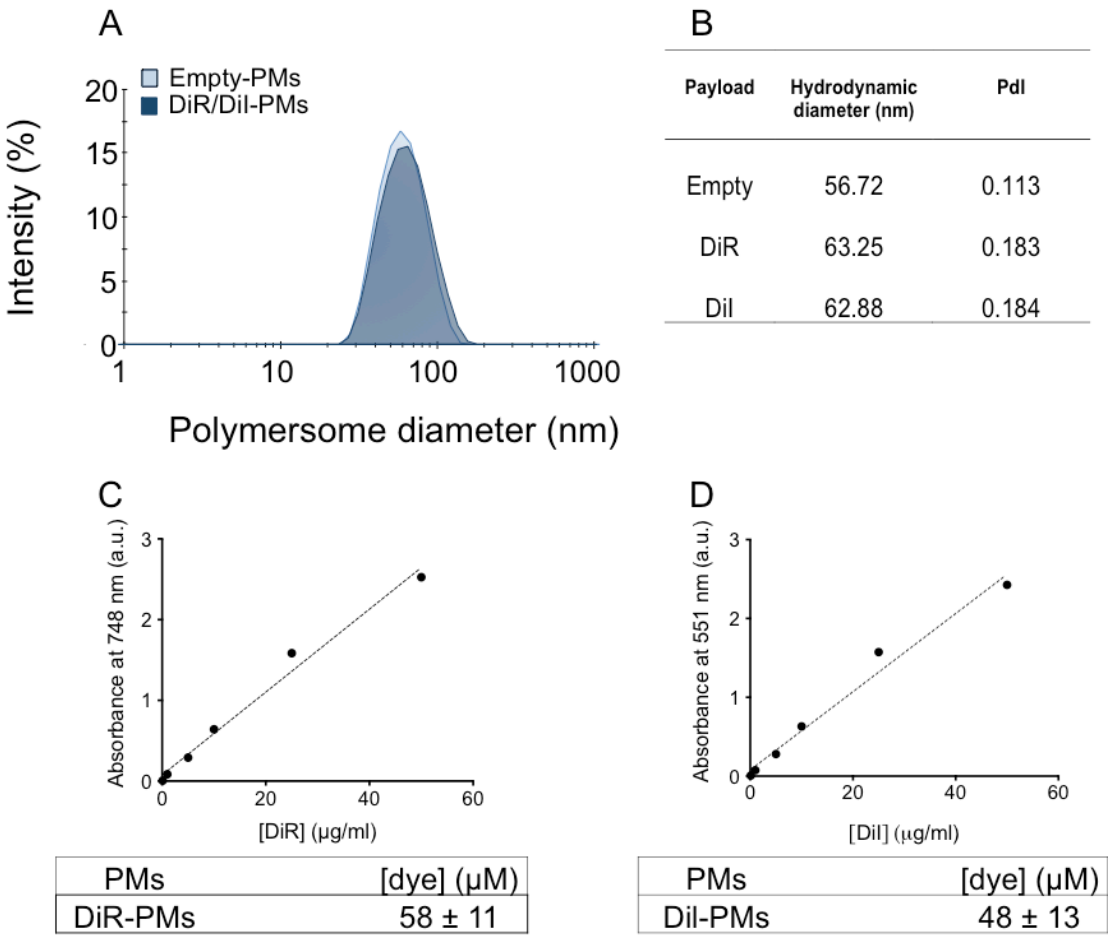

Figure 5.1: **Physical characterisation of PMs loaded with DiR or DiI.**

A: Representative histogram from DLS measurements showing the narrow distribution of the hydrodynamic diameter of DiR-, DiI or empty-PMs formed from 5k-18k block copolymer. **B:** Summary of size and polydispersity index (PDI) of loaded PMs. **C:** Standard curve for DiR absorbance (at 748 nm) showing the concentration of DiR present in the bulk solution of DiR-PMs after a 1:10 dilution. (R^2=0.98). **D:** Standard curve for DiI absorbance (at 748 nm) showing the concentration of DiI present in the bulk solution of DiI-PMs after a 1:10 dilution. (R^2=0.98).

Preliminary studies were performed in order to investigate whether DiR-PMs would produce a fluorescent signal that could be detected by IVIS in the first instance, and then to also assess what concentration of the dye loaded within PMs would give the highest intensity of fluorescence. Figure 5.2 demonstrates that DiR-PMs injected sub-cutaneously produce a fluorescence that is visible using IVIS, and that this is DiR concentration-dependent. PM loaded with a final concentration of DiR equal to ~58 µM

produced a signal that was more than 2 fold brighter than that produced by PMs loaded with 5.8 µM DiR (Figure 5.2).

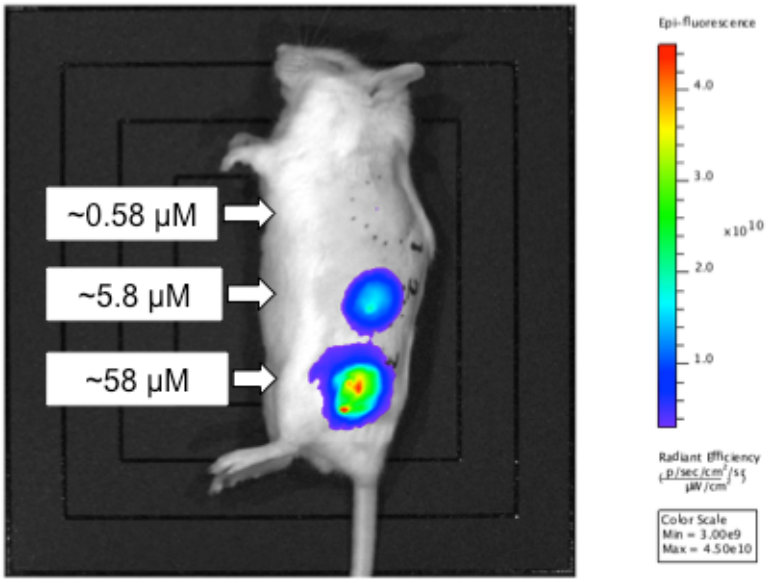

Figure 5.2: **DiR-PMs injected subcutaneously are visible using IVIS.**
IVIS images showing DiR concentration-dependent intensity of fluorescence. Three DiR-PMs preparations (1.5×10^{13}) were loaded with increasing concentrations of DiR (0.58, 5.8 or 58 µM DiR), injected subcutaneously in a culled mouse and imaged by IVIS immediately. (n=1, fluorescence expressed in radiant efficiency, min: 3×10^{9} (a.u.), max: 4.5×10^{10} (a.u.).

5.2.2 PMs distribution *in vivo* following systemic injection in a healthy mouse model.

Having demonstrated that DiR-PMs are detectable by IVIS, further experiments were performed to assess their *in vivo* localisation at different time intervals post tail-vein injection. 2 hours after the administration of 200 µl of DiR-PMs, a weak fluorescent signal is observed on the back of the mice (top panel, left hand side mouse) and on the ventral side, close to the anatomical location of the bladder and the liver (bottom panel, left hand side mouse). However, at 24 hours it is notable that the fluorescence in the region of the liver is increased compared to the previous time-point, and it is still present after 48 hours from the initial injection, but it is less intense than at 24 hours (Figure 5.3). Note that mice treated with empty-PMs do not exhibit a fluorescent signal, and the fluorescence observed in the ventral view on the paws and the mouth (Figure 5.3) is most likely ascribable to the lack of fur in those regions, which enhances the signal detected by IVIS machine (Winnard et al. 2006). This set of results demonstrated that DiR-PMs can

be detected by IVIS and that upon administration in healthy mice, the majority of the signal is localised in the region of the liver. However, considering that the aim of the project is to target injured bone tissue, the next step was to determine the distribution of DiR-PMs following systemic injection in a bone injury model.

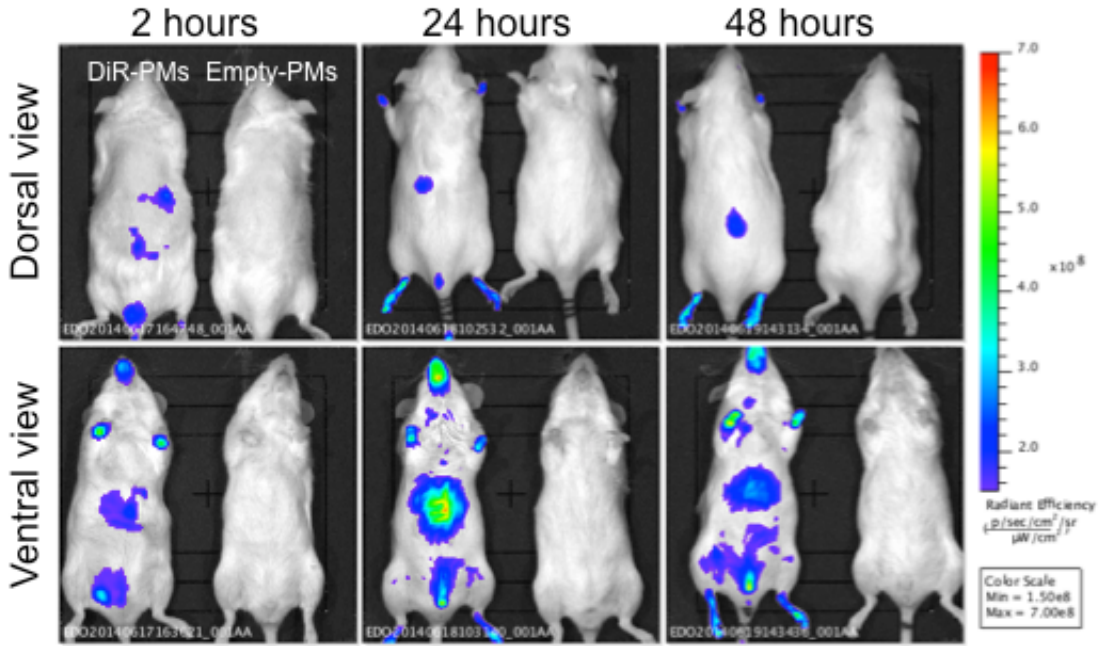

Figure 5.3: **DiR-PMs injected systemically accumulate in the region of the liver of healthy mice.** IVIS images showing the accumulation of DiR fluorescent signal in the liver region of mice injected via the tail-vein with 200 µl of either DIR-PMs (left mouse in each picture) or Empty-PMs (right mouse in each picture). Dorsal and ventral images were taken after 2, 24 or 48 hours post-injection. (n=3 mice, fluorescence expressed in radiant efficiency, min: 1.5 x 10^8 (a.u.), max: 7 x 10^8 (a.u.).

5.2.3 Characterisation of the bone injury.

As model of bone fracture, a unilateral, 1 mm wide, drill-hole bone defect was created in male MF1 mice 3 months old at the distal end of the femur, above the epicondyle (Figure 5.4). This represents a standardised type of mild bone injury, which always resolve in tissues healing and does not require the use of internal/external fixators to stabilise the bone fragments.

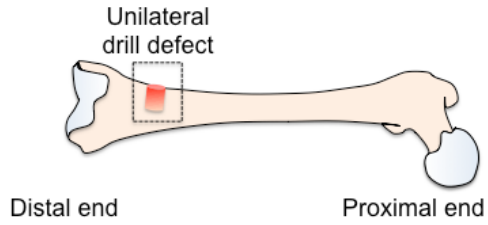

Figure 5.4: **Bone drill defect.**
Pictorial representation of a mouse femur with the localisation of the 1 mm drill defect in the lateral side of the bone above the epicondyle.

In order to first characterise the extent of the damage created with the drill defect, and also to understand the first stages of bone healing, defects were created and the healing process was followed by histological analysis.

The bone drill defect created in the epimetaphysis of the femur spanned from the outer-face of the cortical bone to the inner region of the bone marrow cavity (Figure 5.5A & B). Following fracture, bone fragments (white arrows) can be found within the injury site. Also, due to the damage, the vascular bed inside the tissue is ruptured. This results in the consequent formation of a haematoma (He, Figure 5.5A1 & B1) that comprises a blood clot covering approximately half the depth of the injury and bridging the gap between the two extremities of the bone cortex, and cells. The key component of the blood clot is fibrillar material (green arrow, Figure 5.5B1) that serves as structural support for the for the consequent repair mechanism.

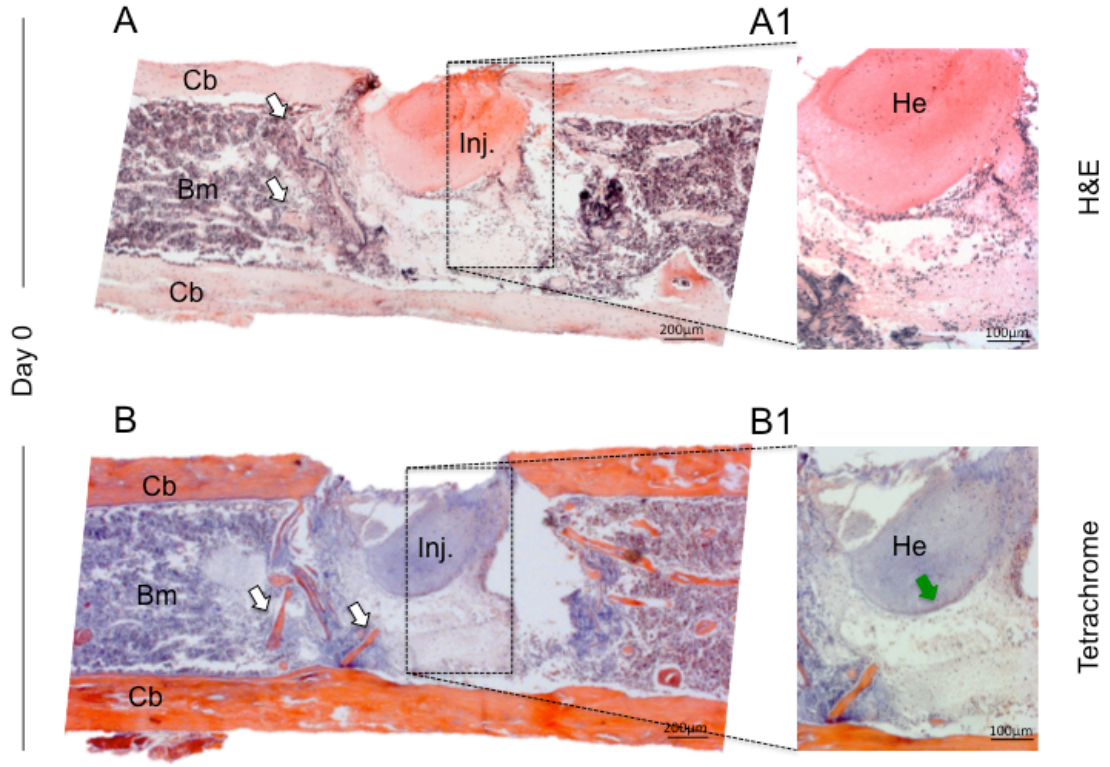

Figure 5.5: **Day 0 of fracture healing.**
A and B: Representative micrograph of the epimetaphysis of the femur at day 0 post-injury consisting of the cortical bone (Cb) and bone marrow cavity (Bm). The borders of the drill hole defect created (Inj) are represented by the dotted lines, and bone fragments are visible (white arrows) **A1 and B1:** Higher magnification of the injured area where a haematoma (He) and fibrillar tissue (green arrow) can be observed. Sections were stained with H&E (A and A1) or tetrachrome (B and B1).

At day 7 post-injury, the inflammatory phase is terminating (reviewed in section 1.2.3.1) and the repair process has begun (Figure 5.6A & B). The blood clot has been replaced by granulation tissue (Gt) (Figure 5.6A1 & B1), which effectively seals the injury (dashed white line), underneath which is the fracture callus (Cal). This is mainly composed of newly mineralised extracellular matrix, namely woven bone (Wb), which is quickly deposited in order to obtain a higher degree of mechanical stability compared to the haematoma (Figure 5.6A1 & B1). By day 10, the fibrous tissue bridging the gap between the cortical extremities is considerably thinner as it is progressively replaced by spicules of woven bone (Figure 5.7A & B). In theses structures, different cellular elements are visible, including chains of osteoblast on the surface of the bone spicules, and osteocytes embedded in their lacunae (Figure 5.7A1 & B1).

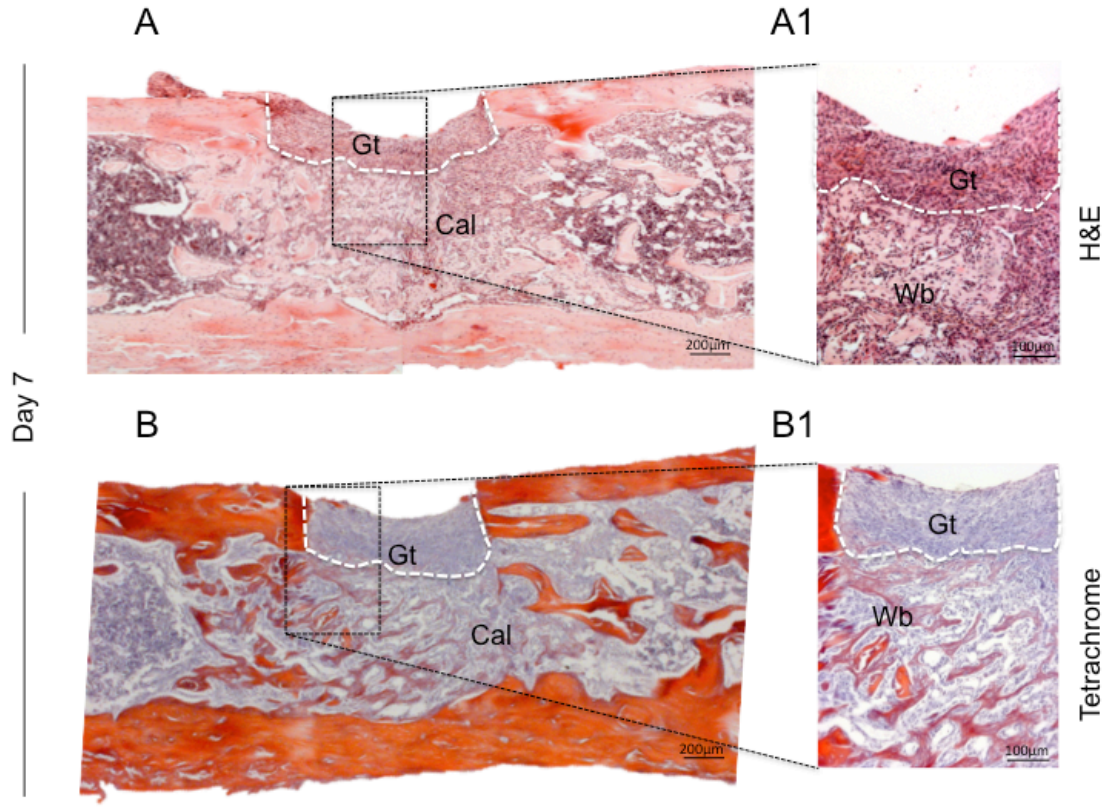

Figure 5.6: **Day 7 of fracture healing.**

A and B: Representative micrograph of the epimetaphysis of the femur at day 7 post-injury the injured area (black dotted line) is filled with extracellular matrix. Here granulation tissue (Gt) seals the injury (dashed white line), while the callus (Cal) is forming. **A1 and B1**: This matrix is comprised of granular tissue (Gt) and woven bone (Wb). Sections were stained with H&E (A and A1) or tetrachrome (B and B1).

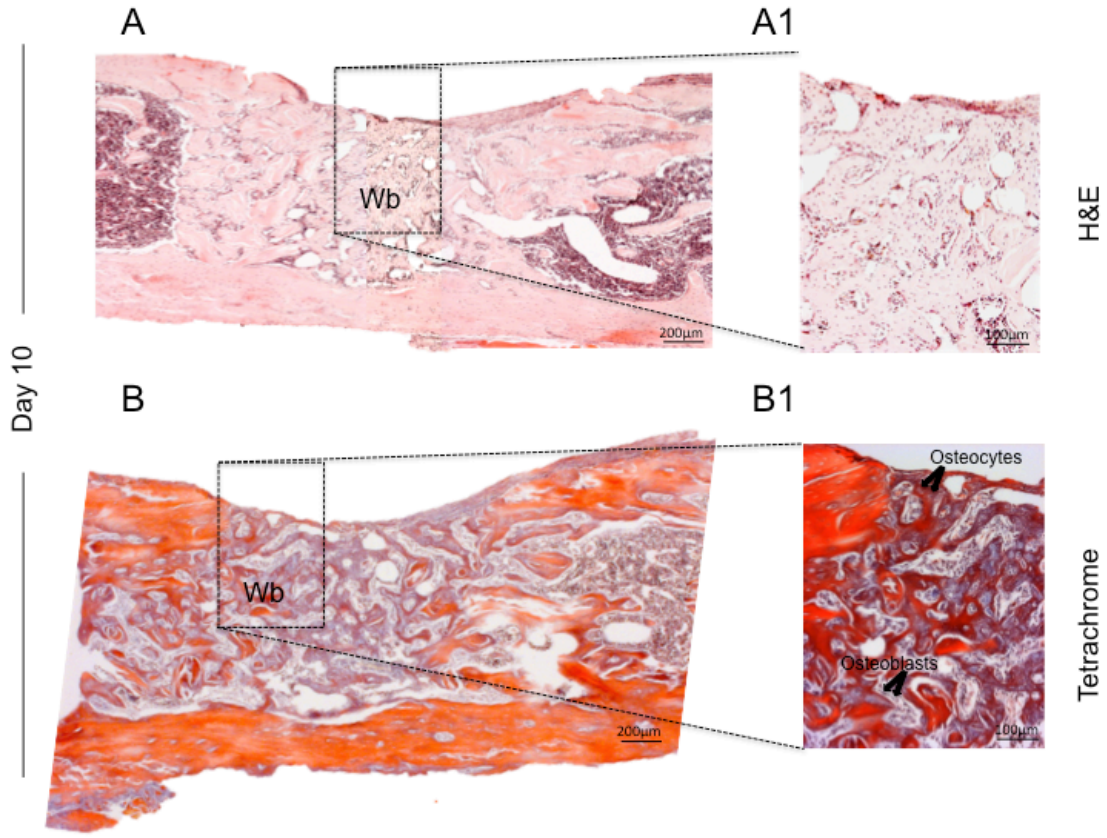

Figure 5.7: **Day 10 of fracture healing.**
A and B: Representative micrograph of the epimetaphysis of the femur at day 10 post-injury, where mostly woven bone (Wb) can be found in the injured area (dotted line). **A1 and B1**: Higher magnification of the injured area showing the presence of osteocytes, embedded in the bone matrix, and chains of osteoblast on the surface of the bone spicules. Sections were stained with H&E (A and A1) or tetrachrome (B and B1).

5.2.4 DiR-PMs accumulate at the fracture site.

Mice with a bone drill defect were injected *via* tail-vein with DiR-PMs and DiI-PMs (200 µl total volume) within 1 hour from the creation of the injury, and then examined using IVIS. Figure 5.8 (top corner, left-hand side image) shows the presence of a weak and widely distributed fluorescence signal 1 hour post-administration of DiR-PMs. 24 hours later, this signal is intensely localised in the area where the bone injury was created (left hind limb), where it persisted until day 10 post initial injection of DiR-PMs

(Figure 5.8). Note that no fluorescence was detected in control mice injected *via* tail-vein with empty-PMs.

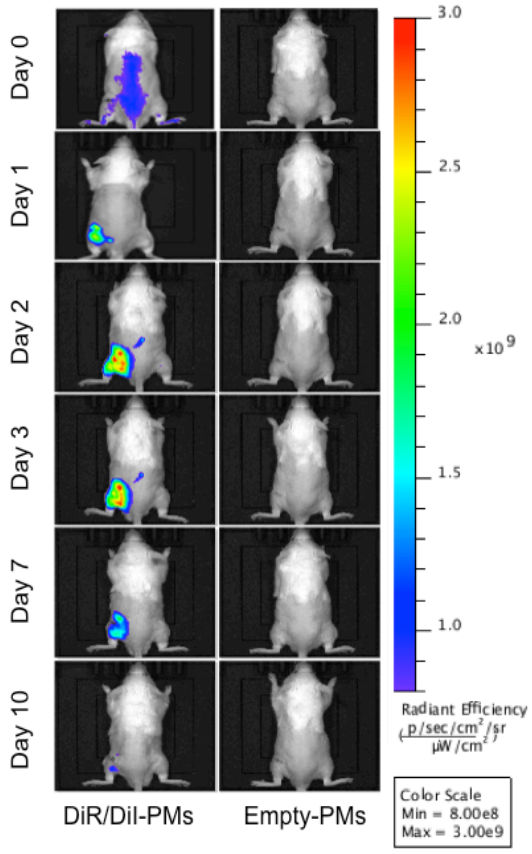

Figure 5.8: **DiR-PMs accumulate at the fracture site after systemic injection.**
Representative IVIS images showing the progressive accumulation of DiR fluorescent signal in the injured area following tail-vein injection of 200 µl of DiR- and DiI-PMs, and the lack of signal in the control mice injected with Empty-PMs. (*n*=≥2). Fluorescence expressed in radiant efficiency, min: 8 x 10^8 (a.u.), max: 3 x 10^9 (a.u.).

Quantitative measurements of the fluorescence intensity over time were obtained by selecting a region of interest around the injured area (blue squares in Figure 5.9A) (see section 2.2.12). The most intense fluorescent signal was measured 48 hours post-injection, after which it progressively dimmed with time (Figure 5.9B). *Ex-vivo* analysis of explanted femurs 7 days post-injection of DiR-PMs revealed the presence of fluorescent signal in the fractured bone and, what was considered background fluorescence, in the contralateral femur (Figure 5.9C).

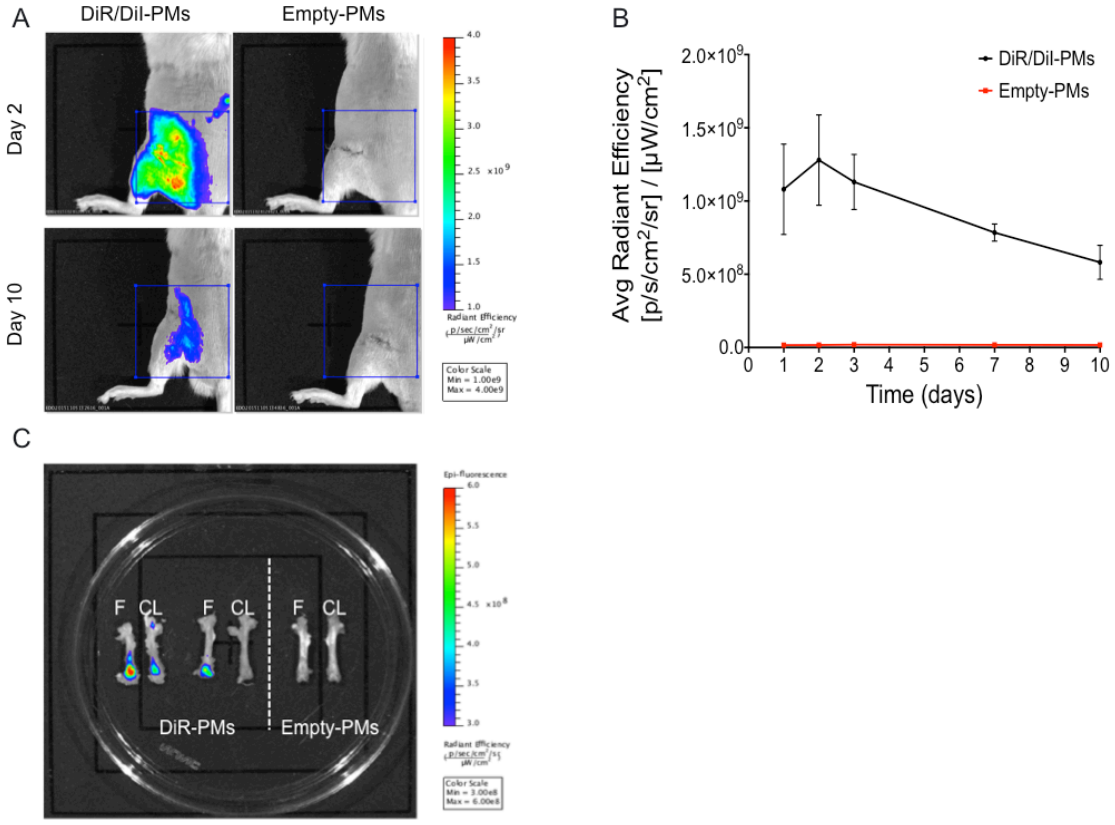

Figure 5.9: **Analysis of the fluorescence measured at the fracture site after systemic injection.**

A: Representative images of injured legs at day 2 and day 10 post tail-vein injection of either DiR/DiI-PMs or empty-PMs showing the region of interest selected (blue squares). **B:** Graph showing image analysis results on the intensity of fluorescence measured in the region of interest, drawn around the injured leg. Following the peak at 48 hours post injection of DiR- DiI-PMs, a progressive decline in intensity over time is observed. Control mice, injected with empty-PMs, showed no fluorescence. **C:** Representative IVIS image showing the localisation of DiR fluorescence in fractured (F) and contralateral (CL) femur after 7 days from the systemic injection of either DiR- DiI-PMs or empty-PMs. Fluorescence expressed in radiant efficiency, min: 3 x 10^8 (a.u.), max: 6 x 10^8 (a.u.).

Fluorescence due to the administered PMs in the injured leg was further confirmed by histological analysis of injured femurs explanted 7 days post systemic injection of DiI-PMs. Using H&E staining, it was possible to distinguish distinct anatomical areas within the injured region, including injury site (Inj), cortical bone (Cb) and bone marrow cavity (Bm) (Figure 5.10A & B). Using fluorescence microscopy, the presence of DiI signal in different regions within the defect (yellow arrows), both in the injury and bone marrow areas, was observed (Figure 5.10A1 & B1). Note the lack of signal in the control mice treated with empty-PMs (Figure 5.10C & D).

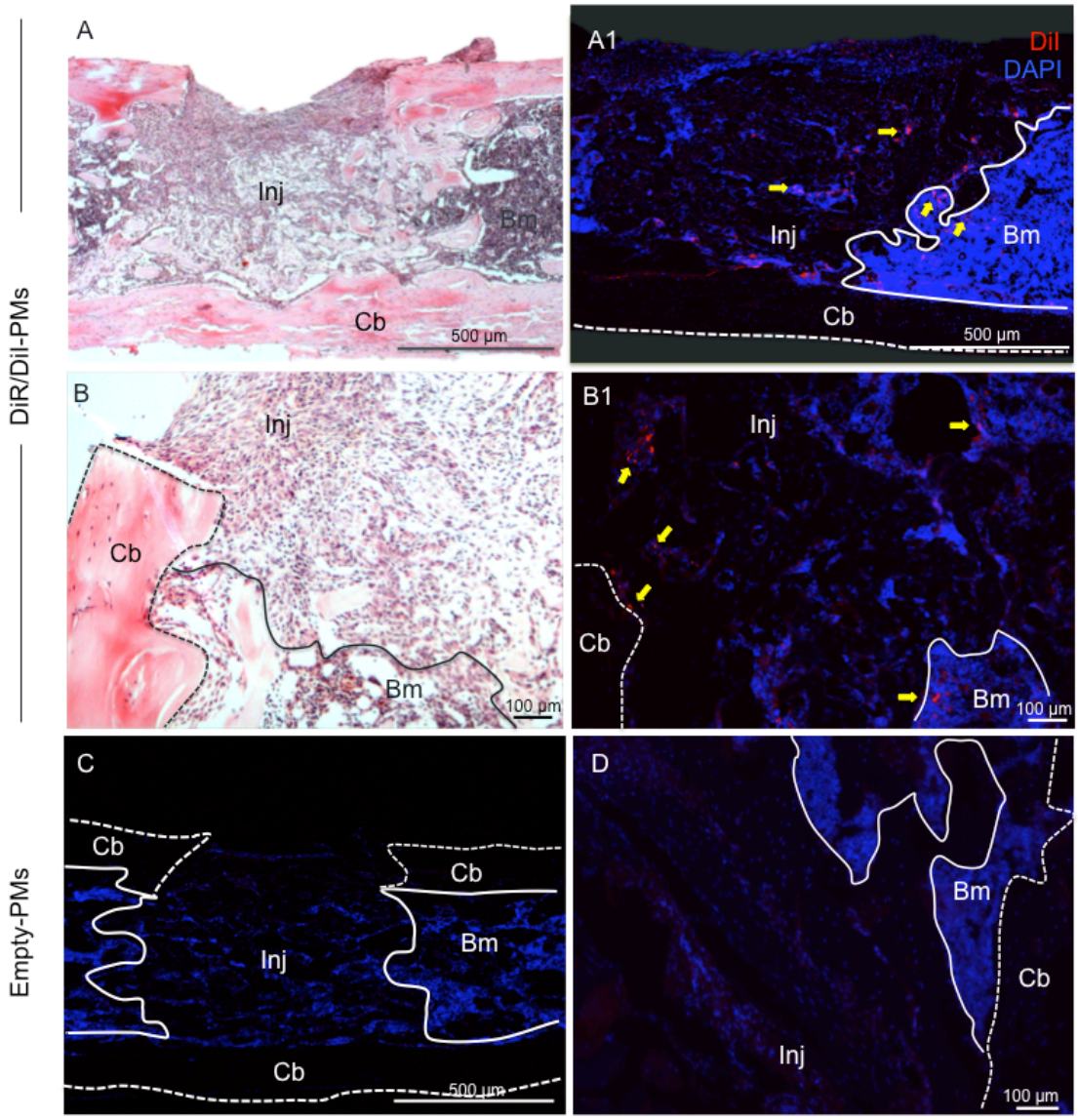

Figure 5.10: **DiI-PMs are localised in the injury area 7 days following systemic administration.**
A, B: Representative histological sections, stained with H&E, of the defect area of the bone 7 days post injury. Images were taken at 2.5x and 10x magnifications, respectively. Inj: injury area, Cb: cortical bone, Bm: bone marrow. **A1, B1:** Representative fluorescence images showing the presence of DiI fluorescence (Red) in both the injured area and the bone marrow cavity (yellow arrows) 7 days post injection of DiI-PMs. Blue: nuclear staining. **C, D:** Representative fluorescence images of femur sections from mice injected with empty-PMs. Blue: nuclear staining.

5.2.5 PMs localise in the liver.

On the basis of the result presented in Figure 5.3, where the presence of PMs in the region of the liver 48 hours after systemic injection was seen, other tissues besides the injured area were investigated for the presence of DiR- and DiI-PMs.

Imaging of the ventral surface of treated mice, revealed a DiR fluorescence signal in the region of the liver 24 hours post systemic injection of DiR-PMs. However, the fluorescent signal was no longer present in that region at day 7 (Figure 5.11). Note that upon direct comparison of dorsal and ventral images, the highest fluorescence signal was observed on the dorsal side, specifically in the injured area, while weak signal was detected in the liver region of 2 days post injection of DiR-PMs (Appendix Figure 14).

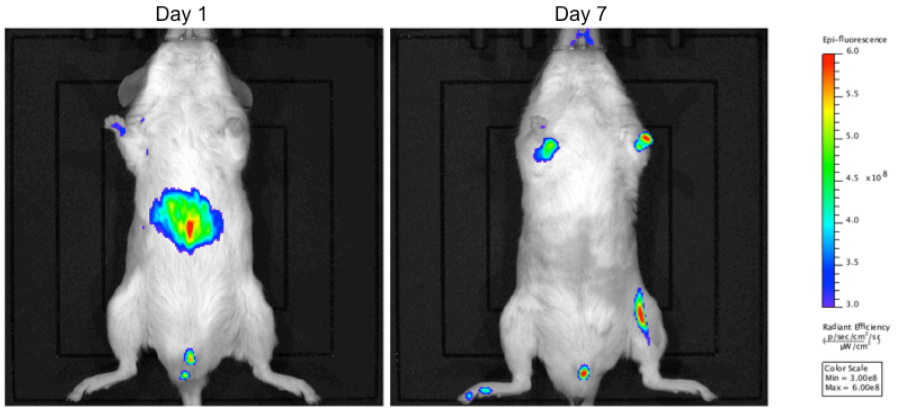

Figure 5.11: **DiR-PMs are present in the liver area of bone injury models 1 day post systemic injection.**

Representative IVIS images showing the presence of localised DiR fluorescence in the liver area 1 day post systemic injection and consequent lack of signal 7 days post systemic administration. Fluorescence expressed in radiant efficiency, min: 3 x 10^8 (a.u.), max: 6 x 10^8 (a.u.).

Analysis of the accumulation within the region of the liver (Figure 5.11) was further carried out by histological analysis, which was also used to investigate whether accumulation of PMs induced hepatotoxicity.

Histological analysis by H&E staining of livers explanted 7 days post treatment with DiR/DiI-PMs, did not show gross structural or morphological alterations (Figure 5.12A) relative to control livers (untreated mice, Figure 5.12D). Despite no evidence of fluorescent signal deriving from PMs localised to the liver area using IVIS at day 7, DiI fluorescence (yellow arrows) was observed extensively in various areas of the livers analysed histologically (Figure 5.12B & C).

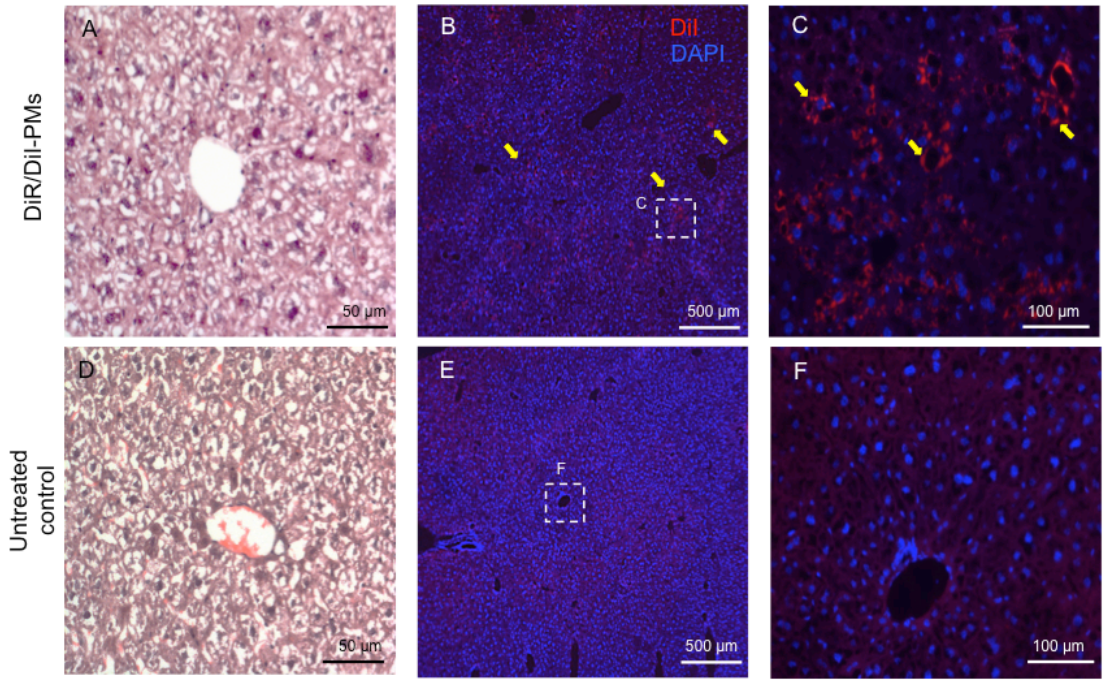

Figure 5.12: **DiI-PMs are present in the liver 7 days following systemic administration but do not induce hepatotoxicity.**

A: Representative histological sections, stained with H&E, showing the lack of morphological and structural alterations 7 days post injection of DiR/DiI-PMs. **B:** Representative fluorescence image showing the presence of DiI fluorescence (Red) in the liver (yellow arrows) 7 days post injection of DiI-PMs. **C:** Higher magnification of an area present in B showing the presence of DiI staining (yellow arrows). **D:** Representative histological sections, stained with H&E, of untreated control livers. **E, F:** Representative fluorescence images of control livers. Blue: nuclear staining.

PMs injected systemically were shown to preferentially accumulate at the injury site and partially distribute in the liver, this raised the issue of whether this accumulation was characteristic of PMs circulating in the blood stream or whether free fluorescent molecules injected systemically achieved a similar distribution. Following the creation of the drill defect in the femur, free DiR (un-encapsulated DiR) was injected systemically at equal concentrations to that injected when loaded in PMs. Moreover, in order to investigate whether the creation of tissue damage in the soft tissue surrounding the bone injury was also contributing to the accumulation of PMs in the injury site, a sham control group was analysed. Sham mice underwent a surgical procedure; however, the femur was exposed but no drill defect was made (see section 2.2.12).

48 hours after systemic administration of DiR/DiI-PMs, intense fluorescent signal was observed in the injury area in both sham and drill defect groups, while very weak (free DiR) or no signal (empty-PMs) was detected (Figure 5.13A). Femurs were extracted and soft tissue was removed before imaging using IVIS. Figure 5.13B shows the high intensity of fluorescence measured in the injured femur of mice injected with DiR-PMs compared to Sham and free DiR control groups (p<0.001) (Figure 5.13C). Note that the majority of the fluorescence signal observed in the sham group was associated with the skin rather than the muscle and bone tissue (Figure 5.14).

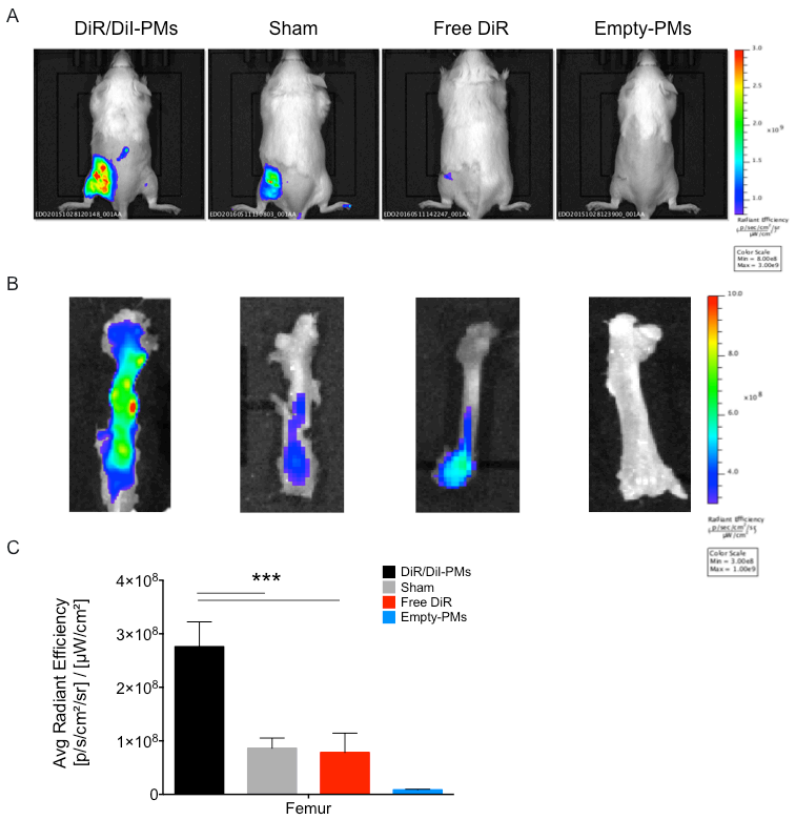

Figure 5.13: **Encapsulation of DiR in PMs favours accumulation at the fracture site.**

A: Representative IVIS images illustrating the higher intensity of fluorescent signal in injured mice 48 hours post treatment with DiR/DiI-PMs compared to sham, free DiR or empty-PMs groups. Fluorescence expressed in radiant efficiency, min: 8 x 10^8 (a.u.), max: 3 x 10^9 (a.u.). **B:** Representative IVIS images of explanted femurs showing the high accumulation of fluorescence in DiR/DiI-PMs injected mice compared to sham, free DiR or empty-PMs groups. Fluorescence expressed in radiant efficiency, min: 3 x 10^8 (a.u.), max: 1 x 10^9 (a.u.). **C:** Graph showing the highest intensity of fluorescence in the DiR/DiI-PMs group. (n=3 mice, mean ± SD, one-way ANOVA) ***p<0.001.

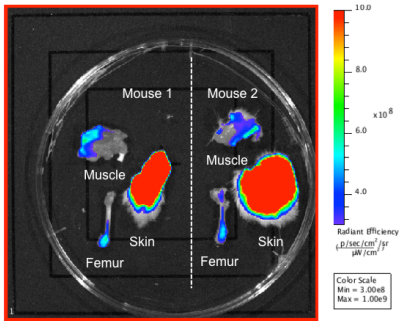

Figure 5.14: **Fluorescent signal preferentially accumulated in the skin of the sham group.**
IVIS image showing the highest intensity of fluorescent signal associated to the injured skin of the sham group 48 hours post treatment with DiR/DiI-PMs. Fluorescence expressed in radiant efficiency, min: 3 x 10^8 (a.u.), max: 1 x 10^9 (a.u.).

Ventral view imaging revealed a strong accumulation of fluorescence signal in the region of the liver of mice treated with free DiR (Figure 5.15A). However, *ex vivo* analysis identified fluorescence in the liver and spleen of all mice other those injected with empty-PMs (Figure 5.15B). However, mice treated with free DiR showed greater fluorescence intensity compared to the other groups (Figure 5.15C & D).

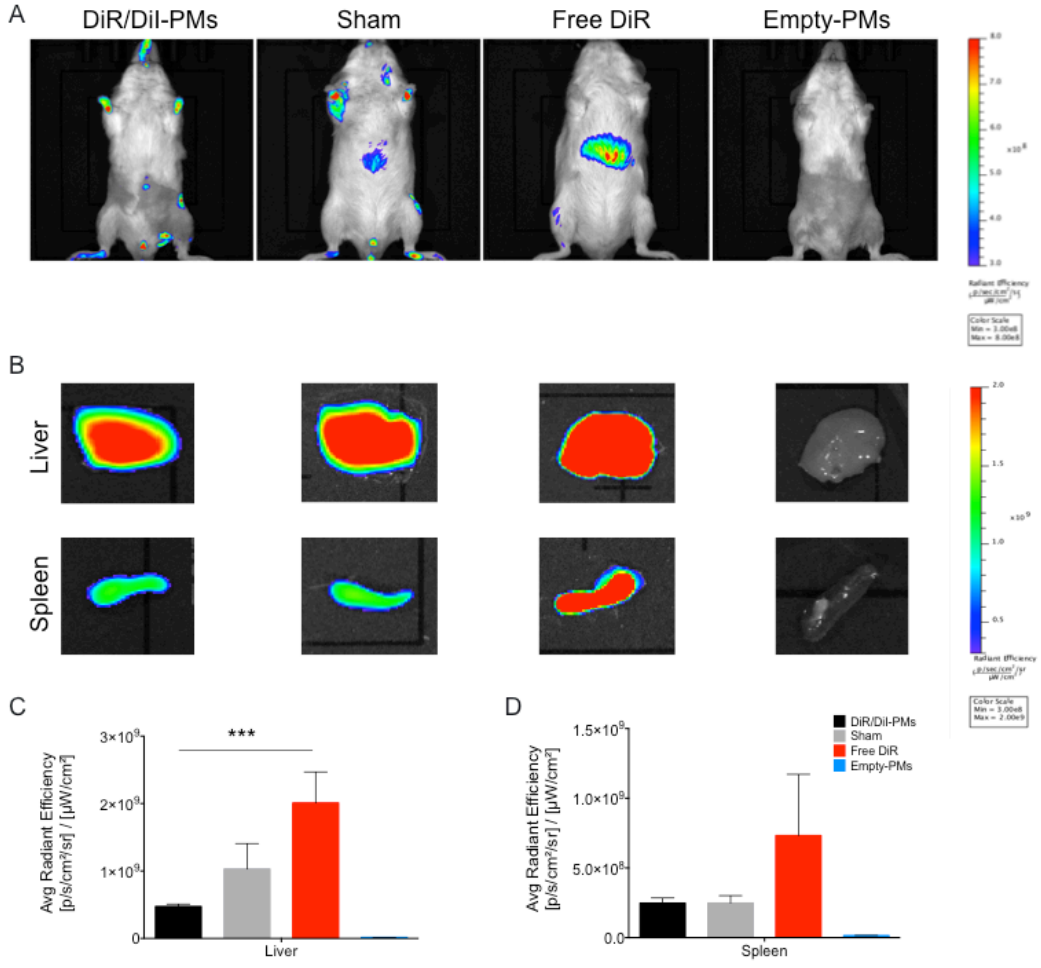

Figure 5.15: **Encapsulation of DiR in PMs favours accumulation at the fracture site.**

A: Representative IVIS images showing the higher intensity of fluorescent signal the liver area 48 hours post treatment with free DiR compared to DiR/DiI-PMs, sham, free DiR or empty-PMs groups. Fluorescence expressed in radiant efficiency, min: 3 x 10^8 (a.u.), max: 8 x 10^8 (a.u.). **B:** Representative IVIS images of explanted livers and spleens showing the high accumulation of fluorescence in free DiR injected mice compared to DiR/DiI-PMs, sham, free DiR or empty-PMs groups. Fluorescence expressed in radiant efficiency, min: 3 x 10^8 (a.u.), max: 2 x 10^9 (a.u.). **C:** Graph showing the highest intensity of fluorescence in the liver of free DiR treated mice. **D:** Graph showing the highest intensity of fluorescence in the spleen of free DiR treated mice. (n=3 mice, mean ± SD, one-way ANOVA). ***p<0.001.

5.2.6 Effects of BIO-PMs on bone fracture healing

The previous experiments reported in this chapter demonstrated the accumulation of PMs injected systemically at the site of bone injury. Despite the lack of clear evidence of the ability of the BIO-PMs to activate the Wnt pathway *in vivo* or the concentration of PMs localising at the fracture site, it was decided to carry out a pilot experiment to test whether BIO-PMs could promote bone fracture healing. This investigation was performed on the basis of previous published data demonstrating the beneficial effects of treatment with a Wnt agonist on bone formation (Minear et al., 2010) and also considering the lack of congruency, in terms of prediction of a positive outcome, between *in vitro* and *in vivo* studies (Hulsart-Billström et al. 2016).

Bone healing was assessed by sequential μ-CT scanning of mice treated once *via* tail-vein injection, with BIO-PMs, empty-PMs or free BIO in equal concentration to that administered through BIO-PMs (198 μM, Figure 4.5). A pictorial summary of the methodology employed is reported in Figure 5.16.

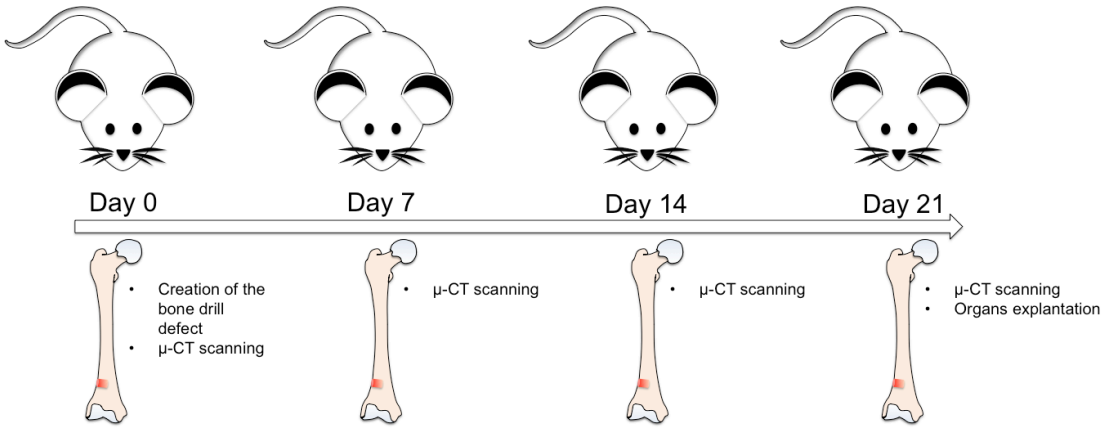

Figure 5.16: **Time-line of the methodology.**
Pictorial summary of the methodology time-line. At day 0, the bone drill defect was created and mice were scanned by μ-CT. The scanning process was repeated every 7 days until day 21 when mice were scanned, culled and their organs collected.

No adverse events were observed following any treatment. Mice were able to ambulate normally less then 6 hours post surgical procedure. μ-CT scanning analysis showed that the healing process was comparable among the three groups. At day 0 all the animals presented a standardised round defect, 1 mm width, spanning from the cortical

bone to the intra-medullary cavity (Figure 5.17 and Appendix Figure 15). At day 7, the defect was still visible with soft tissue arising from the bone marrow cavity beginning to invade the injury area. By day 14, although the margins of the injury could still be distinguished, the defect area was completely bridged by mineralised tissue, which was then further remodelled during the following week (Figure 5.17, Appendix Figure 15).

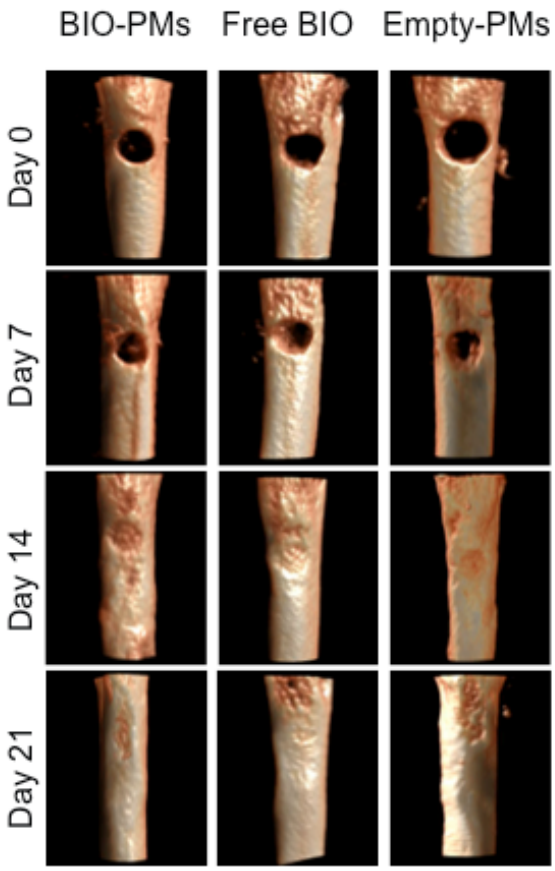

Figure 5.17: **Temporal μ-CT analysis of bone drill healing process.**

Representative μ-CT 3D reconstructions showing, from the outer-view, the temporal progression of the healing process in the three groups investigated (the same femur has been images in each longitudinal analysis).

In order to determine whether the treatments induced differences in terms of re-mineralisation of the bone tissue, a volume of interest containing the injured area was selected and quantitative analysis was performed. No significant differences in terms of tissue volume (TV), bone volume (BV) or percentage of bone volume (BV/TV) were measured among groups. However, treatment with BIO-PMs consistently induced an

increase in both BV and TV compared to both free BIO and empty-PMs treatment (Figure 5.18A, B). Finally, no clear trends in terms of percentage of bone volume were observed (Figure 5.18C).

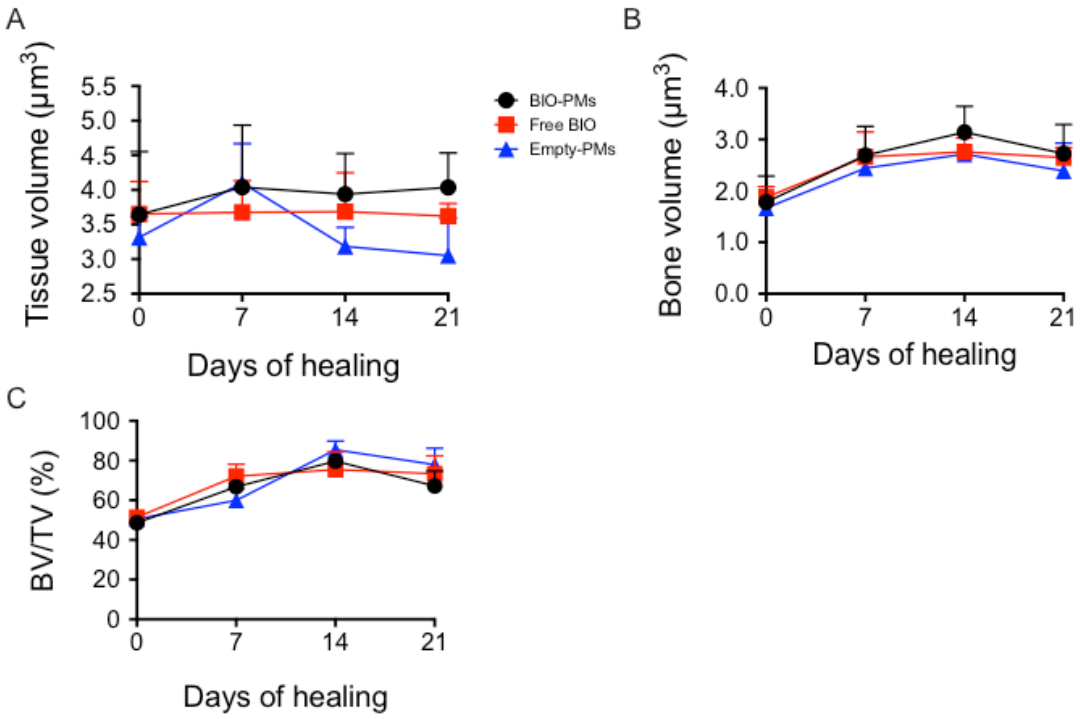

Figure 5.18: **µ-CT analysis of the type of tissue bridging the bone drill defect.**
A: Quantitative analysis showing the increased tissue volume created in the volume of interest (VOI) around the defect in mice treated with BIO-PMs. **B:** Quantitative analysis showing the increased bone volume created in the VOI around the defect in mice treated with BIO-PMs. **C:** Quantitative analysis showing the percentage of volume (BV/TV) created in the VOI around the defect. (n=3 mice, mean ± SD, one-way ANOVA).

Histological examination of the defect site 21 days post injury showed complete bridging of the defect with extensive deposition of mineralised tissue, in accordance to the µ-CT results presented in the previous section (Figure 5.19A-C). Woven bone matrix was laid down on the three treatments, however a higher a proportion of mineralised (red pigmentation) over osteoid tissue (blue pigmentation) was observed in BIO-PMs samples compared to free BIO or empty-PMs (Figure 5.19A1-C1).

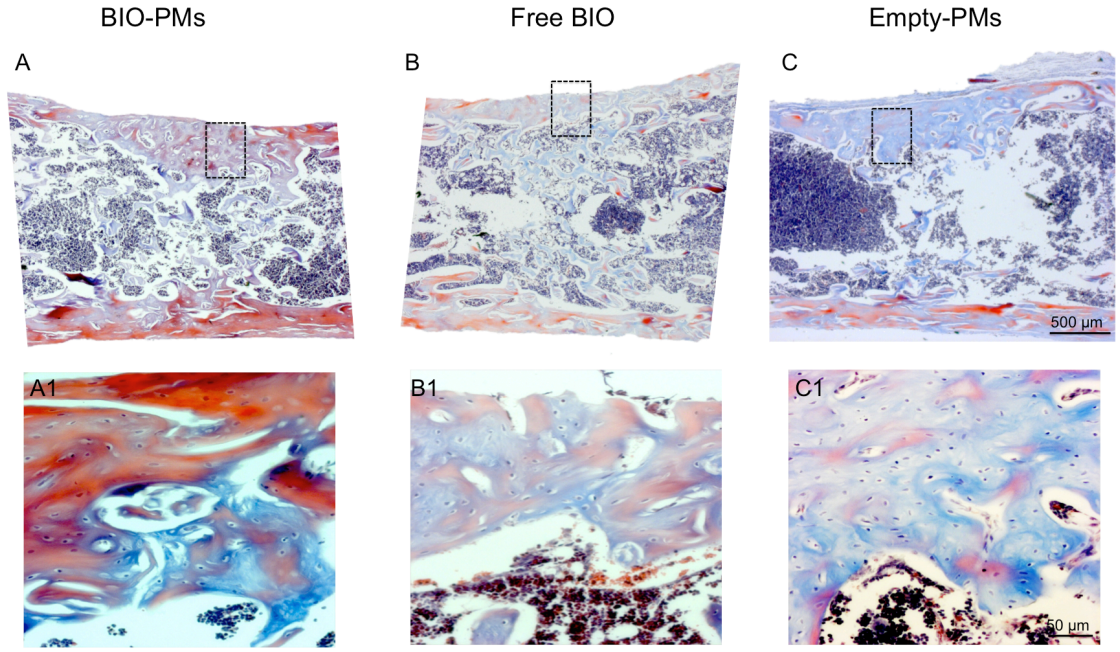

Figure 5.19: **Histological analysis of bone femurs 21 days post treatments with BIO-PMs, free BIO or empty-PMs.**

A: Representative micrograph of the drill defect 21 days post injection of BIO-PMs. **A1:** Higher magnification of the dotted insert in figure A, showing the higher presence of lamellar bone (red) over osteoid bone (blue). **B:** Representative micrograph of the drill defect 21 days post injection of free BIO. **B1:** Higher magnification of the dotted insert in figure B, showing the presence of both lamellar bone (red) and osteoid bone (blue). **C:** Representative micrograph of the drill defect 21 days post injection of free BIO. **C1:** Higher magnification of the dotted insert in figure C, showing the presence of both lamellar bone (red) and osteoid bone (blue). Nuclear staining is in dark brown.

5.3 Discussion

The experiments presented in this chapter were focused on assessing the distribution of PMs *in vivo* following systemic injection, and the effect of a controlled delivery of BIO on bone regeneration in a pilot study.

The main findings observed are:

- PMs injected i.v. in healthy mice accumulate in the region of the liver;
- PMs injected i.v. in mice with a bone injury preferentially distribute into the bone fracture;
- Encapsulation of a fluorescent dye within PMs alters its final distribution in comparison to its free form;
- BIO-PMs promote an increase in bone volume.

PMs loaded with either DiI or DiR had a hydrodynamic size of ~65 nm (Figure 5.1), as did the BIO-PMs (Figure 4.4). Their fluorescent signal was found to localise in the region of the liver 24 hours after tail-vein injection in healthy mice. The size of the PMs plays a fundamental role in determining the final distribution *in vivo*. Despite their proven ability to translocate across pores smaller than their size without breaking (Pegoraro et al), following systemic administration PMs encounter a series of physiologic al barriers (Alexis et al. 2008) with different size 'cut-off' that determine nanoparticles partitioning into tissues (Bertrand & Leroux 2012). Most of the PMs will accumulate in organs of the RES, but depending on their physical-chemical composition they will have the ability to reach all the tissues in the body. Using radio labelled PMs, Brinkhuis and colleagues demonstrated that 4 hours post systemic injection, the majority of the nanoparticles below 90 nm in size were circulating in the blood, while PMs above such threshold where already sequestered in either the liver or spleen. 24 hours after the initial administration, the majority of the PMs had already accumulated in both liver and spleen, regardless of their size (Brinkhuis et al. 2012). Considering the small size of the PMs used in the current experiments, the accumulation of DiR fluorescence in the region of the liver 24 hours after injection is therefore not surprising (Figure 5.3). Other important parameters influencing the distribution of PMs *in vivo* are surface charge (Lee et al. 2011), density of PEG chains (Photos et al. 2003) and the presence of specific binding motifs on

the surface of the PMs. For example, it has been demonstrated that the expression of interleukin 13 peptide or alendronate molecules on the surface of the nanoparticles greatly increases their distribution in tissues of interest: glioma and bone tissue, respectively (Gao et al. 2012; Swami et al. 2014). However, engineering nanoparticles with binding motifs has also been demonstrated to alter the physiological turnover of membrane receptors, therefore influencing molecular mechanism within the cells (Jiang et al. 2008). Concerns have been raised as to whether the cleavage of these targeting motifs from the nanoparticle surface could impair biological processes, as demonstrated by the use of bisphosphonates to target the bone tissue. These molecules alter the balance between bone deposition and resorption by inhibiting osteoclast activity; therefore they may potentially affect bone turnover and consequent regeneration following injury (Fleisch 2001). All considered, by tuning the physical-chemical characteristic of the PMs, their final distribution *in vivo* could be better modulated. Therefore, future experiments could be focused on investigating the accumulation into the injured bone tissue of PMs of different sizes and tethered with different binding motifs.

A major limitation of the results reported in this chapter is the assumption that the fluorescence deriving from either DiR or DiI, is directly related to the physical presence of the PMs in the specific tissue. During their circulation in the blood, PMs could be internalised by neutrophils (Chu et al. 2015), adsorbed on the surface of red blood cells (Anselmo & Mitragotri 2014) or uptake by macrophages. The latest, in particular is a very interesting mechanism. Seminal work from Van Roojien demonstrated that liposomes loaded with clodronate can be used to deplete phagocytic cells in several tissues including liver, spleen and lung (reviewed by van Rooijen & van Kesteren-Hendrikx 2002). On the back of these findings, Afergan and colleagues demonstrated that liposomes are able to deliver serotonin across the blood brain barrier, but this delivery is mainly mediated by circulating macrophages, which function as a "trojan-horse", internalising the nanoparticles in the blood stream, and then transport them into the central nervous system (Afergan et al. 2008). Nevertheless, in order to be exploited for therapeutic purposes, this "trojan-horse" mechanism would require the ability of PMs and/or the payload to escape from the monocyte/macrophage, and this is dependent on the chemistry of the nanoparticles/drug used. Alternatively, PMs specifically targeting macrophages, which play a key role during bone repair, could be exploited in order to modulate the inflammation or the macrophage class switching (see section 1.2.3.1).

Translating these observations to the results reported in this chapter would imply that the fluorescence observed in the tissues is a consequence of cells carrying PMs to destination rather than PMs traveling as discrete entities. It was shown in Chapter 3 that fluorescein-PMs incubated for 3 hours with freshly isolated BMMNCs are internalised by monocytes and granulocytes (Figure 3.22 and Figure 3.24). The fast uptake observed in those experiments may be an indication of a trojan-horse effect, which should be further investigated using Image stream analysis.

Alternatively, fluorescent molecules of DiR of DiI could be transferred from PMs to another lipophilic membrane with a 'kiss and run' mechanism (Hofmann et al. 2014). In this scenario, PMs loaded with any lipophilic compound could release the payload into a phospholipid cellular membrane by simply touching it, without the need for internalisation. The hydrophobic molecule could then be internalised by the cell during physiological process of membrane turnover or lipid droplets intake (Hofmann et al. 2014). Recently, Lin and colleagues demonstrated that PMs fuse with each other through a mechanism that the authors divided in 4 steps: kissing, adhesion, hemifusion and fusion (Lin et al. 2014). So, the presence of a polymeric corona does not prevent fusion mechanisms similar to those observed between cellular vesicles. Also, once administered *in vivo*, PMs surface is covered with serum proteins that alter the properties of the nanocarriers and may favour fusions 'kiss and run' mechanisms (Lynch et al. 2009; Lynch & Dawson 2008). Therefore, it is could be speculated that DiR or DiI may be transferred to other membranes following fusion rather than by internalisation. In future experiments it would be useful to confirm the physical presence of PMs at the tissue of interest, assessing the presence of PEG or PCL by Raman spectroscopy, mass-spectrometry or immune-histochemistry. It would also be interesting to determine the half-life of loaded PMs in the blood in order to have more precise information regarding the pharmacokinetics of the system. This could be achieved by simply collecting blood samples at various time intervals and comparing their fluorescence/absorbance to standard curve of the dyes incorporated within the PMs, possibly using both hydrophilic and hydrophobic molecules in order to control for kiss and run type delivery.

Next, it was demonstrated that following creation of defect in the mouse femur, PMs injected via the tail-vein mainly accumulate within the injury site compared to other tissues (Figure 5.8). Also, the fluorescence characteristic of the PMs is still detectable 7

days post administration (Figure 5.8). This result represents, to the best of our knowledge, the first demonstration of passive accumulation of PMs to a healing bone fracture following systemic treatment. Although very promising, this result may be explained by previously described phenomena. Mastumara and Maeda were the first to report that an albumin-dye complex injected systemically in tumour bearing-mice accumulated in the site of cancerous neoplastic tissue within hours (Matsumura & Maeda 1986). The authors postulated that this EPR effect was caused by a combination of hyper-vascularisation, enhanced permeability of the vascular bed and limited lymphatic drainage. To a certain extent, tumour and early stage bone healing fractures are similar. After the creation of the bone injury, the local vasculature is damaged resulting in bleeding within the area (Groothuis et al. 2010). The haematoma is also characterised by increased vasodilation, mediated by the high release of nitric oxide (Diwan et al. 2000), increased cellularity, due to leucocyte extravasation, and a high concentration of VEGF, which is more than 15 fold higher than in the blood plasma (Street et al. 2000). Such a high concentration of VEGF naturally leads to the formation of new blood vessels, resulting in a marked increase in blood flow into the injured area, by day 3 post fracture (Claes et al. 2012). Dong Wang and colleagues further investigated the EPR effect, demonstrating that similar passive accumulation of macromolecules is observed in basically any inflamed tissue (reviewed by Ren et al. 2016). Nonetheless, this passive accumulation was fundamentally different from the EPR effect as it was mediated by the internalisation of the polymeric-prodrug in resident macrophages, fibroblasts and dendritic cells. Therefore, the authors coined the term extravasation through leaky vasculature and inflammatory cell mediated sequestration (ELVIS) to define such an effect (Quan et al. 2010). However, the possibility that these different prodrugs were internalised by cells in the blood stream has not been investigated by the authors and should be considered also in future experiments using PMs. The accumulation of PMs in the bone fracture site presented in this chapter (Figure 5.8) is most likely due to the same ELVIS effect, whereby PMs travelling in the blood stream end up in proximity of the fracture site where they extravasate in the injured tissue. The extravasation of PMs may be due to the leakiness of the blood vessels, but it is also made likely due to the increased cellularity that forces the nanoparticles towards the walls of the blood vessels, as elegantly showed by Fullstone and colleagues through fluid dynamics modelling of PMs in the blood (Fullstone et al. 2015).

ELVIS mediated polymer based prodrug retention has been shown in several musculoskeletal systems including rheumatoid arthritis (Yuan et al. 2012) and murine models of prosthesis failure (Ren et al. 2014), but only two recent seminal paper addressed the possible effects in a bone fracture model (Jia et al. 2015; Low et al. 2015). Both studies reported the accumulation of micelles at fracture site within 24 hours from the systemic injection. Although in agreement with the results reported in this chapter, a major difference in the studies is the time of injection. The systemic administration of the nanocarriers from Jia and colleagues was 7 days post osteotomy, Low and colleagues waited 2 weeks form the injury insult, while in this project PMs were injected straight after the creation of the injury. Jia and colleagues went on to investigate by FACS the partitioning of the micelles present at the injury in different cell types, and demonstrated uptake from resident macrophages and neutrophils. The results reported in the two studies are somewhat surprising, as the progression of the healing process leads to a reduced vasodilation and extravasation of leukocytes, so a time-dependent reduction in nanoparticles accumulation in the injury site would be expected. However, between one week and four weeks after bone fracture, blood flow in the injured tissue is considerably increased compared to physiological conditions (Claes et al. 2012), and the new formed vessels are not matured so nanoparticles extravasation in this context is more likely. Nevertheless, that macrophages and neutrophils were the cells internalising the micelles 7 days post injury is intriguing. Jia and colleagues used a simvastin prodrug, which is then converted to a statin with high bone anabolic effects mediated through the activation of BMP-2 (Mundy et al. 1999), and despite the internalisation in leukocytes rather than BMP-2 responsive cells (*i.e.* SSC, pre-osteoblasts or mature osteoblast), enhancement of bone healing was observed. In future experiments it would be interesting to use FACS or image stream in order to determine which subcellular populations are internalising PMs at the fracture site, and whether the results demonstrated in chapter 3, where SSCs were taking up PMs (Figure 3.23 and Figure 3.24), are also confirmed in this system. Also, investigating how administration of PMs after different days from the initial bone injury would alter the distribution of PMs in the body is a high priority. This would enable a direct comparison with previous reported data (Jia et al. 2015) that may lead to different therapeutic strategies ranging from the early treatment of acute inflammation, to the influence of the vasculature formation or cellular differentiation. Finally a clear limitation of the study here presented is the animal model used. PMs distribution and ability to

enhance bone healing was assessed in young and healthy animals, in which it is likely that the only tissue inflammation site is represented by the bone fracture created. Also, the use of a unilateral bone drill defect, in which healing always occurs physiologically, may not be the correct type of injury to highlight either positive or negative effects mediated by the use of BIO-PMs. In future experiments it will be important to assess whether PMs can accumulate at the bone fracture site even in the presence of a pre-existing inflammation, for example using aged mice of mouse models of chronic inflammation (Jurk et al. 2014). Moreover, it would be fundamental to investigate whether BIO-PMs promote bone healing in a different type of bone injury such as following the creation of either a critical size defect, which will not heal physiologically, or a segmental defect, which would require bone fragments fixation, and it is more likely to represent a type of fracture that would result in a non-union.

It was demonstrated that DiR-PMs and free DiR have a different distribution, with PMs localising preferentially in the fractured area and free dye accumulating in the liver and spleen (Figure 5.15). Direct comparison between DiR-PMs and DiR is possible, but should be carefully considered because the two have very different physical-chemical characteristics. Very few drugs currently available are as insoluble in water as DiR, therefore drawing any translational conclusion from this experiment would be premature. However, it is possible that a given drug is less affected by the ELVIS mechanism when in its un-encapsulated form than when loaded in PMs. This then becomes very attractive for therapeutic purposes as it may result in reduced 'off-site' effects and increased concentration at the target tissue. Nevertheless, encapsulation of molecules within PMs does not totally preclude 'off-site' effects in the liver and spleen, as PMs accumulates in these organs (Figure 5.3), but as shown earlier in the chapter the use of PEG-PCL PMs did not induce hepatotoxicity (Figure 5.12), in accordance with previous findings (Buckiova et al. 2012). Further experiments aimed to assess whether administering a range of PMs does would result in a different biodistribution of the nanoparticles would be interesting (Panagi et al. 2001). Also, investigation of PMs distribution *in vivo* using IVIS should take into consideration the different depth of the organs imaged. Therefore, in future experiments it would be sensible to couple whole body imaging with analysis of intensity and pattern of fluorescence in excised organs.

The final set of experiments presented aimed to assess the effects of BIO-PMs treatment on bone fracture repair. Although the difference was not statistically significant, an increase in both tissue volume and bone volume following systemic treatment with BIO-PMs compared to the other treatments was observed, particularly after 14 days (Figure 5.17 and Figure 5.18). This study can be considered preliminary, given the small subject number, but permits interesting speculations and provides an insight to future scenarios. As no report regarding the use of Wnt agonists-loaded PMs for bone fracture regeneration is present in the literature, it is difficult to directly compare findings from previously published studies. Minear and colleagues reported enhanced bone regeneration in mice following local treatment with liposomes carrying Wnt3A proteins (Minear et al. 2010). This raises the possibility that local administration of BIO-PM could be more efficacious than the systemic route chosen, but PMs were injected i.v. since it has been demonstrated that the disruption of the haematoma microenvironment with impairs bone healing (Kolar et al. 2010; Park et al. 2002). Additionally, from a clinical perspective, local injection in deep tissues requires the use of additional imaging techniques, in order to achieve precise administration at the injury site, an issue which is significant in the case of multiple fractures. On the other hand, PMs are likely be influenced by the ELVIS effect as well; therefore, the body's own response could be harnessed for a more efficacious targeting. Nevertheless, local administration would probably result in a higher concentration of PMs *per* area of tissue, potentially enhancing the beneficial effects on bone healing observed with BIO-PMs. Therefore, a comparison between the two administration routes would be needed in order to determine relative efficacy of the treatments. A systemic injection has inherent increased risk of 'off-sites' effects compared to local injections. Low and colleagues demonstrated that micellar formulations of BIO administered systemically have a different spatial distribution compared to free BIO, with the micelles being almost 2 fold more concentrated in the fractured bone compared to free drug. The authors did not assess the effect of the treatment on bone healing, but reported accumulation of both BIO-micelles and free BIO in the liver (Low et al. 2015). Accumulation of DiR-PMs in the liver was also observed in this project (Figure 5.12), so it is plausible to speculate that both BIO-PMs and free BIO had accumulated in the liver. Due to time constrictions, histopathological examinations of explanted tissues (*i.e.* liver, spleen, kidneys) was not performed, but it will be important future work in order to determine 'off-site' effects as well as differences between BIO-PMs and free BIO

treatments. Also, the use of transgenic Wnt reporter mice, such as those expressing GFP or LacZ under the control of Axin2 (Jho et al. 2002; Minear et al. 2010), could allow for the identification of the areas subject to Wnt signalling activation and would allow for a better understanding of the spatial localisation of the treatments.

Knowing that the effect that Wnt signalling has on haematopoiesis (Sturgeon et al. 2014), angiogenesis (Min et al. 2011) and SSCs differentiation (Janeczek et al. 2016) differs depending on the timing at which it is activated and its extent in time, and considering the prolonged presence of PMs in the injured area (Figure 5.8), future experiments would aim to discern more specifically the effects of BIO-PMs or free BIO, or other Wnt modulators in the injured area. For example, cellular proliferation or alteration of the cell surface markers in different cell types could be assessed by FACS or image stream. The effects on angiogenesis could be investigated through the use of μ-CT and vascular filler that highlights the presence of blood vessels (Kumar et al. 2010). Furthermore, having confirmed the accumulation of PMs at the fracture site even after 1 or 2 weeks from the creation of the bone injury, multiple and sequential administrations of BIO-PMs could be explored as an avenue that may increase the therapeutic effects of the treatment.

In summary, assuming that the DiR fluorescence is directly related to the physical presence of PMs in the same area, this chapter has demonstrated that PMs accumulate at the bone fracture within 24 hours from the systemic injection. The mechanism behind this passive accumulation could be due to the ELVIS effect, but will be subject of further studies. No firm conclusions could be drawn from the use of BIO-PMs to promote bone regeneration, but the results obtained show promise and will be further investigated.

Chapter 6: General discussion

6.1 Summary of the main findings of the study

Bone fractures represent a socio-economic burden, yet effective systemic treatments aimed to promote and expedite fracture healing are still lacking. In this context, the Wnt signalling pathway is a potential pharmacological target, but its modulation has to be spatially and temporally controlled. In order to achieve such control, the use of polymersomes (PMs) as a drug delivery controlled system was investigated. This study set out to determine whether PMs could function as a delivery system for agents that can activate the Wnt pathway in order to enhancing bone healing.

This investigation started with the experiments presented in **Chapter 3**, which tested the **hypothesis** that *PMs can deliver a model hydrophilic cargo to different cell types, and the number of PMs releasing payload intracellularly can be quantified on a single-cell level.* In order to do so, the **main aim** was to produce PMs loaded with fluorescein, and use them for the qualitative and quantitative assessment of intracellular payload delivery. The results presented have shown that PMs produced by nanoprecipitation can encapsulate and retain high concentrations of fluorescein. Upon encapsulation, fluorescein fluorescence was self-quenched and was detectable only following release from PMs. Therefore, fluorescein-PMs were used as system for real-time detection of PMs internalisation and intracellular payload release by different mammalian cells, ranging from a simple murine fibroblasts cell line to human bone marrow stromal cells (BMSCs). Using fluorescence microscopy and flow cytometry it was demonstrated that fluorescein-PMs are readily internalised by cells and that uptake is time-dependent, but saturation is observed 6 hours post initial incubation. The internalisation of fluorescein-PMs did not induce significant cytotoxicity in any of the cell types investigated and intracellular delivery of fluorescein was also achieved in both adherent and suspension cultured cells. Additionally, after incubation with freshly isolated human bone marrow mononuclear cells BMMNCs, fluorescein-PMs were taken up by granulocytes and monocytes, as well as skeletal stem cells (SSCs). This result was explored confirmed by imaging flow cytometry, which also provided preliminary information regarding the mechanism of uptake of PMs. Finally, the quantification of intracellular payload release from PMs at a single-cell level has been demonstrated for the first time.

The findings presented in Chapter 3 provided the basis for formulating the experimental **hypothesis** in **Chapter 4**: *PMs loaded with the Wnt agonist BIO can activate the*

Wnt pathway in a controlled manner and promote osteogenic differentiation of SSCs. The **main aim** was to produce PMs loaded with the Wnt signalling agonist BIO, to assess their ability to activate the Wnt pathway, and to prime osteogenic commitment of SSCs. The results have shown that PMs can be loaded with BIO and this is stably encapsulated, as demonstrated by the retention of activity following 36 hours of dialysis or after ultracentrifugation. Using Wnt reporter cells it was demonstrated that BIO-PMs activate the pathway and, regardless of the concentration used, they do not induce cytotoxicity, which is in striking contrast to the cell death observed after incubation with free BIO. BIO-PMs induced a sustained activation of the Wnt pathway, which after 48 hours incubation was significantly higher than that measured after free BIO. Finally, gene expression analysis demonstrated that BIO-PMs significantly up-regulated the expression of the Wnt target gene *AXIN-2* and the early markers of osteogenic commitment *RUNX2* and *SP7* in BMSCs. Overall, these results suggest that BIO-PMs activate the Wnt signalling pathway in BMSCs, priming their differentiation towards the osteoblastic phenotype.

In order to explore the potential of BIO-PMs for bone repair *in vivo,* in **Chapter 5** the following two-fold **hypothesis** was tested**:** *following systemic injection in a bone injured mouse, PMs accumulate at the fracture site and, when loaded with BIO, can promote bone fracture healing*. In order to do so, the **main aims** were to investigate the accumulation of PMs into the fracture site upon systemic injection, and to assess the effects on bone fracture healing of a single systemic administration of BIO-PMs. The results confirmed that PMs administered *via* the tail-vein in healthy mice are visible by IVIS and accumulate in the region of the liver. However, when administered in mice carrying a unilateral hind-limb bone defect, the majority of PMs were observed in the injured bone. Histological examination of femurs explanted 7 days after injection confirmed the presence of the dye originally loaded in the nanoparticles within the tissue. On the other hand, un-encapsulated fluorescent dye DiR injected systemically in injured mice was mainly observed in the liver and spleen. These results indicated that a compound administered systemically distributes differently *in vivo* depending on whether or not it is encapsulated within PMs. Finally, in a preliminary study investigating bone healing using μ-CT analysis, it was shown that the systemic administration of BIO-PMs has the potential to stimulate and expedite bone mineralisation following injury.

6.2 Relevance of the findings, limitations and future opportunities

One of the most exciting and promising achievements of this project was the establishment of fluorescein-PMs as a system for quantifying the concentration of payload released intracellularly. Surprisingly, considering the continuous progress in establishing nanoparticles as drug delivery systems, the field is still lacking in basic pharmacological information as to where, when and how much of a payload has been delivered using nanoparticles. This knowledge gap is a challenge to the safety requirements that need to be met for the translation and subsequent clinical application of all medical devices and drugs, including nanomedicines. The current paucity of information regarding the number of nanoparticles internalised at a single cell level and, therefore, the concentration of payload released is a limitation in the use of PMs. This is despite the increasing evidence from *in vivo* studies that delivery using polymeric nanoparticle preparations has clear advantages over the administration of free, un-encapsulated drugs (Xin et al. 2011). Results reported in this thesis demonstrate real-time delivery of a hydrophilic compound in different mammalian cell types, and quantified for the first time the intracellular release of a fluorophore from a hollow polymeric nanocarrier at a single cell level. This result is of great significance as it provides novel and highly relevant information to the research field (Figure 6.1). Furthermore, this quantification system could be applied to the investigation of payload delivery in mixed cell types, or to assess how drugs are re-distributed among cells following replication (Summers et al. 2013). However, the properties of fluorescein pose a **limitation** since it is a hydrophilic molecule, and thus represents only a small sub-set of the pharmaceutical molecules currently investigated or used in clinic (Mitragotri et al. 2014). As such, the quantification of intracellular payload release measured using fluorescein-PMs will have limited translation as other molecules, with higher lipophilicity, will likely distribute and partition differently inside the cells.

Given this, **future experiments** could aim: (I) to test different molecules that are still suitable for real-time investigation of payload release, but also have more clinically relevant physical-chemical properties; (II) to assess intracellular partitioning of two different cargos originally encapsulated within the same PMs; (III) to determine the amount of payload delivered in a specific tissue *in vivo* by further exploiting the quantification methodology proposed in this thesis. These experiments would provide

valuable basic information regarding the kinetics of payload release – information that is much needed in order to bridge the gap separating PMs from clinical applications.

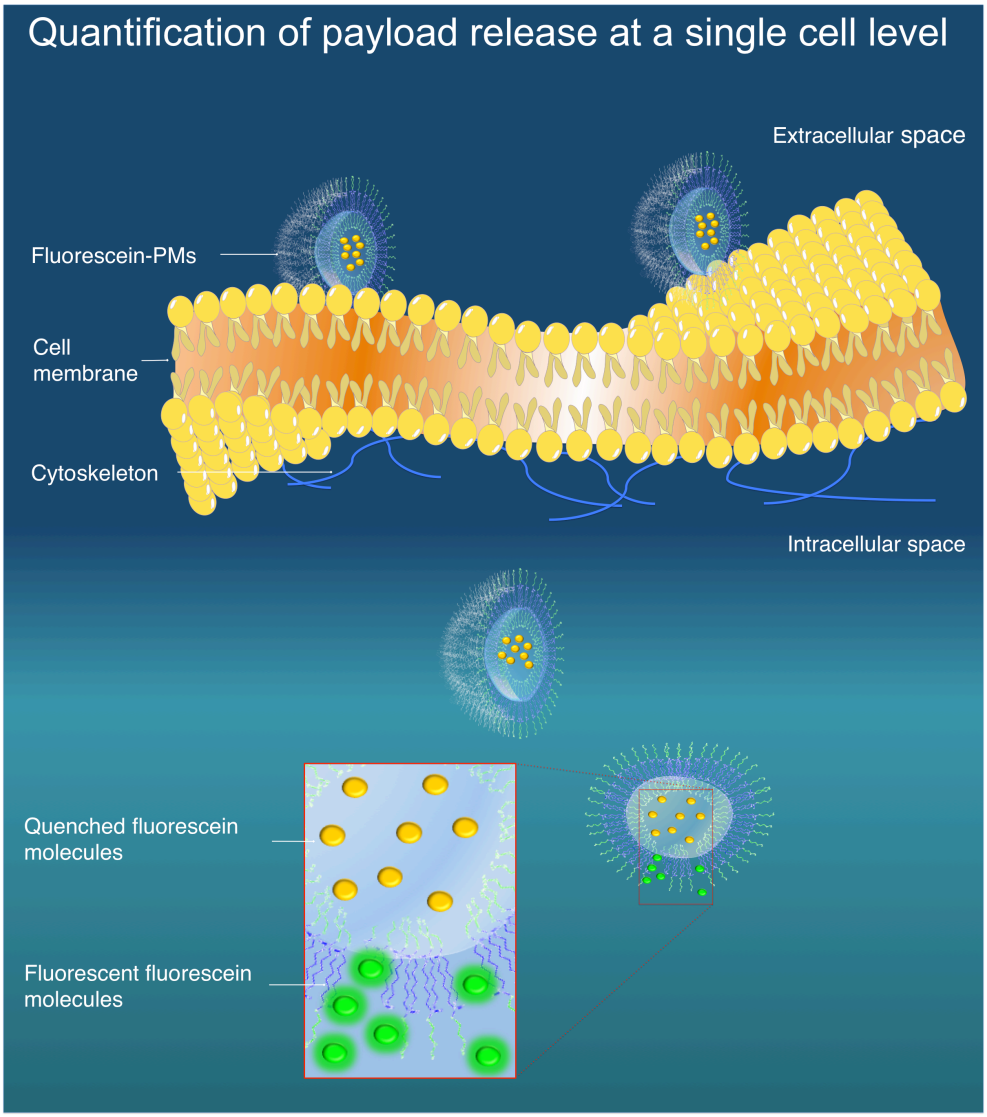

Figure 6.1: **Quantification of intracellular payload released from PMs.**

One of the novelties reported in this project is the methodology for quantifying the amount of payload delivered intracellularly by PMs at a single-cell level.

In Chapter 4, it was demonstrated that PMs could be loaded with BIO and induce significant activation of the Wnt signalling pathway following incubation with either reporter cells or BMSCs. There has not been previous research demonstrating the encapsulation of a GSK-3β inhibitor in PMs, making the results here especially novel.

The crucial role of the Wnt signalling pathway in bone physiology is well known and widely investigated (see section 1.4). Importantly, its pharmacological modulation offers a new and exciting prospect for a range of diseases from osteoporosis to fracture healing (see section 1.5). For example, monoclonal antibodies targeting specific molecules of the Wnt pathway, such as the inhibitors sclerostin and DKK1, have been investigated for improving fracture healing (Einhorn & Gerstenfeld 2015) and showed promising results in mice (Alzahrani et al. 2016) and rats (Liu et al. 2016). However, the use of monoclonal antibodies is limited by inherent high costs of production, poor control over their spatial and temporal activity, and safety concerns regarding possible immunological reactions following their administration. Despite the progress made in the production of antibodies for therapy, humanised and fully human antibodies maintain a degree of immunogenicity that hinder their application (Harding et al. 2010).

Proteins and small molecules agonist of the Wnt pathway are alternatives to the use of antibodies. However, proteins have also high costs of purification and production, whilst a variety of small molecules are commercially available at low costs and represent an attractive option (Rey & Ellies 2010). The activation of the Wnt pathway can be modulated using synthetic small molecules that inhibit the activity of GSK-3β, a kinase involved in the physiological degradation of the intracellular Wnt signalling transducer, β-catenin (see section 1.3.1).

Over the years, several inhibitors of GSK-3β have been shown to have a major impact on the bone tissue. For example a study in rats demonstrated that daily administration of AZD2858, a small molecule inhibiting GSK-3β, induces a dose-dependent increase in trabecular bone mass, while enhancing the overall biomechanical properties of the bone formed (Marsell et al. 2012). Moreover, the same regimen of administration in animal models of bone fracture resulted in a faster healing compared to controls (Sisask et al. 2013). Other studies have reported similar findings using lithium as an inhibitor of GSK-3β, showing increased bone formation and bone mass in mice (Clement-Lacroix et al. 2005), and augmented bone healing after fracture (Chen et al. 2007). With particular focus on fracture healing, Chen and colleagues reported that β-catenin is highly expressed during the entire reparative process, but the stimulation of the Wnt pathway has different effects depending on the timing of its activation.

Consequently, the authors suggested that bone repair could be improved using lithium only when this is administered at latest stages of repair (Chen et al. 2007).

The timing of activation of the Wnt pathway seems to be a fundamental aspect to be considered. Previous work performed in our group using Wnt proteins demonstrated that a transient activation of the Wnt pathway promotes osteogenic differentiation of SSCs, while a prolonged stimulation induces the opposite effect, inhibiting osteo-differentiation (Janeczek et al. 2016). These results were in agreement with previous finding from Kim and colleagues who reported the inhibition of bone regeneration as a consequence of a constitutive activation of the Wnt pathway (Kim et al. 2007). Thus, there are a number of observations that suggest a short stimulation of the Wnt pathway may be beneficial for bone healing, but there are some contrasting findings regarding the daily use of GSK-3β inhibitors such as the ones previously described by Marsell and colleagues and Sisask and colleagues (Marsell et al. 2012; Sisask et al. 2013). Data present in the literature indicate that the Wnt signalling pathway could be used to promote bone healing, but the timing and method of the activation, extracellular (*e.g.* Wnt proteins of monoclonal antibodies) or intracellular (*e.g.* small molecules), have a great influence on the final regenerative outcome and therefore should be carefully considered.

The latter point in particular is very relevant to this project, as it demonstrates that the use of BIO-PMs could promote bone healing. However, in order to use GSK-3β inhibitors as bone anabolic treatments, a better understanding of both the optimal dose and timing of administration is still required (Gambardella et al. 2011). A major **limitation** of the study presented is the use of BIO as an agonist of the Wnt signalling pathway. BIO is a potent inhibitor of GSK-3β, but may not be the most suitable for this specific application due to its off-target effects on several cyclins and protein kinases (Meijer et al. 2003). Non-ATP-competitive molecules may have increased selectivity for GSK-3β since they bind outside of the ATP pocket, and therefore a reduced IC_{50}, and as a result they may be less cytotoxic (Eldar-Finkelman & Martinez 2011). **Future experiments** should be performed in order to find the most suitable Wnt agonist small molecule for enhancing bone regeneration. Nonetheless, this study has demonstrated that PMs can function as an intracellular delivery system for the inhibition of GSK-3β, and this opens to new and exciting perspectives for creating new potential therapies for different diseases.

GSK-3β is involved in numerous physiological intracellular processes but also in a range of diseases, which makes it a lucrative target for new therapies (Phukan et al. 2010). Inhibition of GSK-3β has been shown to promote proliferation of human insulin producing cells (Shen et al. 2015) and to stimulate regeneration in pancreatectomised rats (Figeac et al. 2012). This makes the use of PMs loaded with GSK-3β inhibitors a possible new strategy for treating diabetes and pancreatitis. Furthermore, GSK-3β is also involved in the onset and progression of the Alzheimer's disease (AD), as its uncontrolled activation leads to memory loss, tau protein hyper-phosphorylation and β-amyloid production (Hooper et al. 1991). As a consequence, another small molecule inhibitor of GSK-3β, Tideglusib (also known as NP-12 or NP031112), has been investigated as a potential treatment for this type of dementia and reached phase II of clinical trials (Lovestone et al. 2015). However, these preliminary studies concluded that Tideglusib was efficacious only on small sub-groups of patients, its pharmacological action was nonlinear since lower concentration were more beneficial than higher, and side effects were reported in almost 20% of the cases (Lovestone et al. 2015). These results raise the question as to whether encapsulating the molecules within a carrier would be more beneficial than administration in its free form as it would provide a more controlled inhibition of GSK-3β. This kinase is involved in various processes within the central nervous system including the function of cortical neurons and the development of neuronal terminations (Kremer et al. 2011). The blood brain barrier (BBB) is poorly permeable to nanocarriers; however, nanoparticles surface can be decorated with binding moieties such as Angiopep-2, which is a ligand of the low-density lipoprotein receptor-related protein (LRP) that is also a receptor of the Wnt pathway, and has been shown to greatly favour accumulation in the brain (Xin et al. 2011). Also, the AD is has been described as a glial process indicative on-going brain inflammation (Jaworski et al. 2010), this increases the permeability of the BBB (Rosenberg 2014) and may be exploited for inducing accumulation of PMs in the inflamed tissue through the extravasation through leaky vasculature and inflammatory cell-mediated sequestration (ELVIS) effect. This controlled inhibition of GSK-3β using PMs could represent a novel therapy for treatment of the AD.

A number of other natural and synthetic GSK-3 inhibitors are being tested in preclinical studies, demonstrating the therapeutic potential of these molecules for

different diseases (Eldar-Finkelman & Martinez 2011). However, the highly ubiquitous role of GSK-3β raises concern about its uncontrolled inhibition and regarding the oncogenic potential of molecules inhibiting its function. In fact, uncontrolled inhibition of GSK-3β would lead to the dephosphorylation and consequent accumulation of proto-oncogenes such as c-MYC and c-JUN (Cohen & Goedert 2004). In this context, if the therapeutic potential of GSK-3β inhibition is to be explored, the spatio-temporal control of these inhibitors is needed, and PMs may be the most suitable candidate for exerting such control.

Alternatively, rather than using intracellular active molecules, PMs could be employed to deliver extracellular agonists of the Wnt pathway. This approach may seem counterintuitive, as one would expect the use of nanoparticles exclusively for the precise intracellular delivery of payload; however, by accumulating within a target tissue, as demonstrated in Chapter 5 of this project, PMs could function as a concentrated depot of signalling molecules or source of induction of signalling molecules. In particular, PMs are very modifiable nanocarriers, whose surface could easily be tethered with numerous bone targeting motifs (reviewed by (Low & Kopeček 2012), but also Wnt agonists. For example, DKK-1, SOST or Sfrp-1 are all endogenous extracellular inhibitors of the Wnt pathway that could be antagonised by monoclonal antibodies- or aptamer-functionalised PMs. Similar strategy has been used in cancer research decorating the surface of nanoparticles with motifs that bind matrix metalloproteinases, which are enzymes responsible for remodelling the extracellular matrix and are an attractive chemotherapeutic target (Cathcart et al. 2015). Tethering the nanoparticle surface with antibodies or aptamers would provide an exquisite control over the lifetime, concentration, spatial location and duration of the Wnt activation, which is currently not achievable through immunotherapy (Kahn 2014), but it would results in other limitations. Targeting motifs should be non-cytotoxic, resilient to conjugation methodologies and stable in a biological context (Mout et al. 2012). Most importantly, nanoparticle surface undergoes critical modifications once in contact with serum proteins (Lynch et al. 2009). Salvati and colleagues demonstrated that silica nanoparticles conjugated with transferrin, a glycoprotein that binds transferrin receptor which is highly expressed in cancer, lose their targeting ability following dispersion in biological fluids as a consequence of unspecific protein adsorption (Salvati et al. 2013). Despite these limitations, nanoparticle

functionalization still remains an intriguing option and **future experiments** could be focused on assessing the functionality of PMs conjugated with Wnt signalling agonists.

The results reported in Chapter 5 support of these exciting future perspectives of spatio-temporal controlled delivery using PMs. To the best of our knowledge, this was the first study to demonstrate the accumulation of PMs in injured bone tissue following systemic administration (Figure 5.8). The current findings add to a growing body of literature reporting the preferential localisation of macromolecules and prodrugs in bone fractures following systemic injection (see section 5.1). Furthermore, the present study makes a noteworthy contribution as it demonstrates that PMs also accumulate in the fractured bone when administered immediately after injury creation, which represents another, unreported, novelty. This is a clinically relevant finding as treatment of the early stages of bone fracture may be an original and unexplored approach. The early intervention following tissue injury is fundamental in case of vascular damage or acute stroke. Recently, Korin and colleagues have taken advantage of the shear stress created by vascular occlusion in thrombosis or embolism, to target the accumulation of microscale aggregates of nanoparticles coated with plasminogen activator. These aggregates undergo physical dissociation due to the high shear stress in the injured area and would induce the rapid clot dissolution following systemic injection (Korin et al. 2012). Despite being clinically relevant, the results presented in Chapter 5 of this thesis are **limited** by the investigation of a single time-point of administration. The activation of Wnt signalling immediately after bone fracture may not be the most appropriate time in order to promote bone formation, therefore **future experiments** should focus on investigating PMs distribution following administration at different time-points following fracture. Nevertheless, the localisation of PMs in the injured bone after administration add to previous studies demonstrating the accumulation of prodrugs into the fracture site, when injected systemically 7 or 14 days after the creation of the bone fracture (Jia et al. 2015; Low et al. 2015).

A key theoretical implication of these studies is that a therapeutic window exists, spanning for at least 2 weeks from the original injury, which could be exploited to deliver a number of molecules enhancing bone regeneration. For example, the first stage of bone healing is characterised by acute inflammation, which is characterised by the extravasation of polymorphonuclear neutrophils into the injured tissue (see section 1.2.3.1). The role of

these cells during fracture healing is unclear, but it is known that they are recruited by cellular debris formed as consequence of the injury (Chung et al. 2006) and, among other activities, they produce cytokines that attract macrophages (Bastian et al. 2011; Bastian et al. 2016). Neutrophils should be cleared from the haematoma within 24 hours (Andrew et al. 1994), but once primed by the presence of high concentrations of IL-8 or TNF-α they can persist in the injury site for longer. Previous evidence demonstrated that the high presence of neutrophils in the haematoma has the potential to impair bone healing (Grøgaard et al. 1990) and promote the onset of chronic inflammation (reviewed by Bastian et al. 2011). These data suggest that bone healing is achieved when the inflammation is controlled and resolves in a relatively short time frame. To this end, nanoparticles could be used in order to reverse eventual excess of inflammation. Within the inflamed tissue, the production and release of endogenous specialised pro-resolving lipid mediators (SPMs) initiates the end of the acute inflammatory response (Serhan & Savill 2005). Recent work has shown that polymeric nanoparticles delivering SPMs could limit the recruitment of polymorphonuclear neutrophils in inflamed tissues (Kamaly et al. 2013), and had a protective effect against advanced atherosclerosis (Fredman et al. 2015). The spatio-temporal controlled delivery of SPMs could be investigated for promoting bone healing, especially in patients with chronic inflammation. This approach could also be coupled with the subsequent administration of PMs loaded with a Wnt agonist 3/4 days following fracture, in order to induce the proliferation and osteogenic differentiation of SSCs migrating into the injured tissue. Furthermore, the accumulation of PMs in the fractured bone 14 days after injury could be exploited for the delivery of bone anabolic agents such as bisphosphonates, BMPs or teriparatide, which is a recombinant form of PTH. Although the efficacy of these molecules during fracture healing is uncertain (Goldhahn et al. 2012), it could be speculated that, if delivered at the correct time, these molecules might enhance bone healing.

Non-healing fractures are observed in in 5 to 10% of the cases, but represent a burden to the UK economy costing millions of pounds every year (see section 1.2). It is known that comorbidities (*e.g.* diabetes, vascular diseases, malnutrition) can hinder bone healing (Gaston & Simpson 2007), but currently there is no a reliable way to predict the positive or negative outcome of a bone fracture. However, the increased knowledge of the molecular mechanisms behind a number of pathologies may aid our understanding as to why different patients respond differently to the same pharmacological treatment;

therefore the paradigm 'one disease-one therapy' is regarded by most as a overgeneralisation. This provides the basis for a more stratified therapeutic approach, whereby a personalised therapy is assigned to a patient according to assessments of clinical biomarkers (Trusheim et al. 2007). In this context, nanoparticles could be used as theranostic system, which means that they could serve as a combined therapeutic and diagnostic agent, uncovering potential patient-specific limitations in their regenerative potential. Moreover, theranostic nanoparticles could help to overcome a current limitation to the use of nanoparticles, the off-target drug delivery. In fact, despite the increasing success in localising PMs delivery to specific targets, off-target delivery still occurs (Petros & DeSimone 2010), and defined strategies for assessing the effects of off-target delivery are lacking. In a recent study, Kulkarni and colleagues created a reporter nanoparticle loaded with an effector element, which was a chemotherapy agent, and a reporter element, fluorescent molecule and quencher. Using this system the authors demonstrated the delivery of anticancer treatment to the tumour and the simultaneous monitoring of the effects mediated by such delivery (Kulkarni et al. 2016).

A theranostic nanoparticle could also be functional in bone fracture healing not only for determining real-time delivery and functionality of the system, but also for the early diagnosis of non-union fractures as they would serve as reported of impaired healing. For example, the local and systemic level of some biological markers such as FGF-2 (Granchi et al. 2013) or TGF-β1 (Sarahrudi et al. 2011) have been proposed to be predictors of non-union fractures (Reviewed by Pountos et al. 2013). 'Key-lock' nanoparticles that release a fluorescent and a therapeutic compound in response to altered concentrations of these biological markers could be produced. This would require the design of sophisticated nanoparticles, whereby the molecular marker would act as key for the release of the payloads within PMs, which would act as the lock. Douglas and colleagues used a similar strategy with DNA origami and demonstrated compelling results *in vitro* (Douglas et al. 2009). However, adding functionality to PMs has a marked trade-off. The increasing complexity of the nanoparticle design increases the steps required for the synthesis, and may also condition their safety approval and consequent clinical translation. Nevertheless, the use of PMs provides an exciting new strategy and represents the near future of pharmacology.

6.3 Conclusions

This is the first reported investigation on the potential of PMs for the spatio-temporal controlled delivery of Wnt agonists for bone regeneration. The experiments described in this thesis demonstrate that PMs function as intracellular drug delivery system, even in a rare population of stem cells within the bone marrow, and when loaded with a Wnt agonist, PMs can prime osteogenic differentiation of these SSCs. Importantly, *in vivo* work showed that PMs accumulate at the fracture site post injury. Overall, this study demonstrates that PMs could be exploited as a new systemic treatment for enhancing bone healing after fracture (Figure 6.2).

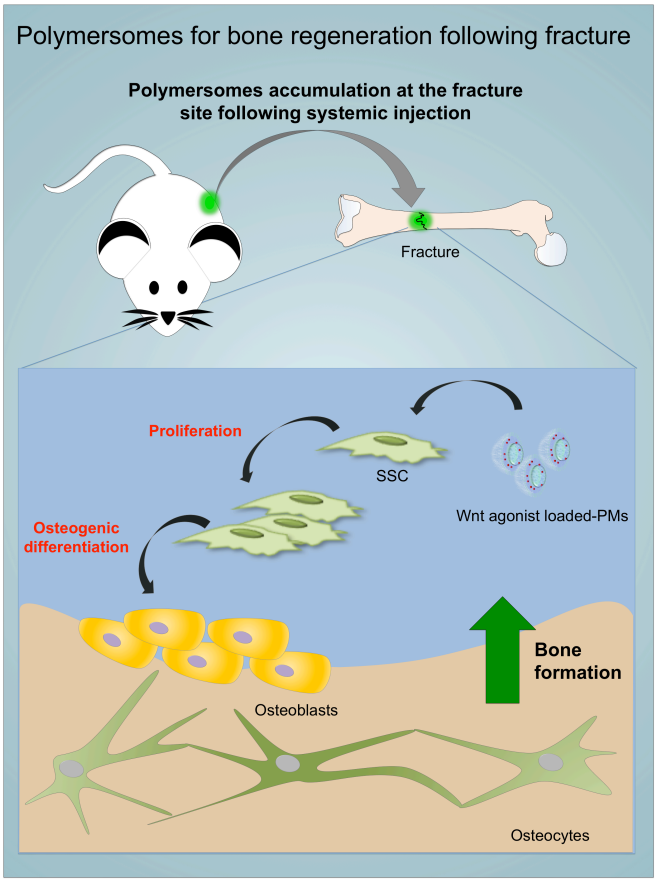

Figure 6.2: **Polymersomes for bone regeneration.**

Graphical representation of the potential use of PMs for the spatio-temporally controlled delivery of Wnt agonists to the bone fracture in order to promote bone healing.

References

Abuchowski, A., van Es, T., et al., 1977. Alteration of immunological properties of bovine serum albumin by covalent attachment of polyethylene glycol. *Journal of Biological Chemstry*, 252(11), pp.3578–3581.

Abuchowski, A., McCoy, J.R., et al., 1977. Effect of covalent attachment of polyethylene glycol on immunogenicity and circulating life of bovine liver catalase. *Journal of Biologycal Chemstry*, 252(11), pp.3582–3586.

Adler, C.P., 1989. [Pathologic bone fractures: definition and classification]. *Langenbecks Archiv für Chirurgie. Supplement II, Verhandlungen der Deutschen Gesellschaft für Chirurgie. Deutsche Gesellschaft für Chirurgie. Kongress*, pp.479–86.

Afergan, E. et al., 2008. Delivery of serotonin to the brain by monocytes following phagocytosis of liposomes. *Journal of Controlled Release*, 132(2), pp.84–90.

Agholme, F. et al., 2010. Sclerostin antibody treatment enhances metaphyseal bone healing in rats. *J Bone Miner Res*, 25(11), pp.2412–2418.

Ahmad, Z. et al., 2014. Polymeric micelles as drug delivery vehicles. *RSC Advances*, 4(33), pp.141–17038.

Ahmed, F. et al., 2006. Biodegradable polymersomes loaded with both paclitaxel and doxorubicin permeate and shrink tumors, inducing apoptosis in proportion to accumulated drug. *Journal of Control Release*, 116(2), pp.150–158.

Ahmed, F. & Discher, D.E., 2004. Self-porating polymersomes of PEG-PLA and PEG-PCL: hydrolysis-triggered controlled release vesicles. *Journal of Control Release*, 96(1), pp.37–53.

Alam, S. et al., 2009. Statin-induced bone morphogenetic protein (BMP) 2 expression during bone regeneration: an immunohistochemical study. *Oral surgery, oral medicine, oral pathology, oral radiology, and endodontics*, 107(1), pp.22–9.

Alexis, F. et al., 2008. Factors affecting the clearance and biodistribution of polymeric nanoparticles. In *Molecular Pharmaceutics*. pp. 505–515.

Almeida, A.J. & Souto, E., 2007. Solid lipid nanoparticles as a drug delivery system for

peptides and proteins. *Advanced drug delivery reviews*, 59(6), pp.478–90.

Alzahrani, M.M., Rauch, F. & Hamdy, R.C., 2016. Does Sclerostin Depletion Stimulate Fracture Healing in a Mouse Model? *Clinical Orthopaedics and Related Research®*, 474(5), pp.1294–1302.

Andrew, J.G. et al., 1994. Inflammatory cells in normal human fracture healing. *Acta Orthopaedica Scandinavica*, 65(4), pp.462-6.

Anselmo, A.C. & Mitragotri, S., 2014. Cell-mediated delivery of nanoparticles: Taking advantage of circulatory cells to target nanoparticles. *Journal of Controlled Release*, 190, pp.531–541.

Arioka, M. et al., 2013. Acceleration of bone development and regeneration through the Wnt/beta-catenin signaling pathway in mice heterozygously deficient for GSK-3beta. *Biochem Biophys Res Commun*, 440(4), pp.677–682.

Aro, H.T. et al., 2011. Recombinant human bone morphogenetic protein-2: a randomized trial in open tibial fractures treated with reamed nail fixation. *The Journal of Bone and Joint Surgery*, 93(9), pp.801–8.

Aspenberg, P. et al., 2008. Additive effects of PTH and bisphosphonates on the bone healing response to metaphyseal implants in rats. *Acta Orthopedica*, 79(1), pp.111–115.

Aspenberg, P., 2005. Drugs and fracture repair. *Acta Orthopedica*, 76(6), pp.741–748.

Aspenberg, P. et al., 2010. Teriparatide for acceleration of fracture repair in humans: a prospective, randomized, double-blind study of 102 postmenopausal women with distal radial fractures. *Journal of Bone and Mineral Research*, 25(2), pp.404–14.

Axelrad, T.W. et al., 2008. Heterotopic ossification after the use of commercially available recombinant human bone morphogenetic proteins in four patients. *The Journal of Bone and Joint Surgery*, 90(12), pp.1617–22.

Babij, P. et al., 2003. High bone mass in mice expressing a mutant LRP5 gene. *Journal of Bone and Mineral Research*, 18(6), pp.960–974.

Baksh, D. & Tuan, R.S., 2007. Canonical and non-canonical Wnts differentially affect the development potential of primary isolate of human bone marrow mesenchymal stem cells. *Journal of Cell Physiology*, 212(3), pp.817–826.

Bangham, A.D. & Horne, R.W., 1964. Negative staining of phospholipids and their structural modification by surface-active agents as observed in the electron microscope. *Journal of Molecular Biology*, 8(5), pp.660-668.

Baron, R. & Kneissel, M., 2013. WNT signaling in bone homeostasis and disease: from human mutations to treatments. *Nature Medicine*, 19(2), pp.179–192.

Bastian, O. et al., 2011. Systemic inflammation and fracture healing. *Journal of leukocyte biology*, 89(5), pp.669–673.

Bastian, O.W. et al., 2016. Neutrophils contribute to fracture healing by synthesizing fibronectin+ extracellular matrix rapidly after injury. *Clinical Immunology*, 164, pp.78–84.

Battaglia, G. & Ryan, A.J., 2005. Bilayers and Interdigitation in Block Copolymer Vesicles. *Journal of the American Chemical Society*, 127(24), pp.8757–8764.

Bennett, C.N. et al., 2005. Regulation of osteoblastogenesis and bone mass by Wnt10b. *Proc Natl Acad Sci U S A*, 102(9), pp.3324–3329.

Bermudez, H. et al., 2002. Molecular Weight Dependence of Polymersome Membrane Structure, Elasticity, and Stability. *Macromolecules*, 35(21), pp.8203–8208.

Bertrand, N. & Leroux, J.C., 2012. The journey of a drug-carrier in the body: An anatomo-physiological perspective. *Journal of Controlled Release*, 161(2), pp.152–163.

Bhandari, M. et al., 2003. Predictors of reoperation following operative management of fractures of the tibial shaft. *Journal of Orthopaedic Trauma*, 17(5), pp.353–61.

Bi, H. et al., 2013. Electroformation of giant unilamellar vesicles using interdigitated ITO electrodes. *J. Mater. Chem. A*, 1(24), p.7125.

Bianco, P., 2014. "Mesenchymal" Stem Cells. *Annu Rev Cell Dev Biol*, 30, pp.677-704.

Bianco, P. et al., 2013. The meaning, the sense and the significance: translating the science of mesenchymal stem cells into medicine. *Nature Medicine*, 19(1), pp.35–42.

Blanazs, A., Armes, S.P. & Ryan, A.J., 2009. Self-Assembled Block Copolymer Aggregates: From Micelles to Vesicles and their Biological Applications. *Macromolecular Rapid Communications*, 30(4–5), pp.267–77.

Le Blanc, K. & Mougiakakos, D., 2012. Multipotent mesenchymal stromal cells and the

innate immune system. *Nature Reviews Immunology*, 12(5), pp.383–396.

Bleul, R., Thiermann, R. & Maskos, M., 2015. Techniques To Control Polymersome Size. *Macromolecules*, 48(20), pp.7396–7409.

Bodine, P.V.N. et al., 2009. A small molecule inhibitor of the Wnt antagonist secreted frizzled-related protein-1 stimulates bone formation. *Bone*, 44(6), pp.1063–1068.

de Boer, J. et al., 2004. Wnt signaling inhibits osteogenic differentiation of human mesenchymal stem cells. *Bone*, 34(5), pp.818–826.

Boland, G.M. et al., 2004. Wnt 3a promotes proliferation and suppresses osteogenic differentiation of adult human mesenchymal stem cells. *Journal of Cellular Biochemistry*, 93(6), pp.1210–1230.

Boyden, L.M. et al., 2002. High Bone Density Due to a Mutation in LDL-Receptor–Related Protein 5. *New England Journal of Medicine*, 346(20), pp.1513–1521.

Böyum, A., 1968. Isolation of mononuclear cells and granulocytes from human blood. Isolation of monuclear cells by one centrifugation, and of granulocytes by combining centrifugation and sedimentation at 1 g. *Scandinavian Journal of Clinical and Laboratory Investigation. Supplementum*, 97, pp.77–89.

BRIGHTON, C.T. & KREBS, A.G., 1972. Oxygen Tension of Healing Fractures in the Rabbit. *The Journal of Bone & Joint Surgery*, 54(2), pp.323–332.

Brighton, C.T. & Krebs, A.G., 1972. Oxygen tension of nonunion of fractured femurs in the rabbit. *Surg Gynecol Obstet*, 135(3), pp.379–385.

Brinkhuis, R.P. et al., 2012. Size Dependent Biodistribution and SPECT Imaging of 111 In-Labeled Polymersomes. *Bioconjugate Chemistry*, 23(5), pp.958–965.

Brinkhuis, R.P. et al., 2012. Size Dependent Biodistribution and SPECT Imaging of 111In-Labeled Polymersomes. *Bioconjugate Chemistry*, 23(5), pp.958–965.

Bruderer, M. et al., 2014. Role and regulation of RUNX2 in osteogenesis. *European cells & materials*, 28, pp.269–86.

Buckiova, D. et al., 2012. Minimally invasive drug delivery to the cochlea through application of nanoparticles to the round window membrane. *Nanomedicine (Lond)*, 7(9), pp.1339–1354.

Cabane, E. et al., 2011. Photoresponsive polymersomes as smart{,} triggerable nanocarriers. *Soft Matterials*, 7(19), pp.9167–9176.

Cabane, E., Malinova, V. & Meier, W., 2010. Synthesis of Photocleavable Amphiphilic Block Copolymers: Toward the Design of Photosensitive Nanocarriers. *Macromolecular Chemistry and Physics*, 211(17), pp.1847–1856.

Cabral, H. & Kataoka, K., 2014. Progress of drug-loaded polymeric micelles into clinical studies. *Journal of Controlled Release*, 190, pp.465–476.

Canton, I. & Battaglia, G., 2012. Endocytosis at the nanoscale. *Chemical Society Review*, 41(7), pp.2718–2739.

Caplan, A.I., 1991. Mesenchymal stem cells. *Journal of Orthopaedic Research : official publication of the Orthopaedic Research Society*, 9(5), pp.641–50.

Caplan, A.I. & Correa, D., 2011. The MSC: an injury drugstore. *Cell stem cell*, 9(1), pp.11–5.

Carano, R & Filvaroff, E., 2003. Angiogenesis and bone repair. *Drug Discovery Today*, 8(21), pp.980-989.

Cathcart, J., Pulkoski-Gross, A. & Cao, J., 2015. Targeting matrix metalloproteinases in cancer: Bringing new life to old ideas. *Genes & Diseases*, 2(1), pp.26–34.

Cawthorn, W.P. et al., 2012. Wnt6, Wnt10a and Wnt10b inhibit adipogenesis and stimulate osteoblastogenesis through a beta-catenin-dependent mechanism. *Bone*, 50(2), pp.477–489.

Chen, G., Deng, C. & Li, Y.-P., 2012. TGF-β and BMP Signaling in Osteoblast Differentiation and Bone Formation. *International Journal of Biological Sciences*, 8(2), pp.272–288.

Chen, Y. et al., 2007. Beta-catenin signaling plays a disparate role in different phases of fracture repair: implications for therapy to improve bone healing. *PLoS Medicine*, 4(7), p.e249.

Cheng, C.J. et al., 2015. A holistic approach to targeting disease with polymeric nanoparticles. *Nature Review Drug Discovery*, 14(4), pp.239–247.

Chernenko, T. et al., 2013. Label-Free Raman Microspectral Analysis for Comparison of

Cellular Uptake and Distribution between Non-Targeted and EGFR-Targeted Biodegradable Polymeric Nanoparticles. *Drug Delivery and Translational Research*, 3(6), p.10.1007/s13346-013-0178-3.

Chernenko, T. et al., 2009. Label-free Raman spectral imaging of intracellular delivery and degradation of polymeric nanoparticle systems. *ACS nano*, 3(11), pp.3552–9.

Cho, E.C., Zhang, Q. & Xia, Y., 2011. The effect of sedimentation and diffusion on cellular uptake of gold nanoparticles. *Nature Nanotechnology*, 6(6), pp.385–391.

Choucair, A., Soo, P.L. & Eisenberg, A., 2005. Active loading and tunable release of doxorubicin from block copolymer vesicles. *Langmuir*, 21(20), pp.9308–13.

Christian, D.A. et al., 2009. Polymersome carriers: from self-assembly to siRNA and protein therapeutics. *European Journal of Pharmceutics and Biopharmaceutics*, 71(3), pp.463–474.

Christian, N.A. et al., 2007. Tat-functionalized near-infrared emissive polymersomes for dendritic cell labeling. *Bioconjugugate Chemestry*, 18(1), pp.31–40.

Chu, D., Gao, J. & Wang, Z., 2015. Neutrophil-Mediated Delivery of Therapeutic Nanoparticles across Blood Vessel Barrier for Treatment of Inflammation and Infection. *ACS Nano*, 9(12), 11800:11.

Chung, R. et al., 2006. Roles of neutrophil-mediated inflammatory response in the bony repair of injured growth plate cartilage in young rats. *Journal of Leukocyte Biology*, 80(6), pp.1272–80.

Claes, L., Recknagel, S. & Ignatius, A., 2012. Fracture healing under healthy and inflammatory conditions. *Nature Review Rheumatology*, 8(3), pp.133–143.

Clarke, B., 2008. Normal bone anatomy and physiology. *Clinical Journal of the American Society of Nephrology*, 3 Suppl 3, pp.S131-9.

Cleaver, O. & Melton, D.A., 2003. Endothelial signaling during development. *Nature Medicine*, 9(6), pp.661–668.

Clement-Lacroix, P. et al., 2005. Lrp5-independent activation of Wnt signaling by lithium chloride increases bone formation and bone mass in mice. *Proc Natl Acad Sci U S A*, 102(48), pp.17406–17411.

Clevers, H. & Nusse, R., 2012. Wnt/beta-catenin signaling and disease. *Cell*, 149(6), pp.1192–1205.

Cohen, P. & Frame, S., 2001. The renaissance of GSK3. *Nature reviews. Molecular cell biology*, 2(10), pp.769–76.

Cohen, P. & Goedert, M., 2004. GSK3 inhibitors: development and therapeutic potential. *Nature Reviews Drug Discovery*, 3(6), pp.479–487.

Cook, D.A. et al., 2014. Wnt-dependent osteogenic commitment of bone marrow stromal cells using a novel GSK3β inhibitor. *Stem cell research*, 12(2), pp.415–27.

Dahabreh, Z., Dimitriou, R. & Giannoudis, P. V, 2007. Health economics: a cost analysis of treatment of persistent fracture non-unions using bone morphogenetic protein-7. *Injury*, 38(3), pp.371–377.

Darney, P.D. et al., 1989. Clinical evaluation of the Capronor contraceptive implant: preliminary report. *American Journal of Obstetrics and Gynecology*, 160(5 Pt 2), pp.1292–5.

Dawson, J.I. & Oreffo, R.O.C., 2013. Clay: New Opportunities for Tissue Regeneration and Biomaterial Design. *Advanced Materials*, 25(30), pp.4069–4086.

Day, T.F. et al., 2005. Wnt/beta-catenin signaling in mesenchymal progenitors controls osteoblast and chondrocyte differentiation during vertebrate skeletogenesis. *Dev Cell*, 8(5), pp.739–750.

Deng, B. et al., 2014. Maresin Biosynthesis and Identification of Maresin 2, a New Anti-Inflammatory and Pro-Resolving Mediator from Human Macrophages J. Wallace, ed. *PLoS ONE*, 9(7), p.e102362.

Deng, Z.-B. et al., 2013. Intestinal mucus-derived nanoparticle-mediated activation of Wnt/β-catenin signaling plays a role in induction of liver natural killer T cell anergy in mice. *Hepatology,* 57(3), pp.1250–61.

Dhamdhere, G.R. et al., 2014. Drugging a Stem Cell Compartment Using Wnt3a Protein as a Therapeutic E. M. Verheyen, ed. *PLoS ONE*, 9(1), p.e83650.

Dimai, H.P. et al., 1998. Alkaline phosphatase levels and osteoprogenitor cell numbers suggest bone formation may contribute to peak bone density differences between two inbred strains of mice. *Bone*, 22(3), pp.211–6.

Dimitriou, R. et al., 2011. Bone regeneration: current concepts and future directions. *BMC Med*, 9, p.66.

Ding, V.M.Y. et al., 2010. FGF-2 modulates Wnt signaling in undifferentiated hESC and iPS cells through activated PI3-K/GSK3β signaling. *Journal of Cellular Physiology*, 225(2), pp.417–428.

Discher, B.M. et al., 1999. Polymersomes: tough vesicles made from diblock copolymers. *Science*, 284(5417), pp.1143–1146.

Discher, D.E. et al., 2007. Emerging Applications of Polymersomes in Delivery: from Molecular Dynamics to Shrinkage of Tumors. *Progress in Polymer Science*, 32(8–9), pp.838–857.

Discher, D.E. & Eisenberg, A., 2002. Polymer vesicles. *Science*, 297(5583), pp.967–973.

Diwan, A.D. et al., 2000. Nitric oxide modulates fracture healing. *Journal of Bone and Mineral Research*, 15(2), pp.342–51.

Douglas, S.M. et al., 2009. Self-assembly of DNA into nanoscale three-dimensional shapes. *Nature*, 459(7245), pp.414–418.

Ducy, P. & Karsenty, G., 1995. Two distinct osteoblast-specific cis-acting elements control expression of a mouse osteocalcin gene. *Molecular and Cellular Biology*, 15(4), pp.1858–69.

Ehrlich, M. et al., 2004. Endocytosis by random initiation and stabilization of clathrin-coated pits. *Cell*, 118(5), pp.591–605.

Eijken, M. et al., 2008. Wnt signaling acts and is regulated in a human osteoblast differentiation dependent manner. *Journal of Cellular Biochemestry*, 104(2), pp.568–579.

Einhorn, T.A., 2005. The science of fracture healing. *Journal of Orthopedic Trauma*, 19(10 Suppl), pp.S4-6.

Einhorn, T.A. & Gerstenfeld, L.C., 2015. Fracture healing: mechanisms and interventions. *Nature Reviews. Rheumatology*, 11(1), pp.45–54.

Eldar-Finkelman, H. & Martinez, A., 2011. GSK-3 Inhibitors: Preclinical and Clinical Focus on CNS. *Frontiers in Molecular Neuroscience*, 4, p.32.

Enochson, L. et al., 2014. GDF5 reduces MMP13 expression in human chondrocytes via

DKK1 mediated canonical Wnt signaling inhibition. *Osteoarthritis and cartilage / OARS, Osteoarthritis Research Society*, 22(4), pp.566–77.

Ensign, L.M., Cone, R. & Hanes, J., 2012. Oral drug delivery with polymeric nanoparticles: the gastrointestinal mucus barriers. *Advanced Drug Delivery Reviews*, 64(6), pp.557–70.

Etheridge, S.L. et al., 2004. Expression profiling and functional analysis of wnt signaling mechanisms in mesenchymal stem cells. *Stem cells*, 22(5), pp.849–60.

Evans, N.D. et al., 2005. Glucose-dependent changes in NAD(P)H-related fluorescence lifetime of adipocytes and fibroblasts in vitro: potential for non-invasive glucose sensing in diabetes mellitus. *Journal of Photochemistry and Photobiology. B, Biology*, 80(2), pp.122–9.

Farokhzad, O.C. & Langer, R., 2009. Impact of nanotechnology on drug delivery. *ACS Nano*, 3(1), pp.16–20.

Figeac, F. et al., 2012. Local in vivo GSK3β knockdown promotes pancreatic β cell and acinar cell regeneration in 90% pancreatectomized rat. *Molecular therapy : the journal of the American Society of Gene Therapy*, 20(10), pp.1944–52.

Fleisch, H., 2001. Can bisphosphonates be given to patients with fractures? *Journal of Bone and Mineral Research*, 16(3), pp.437–40.

Florio, M. et al., 2016. A bispecific antibody targeting sclerostin and DKK-1 promotes bone mass accrual and fracture repair. *Nature Communications*, 7, p.11505.

Fong, K. et al., 2013. Predictors of nonunion and reoperation in patients with fractures of the tibia: an observational study. *BMC Musculoskelet Disorders*, 14, p.103.

Fratzl, P., 2008. Bone fracture: When the cracks begin to show. *Nature Materials*, 7(8), pp.610–612.

Fredman, G. et al., 2015. Targeted nanoparticles containing the proresolving peptide Ac2-26 protect against advanced atherosclerosis in hypercholesterolemic mice. *Science translational medicine*, 7(275), p.275.

Friedenstein, A.J. et al., 1974. Stromal cells responsible for transferring the microenvironment of the hemopoietic tissues. Cloning in vitro and retransplantation in vivo. *Transplantation*, 17(4), pp.331–340.

Friedenstein, A.J., 1980. Stromal mechanisms of bone marrow: cloning in vitro and retransplantation in vivo. *Haematol Blood Transfusion*, 25, pp.19–29.

Friedman, A.D., Claypool, S.E. & Liu, R., 2013. The smart targeting of nanoparticles. *Current Pharmaceutical Design*, 19(35), pp.6315–29.

Fullstone, G. et al., 2015. Modelling the Transport of Nanoparticles under Blood Flow using an Agent-based Approach. *Scientific Reports*, 5, p.10649.

Gaboriaud-Kolar, N., Vougogiannopoulou, K. & Skaltsounis, A.-L., 2015. Indirubin derivatives: a patent review (2010 – present). *Expert Opinion on Therapeutic Patents*, 25(5), pp.583–593.

Gambardella, A. et al., 2011. Glycogen synthase kinase-3alpha/beta inhibition promotes in vivo amplification of endogenous mesenchymal progenitors with osteogenic and adipogenic potential and their differentiation to the osteogenic lineage. *Journal of Bone and Mineral Research*, 26(4), pp.811–821.

Gao, H. et al., 2013. Ligand modified nanoparticles increases cell uptake, alters endocytosis and elevates glioma distribution and internalization. *Scientific Reports.*, 3(2534).

Gao, H. et al., 2012. Precise glioma targeting of and penetration by aptamer and peptide dual-functioned nanoparticles. *Biomaterials*, 33(20), pp.5115–5123.

Gao, Y. et al., 2014. Nanotechnology-based intelligent drug design for cancer metastasis treatment. *Biotechnology Advances*, 32(4), pp.761–77.

Garrett, I.R. et al., 2007. Locally delivered lovastatin nanoparticles enhance fracture healing in rats. *Journal of Orthopedic Research*, 25(10), pp.1351–1357.

Gaston, M.S. & Simpson, A.H., 2007. Inhibition of fracture healing. *Journal of Bone Joint Surg Br*, 89(12), pp.1553–1560.

Gaur, T. et al., 2005. Canonical WNT signaling promotes osteogenesis by directly stimulating Runx2 gene expression. *The Journal of Biological Chemistry*, 280(39), pp.33132–40.

Gaur, T. et al., 2009. Secreted frizzled related protein 1 is a target to improve fracture healing. *Journal of Cellular Physiology*, 220(1), pp.174–81.

Gellynck, K. et al., 2013. Small molecule stimulation enhances bone regeneration but not titanium implant osseointegration. *Bone*, 57(2), pp.405–412.

Geng, Y. et al., 2007. Shape effects of filaments versus spherical particles in flow and drug delivery. *Nature Nanotechnology*, 2(4), pp.249–255.

Geng, Y. & Discher, D.E., 2005. Hydrolytic degradation of poly(ethylene oxide)-block-polycaprolactone worm micelles. *Journal of the American Chemical Society*, 127(37), pp.12780–12781.

Geng, Y. & Discher, D.E., 2006. Visualization of degradable worm micelle breakdown in relation to drug release. *Polymer*, 47(7), pp.2519–2525.

Gerstenfeld, L.C. et al., 2003. Fracture healing as a post-natal developmental process: molecular, spatial, and temporal aspects of its regulation. *Journal of Cell Biochemestry*, 88(5), pp.873–884.

Ghoroghchian, P.P. et al., 2006. Bioresorbable vesicles formed through spontaneous self-assembly of amphiphilic poly(ethylene oxide)-block-polycaprolactone. *Macromolecules*, 39(5), pp.1673–1675.

Giannoudis, P. V et al., 2000. Nonunion of the femoral diaphysis. The influence of reaming and non-steroidal anti-inflammatory drugs. *Journal of Bone and Joint Surgery*, 82(5), pp.655–658.

Giannoudis, P. V et al., 2009. The synergistic effect of autograft and BMP-7 in the treatment of atrophic nonunions. *Clin Orthop Relat Res*, 467(12), pp.3239–3248.

Gibbs, D.M.R. et al., 2016. Bone induction at physiological doses of BMP through localization by clay nanoparticle gels. *Biomaterials*, 99, pp.16–23.

Glass, D.A. et al., 2005. Canonical Wnt signaling in differentiated osteoblasts controls osteoclast differentiation. *Developmental Cell*, 8(5), pp.751–64.

Goldhahn, J. et al., 2012. Implications for fracture healing of current and new osteoporosis treatments: an ESCEO consensus paper. *Calcified Tissue International*, 90(5), pp.343–53.

Gong, Y. et al., 2001. LDL receptor-related protein 5 (LRP5) affects bone accrual and eye development. *Cell*, 107(4), pp.513–523.

Goodship, A.E. et al., 1994. Use of a bisphosphonate (pamidronate) to modulate fracture repair in ovine bone. *Annals of oncology : official journal of the European Society for Medical Oncology / ESMO*, 5 Suppl 7, pp.S53-5.

Gothard, D. et al., 2014. Tissue engineered bone using select growth factors: A comprehensive review of animal studies and clinical translation studies in man. *European Cell Matererials*, 28, pp.166–168.

Gottstein, C. et al., 2013. Precise quantification of nanoparticle internalization. *ACS Nano*, 7(6), pp.4933–4945.

Granchi, D. et al., 2013. Serum levels of fibroblast growth factor 2 in children with orthopedic diseases: Potential role in predicting bone healing. *Journal of Orthopaedic Research*, 31(2), pp.249–256.

Grøgaard, B., Gerdin, B. & Reikerås, O., 1990. The polymorphonuclear leukocyte: has it a role in fracture healing? *Archives of orthopaedic and trauma surgery*, 109(5), pp.268–71.

Gronthos, S. et al., 2003. Molecular and cellular characterisation of highly purified stromal stem cells derived from human bone marrow. *Journal of Cell Science*, 116(Pt 9), pp.1827–35.

Groothuis, A. et al., 2010. Mechanical stimulation of the pro-angiogenic capacity of human fracture haematoma: Involvement of VEGF mechano-regulation. *Bone*, 47(2), pp.438–444.

Grundnes, O. & Reikerås, O., 2000. Effects of macrophage activation on bone healing. *Journal of Orthopaedic Science : official journal of the Japanese Orthopaedic Association*, 5(3), pp.243–7.

Grundnes, O. & Reikerås, O., 1993. The importance of the hematoma for fracture healing in rats. *Acta orthopaedica Scandinavica*, 64(3), pp.340–2.

Grzybowski, B.A. et al., 2009. Self-assembly: from crystals to cells. *Soft Matter*, 5(6), p.1110.

Gu, W. et al., 2013. Nanotechnology in the targeted drug delivery for bone diseases and bone regeneration. *International Journal of Nanomedicine*, 8, pp.2305–2317.

Guan, L., Rizzello, L. & Battaglia, G., 2015. Polymersomes and their applications in cancer delivery and therapy. *Nanomedicine (London, England)*, 10(17), pp.2757–2780.

Guilbault, G.G., Sadar, M.H. & Peres, K., 1969. Fluorometric determination of carbohydrates. *Analytical Biochemistry*, 31, pp.91–101.

Gunn, W.G. et al., 2011. Pharmaceutical inhibition of glycogen synthetase kinase-3beta reduces multiple myeloma-induced bone disease in a novel murine plasmacytoma xenograft model. *Blood*, 117(5), pp.1641–1651.

Guo, J. et al., 2010. Suppression of Wnt signaling by Dkk1 attenuates PTH-mediated stromal cell response and new bone formation. *Cell Metabolism*, 11(2), pp.161–71.

Haraldsson, B., Nyström, J. & Deen, W.M., 2008. Properties of the glomerular barrier and mechanisms of proteinuria. *Physiological Reviews*, 88(2), pp.451–87.

Harding, F.A. et al., 2010. The immunogenicity of humanized and fully human antibodies: residual immunogenicity resides in the CDR regions. *mAbs*, 2(3), pp.256–65.

Hardy, R. & Cooper, M.S., 2009. Bone loss in inflammatory disorders. *Journal of Endocrinol*, 201(3), pp.309–320.

Harris, S.E. et al., 2009. Effects of transforming growth factor β on bone nodule formation and expression of bone morphogenetic protein 2, osteocalcin, osteopontin, alkaline phosphatase, and type I collagen mRNA in long-term cultures of fetal rat calvarial osteoblasts. *Journal of Bone and Mineral Research*, 9(6), pp.855–863.

Hayrapetyan, A., Jansen, J.A. & van den Beucken, J.J.J.P., 2015. Signaling pathways involved in osteogenesis and their application for bone regenerative medicine. *Tissue Engineering. Part B, Reviews*, 21(1), pp.75–87.

Hirao, M. et al., 2006. Oxygen tension regulates chondrocyte differentiation and function during endochondral ossification. *Journal of Biol Chemestry*, 281(41), pp.31079–31092.

Ho, M.H. et al., 2011. Highly efficient release of lovastatin from poly(lactic-co-glycolic acid) nanoparticles enhances bone repair in rats. *Journal of Orthopaedic Research*, 29(10), pp.1504–1510.

Hoessel, R. et al., 1999. Indirubin, the active constituent of a Chinese antileukaemia medicine, inhibits cyclin-dependent kinases. *Nature Cell Biology*, 1(1), pp.60–67.

Hoffman, M.D. & Benoit, D.S., 2013. Agonism of Wnt-beta-catenin signalling promotes mesenchymal stem cell (MSC) expansion. *Journal of Tissue Engeneering and Regenerative*

Medicine, 9(11), 12-26.

Hofmann, D. et al., 2014. Drug delivery without nanoparticle uptake: delivery by a kiss-and-run mechanism on the cell membrane. *Chemical Communications*, 50(11), pp.1369–1371.

Hollinger, J.O. et al., 2008. Recombinant human platelet-derived growth factor: biology and clinical applications. *The Journal of Bone and Joint Surgery*, 90 Suppl 1, pp.48–54.

Holroyd, C., Cooper, C. & Dennison, E., 2008. Epidemiology of osteoporosis. *Best Practice & Research Clinical Endocrinology & Metabolism*, 22(5), pp.671–685.

Hooper, G.J., Keddell, R.G. & Penny, I.D., 1991. Conservative management or closed nailing for tibial shaft fractures. A randomised prospective trial. *The Journal of Bone and Joint Surgery*, 73(1), pp.83–5.

Howse, J.R. et al., 2009. Templated formation of giant polymer vesicles with controlled size distributions. *Nature materials*, 8(6), pp.507–11.

Hsu, R.J. et al., 2012. WNT10A plays an oncogenic role in renal cell carcinoma by activating WNT/beta-catenin pathway. *PLoS One*, 7(10), p.e47649.

Hulsart-Billström, G. et al., 2016. A surprisingly poor correlation between in vitro and in vivo testing of biomaterials for bone regeneration: results of a multicentre analysis. *European cells & Materials*, 31, pp.312–22.

Hunter, D.J. et al., 2015. Wnt Acts as a Pro-Survival Signal to Enhance Dentin Regeneration. *Journal of Bone and Mineral Research*, 30(7), pp.1120-9.

Hunter, J., 1837. Collected works. *London: Longman Rees*, 4.

Hurst, S.M. et al., 2001. IL-6 and Its Soluble Receptor Orchestrate a Temporal Switch in the Pattern of Leukocyte Recruitment Seen during Acute Inflammation. *Immunity*, 14(6), pp.705–714.

Janeczek, A.A. et al., 2015. Skeletal Stem Cell Niche of the Bone Marrow. In pp. 245–279.

Janeczek, A.A. et al., 2016. Transient Canonical Wnt Stimulation Enriches Human Bone Marrow Mononuclear Cell Isolates for Osteoprogenitors. *Stem cells (Dayton, Ohio)*, 34(2), pp.418–30.

Jaworski, T. et al., 2010. Modeling of Tau-Mediated Synaptic and Neuronal Degeneration in Alzheimer's Disease. *International Journal of Alzheimer's Disease*, 2010, pp.1–10.

Jho, E. -h. et al., 2002. Wnt/ -Catenin/Tcf Signaling Induces the Transcription of Axin2, a Negative Regulator of the Signaling Pathway. *Molecular and Cellular Biology*, 22(4), pp.1172–1183.

Jia, Z. et al., 2015. Simvastatin prodrug micelles target fracture and improve healing. *Journal of Controlled Release*, 200, pp.23–34.

Jiang, W. et al., 2008. Nanoparticle-mediated cellular response is size-dependent. *Nature Nanotechnology*, 3(3), pp.145–150.

Jørgensen, N.R. & Schwarz, P., 2011. Effects of anti-osteoporosis medications on fracture healing. *Current Osteoporosis Reports*, 9(3), pp.149–55.

Jurk, D. et al., 2014. Chronic inflammation induces telomere dysfunction and accelerates ageing in mice. *Nature Communications*, 24(2), 4172.

Kahn, M., 2014. Can we safely target the WNT pathway? *Nature reviews. Drug discovery*, 13(7), pp.513–32.

Kamaly, N. et al., 2016. Degradable Controlled-Release Polymers and Polymeric Nanoparticles: Mechanisms of Controlling Drug Release. *Chemical Reviews*, 116(4), pp.2602–2663.

Kamaly, N. et al., 2013. Development and in vivo efficacy of targeted polymeric inflammation-resolving nanoparticles. *Proceedings of the National Academy of Sciences*, 110(16), pp.6506–6511.

Kanakaris, N.K. & Giannoudis, P. V, 2007. The health economics of the treatment of long-bone non-unions. *Injury*, 38 Suppl 2, pp.77-84.

Kato, M. et al., 2002. Cbfa1-independent decrease in osteoblast proliferation, osteopenia, and persistent embryonic eye vascularization in mice deficient in Lrp5, a Wnt coreceptor. *Journal of Cell Biology*, 157(2), pp.303–314.

Kawaguchi, H. et al., 2010. A local application of recombinant human fibroblast growth factor 2 for tibial shaft fractures: A randomized, placebo-controlled trial. *Journal of Bone and Mineral Research*, 25(12), pp.2735–43.

Keaveny, T.M. et al., 2008. Femoral bone strength and its relation to cortical and trabecular changes after treatment with PTH, alendronate, and their combination as assessed by finite element analysis of quantitative CT scans. *Journal of Bone and Mineral Research*, 23(12), pp.1974–1982.

Khosla, S. & Shane, E., 2016. A Crisis in the Treatment of Osteoporosis. *Journal of Bone and Mineral Research*, 31(8), pp.1485–1487.

Kilgore, M.L. et al., 2009. Health care expenditures associated with skeletal fractures among Medicare beneficiaries, 1999-2005. *Journal of Bone and Mineral Research*, 24(12), pp.2050–2055.

Kim, J.-B. et al., 2007. Bone regeneration is regulated by wnt signaling. *Journal of Bone and Mineral Research*, 22(12), pp.1913–1923.

Kim, J.A. et al., 2012. Role of cell cycle on the cellular uptake and dilution of nanoparticles in a cell population. *Nature Nanotechnology*, 7(1), pp.62–8.

Klein, P.S. & Melton, D.A., 1996. A molecular mechanism for the effect of lithium on development. *Proceedings of the National Academy of Sciences*, 93(16), pp.8455–9.

Klein, P et al., 2003. The initial phase of fracture healing is specifically sensitive to mechanical conditions. *Journal of Orthopaedic Research*, 21(4), pp.662-669.

Kohler, E.E. et al., 2014. Low-Dose 6-Bromoindirubin-3′-oxime Induces Partial Dedifferentiation of Endothelial Cells to Promote Increased Neovascularization. *STEM CELLS*, 32(6), pp.1538–1552.

Kolar, P. et al., 2010. The early fracture hematoma and its potential role in fracture healing. *Tissue Engineering Part B Review*, 16(4), pp.427–434.

Komatsu, D.E. et al., 2010. Modulation of Wnt signaling influences fracture repair. *J Orthopedic Research*, 28(7), pp.928–936.

Kon, T. et al., 2001. Expression of osteoprotegerin, receptor activator of NF-kappaB ligand (osteoprotegerin ligand) and related proinflammatory cytokines during fracture healing. *Journal of Bone and Mineral Research,* 16(6), pp.1004–1014.

Korin, N. et al., 2012. Shear-activated nanotherapeutics for drug targeting to obstructed blood vessels. *Science*, 337(6095), pp.738–42.

Krause, U. et al., 2010. Pharmaceutical modulation of canonical Wnt signaling in multipotent stromal cells for improved osteoinductive therapy. *Proceedings of the National Academy of Sciences*, 107(9), pp.4147–4152.

Krause, U. et al., 2010. Pharmaceutical modulation of canonical Wnt signaling in multipotent stromal cells for improved osteoinductive therapy. *Proceedings of the National Academy of Sciences* 107(9), pp.4147–4152.

Kremer, A. et al., 2011. GSK3 and Alzheimer's Disease: Facts and Fiction…. *Frontiers in Molecular Neuroscience*, 4, p.17.

Kulkarni, A. et al., 2016. Reporter nanoparticle that monitors its anticancer efficacy in real time. *Proceedings of the National Academy of Sciences,* 113(15), pp.201603455.

Kumar, S. et al., 2010. Mesenchymal Stem Cells Expressing Osteogenic and Angiogenic Factors Synergistically Enhance Bone Formation in a Mouse Model of Segmental Bone Defect. *Molecular Therapy*, 18(5), pp.1026–1034.

Kurien, T., Pearson, R.G. & Scammell, B.E., 2013. Bone graft substitutes currently available in orthopaedic practice: the evidence for their use. *The Bone & Joint Journal*, 95–B(5), pp.583–97.

Lack, W.D. et al., 2014. Any Cortical Bridging Predicts Healing of Tibial Shaft Fractures. *The Journal of Bone and Joint Surgery,* 96(13), pp.1066–1072.

Lao, L.L., Venkatraman, S.S. & Peppas, N.A., 2008. Modeling of drug release from biodegradable polymer blends. *European Journal of Pharmaceutics and Biopharmaceutics*, 70(3), pp.796–803.

Lasic, D.D. & Papahadjopoulos, D., 1998. *Medical applications of liposomes*, Elsevier.

Leckband, D. & Israelachvili, J., 2001. Intermolecular forces in biology. *Quarterly Reviews of Biophysics*, 34(2), pp.105–267.

Leclerc, S. et al., 2001. Indirubins inhibit glycogen synthase kinase-3 beta and CDK5/p25, two protein kinases involved in abnormal tau phosphorylation in Alzheimer's disease. A property common to most cyclin-dependent kinase inhibitors? *Journal of Biological Chemistry*, 276(1), pp.251–260.

Lee, J.S. et al., 2011. Circulation kinetics and biodistribution of dual-labeled polymersomes with modulated surface charge in tumor-bearing mice: Comparison

with stealth liposomes. *Journal of Controlled Release*, 155(2), pp.282–288.

Li, C. et al., 2011. Increased callus mass and enhanced strength during fracture healing in mice lacking the sclerostin gene. *Bone*, 49(6), pp.1178–85.

Li, J. et al., 2000. Concentration of bisphosphonate (incadronate) in callus area and its effects on fracture healing in rats. *Journal of Bone and Mineral Research*, 15(10), pp.2042–51.

Li, S. et al., 2002. Hydrolytic and enzymatic degradations of physically crosslinked hydrogels prepared from PLA/PEO/PLA triblock copolymers. *Journal of Materials Science. Materials in medicine*, 13(1), pp.81–6.

Li, S.D. & Huang, L., 2009. Nanoparticles evading the reticuloendothelial system: role of the supported bilayer. *Biochimica et Biophysica Acta*, 1788(10), pp.2259–2266.

Li, Y.F. et al., 2010. Systemic treatment with strontium ranelate promotes tibial fracture healing in ovariectomized rats. *Osteoporosis International,* 21(11), pp.1889–97.

Liang, C. et al., 2015. Aptamer-functionalized lipid nanoparticles targeting osteoblasts as a novel RNA interference–based bone anabolic strategy. *Nature Medicine*, 21(3), pp.288–294.

Lin, Y.-L. et al., 2014. The fusion mechanism of small polymersomes formed by rod-coil diblock copolymers. *Soft matter*, 10(10), pp.1500–11.

Ling, L., Nurcombe, V. & Cool, S.M., 2009. Wnt signaling controls the fate of mesenchymal stem cells. *Gene*, 433(1–2), pp.1–7.

Lissenberg-Thunnissen, S.N. et al., 2011. Use and efficacy of bone morphogenetic proteins in fracture healing. *International Orthopaedics*, 35(9), pp.1271–80.

Little, R.D. et al., 2002. A mutation in the LDL receptor-related protein 5 gene results in the autosomal dominant high-bone-mass trait. *American Journal of Human Genetetics*, 70(1), pp.11–19.

Liu, F. et al., 2015. Temperature-Sensitive Polymersomes for Controlled Delivery of Anticancer Drugs. *Chemistry of Materials*, 27(23), pp.7945–7956.

Liu, G. et al., 2009. Canonical Wnts function as potent regulators of osteogenesis by human mesenchymal stem cells. *The Journal of Cell Biology*, 185(1), pp.67–75.

Liu, J. et al., 2011. Enhancement of canonical Wnt/beta-catenin signaling activity by HCV core protein promotes cell growth of hepatocellular carcinoma cells. *PLoS One*, 6(11), p.e27496.

Liu, J. et al., 2014. Real-Time In Vivo Quantitative Monitoring of Drug Release by Dual-Mode Magnetic Resonance and Upconverted Luminescence Imaging. *Angewandte Chemie International Edition*, 53(18), pp.4551–4555.

Liu, L. et al., 2011. 6-Bromoindirubin-3'-oxime inhibits JAK/STAT3 signaling and induces apoptosis of human melanoma cells. *Cancer research*, 71(11), pp.3972–3979.

Liu, Y. et al., 2016. Effects of Sclerostin Antibody on the Healing of Femoral Fractures in Ovariectomised Rats. *Calcified Tissue International*, 98(3), pp.263–274.

Loi, F. et al., 2016. Inflammation, fracture and bone repair. *Bone*, 86, pp.119–130.

Lomas, H. et al., 2010. Efficient encapsulation of plasmid DNA in pH-sensitive PMPC-PDPA polymersomes: Study of the effect of PDPA block length on copolymer-DNA binding affinity. *Macromolecular Bioscience*, 10(5), pp.513–530.

Lomas, H. et al., 2010. Efficient encapsulation of plasmid DNA in pH-sensitive PMPC-PDPA polymersomes: study of the effect of PDPA block length on copolymer-DNA binding affinity. *Macromolecular Bioscience*, 10(5), pp.513–530.

Loverde, S.M. et al., 2010. Curvature-driven molecular demixing in the budding and breakup of mixed component worm-like micelles. *Soft Matter*, 6(7), p.1419.

Lovestone, S. et al., 2015. A phase II trial of tideglusib in Alzheimer's disease. *Journal of Alzheimer's disease : JAD*, 45(1), pp.75–88.

Low, S.A. et al., 2015. Biodistribution of Fracture-Targeted GSK3β Inhibitor-Loaded Micelles for Improved Fracture Healing. *Biomacromolecules*, 16(10), pp.3145–3153.

Low, S. & Kopeček, J., 2012. Targeting polymer therapeutics to bone. *Advanced drug delivery reviews*, 64(12), pp.1189–1204.

Lynch, I. & Dawson, K.A., 2008. Protein-nanoparticle interactions. *Nano Today*, 3(1–2), pp.40–47.

Lynch, I., Salvati, A. & Dawson, K.A., 2009. Protein-nanoparticle interactions: What does the cell see? *Nature Nanotechnology*, 4(9), pp.546–547.

Lyon, T. et al., 2013. Efficacy and safety of recombinant human bone morphogenetic protein-2/calcium phosphate matrix for closed tibial diaphyseal fracture: a double-blind, randomized, controlled phase-II/III trial. *The Journal of Bone and Joint Surgery. American volume*, 95(23), pp.2088–96.

Mabrouk, E. et al., 2009. Bursting of sensitive polymersomes induced by curling. *Proceedings of the National Academy of Sciences*, 106(18), pp.7294–7298.

MacNabb, C., Patton, D. & Hayes, J.S., 2016. Sclerostin Antibody Therapy for the Treatment of Osteoporosis: Clinical Prospects and Challenges. *Journal of Osteoporosis*, 2016, p.6217286.

Maeda, H. et al., 2000. Tumor vascular permeability and the EPR effect in macromolecular therapeutics: a review. *Journal of Controlled Release*, 65(1–2), pp.271–284.

Maeda, Y. et al., 2013. Bone healing by sterilizable calcium phosphate tetrapods eluting osteogenic molecules. *Biomaterials*, 34(22), pp.5530–5537.

Mai, Y. & Eisenberg, A., 2012. Self-assembly of block copolymers. *Chemical Society Reviews*, 41(18), pp.5969–5985.

Majno, G. & Joris, I., 1978. Endothelium 1977: a review. *Advances in Experimental Medicine and Biology*, 104, pp.169–225, 481–526.

Marie, P.J., 2007. Strontium ranelate: New insights into its dual mode of action. *Bone*, 40(5), pp.S5–S8.

Marsell, R. et al., 2012. GSK-3 inhibition by an orally active small molecule increases bone mass in rats. *Bone*, 50(3), pp.619–627.

Marsell, R. & Einhorn, T.A., 2011. The biology of fracture healing. *Injury*, 42(6), pp.551–555.

Martin, L. et al., 2009. Inhibition of glycogen synthase kinase-3beta downregulates total tau proteins in cultured neurons and its reversal by the blockade of protein phosphatase-2A. *Brain Research*, 1252, pp.66–75.

Marx, R.E. et al., 1998. Platelet-rich plasma: Growth factor enhancement for bone grafts. *Oral Surgery, Oral Medicine, Oral Pathology, Oral Radiology, and Endodontology*, 85(6), pp.638–646.

Mason, J.J. & Williams, B.O., 2010. SOST and DKK: Antagonists of LRP Family Signaling as Targets for Treating Bone Disease. *Journal of osteoporosis*, 2010:460120.

Massignani, M. et al., 2009. Controlling cellular uptake by surface chemistry, size, and surface topology at the nanoscale. *Small*, 5(21), pp.2424–2432.

Massignani, M., Canton, I., et al., 2010. Enhanced fluorescence imaging of live cells by effective cytosolic delivery of probes. *PLoS ONE*, 5(5).

Massignani, M., Lomas, H. & Battaglia, G., 2010. Polymersomes: A Synthetic Biological Approach to Encapsulation and Delivery. In Springer Berlin Heidelberg, pp. 115–154.

Matsumura, Y. & Maeda, H., 1986. A new concept for macromolecular therapeutics in cancer chemotherapy: mechanism of tumoritropic accumulation of proteins and the antitumor agent smancs. *Cancer research*, 46(12 Pt 1), pp.6387–92.

McClung, M.R. et al., 2014. Romosozumab in postmenopausal women with low bone mineral density. *The New England journal of Medicine*, 370(5), pp.412–20.

Mehta, M. et al., 2012. Biomaterial delivery of morphogens to mimic the natural healing cascade in bone. *Advanced Drug Delivery Reviews*, 64(12), pp.1257–1276.

Meijer, L. et al., 2003. GSK-3-selective inhibitors derived from Tyrian purple indirubins. *Chemical Biololgy*, 10(12), pp.1255–1266.

Mendez-Ferrer, S. et al., 2010. Mesenchymal and haematopoietic stem cells form a unique bone marrow niche. *Nature*, 466(7308), pp.829–834.

Mercado, A.E. et al., 2009. Release characteristics and osteogenic activity of recombinant human bone morphogenetic protein-2 grafted to novel self-assembled poly(lactide-co-glycolide fumarate) nanoparticles. *Journal of Control Release*, 140(2), pp.148–156.

Meyer, U. et al., 2014. Early changes in bone density, microarchitecture, bone resorption, and inflammation predict the clinical outcome 12 weeks after conservatively treated distal radius fractures: an exploratory study. *Journal of Bone and Mineral Research*, 29(9), pp.2065–73.

Min, J.-K. et al., 2011. The WNT antagonist Dickkopf2 promotes angiogenesis in rodent and human endothelial cells. *The Journal of Clinical Investigation*, 121(5), pp.1882–93.

Minear, S. et al., 2010. Wnt Proteins Promote Bone Regeneration. *Science Translational Medicine*, 2(29), p.29ra30.

Mitragotri, S., Burke, P.A. & Langer, R., 2014. Overcoming the challenges in administering biopharmaceuticals: formulation and delivery strategies. *Nature Reviews. Drug discovery*, 13(9), pp.655–72.

Modi, S. & Anderson, B.D., 2013. Determination of drug release kinetics from nanoparticles: overcoming pitfalls of the dynamic dialysis method. *Molecular Pharmaceutics*, 10(8), pp.3076–3089.

Moghimi, S.M., Hunter, A.C. & Murray, J.C., 2001. Long-circulating and target-specific nanoparticles: theory to practice. *Pharmacological Reviews*, 53(2), pp.283–318.

Moghimi, S.M. & Szebeni, J., 2003. Stealth liposomes and long circulating nanoparticles: critical issues in pharmacokinetics, opsonization and protein-binding properties. *Progress in Lipid Research*, 42(6), pp.463–478.

Mout, R. et al., 2012. Surface functionalization of nanoparticles for nanomedicine. *Chemical Society Reviews*, 41(7), p.2539.

Mundy, G. et al., 1999. Stimulation of bone formation in vitro and in rodents by statins. *Science*, 286(5446), pp.1946–9.

Nagy, J.A. et al., 2008. Vascular permeability, vascular hyperpermeability and angiogenesis. *Angiogenesis*, 11(2), pp.109–19.

Nakashima, K. et al., 2002. The novel zinc finger-containing transcription factor osterix is required for osteoblast differentiation and bone formation. *Cell*, 108(1), pp.17–29.

Napoli, A. et al., 2004. Oxidation-responsive polymeric vesicles. *Nature Materials*, 3(3), pp.183–189.

Nusse, R., 2005. Wnt signaling in disease and in development. *Cell Research*, 15(1), pp.28–32.

Oerlemans, C. et al., 2010. Polymeric Micelles in Anticancer Therapy: Targeting, Imaging and Triggered Release. *Pharmaceutical Research*, 27(12), pp.2569–2589.

Oltra, N.S., Nair, P. & Discher, D.E., 2014. From stealthy polymersomes and filomicelles to "self" Peptide-nanoparticles for cancer therapy. *Annual Review of*

Chemical Biomolecular Engineering, 5, pp.281–299.

Oryan, A. et al., 2014. Bone regenerative medicine: classic options, novel strategies, and future directions. *Journal of Orthopedic Surgery Research*, 9(1), p.18.

Panagi, Z. et al., 2001. Effect of dose on the biodistribution and pharmacokinetics of PLGA and PLGA–mPEG nanoparticles. *International Journal of Pharmaceutics*, 221(1–2), pp.143–152.

Pang, Z. et al., 2012. Intracellular delivery mechanism and brain delivery kinetics of biodegradable cationic bovine serum albumin-conjugated polymersomes. *International Journal of Nanomedicine*, 7, pp.3421–3432.

Park, S.-H. et al., 2002. Effect of repeated irrigation and debridement on fracture healing in an animal model. *Journal of Orthopaedic Research : official publication of the Orthopaedic Research Society*, 20(6), pp.1197–204.

Patel, S.K., Lavasanifar, A. & Choi, P., 2010. Molecular dynamics study of the encapsulation capability of a PCL-PEO based block copolymer for hydrophobic drugs with different spatial distributions of hydrogen bond donors and acceptors. *Biomaterials*, 31(7), pp.1780–6.

Pautke, C. et al., 2004. Characterization of osteosarcoma cell lines MG-63, Saos-2 and U-2 OS in comparison to human osteoblasts. *Anticancer Research*, 24(6), pp.3743–3748.

Pearson, R.T. et al., 2013. Effect of pH and Temperature on PMPC–PDPA Copolymer Self-Assembly. *Macromolecules*, 46(4), pp.1400–1407.

Pederson, L. et al., 2008. Regulation of bone formation by osteoclasts involves Wnt/BMP signaling and the chemokine sphingosine-1-phosphate. *Proceedings of the National Academy of Sciences*, 105(52), pp.20764–20769.

Petrie Aronin, C.E. et al., 2010. The enhancement of bone allograft incorporation by the local delivery of the sphingosine 1-phosphate receptor targeted drug FTY720. *Biomaterials*, 31(25), pp.6417–6424.

Petros, R.A. & DeSimone, J.M., 2010. Strategies in the design of nanoparticles for therapeutic applications. *Nature reviews. Drug discovery*, 9(8), pp.615–27.

Photos, P.J. et al., 2003. Polymer vesicles in vivo: correlations with PEG molecular weight. *Journal of Controlled Release*, 90(3), pp.323–334.

Phukan, S. et al., 2010. GSK3beta: role in therapeutic landscape and development of modulators. *British Journal of Pharmacology*, 160(1), pp.1–19.

Pittenger, M.F. et al., 1999. Multilineage potential of adult human mesenchymal stem cells. *Science*, 284(5411), pp.143–147.

Pivonka, P. & Dunstan, C.R., 2012. Role of mathematical modeling in bone fracture healing. *BoneKEy Rep*, 1:221.

Popelut, A. et al., 2010. The acceleration of implant osseointegration by liposomal Wnt3a. *Biomaterials*, 31(35), pp.9173–9181.

Pountos, I. et al., 2013. Fracture non-union: Can biomarkers predict outcome? *Injury*, 44(12), pp.1725–1732.

Prausnitz, M.R. & Langer, R., 2008. Transdermal drug delivery. *Nature Biotechnology*, 26(11), pp.1261–8.

Qin, S.H. et al., 2006. Temperature-controlled assembly and release from polymer vesicles of poly(ethylene oxide)-block-poly(N-isopropylacrylamide). *Advanced Materials*, 18(21), p.2905.

Qiu, F. et al., 2014. Real-Time Monitoring of Anticancer Drug Release with Highly Fluorescent Star-Conjugated Copolymer as a Drug Carrier. *Biomacromolecules*, 15(4), pp.1355–1364.

Quan, L.-D. et al., 2010. Pharmacokinetic and biodistribution studies of N-(2-hydroxypropyl)methacrylamide copolymer-dexamethasone conjugates in adjuvant-induced arthritis rat model. *Molecular Pharmaceutics*, 7(4), pp.1041–9.

Quarto, N., Behr, B. & Longaker, M.T., 2010. Opposite spectrum of activity of canonical Wnt signaling in the osteogenic context of undifferentiated and differentiated mesenchymal cells: implications for tissue engineering. *Tissue Engineering Part A*, 16(10), pp.3185–3197.

Rameez, S., Alosta, H. & Palmer, A.F., 2008. Biocompatible and biodegradable polymersome encapsulated hemoglobin: a potential oxygen carrier. *Bioconjugate Chemistry*, 19(5), pp.1025–1032.

Rautio, J. et al., 2008. Prodrugs: design and clinical applications. *Nature reviews. Drug discovery*, 7(3), pp.255–70.

Rawadi, G. et al., 2003. BMP-2 controls alkaline phosphatase expression and osteoblast mineralization by a Wnt autocrine loop. *Journal of Bone and Miner Research*, 18(10), pp.1842–1853.

Ren, K. et al., 2014. Macromolecular prodrug of dexamethasone prevents particle-induced peri-implant osteolysis with reduced systemic side effects. *Journal of Controlled Release*, 175, pp.1–9.

Ren, K. et al., 2016. Nanomedicine for the Treatment of Musculoskeletal Diseases. In Z.-R. Lu & S. Sakuma, eds. *Nanomaterials in Pharmacology*. New York, NY: Springer New York, pp. 389–412.

Rey, J.P. & Ellies, D.L., 2010. Wnt modulators in the biotech pipeline. *Developmental Dynamics*, 239(1), pp.102–114.

Reya, T. et al., 2003. A role for Wnt signalling in self-renewal of haematopoietic stem cells. *Nature*, 423(6938), pp.409–414.

Reya, T. & Clevers, H., 2005. Wnt signalling in stem cells and cancer. *Nature*, 434(7035), pp.843–850.

Riggs, B.L. & Melton 3rd, L.J., 1995. The worldwide problem of osteoporosis: insights afforded by epidemiology. *Bone*, 17(5 Suppl), pp.505–511.

Robling, A.G. et al., 2008. Mechanical stimulation of bone in vivo reduces osteocyte expression of Sost/sclerostin. *The Journal of Biological Chemistry*, 283(9), pp.5866–75.

van Rooijen, N. & van Kesteren-Hendrikx, E., 2002. Clodronate liposomes: perspectives in research and therapeutics. *Journal of Liposome Research*, 12(1–2), pp.81–94.

Rosenberg, G.A., 2014. Blood-Brain Barrier Permeability in Aging and Alzheimer's Disease. *The journal of prevention of Alzheimer's Disease*, 1(3), p.138.

Rucci, N., 2008. Molecular biology of bone remodelling. *Clinical cases in mineral and bone metabolism : the official journal of the Italian Society of Osteoporosis, Mineral Metabolism, and Skeletal Diseases*, 5(1), pp.49–56.

Ruge, C.A., Kirch, J. & Lehr, C.-M., 2013. Pulmonary drug delivery: from generating aerosols to overcoming biological barriers-therapeutic possibilities and technological challenges. *The Lancet. Respiratory Medicine*, 1(5), pp.402–13.

Russell, R.G.G. et al., 2008. Mechanisms of action of bisphosphonates: similarities and differences and their potential influence on clinical efficacy. *Osteoporosis international : a journal established as result of cooperation between the European Foundation for Osteoporosis and the National Osteoporosis Foundation of the USA*, 19(6), pp.733–59.

Sacchetti, B. et al., 2007. Self-Renewing Osteoprogenitors in Bone Marrow Sinusoids Can Organize a Hematopoietic Microenvironment. *Cell*, 131(2), pp.324–336.

Sahay, G., Alakhova, D.Y. & Kabanov, A. V, 2010. Endocytosis of nanomedicines. *Journal of Controlled Release*, 145(3), pp.182–195.

Salvati, A. et al., 2013. Transferrin-functionalized nanoparticles lose their targeting capabilities when a biomolecule corona adsorbs on the surface. *Nature Nanotechnology*, 8(2), pp.137–143.

Sanson, C. et al., 2010. A simple method to achieve high doxorubicin loading in biodegradable polymersomes. *Journal of Controlled Release*, 147(3), pp.428–35.

Sarahrudi, K. et al., 2011. Elevated transforming growth factor-beta 1 (TGF-β1) levels in human fracture healing. *Injury*, 42(8), pp.833–837.

Sato, N. et al., 2004. Maintenance of pluripotency in human and mouse embryonic stem cells through activation of Wnt signaling by a pharmacological GSK-3-specific inhibitor. *Nature Medicine*, 10(1), pp.55–63.

Scarpa, E. et al., 2016. Quantification of intracellular payload release from polymersome nanoparticles. *Scientific Reports*, 6, p.29460.

Schlundt, C. et al., 2015. Macrophages in bone fracture healing: Their essential role in endochondral ossification. *Bone*.

Schmidt-Bleek, K. et al., 2012. Inflammatory phase of bone healing initiates the regenerative healing cascade. *Cell and Tissue Research*, 347(3), pp.567–73.

Schneckenburger, H. et al., 2004. Fluorescence lifetime imaging (FLIM) of rhodamine 123 in living cells. *Photochemical & Photobiological Sciences : Official journal of the European Photochemistry Association and the European Society for Photobiology*, 3(1), pp.127–31.

Schugar, R.C., Robbins, P.D. & Deasy, B.M., 2007. Small molecules in stem cell self-renewal and differentiation. *Gene Therapy*, 15(2), pp.126–135.

Semmling, M. et al., 2008. A novel flow-cytometry-based assay for cellular uptake studies of polyelectrolyte microcapsules. *Small*, 4(10), pp.1763–1768.

Serhan, C.N., Chiang, N. & Dalli, J., 2015. The resolution code of acute inflammation: Novel pro-resolving lipid mediators in resolution. *Seminars in Immunology*, 27(3), pp.200–15.

Serhan, C.N. & Savill, J., 2005. Resolution of inflammation: the beginning programs the end. *Nature Immunology*, 6(12), pp.1191–7.

Shah, D.A. et al., 2011. Regulation of stem cell signaling by nanoparticle-mediated intracellular protein delivery. *Biomaterials*, 32(12), pp.3210–3219.

Shaikh, J. et al., 2009. Nanoparticle encapsulation improves oral bioavailability of curcumin by at least 9-fold when compared to curcumin administered with piperine as absorption enhancer. *European Journal of Pharmaceutical Sciences*, 37(3–4), pp.223–230.

Shapiro, F., 1988. Cortical bone repair. The relationship of the lacunar-canalicular system and itracellular gap junctions to the repair process. *The Journal of bone and joint surgery*, 70(7), pp.1067-1081.

Shen, W. et al., 2015. Inhibition of DYRK1A and GSK3B induces human β-cell proliferation. *Nature Communications*, 6, p.8372.

Shi, J. et al., 2010. Nanotechnology in drug delivery and tissue engineering: from discovery to applications. *Nano Letters*, 10(9), pp.3223–3230.

Shuai, X. et al., 2004. Micellar carriers based on block copolymers of poly(??-caprolactone) and poly(ethylene glycol) for doxorubicin delivery. *Journal of Controlled Release*, 98(3), pp.415–426.

Silkstone, D., Hong, H. & Alman, B.A., 2008. Beta-catenin in the race to fracture repair: in it to Wnt. *Nature Clinical Practice Rheumatology*, 4(8), pp.413–419.

Simmons, P.J. & Torok-Storb, B., 1991. Identification of stromal cell precursors in human bone marrow by a novel monoclonal antibody, STRO-1. *Blood*, 78(1), pp.55–62.

Simpson, D.M. & Ross, R., 1972. The neutrophilic leukocyte in wound repair a study with antineutrophil serum. *The Journal of Clinical Investigation*, 51(8), pp.2009–23.

Sineva, G.S. & Pospelov, V.A., 2010. Inhibition of GSK3beta enhances both adhesive and signalling activities of beta-catenin in mouse embryonic stem cells. *Biology of the cell / under the auspices of the European Cell Biology Organization*, 102(10), pp.549–60.

Sisask, G. et al., 2013. Rats treated with AZD2858, a GSK3 inhibitor, heal fractures rapidly without endochondral bone formation. *Bone*, 54(1), pp.126–132.

Sjöback, R., Nygren, J. & Kubista, M., 1995. Absorption and fluorescence properties of fluorescein. *Spectrochimica Acta Part A: Molecular and Biomolecular Spectroscopy*, 51(6), pp.7–21.

Skoglund, B., Forslund, C. & Aspenberg, P., 2002. Simvastatin improves fracture healing in mice. *Journal of Bone and Mineral Research*, 17(11), pp.2004–8.

Smus, J.P. et al., 2015. Tracking adipogenic differentiation of skeletal stem cells by label-free chemically selective imaging. *Chemical Science*, 6(12), pp.7089–7096.

Song, L. et al., 2012. Loss of wnt/beta-catenin signaling causes cell fate shift of preosteoblasts from osteoblasts to adipocytes. *Journal of Bone and Miner Research*, 27(11), pp.2344–2358.

Sood, N. et al., 2013. Biodegradable Polymersomes for the Delivery of Gemcitabine to Panc-1 Cells. *Journal of Pharmaceutics*, 2013, pp.1–10.

Sorrell, I. et al., 2014. Combined mathematical modelling and experimentation to predict polymersome uptake by oral cancer cells. *Nanomedicine*, 10(2), pp.339–348.

van Staa, T.P. et al., 2001. Epidemiology of fractures in England and Wales. *Bone*, 29(6), pp.517–522.

Stevens, M.M., 2008. Biomaterials for bone tissue engineering. *Materials Today*, 11(5), pp.18–25.

Stevenson, M. et al., 2007. The clinical effectiveness and cost-effectiveness of strontium ranelate for the prevention of osteoporotic fragility fractures in postmenopausal women. *Health Technology Assessment,* 11(4), pp.1–134.

Straubinger, R.M. et al., 1983. Endocytosis of liposomes and intracellular fate of encapsulated molecules: encounter with a low pH compartment after internalization in coated vesicles. *Cell*, 32(4), pp.1069–1079.

Street, J. et al., 2000. Is human fracture hematoma inherently angiogenic? *Clinical Orthopaedics and Related Research*, (378), pp.224–37.

Street, J. et al., 2002. Vascular endothelial growth factor stimulates bone repair by promoting angiogenesis and bone turnover. *Proceedings of the National Academy of Sciences*, 99(15), pp.9656–61.

Sturgeon, C.M. et al., 2014. Wnt signaling controls the specification of definitive and primitive hematopoiesis from human pluripotent stem cells. *Nature Biotechnology*, 32(6), pp.554–561.

Suen, P.K. et al., 2014. Sclerostin monoclonal antibody enhanced bone fracture healing in an open osteotomy model in rats. *Journal of Orthopedic Research*, 32(8), pp.997–1005.

Summers, H.D. et al., 2013. Quantification of Nanoparticle Dose and Vesicular Inheritance in Proliferating Cells. *ACS Nano*, 7(7), pp.6129–6137.

Summers, H.D. et al., 2011. Statistical analysis of nanoparticle dosing in a dynamic cellular system. *Nature nanotechnology*, 6(3), pp.170–174.

Sun, H. et al., 2006. The in vivo degradation, absorption and excretion of PCL-based implant. *Biomaterials*, 27(9), pp.1735–1740.

Swami, A. et al., 2014. Engineered nanomedicine for myeloma and bone microenvironment targeting. *Proceedings of the National Academy of Sciences,* 111(28), pp.10287–10292.

Tarantino, U. et al., 2010. Strontium Ranelate and bone healing: report of two cases. *Clinical Cases in Mineral and Bone Metabolism,* 7(1), pp.65–8.

Tare, R.S. et al., 2012. Isolation, Differentiation, and Characterisation of Skeletal Stem Cells from Human Bone Marrow In Vitro and In Vivo. *Methods in Molecular Biology,* pp. 83–99.

Tashjian, A.H. & Gagel, R.F., 2006. Teriparatide [Human PTH(1-34)]: 2.5 Years of Experience on the Use and Safety of the Drug for the Treatment of Osteoporosis. *Journal of Bone and Mineral Research*, 21(3), pp.354–365.

Tavassoli, M. & Crosby, W.H., 1968. Transplantation of marrow to extramedullary sites. *Science*, 161(3836), pp.54–6.

Tiwari, S.K. et al., 2014. Curcumin-loaded nanoparticles potently induce adult neurogenesis and reverse cognitive deficits in Alzheimer's disease model via canonical Wnt/beta-catenin pathway. *ACS Nano*, 8(1), pp.76–103.

Torchilin, V.P., 2005. Recent advances with liposomes as pharmaceutical carriers. *Nature reviews. Drug Discovery*, 4(2), pp.145–60.

Trusheim, M.R., Berndt, E.R. & Douglas, F.L., 2007. Stratified medicine: strategic and economic implications of combining drugs and clinical biomarkers. *Nature Reviews Drug Discovery*, 6(4), pp.287–293.

Ulery, B.D., Nair, L.S. & Laurencin, C.T., 2011. Biomedical Applications of Biodegradable Polymers. *Journal of Polymer Science. Part B, Polymer physics*, 49(12), pp.832–864.

Unciti-Broceta, J.D. et al., 2015. Number of Nanoparticles per Cell through a Spectrophotometric Method - A key parameter to Assess Nanoparticle-based Cellular Assays. *Scientific Reports*, 5, p.10091.

Veeman, M.T., Axelrod, J.D. & Moon, R.T., 2003. A second canon. Functions and mechanisms of beta-catenin-independent Wnt signaling. *Developmental Cell*, 5(3), pp.367–377.

Virk, M.S. et al., 2013. Systemic administration of sclerostin antibody enhances bone repair in a critical-sized femoral defect in a rat model. *The Journal of Bone and Joint Surgery*, 95(8), pp.694–701.

Vougogiannopoulou, K. et al., 2008. Soluble 3',6-substituted indirubins with enhanced selectivity toward glycogen synthase kinase -3 alter circadian period. *Journal of Medical Chemistry*, 51(20), pp.6421–6431.

Walkey, C.D. et al., 2012. Nanoparticle size and surface chemistry determine serum protein adsorption and macrophage uptake. *Journal of the American Chemistry Society*, 134(4), pp.2139–2147.

Wallace, S.J. et al., 2012. Drug release from nanomedicines: Selection of appropriate encapsulation and release methodology. *Drug Delivivery and Translational Research*, 2(4), pp.284–292.

Wang, Y. et al., 2014. Plasticity of mesenchymal stem cells in immunomodulation:

pathological and therapeutic implications. *Nature Immunology*, 15(11), pp.1009–1016.

Wang, Y. & Grainger, D.W., 2012. RNA therapeutics targeting osteoclast-mediated excessive bone resorption. *Advanced drug delivery reviews*, 64(12), pp.1341–57.

Watanabe, T. et al., 2012. Increasing participation of sclerostin in postnatal bone development, revealed by three-dimensional immunofluorescence morphometry. *Bone*, 51(3), pp.447–458.

Wayakanon, K. et al., 2013. Polymersome-mediated intracellular delivery of antibiotics to treat Porphyromonas gingivalis-infected oral epithelial cells. *FASEB Journal*, 27(11), pp.4455–4465.

Weinstein, J.N. et al., 1978. Antibody-mediated targeting of liposomes. Binding to lymphocytes does not ensure incorporation of vesicle contents into the cells. *Biochimica et Biophysica Acta*, 509(2), pp.272–288.

Weinstein, J.N. et al., 1977. Liposome-cell interaction: transfer and intracellular release of a trapped fluorescent marker. *Science*, 195(4277), pp.489–492.

Wilkins, K.E., 2005. Principles of fracture remodeling in children. *Injury*, 36 Suppl 1, pp.3-11.

Willenborg, S. et al., 2012. CCR2 recruits an inflammatory macrophage subpopulation critical for angiogenesis in tissue repair. *Blood*, 120(3), pp.613–25.

Winnard, P.T., Kluth, J.B. & Raman, V., 2006. Noninvasive optical tracking of red fluorescent protein-expressing cancer cells in a model of metastatic breast cancer. *Neoplasia*, 8(10), pp.796–806.

Wong, E. et al., 2013. A novel low-molecular-weight compound enhances ectopic bone formation and fracture repair. *The Journal of Bone and Joint Surgery,* 95(5), pp.454–61.

Woodruff, M.A. & Hutmacher, W., 2010. The return of a forgotten polymer: Polycaprolactone in the 21st century. *Progress in Polymer Science*, 35(10), pp.1217-1256.

Worthley, D. et al., 2015. Gremlin 1 identifies a skeletal stem cell with bone, cartilage, and reticular stromal potential. *Cell*, 160(1-2), pp.269-284.

Wu, A.C. et al., 2013. Unraveling macrophage contributions to bone repair. *BoneKEy reports*, 2, p.373.

Wu, Y. et al., 2015. GSK3 inhibitors CHIR99021 and 6-bromoindirubin-3′-oxime inhibit microRNA maturation in mouse embryonic stem cells. *Scientific Reports*, 5, p.8666.

Xiao, Z. et al., 2002. Indirubin and meisoindigo in the treatment of chronic myelogenous leukemia in China. *Leukemia & Lymphoma*, 43(9), pp.1763–8.

Xin, H. et al., 2011. Angiopep-conjugated poly(ethylene glycol)-co-poly(epsilon-caprolactone) nanoparticles as dual-targeting drug delivery system for brain glioma. *Biomaterials*, 32(18), pp.4293–4305.

Xing, Z. et al., 2010. Multiple roles for CCR2 during fracture healing. *Disease Models & Mechanisms*, 3(7–8), pp.451–8.

Xu, H. et al., 2014. Role of Wnt signaling in fracture healing. *BMB reports*, 47(12), pp.666–72.

Yuan, F. et al., 2012. Development of macromolecular prodrug for rheumatoid arthritis. *Advanced Drug Delivery Reviews*, 64(12), pp.1205–19.

Zahoor, M. et al., 2014. Indirubin-3'-oxime reverses bone loss in ovariectomized and hindlimb-unloaded mice via activation of the Wnt/β-catenin signaling. *Journal of Bone and Mineral Research*, 29(5), pp.1196–205.

Zahoor, M., Cha, P.H. & Choi, K.Y., 2014. Indirubin-3'-oxime, an activator of Wnt/beta-catenin signaling, enhances osteogenic commitment of ST2 cells and restores bone loss in high-fat diet-induced obese male mice. *Bone*, 65, pp.60–68.

Zamani, A., Omrani, G.R. & Nasab, M.M., 2009. Lithium's effect on bone mineral density. *Bone*, 44(2), pp.331–334.

Zhang, H. et al., 2006. Microfluidic Production of Biopolymer Microcapsules with Controlled Morphology. *Journal of the American Chemical Society*, 128(37), pp.12205–12210.

Zhang, L. et al., 2012. Paclitaxel-loaded polymeric micelles based on poly(varepsilon-caprolactone)-poly(ethylene glycol)-poly(varepsilon-caprolactone) triblock copolymers: in vitro and in vivo evaluation. *Nanomedicine*, 8(6), pp.925–934.

Zhu, Z., 2014. Flash nanoprecipitation: prediction and enhancement of particle stability via drug structure. *Molecular Pharmaceutics*, 11(3), pp.776–786.

Zimmermann, G. et al., 2009. Treatment of tibial shaft non-unions: bone morphogenetic proteins versus autologous bone graft. *Injury*, 40 Suppl 3, pp.50-53.

Appendix

7.1 Materials and methods

Polymersomes production	Supplier
α-amino-ω-hydroxy terminated NH_2-PEG (5.8k)-b-PCL (19k)	Polymer Source Inc
PEG (5k)-b-PCL (18k)	Polymer Source Inc
Fluorescein	Sigma Aldrich
BIO	Sigma Aldrich
DMF	Sigma Aldrich
PBS	
0.22 μm filters	Minisart
Dialysis tubing (10,000 MWCO)	Sigma Aldrich
Sephadex columns (G-25)	Sigma Aldrich
DiR	Perkin Elmer
DiI	Sigma Aldrich

Polymersomes production

Medium and reagents used for L929, MG63 and murine 3T3 reporter cells	Supplier
DMEM supplemented with:	Sigma Aldrich
10 % FBS (v/v)	Gibco
100 U/ml penicillin and 100 μg/ml streptomycin	PAA
Trypsin	Lonza
Medium and reagents used for BMMNCs isolation	
αMEM with 2.2 g of sodium bicarbonate supplemented with:	Gibco
100 U/ml penicillin and 100 μg/ml streptomycin	PAA
LymphoprepTM Density Gradient Medium	Axis-Shield
Virkon tablets	DuPont
Trypan blue	Sigma Aldrich
Easy Lyse Erythrocyte Lysing Reagent	Dako
Medium and reagents used for BMMNCs culture (basal)	
αMEM with 2.2 g of sodium bicarbonate supplemented with:	Gibco
10 % FBS (v/v)	Gibco
100 U/ml penicillin and 100 μg/ml streptomycin	PAA
Trypsin	Lonza
Medium used for BMMNCs culture (osteogenic)	
αMEM supplemented with:	Gibco
10 % FBS (v/v)	Gibco
100 U/ml penicillin and 100 μg/ml streptomycin	PAA
100 μM sodium-2-ascorbate	Sigma Aldrich
5 mM β-glycerophosphate	Sigma Aldrich
10 nM dexamethasone	Sigma Aldrich
Trypsin	Lonza

Cell culture reagents

Confocal microscopy	Supplier
Hoechest 33342	Life Technologies

Confocal microscopy

Solutions and reagents used for Flow cytometry and Image Stream	Supplier	Concentration
MACS buffer for washed and staining		
PBS		
0.5 % BSA	Sigma Aldrich	
2 mM EDTA	Promega	
Flow cytometry blocking buffer		
PBS		
1 % BSA (v/v)	Sigma Aldrich	
2 mM EDTA	Promega	
3 % goat (v/v)	Sigma Aldrich	
Permeabilisation buffer		
PBS		
0.1 % Triton X-100	Sigma Aldrich	
Primary antibodies		
Mouse anti-human STRO-1 IgM	R&D systems	1 in 100
Mouse Isotype control IgM from murine myeloma	Invitrogen	1 in 40
Mouse anti-human CD14 Pacific Blue	BioLegend	1 in 20
Mouse Isotype control IgG1 Pacific Blue	BioLegend	1 in 40
Mouse anti-human GPA PE	BioLegend	1 in 40
Mouse Isotype control IgG2a PE	BioLegend	1 in 40
Mouse anti-human LAMP1 PE	BioLegend	1 in 40
Mouse Isotype control IgG1 PE	BioLegend	1 in 40
Secondary antibodies		
Goat anti-mouse IgM AF488	Invitrogen	1 in 200
MACS rat anti-mouse IgM microbeads	Miltenyi Biotec	1 in 10

Reagents for flow cytometry and Image Stream

AlamarBlue assay	Supplier
AlamarBlue reagent	Thermo Fisher

AlamarBlue assay

Medium and reagents used for murine 3T3 Wnt reporter cells assay	Supplier
αMEM with 2.2 g of sodium bicarbonate supplemented with:	Sigma Aldrich
5 % FBS (v/v)	Gibco
100 U/ml penicillin and 100 μg/ml streptomycin	PAA
25 mM HEPES	Fisher
Luciferase substrate and buffer Steady Glo	Promega
Wnt3A protein	R&D systems
Trypsin	Lonza

Luciferase assay

qRT-PCR assay	Supplier
RNeasy Mini Kit	Qiagen
SuperScript® VILO™ cDNA Synthesis Kit	Invitrogen
SYBR Green PCR Master Mix	Applied Biosystems

qRT-PCR

Abbreviation	Gene and transcript ID	Gene name	Sequence	Product length
Wnt target genes				
AXIN2	Gene ID: 8313 NM_004655.3	axin-2; axin-like protein; axis inhibition protein 2; conductin	F:5'CAAGGGCCAGGTCACCAA3' R:5'CCCCCAACCCATCTTCG3'	68bp
CMYC	Gene ID: 4609 NM_002467.4	myelocytomatosis viral oncogene homolog; proto-oncogene c-Myc	F:5'CACCACCAGCAGCGACTC3' R:5'GCCTGCCTCTTTTCCACA3'	78bp
CCND1	Gene ID: 595 NM_053056.2	cyclin D1	F:5'CTACCGCCTCACACGCTT3' R:5'CTTGGGGTCCATGTTCTGC3'	130bp
Osteogenic genes				
SP7	Gene ID: 121340 NM_001173467.1	Osterix; Sp7 transcription factor	F:5'ATGGGCTCCTTTCACCTG3' R:5'GGGAAAAGGGAGGGTAATC3'	75bp
RUNX2	Gene ID: 860 NM_001024630.3	runt-related transcription factor 2; CBF-alpha-1	F:5'GTAGATGGACCTCGGGAACC3' R:5'GAGGCGGTCAGAGAACAAAC3'	78bp
Housekeeping genes				
ACTB	Gene ID: 60 NM_001101.3	actin beta	F:5'GGCATCCTCACCCTGAAGTA3' R:5'AGGTGTGGTGCCAGATTTTC3'	82bp
GAPDH	Gene ID: 2597 NM_001289745.1	glyceraldehyde-3-phosphate dehydrogenase; G3PD; GAPD	F:5'CCAGGTGGTCTCCTCTGACTTC3' R:5'TCATACCAGGAAATGAGCTTGACA3'	108bp

Primers used in the qRT-PCR

PicoGreen assay	Supplier
Quant-iT™ PicoGreen® dsDNA reagent	Thermo Fisher
Lambda DNA standard	Thermo Fisher

PicoGreen assay

Alkaline phosphatase activity assay	Supplier
CelLytic	Sigma Aldrich
0.04 g Alkaline phosphatase substrate	Sigma Aldrich
5 ml 1.5 M Alkaline buffer solution (Sigma)	Sigma Aldrich
20 ml dH2O	
Alkaline phosphatase standard	Sigma Aldrich

Alkaline phosphatase assay

Histological analysis	Supplier
OCT	Thermo Fisher
Histoclear	National Diagnostics
Paraffin	Leica
Hydromount	National Diagnostics
DAPI	Sigma

Reagents for histology

Hematoxylin and Eosin staining	Time (minutes)
Histoclear	7
Histoclear	7
Ethanol 100%	2
Ethanol 100%	2
Ethanol 90%	2
Ethanol 50%	2
Water	2
Weigert's haematoxylin (A+B)	8
Water	1
1% acidic alcohol	15 sec
Water	3
Eosin	12
Ethanol 50%	1
Ethanol 90%	1
Ethanol 100%	1
Ethanol 100%	1
Histoclear	1
Histoclear	1
Mount in DPX	

Haematoxylin and Eosin staining

Tetrachrome staining	Time (minute)
Histoclear	7
Histoclear	7
Ethanol 100%	2
Ethanol 100%	2
Ethanol 90%	2
Ethanol 50%	2
Water	2
Weigert's haematoxylin (A+B)	8
Water	1
1% acidic alcohol	15 sec
Water	1
Eosin	12
Ethanol 90%	2
1 % Phosophotungstic acid	5
0.1 % Anilin blue in 1 % acetic acid	8
Water	1
1 % Orange G in saturated picric acid, 1 in 10	3
Water	1
2 % ponceau 2R in 1 % acetic acid and 2 % crystal ponceau in 1 % acetic acid, 4:1 ratio	6
Water	1
Ethanol 50%	1
Ethanol 90%	1
Ethanol 100%	1
Ethanol 100%	1
Histoclear	1
Histoclear	1
Mount in DPX	

Tetrachrome staining

Equipment	Supplier
BD FACS Canto II	BD Biosciences
BD FACS Calibur	BD Biosciences
Centrifuge Megafuge 1.0R	Heraeus
Centrifuge 5415R	Eppendorf
Crytome Microm H500 Cryostat	Thermo Fisher
DLS	Malvern
ELx800 colorimetric microplate reader	Biotek
Extruder	Avanti Polar Lipids
FACS Guava	Merk Millipore
FLx800 fluorescence microplate reader	Biotek
FluoroMax-4	Horiba Scientific
ImageStream X MkII	Merk Millipore
IVIS Lumnia III	Perkin Elmer
MACSmixTM tube rotator	Miltenyi Biotec
Microscope	Zeiss Axiovert
Microscope	Nikon
Microscope Confocal	Leica
Microtome HM355 S	Microm International GmbH
NanoDrop ND-1000	Thermo Fisher
NanoDrop ND-2000c	Thermo Fisher
NanoSight LM-10	Malvern
PCR machine Veriti	Applied Biosystems
Real-Time PCR system 7500	Applied Biosystems
Skyscan 1179	Burker
Ultracentrifuge Optima Max	Beckman Coulter
VarioscanFlash luminometric microplate reader	Thermo Scientific

Equipment

7.2 Chapter 3: supplementary data

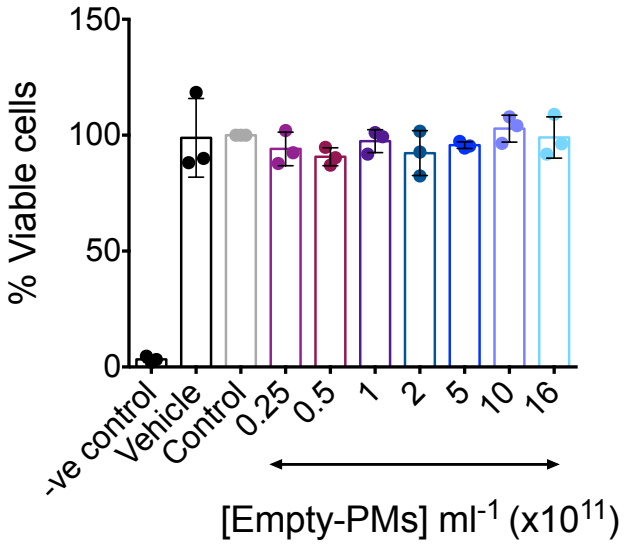

Appendix Figure 1: **PMs do not induce cytotoxicity.**

Bar chart depicting no difference in percentage of viable L929 cells after 24 hours incubation with increasing concentrations of empty-PMs formed using 5.8k-19k copolymer compared to untreated cells (control). Vehicle was represented by PBS and –ve control was water.

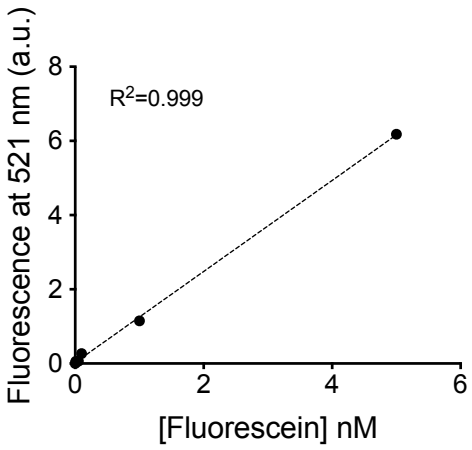

Appendix Figure 2: **Standard curve of fluorescein fluorescence.**

Graph depicting the intensity of fluorescence of increasing concentrations of fluorescein in a solution containing cell lysate measured by spectrophotometry (at λ = 521 nm).

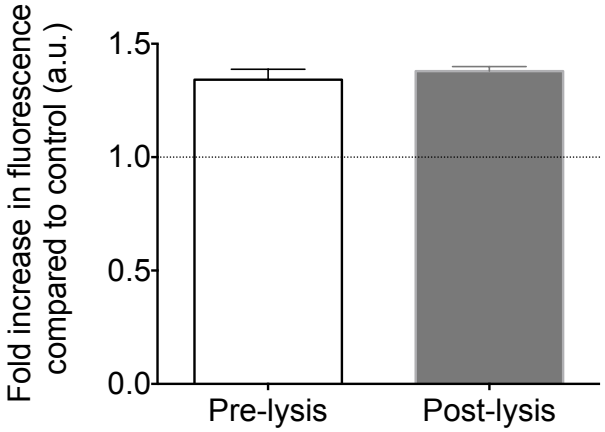

Appendix Figure 3: **Fluorescence pre- and post-lysis.**

Relative levels of fluorescence of L929 cells incubated with fluorescein- PMs *pre*- and *post*-lysis. Fluorescence is normalised against autofluorescence from control cells where no fluorescein-PMs were added (dashed line). Data presented as mean ± SD, n=3.

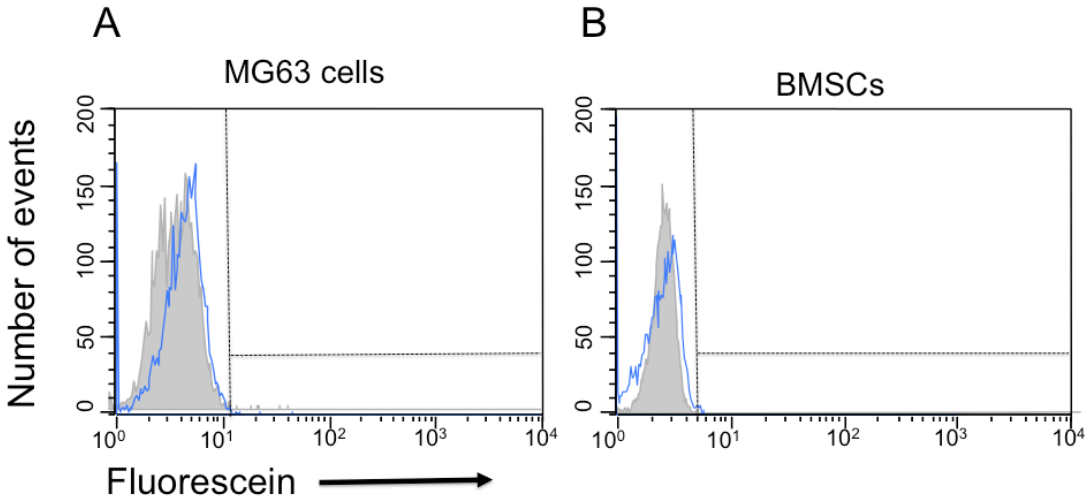

Appendix Figure 4: **Empty-PMs do not produce detectable fluorescein signal following incubation with MG63 cells or BMSCs.**

A: Representative flow cytometry histogram of MG63 cells incubated for 24 hours (blue) with empty-PMs showing negligible difference in terms of fluorescence intensity between treated cells and untreated control (grey). **B:** Representative flow cytometry histogram of BMSC incubated for 24 hours (blue) with empty-PMs showing negligible difference in terms of fluorescence intensity between treated cells and untreated control (grey).

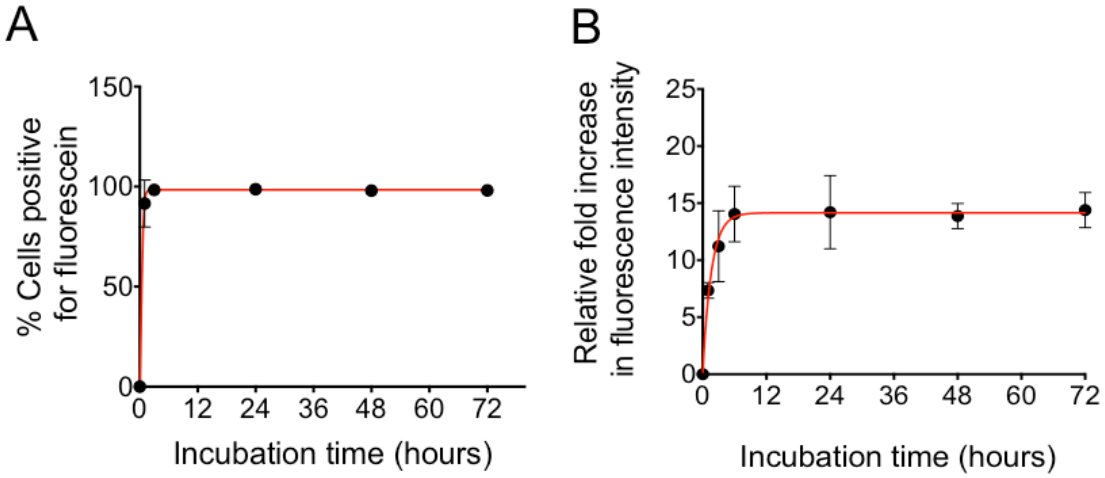

Appendix Figure 5: **Saturation of fluorescein-PM internalisation by BMMNCs.**

A: Graph depicting the progressive increase in the percentage of cells positive for fluorescein over-time. (*n*=3, mean ± SD). **B:** Graph depicting saturation in relative increase in mean fluorescence intensity of cells incubated with fluorescein-PMs at 6 hours post incubation. Data presented as mean ± SD, *n*=3.

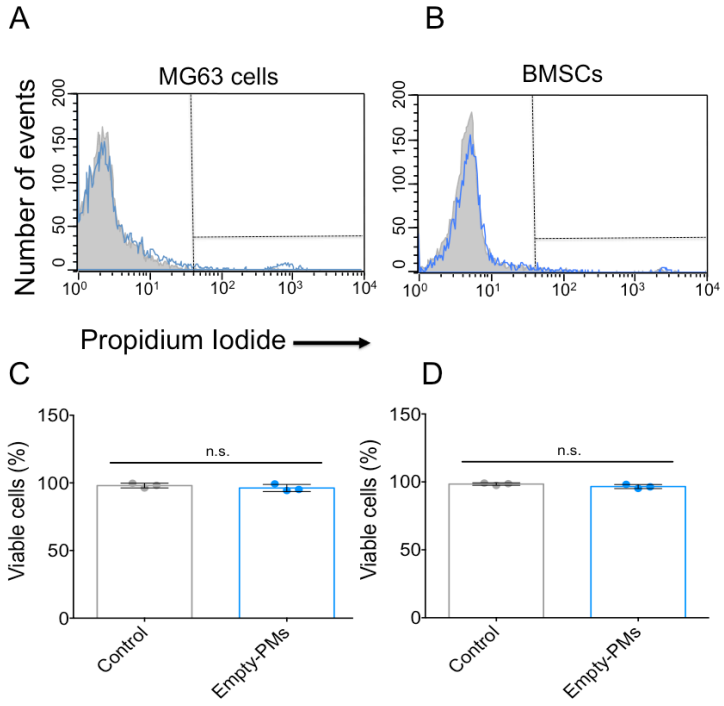

Appendix Figure 6: **Empty-PMs do not induce cytotoxicity in MG63 cells or BMSCs**

A: Representative histogram of MG63 cells incubated for 24 hours (blue) with empty-PMs. **B:** Representative histogram of BMSCs incubated for 24 hours (blue) with empty-PMs. Both graphs show the negligible difference in terms of fluorescence intensity between treated cells and untreated control (grey). **C:** Histogram showing the percentage of viable MG63 cells after 24 hour incubation with empty-PMs. **D:** Histogram showing the percentage of viable BMSCs after 24 hour incubation with empty-PMs. Data presented as mean ± SD, one-way ANOVA, with Dunn's post-hoc correction, *n*=3. Multiple comparison: ns = non significant.

7.2.1 Characterisation of polymersomes produced using the 5k-18k copolymer.

Due to cessation of manufacture of the NH_2–PEG 5.8k-PCL 19k polymer, and due to an unavoidable limitation in its supply for making PMs, another polymer, 5k-18k, was used and PMs produced were investigated for their ability to deliver fluorescein intracellularly.

Fluorescein-PMs produced using 5k-18k block copolymer had the same orange colouration observed using the other block copolymer, but their hydrodynamic size was notably smaller compared to the other preparation (61.15 nm, PdI of 0.181 *vs.* 86 nm, PdI of 0.103) (Appendix Figure 7A & B). Using NTA, it was measured a concentration of 1.5 x 10^{13} fluorescein-PMs ml^{-1} (Appendix Figure 7C), and using light absorbance it was measured that a concentration of 10.85 ± 3.90 μM of fluorescein was stably present in the bulk solution of PMs for one week (Appendix Figure 7D). This concentration is ~24 fold less than in the other preparation (Figure 3.2), and resulted in an average of 7.23 x 10^{-22} moles of fluorescein loaded *per* PMs, which is ~7.5 fold less than the 5.48 x 10^{-21} moles calculated in the other fluorescein-PMs.

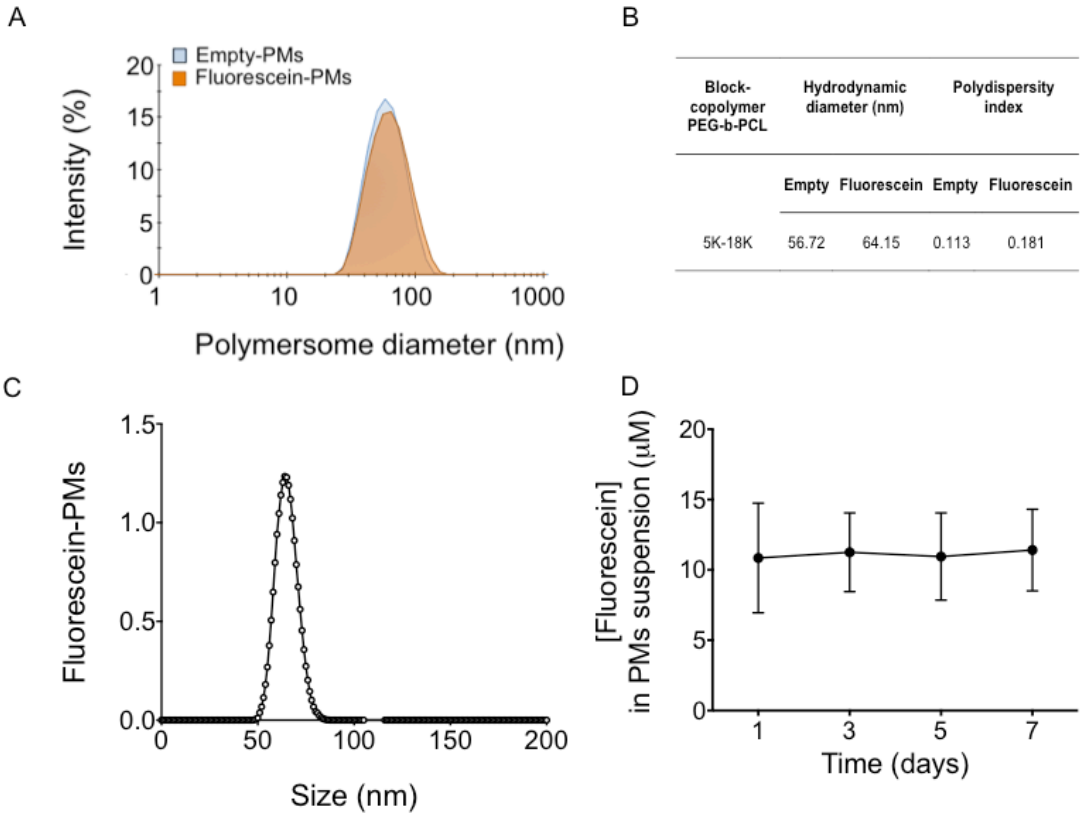

Appendix Figure 7: **Physical characterisation of PMs produced using 5k-18k block copolymer and loaded with fluorescein.**

A: Representative histogram from DLS measurements showing the narrow distribution of the hydrodynamic diameter of both empty- and fluorescein-PMs formed from 5k-18k block copolymer. **B:** Summary of size and PDI of empty and fluorescein-PMs. **C:** Dot plot derived from NTA depicting size and concentration *per* ml of fluorescein-PMs. **D:** Graph showing the concentration of fluorescein present in solution (10.85 ± 3.90 μM) as well as fluorescein retention in PMs over the course of one week measured by light absorbance (at λ = 494 nm). Data presented as mean ± SD, *n*=3.

7.2.2 Uptake of fluorescein-loaded PMs formed by the 5k-18k block copolymer in cultured BMSCs.

Next it was validated whether this new type of fluorescein-PMs were also internalised with similar kinetics to the previous preparation. BMSCs were incubated with fluorescein-PMs for 24 hours, time at which cells showed saturation of fluorescein with the previous PM formulation, and uptake was assessed by flow cytometry. Appendix Figure 8, graphs A and B show that 99.4 ± 0.17% of the cells stained positively for fluorescein, similar to the previous preparation (98 ± 1.1%) (Figure 3.13). However, the relative cellular fluorescence intensity measured following 24 hours incubation with the

new preparation (9.3 ± 0.2 fold increase over control, (Appendix Figure 8C) was reduced compared to the old type of PMs (14.2 ± 3.2 fold increase over control).

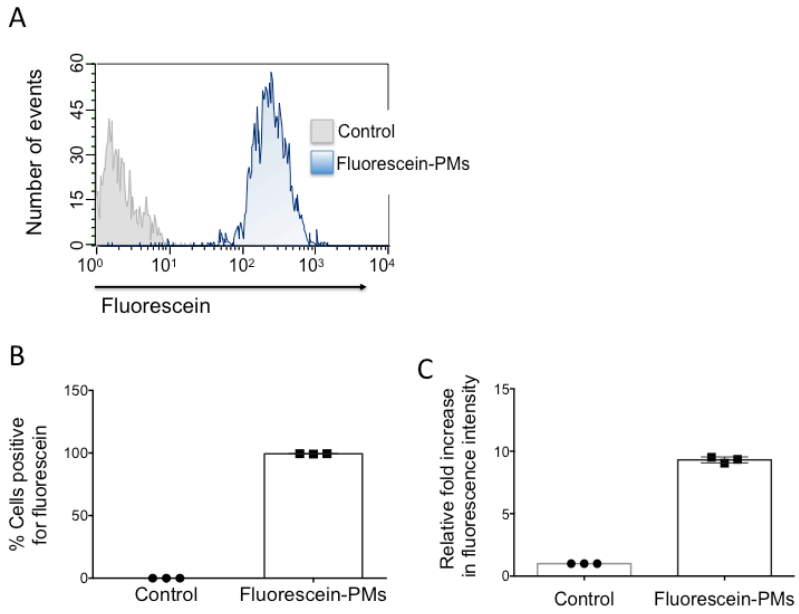

Appendix Figure 8: **BMSCs uptake 5k-18k fluorescein-PMs.**

A: Representative flow cytometry histogram plot of BMSCs incubated for 24 hours (blue) with 5k-18k fluorescein-PMs. The graph shows the progressive increase in fluorescence intensity of cells treated with fluorescein-PMs compared to 99% of the control untreated cells (grey). Dotted lines indicate the markers set to discriminate between positive and negative cells. **B:** Graph depicting the percentage of cells positive for fluorescein after 24 hours incubation with 5k-18k fluorescein-PMs. Data presented as mean ± SD, *n*=3. **D:** Graph depicting relative increase in mean fluorescence intensity of cells incubated with fluorescein-PMs 24 hours. Data presented as mean ± SD, *n*=3.

7.2.3 Quantification of uptake of new PMs and fluorescein release in BMSCs

Having demonstrated that the two PM preparations differ not only in their physical properties (size and concentration of fluorescein loaded), but also in the concentration of fluorescein delivered intracellularly, as shown by the reduced cellular fluorescence intensity measured after 24 hours incubation, it was decided to quantify the number of PMs releasing fluorescein intracellularly with this new formulation.

After 24 hours incubation with 1.5 x 10^{12} Fluorescein-PMs, BMSCs had an average intracellular concentration of fluorescein equal to 1.37 x 10^{-10} nanomoles *per* cell (Appendix Figure 9), which is 3.3 fold less than the concentration measured using fluorescein-PMs formed from the 5.8k-19k polymer (Figure 3.16).

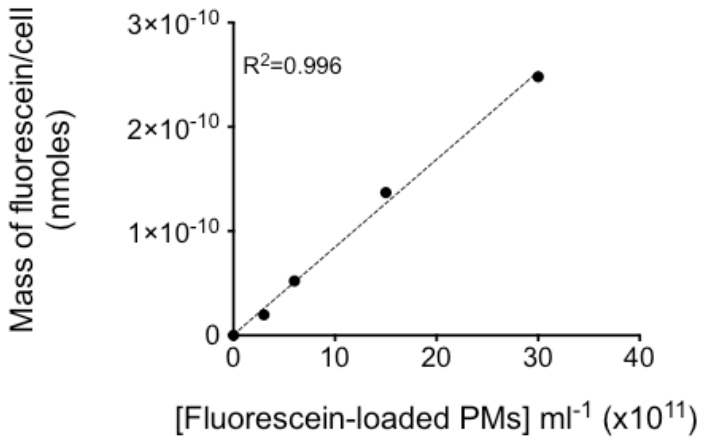

Appendix Figure 9: **Estimation of the concentration of fluorescein released in BMMNCs from PMs formed from 5k-18k copolymer.**

Graph showing the linear relationship between the mass of fluorescein *per* cell and the concentration of fluorescein-PMs (formed using the 5k-18k block copolymer) incubated with BMMNCs. $R^2 = 0.996$.

Having calculated that 7.23×10^{-22} moles of fluorescein are loaded in each PM (see section 3.2.6), it was estimated that on average 189 ± 8 PMs have released payload in BMSCs. This value is ~2.8 fold more than what was calculated using the other PM preparation, and it is in close agreement with flow cytometry data which resulted in a median of 203 PMs releasing fluorescein intracellularly *per* cell (Appendix Figure 10).

A

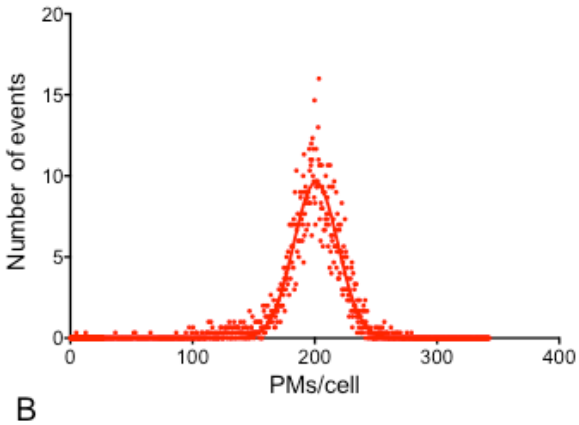

B

Estimated number of PMs releasing fluorescein *per* cell			
Min	**Max**	**Range**	**Median**
32 ± 47	275 ± 4	243 ± 47	203

Appendix Figure 10: **Quantification of the number of 5k-18k PMs releasing fluorescein in BMMNCs at single cell level.**

A: Representative graph depicting the number of PMs releasing fluorescein intracellularly *per* cell after incubation with 5k-18k fluorescein-PMs. **B:** Table summarising the minimum (Min), maximum (Max), range (Max-Min) and median number of PMs *per* cell after incubation with 5k-18k fluorescein-PMs.

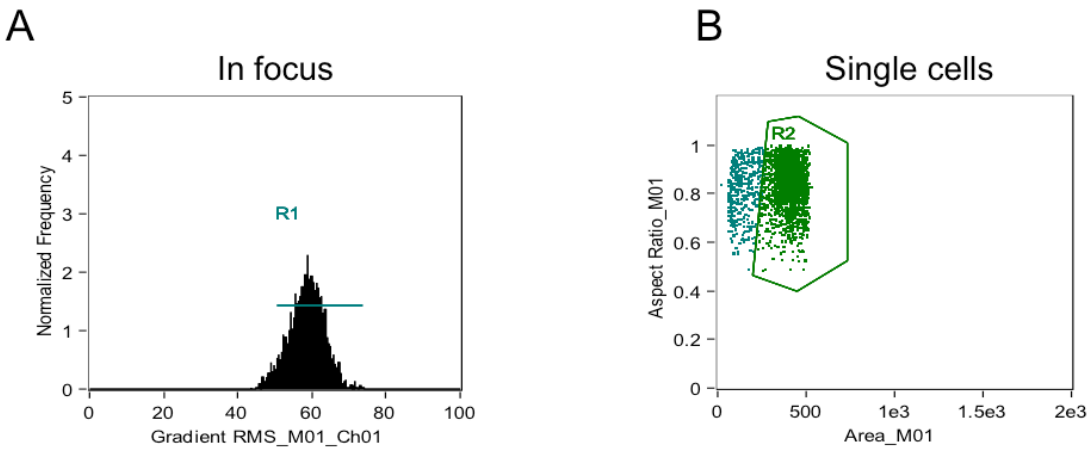

Appendix Figure 11: **Image Stream gating strategy for assessment of fluorescein and LAMP-1 co-localisation.**

A: Histogram showing the population of cells which was considered 'in focus' after acquisition. R1 is the gate set to analyse the following sub-population. **B:** Dot plot showing the cells in focus (R1 from A) and divided in single cells or doublets according to their physical parameters (Area and Aspect Ratio). R2 is the gate indicating single cells.

7.3 Chapter 4: supplementary data

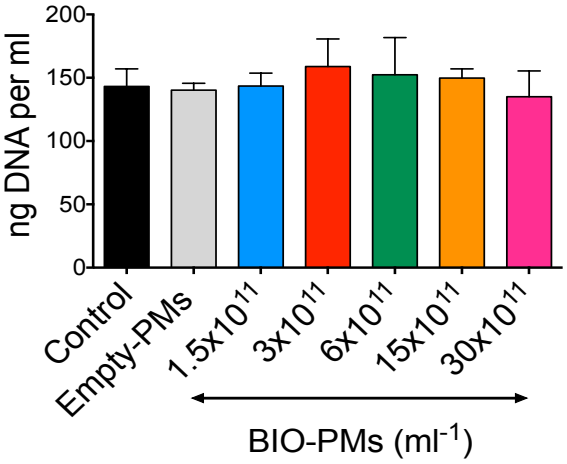

Appendix Figure 12: **Wnt reporter cells proliferation following 24 hours incubation with BIO-PMs.**

3T3 luciferase reporter cells were incubated for ~24 hours increasing concentrations of BIO-PMs and then the total amount of double strand DNA was quantified using PicoGreen assay. No statistical significant difference was found among the groups investigated. (n=3, mean ± SD, one-way ANOVA).

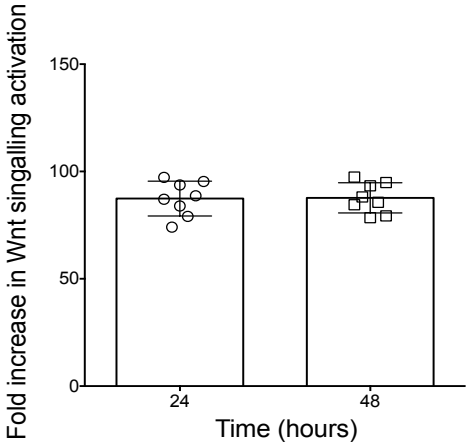

Appendix Figure 13: **Activity of 5 μM BIO after 24 or 48 hours incubation.**

Bar chart showing the lack of differences in activity between 5 μM BIO after incubation on reporter cells for 24 or 48 hours. (n=8, mean ± SD, student t-test). Values are normalised against untreated cells, and are expressed as relative activation of cells treated with 5 μM BIO for 24 hours.

7.4 Chapter 5: supplementary data

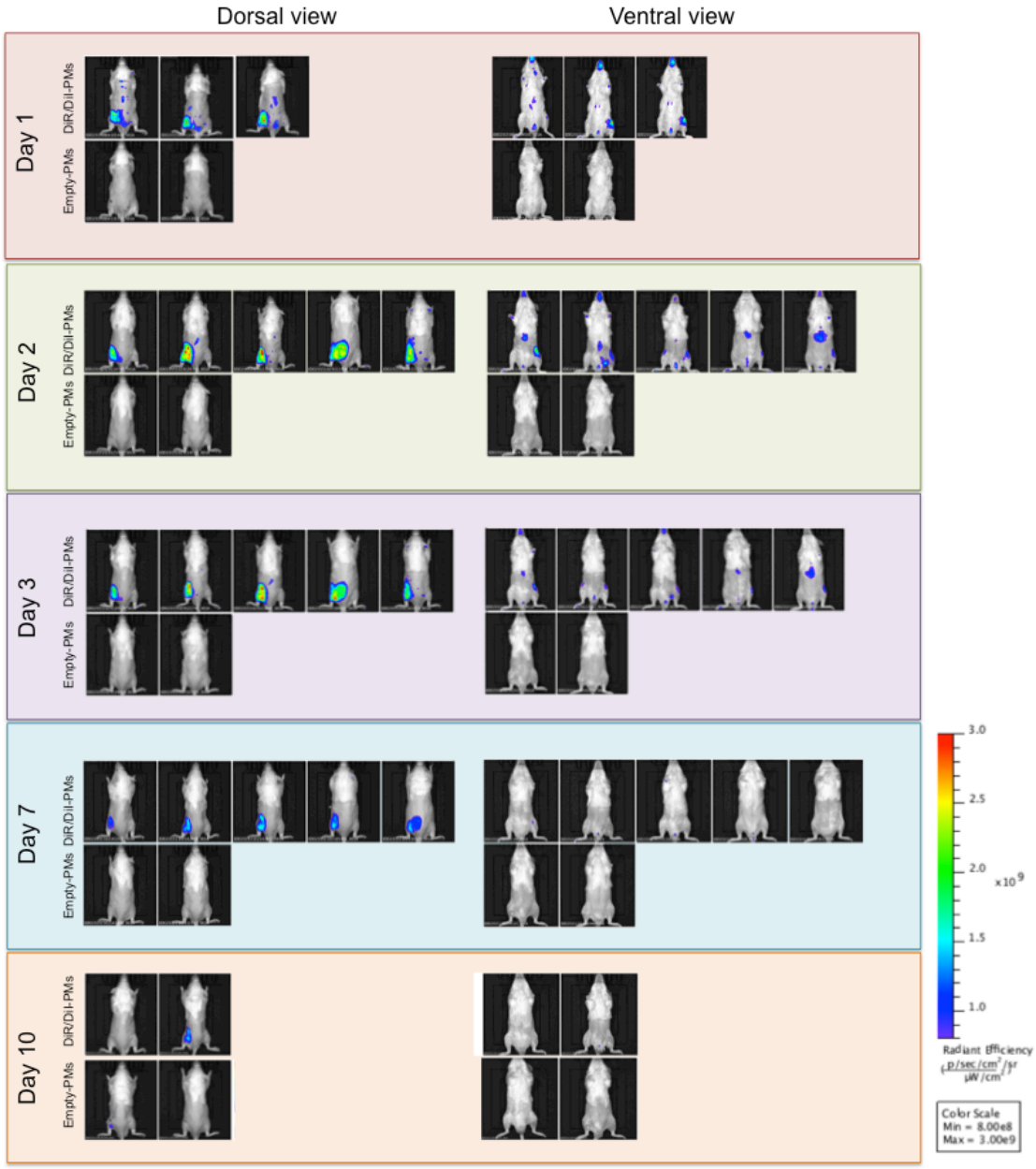

Appendix Figure 14: **Temporal IVIS analysis of PMs distribution *in vivo.***

IVIS images showing the temporal and spatial distribution of the DiR fluorescent signal, on both the dorsal and ventral view, in mice systemically treated with either DiR/DiI-PMs or empty-PMs. Fluorescence expressed in radiant efficiency, min: 8 x 10^8 (a.u.), max: 3 x 10^9 (a.u.).

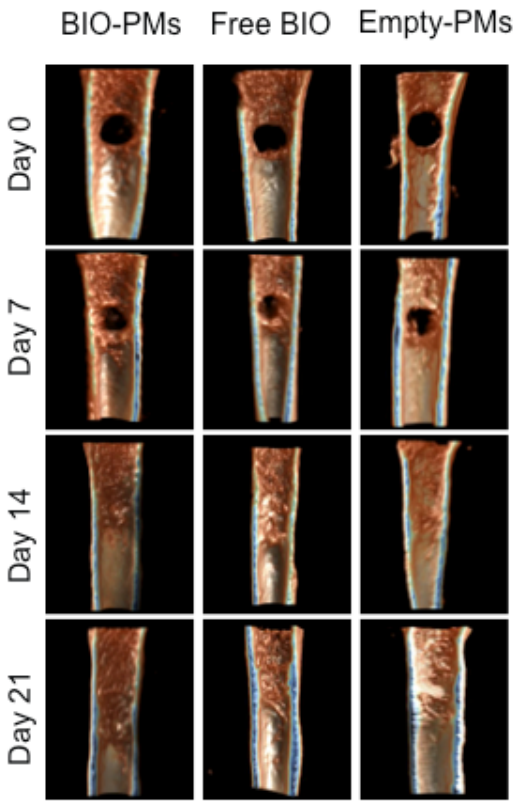

Appendix Figure 15: **Bone drill healing process**

Representative μ-CT 3D reconstructions showing, from the outer-view, the temporal progression of the healing process in the three groups investigated.

7.5 Quantification of intracellular payload release from polymersome nanoparticles.

www.nature.com/scientificreports

SCIENTIFIC REPORTS

OPEN

Quantification of intracellular payload release from polymersome nanoparticles

Received: 15 March 2016
Accepted: 13 June 2016
Published: 11 July 2016

Edoardo Scarpa[1,2], Joanne L. Bailey[2], Agnieszka A. Janeczek[1,2], Patrick S. Stumpf[1,2], Alexander H. Johnston[2], Richard O. C. Oreffo[1,2], Yin L. Woo[3,4], Ying C. Cheong[1], Nicholas D. Evans[1,2,5] & Tracey A. Newman[2,6]

Polymersome nanoparticles (PMs) are attractive candidates for spatio-temporal controlled delivery of therapeutic agents. Although many studies have addressed cellular uptake of solid nanoparticles, there is very little data available on intracellular release of molecules encapsulated in membranous carriers, such as polymersomes. Here, we addressed this by developing a quantitative assay based on the hydrophilic dye, fluorescein. Fluorescein was encapsulated stably in PMs of mean diameter 85 nm, with minimal leakage after sustained dialysis. No fluorescence was detectable from fluorescein PMs, indicating quenching. Following incubation of L929 cells with fluorescein PMs, there was a gradual increase in intracellular fluorescence, indicating PM disruption and cytosolic release of fluorescein. By combining absorbance measurements with flow cytometry, we quantified the real-time intracellular release of a fluorescein at a single-cell resolution. We found that 173 ± 38 polymersomes released their payload *per* cell, with significant heterogeneity in uptake, despite controlled synchronisation of cell cycle. This novel method for quantification of the release of compounds from nanoparticles provides fundamental information on cellular uptake of nanoparticle-encapsulated compounds. It also illustrates the stochastic nature of population distribution in homogeneous cell populations, a factor that must be taken into account in clinical use of this technology.

Polymersomes (PMs) are nano-sized artificial vesicles made from synthetic polymers such as poly (ε-caprolactone)-*block*-poly(ethylene glycol), (PEG-*b*-PCL). PMs formed from amphiphilic PEG-*b*-PCL block copolymers self-assemble in aqueous solution with the hydrophobic PCL units forming a spherical membrane surrounded by a hydrophilic PEG corona. PMs can be used to carry and deliver a variety of payloads including plasmids[1], low molecular weight compounds[2] and proteins[3] into cells. Furthermore, PMs can be readily modified to display surface moieties, e.g. short peptide sequences that promote uptake or confer specificity to certain cell types[4]. Modification of the chemical make-up of PMs can lead to alteration of the release kinetics of encapsulated compounds. There are numerous examples of PMs that release their payload in response to stimuli including alterations in pH[5,6], temperature[7], oxidation[8] and light[9,10]. This responsiveness can be extended by using variable ratios of blends of different copolymers to tune PM release kinetics[11]. The exquisite control that such technologies can provide has resulted in significant interest in the potential of PMs to probe cell behaviour and enable drug delivery. There are numerous clinical trials being undertaken, predominantly in oncology, which are aiming to achieve better patient outcomes by exploiting the benefits that PM based delivery systems offer.

Polymeric nanoparticles are recognised to have considerable translational potential when considered holistically as drug delivery systems. This approach to disease targeting considers every step of the drug delivery pathway, including reliable scalable PM synthesis, route of administration, biodistribution and pharmacokinetics,

[1]Centre for Human Development, Stem Cells and Regeneration, University of Southampton Faculty of Medicine, Tremona Road, Southampton, SO16 6YD, United Kingdom. [2]Institute for Life Sciences, Centre for Biological Sciences, B85, University Road, University of Southampton, United Kingdom. [3]Department of Obstetrics and Gynaecology, Faculty of Medicine, University of Malaya, Kuala Lumpur, 50603, Malaysia. [4]University of Malaya Cancer Research Institute (UMCRI), University of Malaya, Kuala Lumpur, 50603, Malaysia. [5]Bioengineering Sciences Group, Faculty of Engineering and the Environment, University of Southampton, Highfield, Southampton, SO17 1BJ, United Kingdom. [6]Clinical and Experimental Sciences, Medicine, University of Southampton, SO17 1BJ, United Kingdom. Correspondence and requests for materials should be addressed to N.D.E. (email: n.d.evans@soton.ac.uk) or T.A.N. (email: tan@soton.ac.uk)

through to clearance and excretion[12]. Despite this there remains a need for the quantification of PM uptake by cells and consequent intracellular payload release, which are both essential in determining the pharmacokinetics of drug-delivery and consequent cellular effects. Such information is also important for understanding the concentration of molecules delivered via native carriers, for example, exocytosed vesicles[13]. There is an extensive literature on methods for qualitatively and quantitatively determining the cellular internalisation of nanoparticles. The majority of these methods, however, have relied upon nanoparticles that exhibit intrinsic fluorescence, such as fluorescently labelled PMs[14] or quantum dots[15]. These methods have been very successful in answering important questions about the kinetics of nanoparticle uptake, but have a number of drawbacks, including an inability to distinguish nanoparticles that are internalised from those that are associated with the external leaflet of cell membranes. Experimental approaches to confirm whether particles are intra-, or peri-cellular have been achieved through the combination of post-hoc correction of measurements collected from flow cytometry and confocal fluorescent analyses[14,16] or by using imaging cytometry[17]. While these approaches are useful for determining uptake of nanoparticles, they still do not provide a method of quantifying intracellular drug release from nanoparticles.

Real-time drug delivery has been investigated previously through the use of fluorescent compounds. Latent fluorophores are molecules that become fluorescent after the release of a quencher[18–20], or in which the emission and/or excitation wavelength is shifted depending upon chemical dissociation[21], a cleavage event[22] or a change in pH (SNARFs)[23]. These fluorescent techniques often require complex coupling chemistries, and they are rarely quantitative. In other work, Battaglia and colleagues have demonstrated that PMs can be used to deliver encapsulated or conjugated dyes to a variety of different cell types with minimal effects on cell viability[24–26]. Further development of these methods would be highly advantageous for quantification of nanoparticle delivery and payload release, particularly when combined with methods that determine whether a delivery molecule is entrapped in a PM or released into the cytosol.

In order to address these challenges, we have exploited some key characteristics of the disodium salt of fluorescein, a water soluble weakly membrane-permeable molecule. Fluorescein has a high quantum yield and an excitation of λ_{ex} 496 nm and emission at λ_{em} 521 nm. However, when fluorescein is highly concentrated in aqueous solution it self-quenches. Self-quenching fluorophores have previously been utilised in the liposome drug delivery field[27,28]. These molecules were instrumental in the discovery that some liposome preparations deliver their cargo to cells by endocytosis followed by drug escape from endosomes and early lysosomes, rather than by direct plasma membrane fusion[29]. We hypothesised that encapsulation of fluorescein in the aqueous core of PMs above the quenching concentration would create non-fluorescent nanoparticles carrying a cargo which would fluoresce once released. As PM disruption needs to occur for the fluorophore to be released, we reasoned that this could be used as a tool to quantify the intracellular release of this hydrophilic payload. Fluorescence is observed only when the payload is released and dispersed at a lower concentration within the cell (Fig. 1). We utilize these properties to provide a new method for the quantification of intracellular release of a hydrophilic payload in mammalian cells. L929 fibroblasts were co-incubated with quenched fluorescein-loaded PMs, the time-course and quantity of loaded PMs releasing the payload intracellularly was measured at single cell resolution using flow cytometry and fluorescence spectroscopy.

Results and Discussion

Polymersomes stably encapsulate and retain fluorescein at high concentrations. We first tested the hypothesis that PMs are able to carry and stably retain the hydrophilic fluorophore, fluorescein, and that its fluorescence emission would be quenched on high concentration encapsulation in the PM core. PMs were produced by nanoprecipitation[30] in an aqueous solution containing a high concentration (0.1 M) of fluorescein. In this situation block copolymers self-assemble into vesicular polymersomes, with the aqueous solution retained in their cores.

PMs were formed from 5.8K-19K-NH_2 block copolymers. In previous work, we have produced PEG-PCL PM with this class of block copolymer, and we demonstrated the functionality of these PMs as a payload carrier *in vivo*[31] but as yet we have not examined its cellular uptake by cells, *in vitro* or *in vivo*. After fluorescein encapsulation, no significant changes were found in hydrodynamic radius or polydispersity, which is a measure of the width of the particles size distribution and which is considered to be less than 0.2 for homogeneous preparations[32] (Fig. 2A), and 5.8K-19K-NH_2 PMs were stable over a period of 3 weeks, with no measurable change in either of these variables (Fig. 2B).

Nanoparticle tracking analysis (NTA), a technique that enables the visualisation, sizing and quantification of nanoparticles in suspension by the use of a highly sensitive video camera[33], revealed a hydrodynamic diameter value of 85 ± 33.6 nm for 5.8K-19K-NH_2 PMs, in close agreement with the value obtained by dynamic light scattering (DLS) (hydrodynamic diameter of 86 nm and PdI of 0.103). NTA analysis determined the PM concentration to be 5.0×10^{13} nanoparticles ml^{-1} (Fig. 2C). This type of measurement allows for a precise quantification of the final PM concentration, overcoming calculations purely based on assumptions of PM physical characteristics (i.e. membrane thickness, area of the molecules and copolymer weight)[14,24].

Encapsulation of fluorescein (0.1 M), followed by dialysis of the PMs and size exclusion chromatography, resulted macroscopically in a PM suspension that was dark orange in colour, with none of the characteristic yellow appearance of fluorescein in solution (Fig. 3A). Confirming this, no detectable fluorescence was found in the PM suspension by fluorescence spectroscopy when compared to equivalent concentration of fluorescein, indicating quenching of the PM-encapsulated fluorescein and absence of free fluorescein (Fig. 3B). The concentration of fluorescein in PM preparations was measured using absorbance spectroscopy. A linear relationship was found between PM concentration and absorbance at concentrations $< 50\,\mu M$ (Fig. 3C). Fitting of absorbance measurements of PMs to an absorbance standard curve for fluorescein, allowed us to determine a concentration of $273 \pm 7.4\,\mu M$ fluorescein in PMs at a concentration of 5×10^{13} PMs ml^{-1}. From this, we calculate a mass of

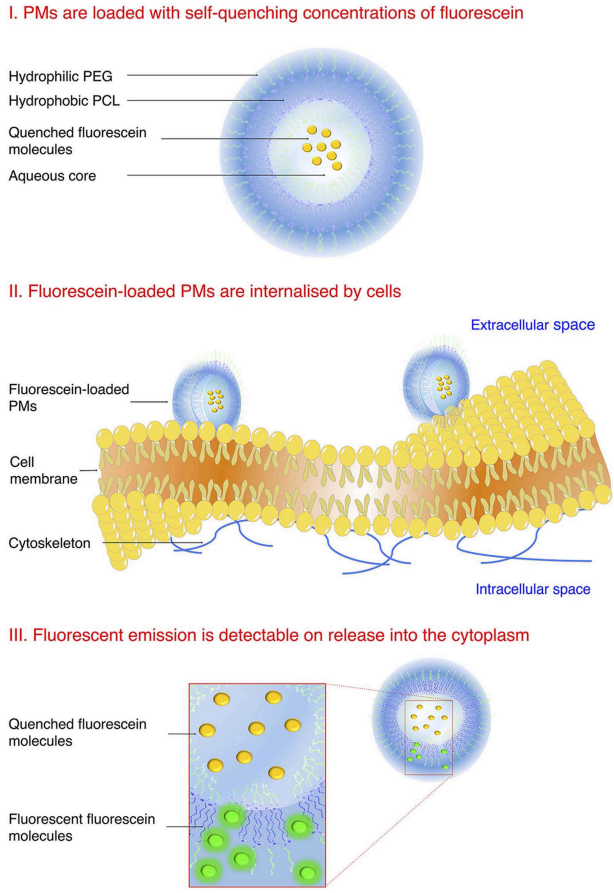

Figure 1. The principle of use of quenched fluorescein to measure intracellular payload delivery (I) PEG-b-PCL block copolymers self-assemble in an aqueous environment to form polymersome structures. The PCL units of the polymer form a hydrophobic membrane, the PEG units form a hydrophilic corona and line the interior cavity of the polymersome. (II) When carrying a payload of sodium fluorescein above the quenching concentration the polymersome is non-fluorescent. Upon cellular internalisation (III) payload release can be visualized as the fluorescein disperses and falls below the quenching concentration.

5.48×10^{-21} moles of fluorescein per PM. Note that there is no absorbance interference from the block copolymer at this wavelength (no significant difference between absorbance of PM suspension compared to PBS background reading at 494 nm). Furthermore, note that the absorbance curve for fluorescein is linear between 0 and 50 μM, but becomes non-linear due to complete absorbance at high concentrations. All measurements were made in the linear range of absorbance for fluorescein[34].

The concentration of fluorescein inside the PM aqueous core was stable over the course of a week (Fig. 3D), indicating that there was no significant loss of internalised fluorescein from the PMs, despite the high concentration gradient across the PM shell membrane following dialysis and storage in aqueous solvent. Confirming this, only very low concentrations of free fluorescein (1 μM ± 0.1 μM) were found in the supernatant of ultracentrifuged polymersome preparations (See Supplementary Fig. S1). Together these experiments demonstrate that PMs trap fluorescein and that its fluorescence is quenched at the concentrations present inside the PMs[27,35]. The

A

Block-copolymer PEG-b-PCL	Hydrodynamic diameter (nm)		Polydispersity index	
	PBS	Fluorescein	PBS	Fluorescein
5.8K-19K-NH_2	83.46	85.90	0.124	0.103

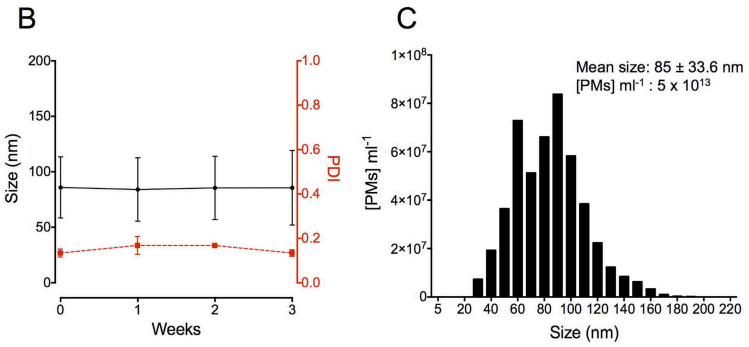

Figure 2. Characterization of PEG-PCL polymersomes (PMs). (**A**) Size and polydispersity index (PDI) of PMs formed from 5.8K-19K-NH2 block-copolymer, measured by dynamic light scattering (DLS). (**B**) Size (black) and PDI (red) stability of 5.8K-19K-NH2 (PEG-b-PCL) fluorescein-loaded PMs over the course of 3 weeks. Data presented as mean ± S.D. (**C**) Histogram depicting size and concentration per ml of fluorescein-loaded PMs measured by nanoparticle tracking analysis (NTA).

physical characteristics of the PMs are unaffected by the inclusion of fluorescein, and the PMs retain fluorescein stably without significant leakage over prolonged time periods at room temperature.

In previous studies, a similar method was used to incorporate fluorescein and its derivative carboxyfluorescein in liposome carriers. In these studies, liposomes were found to be permeable to fluorescein, but relatively impermeable to carboxyfluorescein (which differs from fluorescein by an extra carboxyl group at the 5- and 6-position, making it more hydrophilic)[27,36]. PMs are known to be less permeable for a variety of molecules compared to liposomes (for example they are an order of magnitude less permeable to water than liposomes)[37], and the current data suggests that this is true for fluorescein, with insignificant leakage even after a period of several days.

Fluorescein-loaded PMs are actively taken up by mammalian cells and subsequently release their payload intracellularly. To determine whether PMs are taken up and their contents are released in mammalian cells, fluorescein-loaded PMs were added in solution to cultures of the mammalian fibroblast cell line, L929. Fibroblasts are known to be pivotal in contributing to the progression of several malignancies including endometrial cancer[38], and therefore represent a possible target for nanoparticle-based therapeutic approaches. Following co-incubation of cell-cycle synchronised (serum-starved) L929 cells with fluorescein-loaded PMs, a time-dependent increase in the fluorescence of cells from approximately 15 minutes after the start of the incubation was observed, as seen in confocal images (Fig. 4A). This indicates uptake of PMs and intracellular release of fluorescein. Quantification of cellular fluorescence revealed a gradual increase over a period of one hour, with evidence of significantly higher intracellular payload release than that measured in controls, incubated with free (un-encapsulated) fluorescein, within 15 minutes ($p < 0.05$) (Fig. 4B) of the start of the experiment. These results indicate that PMs loaded with a high concentration of fluorescein release their cargo intracellularly, and that fluorescence of the dye molecules is no longer quenched on release. Encapsulated dyes such as rhodamine B and propidium iodide, were shown to be released intracellularly from polymersomes following uptake[24]. The polymersomes studied were fabricated to include a pH-sensitive poly (2-(di-isopropylamino) ethylmethacrylate) (PDPA) block. On exposure to a pH ~6.5, equivalent to lysosomal pH of, the PDPA underwent dissociation of the di-block polymers, leading to release of encapsulated agents in short (ms) timeframes. PCL-PEG co-block polymer is less pH sensitive, and undergoes hydrolysis and degradation over relatively longer time frames[11,39]. It is therefore somewhat surprising that we measured dye release under such short time frames (minutes). We suggest

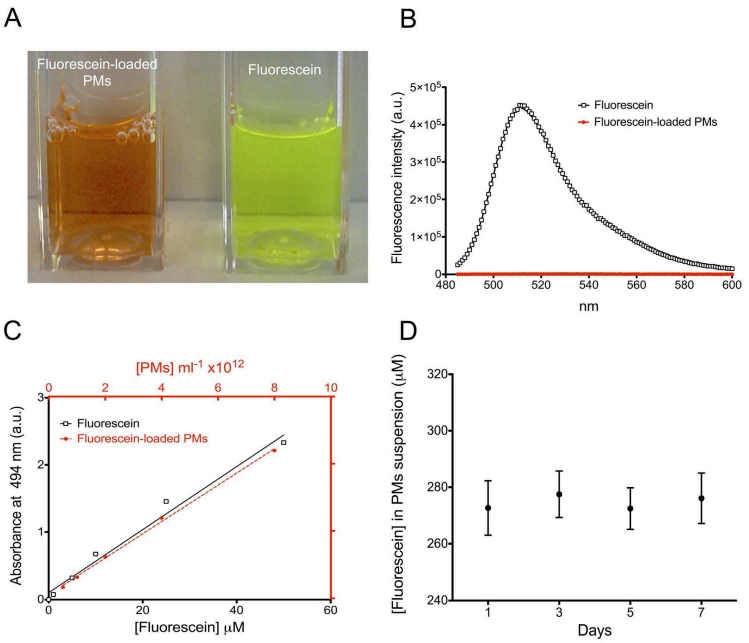

Figure 3. High concentration packaging of fluorescein in PMs quenches fluorescence. (**A**) Picture showing the difference in color of fluorescein-loaded PMs and fluorescein at equal concentrations. (**B**) Absence of fluorescence emission from fluorescein-loaded PMs (red) compared to equivalent concentration of free fluorescein (274 μM) (black) measured by spectrophotometry. (**C**) Absorbance measurements (at 494 nm) of increasing concentrations of fluorescein-loaded PMs and free fluorescein. (**D**) Retention of fluorescein in loaded-PMs over the course of one week measured by absorbance (at 494 nm). Data presented as mean ± S.D. of three independent measurements.

that, due to the presence of PCL which is a highly hydrolase-sensitive polyester[40], the release in our experiments may be facilitated by lysosomal acid hydrolases after initial partitioning of PM in early endosomes and lysosomes. Hydrolysis of polyesters, which induces the destabilisation of the vesicle structure is likely leading to the accelerated release of fluorescein at physiological temperature (~37 °C) compared to the storage temperature of the PM preparation (room temperature)[41]. Further high-resolution imaging studies would enable better characterisation of this process. Additionally, it is likely that the observed fluorescence release originates from only a proportion of internalised PMs (as the fluorescence of fluorescein in intact PMs will remain quenched). Future studies may address this by comparing fluorescence release of quenched dyes in, for example, pH sensitive PMs compared to more environmentally robust PMs.

To quantify the rate and magnitude of PM-mediated fluorescein release in cultured cells on a cell-by-cell basis, we used flow cytometry. As in the confocal microscopy experiments, time-dependent increases in fluorescence were detected in populations of cells exposed to PMs. After 1h, 36 ± 9% of cells showed increases in fluorescence above that of any cell co-incubated with a PBS-loaded control, and 95.4 ± 0.6% of cells after 24 hours. This suggests that nearly all cells in the treated populations had taken up PMs and undergone intracellular release of PM-encapsulated fluorescein over this time period (Fig. 4C,D; note 4D is data obtained from 3 separate experiments; data from one experiment is shown in the cytometry plot in 4C).Time periods of exposure for longer than 24 hours did not result in any further uptake (Supplementary Fig. S2). Uptake of PMs had no significant effect on cell viability (See Supplementary Fig. S3), in agreement with other published studies on similar PMs[25]. Confirming our earlier confocal observations, there was also significant heterogeneity in fluorescein release within the cell populations, despite the cell cycle being synchronised (note the variability in fluorescence in the cells shown in the images captured by confocal microscopy and in the flow cytometry histograms Fig. 4A,C respectively).

Next we tested the hypothesis that PM uptake is an active, energy-dependent process. To achieve this, we assayed uptake at low temperature and after treatment with the ATP synthase inhibitor sodium azide. The relative

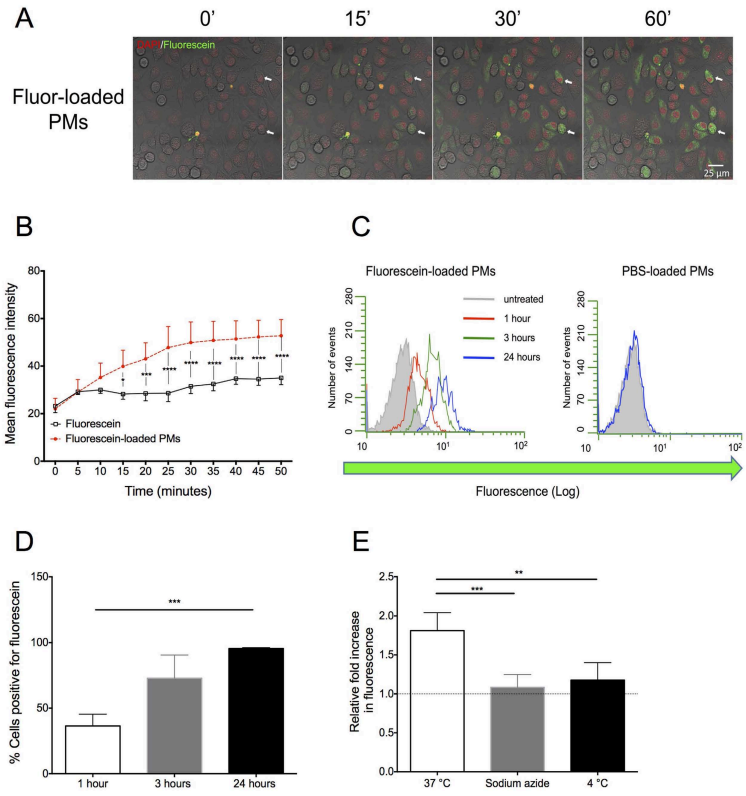

Figure 4. Fluorescein-loaded PMs are actively taken up by mammalian cells and subsequent release their payload intracellularly. (**A**) Time-lapse imaging of L929 cells incubated with fluorescein-loaded PMs shows time-dependent intracellular release of fluorescein. Images were taken up to 1 hour after the addition of the fluorescein-loaded PMs and are a projection of a single z-stack. Green: cells positive for fluorescein. Red: nuclear staining. White arrows indicate two cells showing a change in fluorescence across the experimental time-course. (**B**) Image analysis of the mean fluorescence intensity of L929 cells incubated with fluorescein-loaded PMs (dot) or fluorescein (square) for one hour. The results show a steady and significant increase in cells exposed to PMs as opposed to un-encapsulated fluorescein. Data presented as mean ± S.D. Statistical analysis is two-way ANOVA. (**C**) Representative flow cytometry histogram plot of L929 cells incubated for 1 (red), 3 (green) or 24 hours (blue) with either fluorescein-loaded PMs or PBS-loaded PMs. (**D**) Percentage of cells positive for fluorescein after 1, 3 or 24 hours incubation with fluorescein-loaded PMs. Data presented as mean ± S.D. Statistical analysis is Kruskal-Wallis one way ANOVA on ranks followed by Dunn's post-hoc test. (**E**) Relative levels of fluorescence of L929 cells incubated with fluorescein-loaded PMs for 5 minutes under 3 conditions: at 37 °C, at 4 °C and at 37 °C with sodium azide. Fluorescence is normalized against autofluorescence from control cells where no fluorescein-loaded PMs were added (dashed line). Data presented as mean ± S.D. Statistical analysis is one way ANOVA followed by Tukey's post-hoc test. *$p < 0.05$, **$p < 0.01$, ***$p < 0.001$, ****$p < 0.0001$.

increase in intracellular fluorescence of L929 cells incubated for 5 minutes with fluorescein-loaded PMs was significantly higher at 37 °C compared to cells incubated at 4 °C ($p < 0.01$), or those treated with the mitochondrial energy inhibitor sodium azide ($p < 0.001$) (Fig. 4E). Negligible cellular fluorescence was found after incubation of L929 cells with fluorescein at a concentration equivalent to that measured as a residual, un-encapsulated, concentration found in all PM preparations (~1 µM, See Supplementary Fig. S4), excluding a potential passive uptake of fluorescein from the culture medium. Together, these results illustrate that PEG-PCL PMs are quickly internalised

A

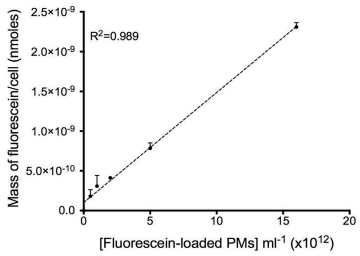

B

[Fluorescein-loaded PMs] ml^{-1} ($x10^{12}$)	Mass of fluorescein (nanomoles)		Estimated number of PMs $cell^{-1}$
	In well	Per cell ($x10^{-9}$)	
0.5	0.18 ± 0.05	0.181	33 ± 15
1	0.3 ± 0.1	0.308	56 ± 24
2	0.41 ± 0.03	0.413	75 ± 4
5	0.78 ± 0.09	0.784	143 ± 12
16	2.30 ± 0.05	2.308	421 ± 10

Figure 5. The intracellular mass of fluorescein is proportional to extracellular PM concentration. (**A**) Graph depicting the linear relationship between the mass of fluorescein per cell and the concentration of fluorescein-loaded PMs incubated with the cells. $R^2 = 0.989$. Data presented as mean ± S.D. (**B**) Mass of fluorescein per well and per cell, as well as estimated number of PMs per cell following 24 hour incubation with increasing concentrations of fluorescein-loaded PMs. Data presented as mean ± S.D.

by mammalian cells, in a time-dependent manner, do not induce cytotoxicity, and that this process is an active and energy-dependent process, in agreement with previous reported findings[14,31,42–45].

Our experimental setup did not allow for the distinction between the different energy-dependent mechanisms of endocytosis (clathrin-mediated endocytosis, macropinocytosis, caveolae-mediated endocytosis and clathrin and caveolae-independent endocytosis). Nevertheless, our results corroborate findings from Xin *et al.* who demonstrated that PEG-PCL nanoparticles, which display a specific receptor-binding motif (Angiopep-2) on their surface are internalised by cells *via* energy dependent mechanisms, in particular caveolae-mediated endocytosis[44]. While the use of inhibitors of specific pathways of endocytosis (e.g. sodium azide, filipin and cytochalasin D) allow for a more detailed characterisation of the internalisation process, they may also impair the physiological cellular response inducing preferential cellular uptake *via* specific pathways. Chernenko *et al.* demonstrated the compartmentalisation of PEG-PCL nanoparticles in secondary endosomes of Hela cells by following the vibrational signature of PCL molecules and their released cargo using label-free Raman imaging[46,47]. The ability to distinguish specific routes of cellular uptake would be beneficial in defining the sub-cellular partitioning of either PMs and payload and could be investigated in future experiments, but the quantification of payload released intracellularly is equally important.

Intracellular payload release can be quantified at single-cell resolution, revealing heterogeneity in cellular delivery. In order to determine the amount of fluorescein delivered intracellularly, a defined number of cells were pre-incubated with PMs for 24 hours. Cells were washed thoroughly with PBS in order to remove excess PMs present in solution but not internalised by cells, and were then lysed and the concentration of intracellular fluorescein was measured using a standard curve for fluorescence. The quantum yield of fluorescein is known to be affected by its molecular nanoenvironment (eg pH, charge, protein binding)[34]. In order to control for these factors, the standard curve was determined by measurement in a solution equivalent to that produced by lysed cells (See Supplementary Fig. S5). A linear relationship was found between the initial concentrations of PMs incubated with cells and the amount of fluorescein recovered from within the cells after 24 hours (Fig. 5A). In addition, we found no difference in the total intensity of aliquots of cells before and after cell lysis (See Supplementary Fig. S6), indicating that the quantum yield of fluorescein is relatively unaffected by its molecular microenvironment following intracellular release. This is somewhat surprising as it is known that decreasing the pH leads to a decrease in the quantum yield of the fluorophore[48]. Since some data suggest the partitioning of PMs into endosomes and lysosomes[46], where pH can range from 6.5 for endosomes to 5 for lysosome, it may be the case that in this study, fluorescein is largely partitioned in early endosomes or in the cytoplasmic space, where the pH is higher. Longer periods of incubation (>24 hours), with an associated increase in the

A

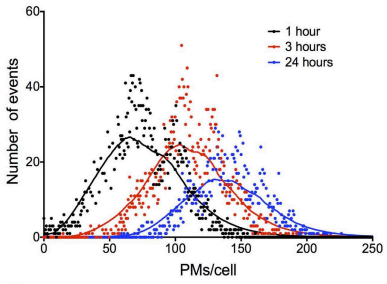

B

Estimated number of PMs releasing fluorescein *per* cell				
Hours	Min	Max	Range	Median
1	7 ± 13	216 ± 53	209 ± 54	127
3	5 ± 8	243 ± 68	238 ± 74	141
24	41 ± 35	329 ± 97	288 ± 126	172

Figure 6. Intracellular payload release can be quantified at single-cell resolution and reveals heterogeneity in cellular delivery (**A**) Estimated number of PMs internalized per cell after 1 hour (black), 3 hours (red) or 24 hour (blue) incubation with fluorescein-loaded PMs. Data is representative of a single experiment. (**B**) Estimated minimum (Min), maximum (Max), range (Max-Min), median and mean number of PMs per cell after 1, 3 or 24 hours incubation with fluorescein-loaded PMs.

lysosomal partitioned cargo would be predicted to cause reductions in the measured intracellular quantum yield of fluorescein in comparison to post-lysis. Despite this, we cannot rule out the possibility that our estimations of intracellular fluorescein may be subject to error. As fluorescein may be in various stages of release and therefore at heterogeneous concentrations within the cells, and as our methods of cell disruption may not completely disrupt intracellular organelles including endosomes and lysosomes, the recovered fluorescence yield may be an underestimation of true intracellular fluorescein concentration. Other methods, such as high performance liquid chromatography, may be used in the future to provide an additional layer of certainty of the absolute intracellular concentration of the dye. Notably, Gottstein *et al.* used a correction factor to normalise the intracellular solid fluorescence of polystyrene nanoparticles to their external fluorescence[16]. While this is an elegant method for determining the intracellular uptake of cohesive, solid fluorescent capsules, it would be more difficult to employ this technique in the current study. In Gottstein *et al.'s* report, the nanoparticles are not subject to changes in the local molecular concentration through diffusion and are less subject to intermolecular interactions since most of the nanoparticles are labelled with the fluorophores and this is not contained within the particles. Future studies may address local changes in the microenvironment in combination with measurements of concentration by fluorescence. This may be achieved by, for example, pH sensitive dyes, such as SNARFs employed by Semmling *et al.*[23]. Or alternatively, time resolved fluorescence could be used to determine the relative concentrations of a fluorophore in one molecular microenvironment compared to another. In previous studies, this technique has been used to measure the relative amount of fluorophores in mitochondria compared to cytosol[49,50].

At 24 hours, cells incubated with the concentration of PMs used in Fig. 4 (5×10^{12} PMs ml^{-1}) contained 7.85×10^{-10} nanomoles of fluorescein *per* cell (Fig. 5B). Based on our earlier calculations, the mass of fluorescein in a PM is 5.48×10^{-21} moles, enabling the number of nanoparticles releasing their cargo in cells to be calculated using the following formula:

$$Q_{cell} = \frac{N_{cell}}{N_{PM}} \quad (1)$$

where Q_{cell} is the average number of PMs releasing their payload *per* cell, N_{cell} is the number of moles of fluorescein *per* cell and N_{PM} is the number of moles of fluorescein *per* nanoparticle. Calculations are presented in Fig. 5B. At a PM concentration of 5×10^{12} ml^{-1}, this indicates that an average number of ~143 ± 12 PMs are internalised and release their contents *per* cell over a period of 24 hours (Fig. 5B).

Fluorescence spectroscopy only provides an average quantification of fluorescein release from PMs, therefore flow cytometry was used to determine cell-specific nanoparticle payload release, and the inherent degree of

variability in the cellular population. By normalising fluorescence intensity data from flow cytometric analysis to measurements of intracellular PM release obtained by fluorescence spectroscopy (above), the PM payload release was calculated for every cell in a flow cytometric analysis at 1, 3 and 24 hours post addition of PMs (Fig. 6A). As expected, we measured an increase in the mean intracellular release with respect to time[14,24], but also an increase in the variability of fluorescein load in the cellular population. This was despite serum starvation, which synchronises the cell cycle, prevents cell division and reduces intra-population uptake variability[51]. The observed cell-to-cell variability in PM release of fluorescein may be attributed to the stochastic nature of cell-PM interactions during the internalisation process, resulting from a combination of factors including PM agglomeration and clustering and variable cellular surface receptor dynamics[52,53]. In addition, our analysis assumes that PMs of all sizes have an equal chance of being taken up and releasing their contents per cell, regardless of size. This may be an over simplification, as size is known to affect the rate and efficiency of uptake[24,54]. Since the mass of fluorescein that each PM contains is proportional to volume rather than diameter, measurements of uptake may be particularly sensitive to variations in the uptake of PMs at the large end of the dispersion profile, This observation underlines the need for further quantitative analysis of putative drug release at a single-cell resolution.

Single cell analyses demonstrated a time-dependent increase in the maximum number of PMs releasing their contents intracellularly *per* cell (217 ± 53, 243 ± 68 and 329 ± 35 PMs *per* cell after 1, 3 and 24 hour incubations respectively). This reflects a wider range (Max PMs *per* cell – Min PMs *per* cell) of PMs internalised after different incubation periods and describes an incremental heterogeneity in PM dye release within the cellular population (Fig. 6B). Furthermore, in the single cell analysis, the estimated median value of PMs *per* cell after 24 hour incubation ($\sim 173 \pm 38$) is very similar to the values calculated from the fluorescence spectroscopy quantification ($\sim 143 \pm 12$) (Fig. 5B). Comparing the number of nanoparticles internalised *per* cell quantified in different studies is fraught with difficulty, considering the diversity of cells, nanoparticles and cell culture conditions used. Nevertheless, very recently Unciti-Broceta *et al.* estimated the number of nanoparticles needed *per* cell in order to achieve nanoparticle uptake in 50% of a cell population[55]. The figure estimated by the authors for 3 different cell lines are in the same order of magnitude to the number of nanoparticles *per* cell calculated here and similar to previous reports[16,56]. In another study, Massignani *et al.* recently used either the encapsulation, or conjugation, of rhodamine B to diblock polymers composed of PMPC25–PDPA70 and PEG23–PDPA15 diblock copolymers[24]. The authors reported values of 10^6–10^7 PMs internalised/cell, several orders of magnitude higher than our current study. This difference is striking, but can be partially explained by the higher concentration of PMs used in this study (10^{16}/mL), differences in the PM chemistry and encapsulation efficiency of the dye molecules used, and finally differences in the degradability of the PMs used – in our study, we quantified only the amount of fluorescein that was released from PMs, and we did not measure dye which remained quenched within intact PMs.

The quantification method described here could be extended to different PM preparations and importantly enables single cell analysis to be performed. Another factor that influences the kinetics of PM uptake and subsequent intracellular release is potential PM depletion from the culture medium, particularly when nanoparticle uptake in a given time period is comparable with the number of nanoparticles available *per* cell[17,57]. In a recent study using solid PEG-conjugated polystyrene nanoparticles however, Unciti-Broceta *et al.* found that a ratio of 1000–4000 nanoparticles per cell was saturating, with nanoparticle concentration becoming rate limiting only below 2000 nanoparticles per cell[55]. In our experiments we calculate a concentration of $> 1 \times 10^6$ PMs/cell, and so it is unlikely that the depletion of nanoparticles from the medium has any significant effect on the rate of uptake.

Conclusion

All drug-delivery systems must undergo extensive characterisation prior to evaluation in clinical trials[58]. There is evidence from *in-vivo* studies in animals that delivery using polymeric nanoparticle preparations has clear advantages over administration of free drug, with fewer off-target and toxic effects[59]. Studies correlating preclinical findings and data from human trials have found that there is good correlation between the biodistribution and clearance of the particles between these two study types[60] and several polymeric nanoparticle delivery systems, e.g. Genexol-PM, are now in phase 2 clinical trials[61]. However a current limitation with the use of polymersomes (PMs) for controlled drug delivery is the paucity of information regarding the number of nanoparticles internalised at a single cell level and therefore the concentration of payload released. We exploited the characteristics of sodium fluorescein to demonstrate real-time delivery of a hydrophilic compound in a mammalian fibroblast cell line using PMs. To our knowledge, this is the first attempt to quantify the intracellular release of a fluorophore from a hollow polymeric nanocarrier at a single cell level. When nanoparticles are considered as possible delivery vehicles for therapeutic molecules at a cellular and sub-cellular level, the heterogeneity of distribution within a population is a critical factor that should be considered. The simple methodology proposed here could be extended to quantify the cellular internalisation of PMs formed from different materials, including stimuli responsive PMs. Additionally, this method could be used to determine the relative partitioning of a putative drug in populations of mixed cell types, as will invariably be the case in *in vivo* studies, and how drugs partition during cell division[17]. It provides a methodology with which to better understand how the kinetics of cellular uptake might be affected by cell type, nanoparticle polymer chemistry, and the addition of nanoparticle surface moieties. We believe that these types of investigations are much needed in order to fully exploit the potential of nanoparticles, particularly PMs for clinical applications.

Material and Methods

PM preparation. The following methodology was adapted from previously reported work[30]. PMs were prepared by dissolving α-amino-ω-hydroxy terminated (NH_2)-PEG-b-PCL (6.0 mg) (Polymer Source, Dorval, Canada) in dimethylformamide (DMF) (0.4 ml). The amphiphilic copolymer used had an average molar mass (M_n) of 5.8×10^3 g/mol for the PEG block and 19×10^3 g/mol for the PCL block. The solution was then placed in an ultrasonic bath to aid dissolution. A 0.1 M sodium fluorescein (Sigma-Aldrich, Poole, UK) solution (10% DMF

in 0.1 M phosphate buffer (PBS)) in PBS was prepared. The polymer solution was then added drop-wise (~1 drop every 8 seconds) to the sodium fluorescein (1.60 mL) with rapid stirring. The sample was then dialyzed (regenerated cellulose, 10,000 MWCO, Sigma-Aldrich, Poole, UK) against PBS (400 mL), replacing the buffer solution 4 times over the course of 48 hours. Fluorescein-loaded PMs were then removed from the dialysis tubing and filtered through a size separation column (Sephadex G-25, Sigma-Aldrich, Poole, UK) to remove any remaining un-encapsulated fluorescein.

Dynamic light scattering (DLS). DLS analysis (Zetasizer Nano ZS ZEN3600, Malvern Corp, Worcestershire, UK) was performed by diluting PMs (100 μl) in MilliQ PBS (1900 μl). Prior to the analysis, samples were filtered into a plastic cuvette through a cellulose acetate syringe filter (0.2 μm) (Minisart, Sigma-Aldrich, Poole, UK). Measurements were completed at 20 °C with the light detected at a scattering angle of 173°. Data was collected 13 times/sample. Acquisition was for 5 seconds and each measurement was carried out in triplicate.

Nanoparticle tracking analysis (NTA). A NanoSight device (LM10, Malvern Corp, Worcestershire, UK) was used to measure both PMs hydrodynamic size and concentration. PMs were diluted (1 μl) in MilliQ PBS (100 ml), filtered and loaded in the detection cell prior to measurement.

Fluorescence intensity. Fluorescein-loaded PMs and solutions of fluorescein of equivalent concentration (274 μM) were analysed for fluorescence intensity over a range of wavelengths (increment of 1 nm from 485 nm to 600 nm) using a FluoroMax-4 (Horiba Scientific, Stanmore, UK). Release of fluorescein into supernatant after storage was also measured using a FluoroMax-4 (Horiba Scientific, Stanmore, UK).

Fluorescein encapsulation and release *in vitro*. The concentration of sodium fluorescein was calculated by measuring the UV absorbance (Nanodrop 2000c, Thermo Fisher Scientific, Basingstoke, UK) compared to stock solutions. To determine the kinetics of sodium fluorescein release, PM samples were kept at room temperature (20 °C) under constant dialysis (regenerated cellulose, 10,000 MWCO, Sigma-Aldrich, Poole, UK) against PBS. At various intervals over a total of 7 days PM samples were collected. 1 mL aliquots of each sample was then passed through a size separation column, before measurement of UV absorbance (Nanodrop 2000c, Thermo Fisher Scientific, Basingstoke, UK). Each experiment was performed in triplicate. All of the preparations give a 3 mg/mL solution of PMs. For all *in vitro* experiments PM samples were used immediately and were sterile filtered through a 0.2 μm cellulose acetate syringe filter before use.

Cell culture. Mouse L929 Fibroblasts (ATCC) were maintained in Dulbecco's Modified Eagle medium (DMEM) (Thermo Fisher Scientific, Basingstoke, UK) supplemented with 10% (V/V) fetal bovine serum (FBS) (Thermo Fisher Scientific, Basingstoke, UK), 100 U/ml of penicillin (Thermo Fisher Scientific, Basingstoke, UK) and 100 μg/ml of streptomycin (Thermo Fisher Scientific, Basingstoke, UK). The cells were incubated at 37 °C and 5% CO_2. For fluorescence microscopy and cytofluorimetric analysis, 24 hours before an experiment the medium was replaced with DMEM supplemented with low serum (0.5% V/V), 100 U/ml of penicillin (Thermo Fisher Scientific, Basingstoke, UK) and 100 μg/ml of streptomycin (Thermo Fisher Scientific, Basingstoke, UK).

Confocal microscopy. L929 cells were seeded at a density of 50,000 cells/cm^2. The medium was replaced with DMEM supplemented with low serum 24 hours before the experimental assay. 2 hours before PM addition, the medium was replaced with piperazine-N,N′-bis (2-ethanesulfonic acid) (PIPES) buffer supplemented with 0.5% serum. Fluorescein-loaded PMs were added (5×10^{12} PMs ml^{-1}) to the cells and images were taken every 60 seconds over 60 minutes using a TCS SP5 laser scanning confocal microscope (Leica, Milton Keynes, UK). Cell nuclei were stained with Hoechst 33342 (Thermo Fisher Scientific, Basingstoke, UK). A 63 × 1.30 glycerol immersion objective was used. Negative controls were, PBS-loaded PMs (5×10^{12} PMs) and a 10 mM solution of fluorescein. Image analysis was performed by randomly selecting 20 cells of interest and measuring the mean fluorescence intensity at each time point.

Energy-dependent internalization. L929 cells were seeded at a density of 50,000 cells/cm^2. The medium was replaced with DMEM supplemented with low serum 24 hours before the experimental assay. PMs were added to the cells (5×10^{12} PMs ml^{-1}) and incubated for 5 mins, after which the medium was removed and replaced with fresh DMEM supplemented with low serum. After 1 hour the cells were washed x3 with ice-cold PBS, fixed in 4% paraformaldehyde for 15 minutes and imaged using an Axiovert200 inverted microscope (Zeiss, Birmingham, UK). To inhibit energy dependent processes, sodium azide (1 mg/ml) was added for 20 minutes prior to adding fluorescein-loaded PMs. For experiments at 4 °C, cells were equilibrated by keeping them on ice for 30 minutes prior to adding fluorescein-loaded PMs. The medium, PBS and 4% paraformaldehyde were kept on ice. Cells were fixed for 20 minutes. Using Image J software line scans of the width of the cell were taken from the images to give the mean fluorescence *per* cell. Relative fluorescence was calculated normalizing against the auto-fluorescence of the control.

Cytofluorimetry. L929 cells were seeded in 6 well plates at a density of 1×10^4 cells/well. The medium was replaced with DMEM supplemented with low serum 24 hours before the experimental assay. PMs were added to the cells (5×10^{12} PMs ml^{-1}) and incubated for 1, 3 or 24 hours. Medium was removed at the designated time points, cells were washed using PBS, detached using trypsin and re-suspended in 500 μl of PBS. For propidium iodide (PI) (Sigma-Aldrich, Poole, UK) staining, a solution of 2 mg/ml (1 μl) was added to each sample just before cytofluorimetric analysis (Guava easyCyte, Millipore, Milton, UK).

Quantification of the number of PMs per cell. L929 cells were seeded in a 6 well plate at a density of 100,000 cells/well and incubated for 24 hours with increasing concentrations of fluorescein-loaded PMs (from 5×10^{10} to 2×10^{12} PMs ml^{-1}). Then, cells were washed with PBS twice to remove the excess of PMs that were not internalised and lysed using a solution of HEPES (20 mM), NaCl (125 mM) and sodium dodecyl sulphate (SDS) (2%). The relative optical density (O.D.) was measured at 521 nm using a Varioscan Flash microplate reader (Thermo Fisher Scientific, Basingstoke, UK). A fluorescein calibration curve was produced by dilution of a stock solution of fluorescein (100 mM) (Sigma-Aldrich, Poole, UK) in PBS supplemented with cell lysate. Mass of fluorescein PM^{-1} was calculated as the ratio between the mass of fluorescein present in PMs solution by the concentration of PMs ml^{-1}. For quantification at the single cell level, raw data was extracted from FCS files using Matlab (Mathworks, Cambridge, UK) and analysed using Microsoft Excel.

Statistical analysis. The data was tested for normal distribution using the D'Agostino-Pearson normality test using graph pad prism software (GraphPad Software, La Jolla, USA). Parametric tests were carried out for normally distributed data, whereas non-parametric tests were used for skewed data. Comparisons between different treatments were made using one-way or two-way ANOVA, followed by either Tukey's or Dunn's post hoc test. Statistical significance was defined as $^{*}p < 0.05$, $^{**}p < 0.01$, $^{***}p < 0.001$, $^{****}p < 0.0001$ and n.s. $p \geq 0.05$.

References

1. Lomas, H. *et al.* Efficient encapsulation of plasmid DNA in pH-sensitive PMPC-PDPA polymersomes: study of the effect of PDPA block length on copolymer-DNA binding affinity. *Macromol Biosci* **10,** 513–530 (2010).
2. Nahire, R. *et al.* Multifunctional polymersomes for cytosolic delivery of gemcitabine and doxorubicin to cancer cells. *Biomaterials* **35,** 6482–6497 (2014).
3. Liu, G. *et al.* The highly efficient delivery of exogenous proteins into cells mediated by biodegradable chimaeric polymersomes. *Biomaterials* **31,** 7575–7585 (2010).
4. Roy, S. *et al.* Cell-specific targeting in the mouse inner ear using nanoparticles conjugated with a neurotrophin-derived peptide ligand: potential tool for drug delivery. *Int J Pharm* **390,** 214–224 (2010).
5. Gallon, E. *et al.* Triblock Copolymer Nanovesicles for pH-Responsive Targeted Delivery and Controlled Release of siRNA to Cancer Cells. *Biomacromolecules* **16,** 1924–1937 (2015).
6. Li, N. *et al.* Co-delivery of doxorubicin hydrochloride and verapamil hydrochloride by pH-sensitive polymersomes for the reversal of multidrug resistance. *RSC Adv.* **5,** 77986–77995 (2015).
7. Yangwei, D. *et al.* Poly(ε-caprolactone)-block-Polysarcosine by Ring-Opening Polymerization of Sarcosine N-Thiocarboxyanhydride: Synthesis and Thermo-responsive Self-Assembly. *Biomacromolecules* doi: 10.1021/acs.biomac.5b00930 (2015).
8. Lale, S. V., Kumar, A., Prasad, S., Bharti, A. C. & Koul, V. Folic Acid and Trastuzumab Functionalized Redox Responsive Polymersomes for Intracellular Doxorubicin Delivery in Breast Cancer. *Biomacromolecules* **16,** 1736–1752 (2015).
9. Vasdekis, A. E., Scott, E. A., O'Neil, C. P., Psaltis, D. & Hubbell, J. A. Precision Intracellular Delivery Based on Optofluidic Polymersome Rupture. *ACS Nano* **6,** 7850–7857 (2012).
10. Cabane, E., Malinova, V., Menon, S., Palivan, C. G. & Meier, W. Photoresponsive polymersomes as smart{,} triggerable nanocarriers. *Soft Matter* **7,** 9167–9176 (2011).
11. Ahmed, F. & Discher, D. E. Self-porating polymersomes of PEG-PLA and PEG-PCL: hydrolysis-triggered controlled release vesicles. *J Control Release* **96,** 37–53 (2004).
12. Cheng, C. J., Tietjen, G. T., Saucier-Sawyer, J. K. & Saltzman, W. M. A holistic approach to targeting disease with polymeric nanoparticles. *Nat Rev Drug Discov* advance on (2015).
13. Chen, X., Barg, S. & Almers, W. Release of the styryl dyes from single synaptic vesicles in hippocampal neurons. *J. Neurosci.* **28,** 1894–1903 (2008).
14. Sorrell, I. *et al.* Combined mathematical modelling and experimentation to predict polymersome uptake by oral cancer cells. *Nanomedicine* **10,** 339–348 (2014).
15. Zhang, L. W. & Monteiro-Riviere, N. A. Mechanisms of quantum dot nanoparticle cellular uptake. *Toxicol. Sci.* **110,** 138–55 (2009).
16. Gottstein, C., Wu, G., Wong, B. J. & Zasadzinski, J. A. Precise quantification of nanoparticle internalization. *ACS Nano* **7,** 4933–4945 (2013).
17. Summers, H. D. *et al.* Quantification of Nanoparticle Dose and Vesicular Inheritance in Proliferating Cells. *ACS Nano* **7,** 6129–6137 (2013).
18. Qiu, F. *et al.* Real-Time Monitoring of Anticancer Drug Release with Highly Fluorescent Star-Conjugated Copolymer as a Drug Carrier. *Biomacromolecules* **15,** 1355–1364 (2014).
19. Wu, E. C. *et al.* Oxidation-triggered release of fluorescent molecules or drugs from mesoporous Si microparticles. *ACS Nano* **2,** 2401–2409 (2008).
20. Cui, W. *et al.* Fluorescent nanoparticles of chitosan complex for real-time monitoring drug release. *Langmuir* **27,** 8384–8390 (2011).
21. Liu, J. *et al.* Real-Time *In Vivo* Quantitative Monitoring of Drug Release by Dual-Mode Magnetic Resonance and Upconverted Luminescence Imaging. *Angew. Chemie Int. Ed.* **53,** 4551–4555 (2014).
22. Weinstain, R., Segal, E., Satchi-Fainaro, R. & Shabat, D. Real-time monitoring of drug release. *Chem Commun* **46,** 553–555 (2010).
23. Semmling, M. *et al.* A novel flow-cytometry-based assay for cellular uptake studies of polyelectrolyte microcapsules. *Small* **4,** 1763–1768 (2008).
24. Massignani, M. *et al.* Controlling cellular uptake by surface chemistry, size, and surface topology at the nanoscale. *Small* **5,** 2424–2432 (2009).
25. Massignani, M. *et al.* Enhanced fluorescence imaging of live cells by effective cytosolic delivery of probes. *PLoS One* **5,** (2010).
26. LoPresti, C. *et al.* Controlling Polymersome Surface Topology at the Nanoscale by Membrane Confined Polymer/Polymer Phase Separation. *ACS Nano* **5,** 1775–1784 (2011).
27. Weinstein, J. N., Yoshikami, S., Henkart, P., Blumenthal, R. & Hagins, W. A. Liposome-cell interaction: transfer and intracellular release of a trapped fluorescent marker. *Science (80-.).* **195,** 489–492 (1977).
28. Weinstein, J. N., Blumenthal, R., Sharrow, S. O. & Henkart, P. A. Antibody-mediated targeting of liposomes. Binding to lymphocytes does not ensure incorporation of vesicle contents into the cells. *Biochim Biophys Acta* **509,** 272–288 (1978).
29. Straubinger, R. M., Hong, K., Friend, D. S. & Papahadjopoulos, D. Endocytosis of liposomes and intracellular fate of encapsulated molecules: encounter with a low pH compartment after internalization in coated vesicles. *Cell* **32,** 1069–1079 (1983).
30. Johnston, A. H., Dalton, P. D. & Newman, T. A. Polymersomes, smaller than you think; ferrocene as a TEM probe to determine core structure. *J. Nanoparticle Res.* **12,** 1997–2001 (2010).
31. Buckjova, D. *et al.* Minimally invasive drug delivery to the cochlea through application of nanoparticles to the round window membrane. *Nanomedicine (Lond)* **7,** 1339–1354 (2012).
32. Saremi, S., Atyabi, F., Akhlaghi, S. P., Ostad, S. N. & Dinarvand, R. Thiolated chitosan nanoparticles for enhancing oral absorption of docetaxel: preparation, *in vitro* and *ex vivo* evaluation. *Int. J. Nanomedicine* **6,** 119–28 (2011).

33. Filipe, V., Hawe, A. & Jiskoot, W. Critical evaluation of Nanoparticle Tracking Analysis (NTA) by NanoSight for the measurement of nanoparticles and protein aggregates. *Pharm Res* **27,** 796–810 (2010).
34. Sjöback, R., Nygren, J. & Kubista, M. Absorption and fluorescence properties of fluorescein. *Spectrochim. Acta Part A Mol. Biomol. Spectrosc.* **51,** L7–L21 (1995).
35. Niesman, M. R., Khoobehi, B. & Peyman, G. A. Encapsulation of sodium fluorescein for dye release studies. *Invest Ophthalmol Vis Sci* **33,** 2113–2119 (1992).
36. Weinstein, J. N., Blumenthal, R. & Klausner, R. D. Carboxyfluorescein leakage assay for lipoprotein-liposome interaction. *Methods Enzymol.* **128,** 657–68 (1986).
37. Discher, B. M. *et al.* Polymersomes: tough vesicles made from diblock copolymers. *Science (80-.).* **284,** 1143–1146 (1999).
38. Subramaniam, K. S. *et al.* Cancer-associated fibroblasts promote proliferation of endometrial cancer cells. *PLoS One* **8,** e68923 (2013).
39. Geng, Y. & Discher, D. E. Hydrolytic degradation of poly(ethylene oxide)-block-polycaprolactone worm micelles. *J Am Chem Soc* **127,** 12780–12781 (2005).
40. Li, S., Molina, I., Martinez, M. B. & Vert, M. Hydrolytic and enzymatic degradations of physically crosslinked hydrogels prepared from PLA/PEO/PLA triblock copolymers. *J. Mater. Sci. Mater. Med.* **13,** 81–6 (2002).
41. Ahmed, F. *et al.* Shrinkage of a rapidly growing tumor by drug-loaded polymersomes: pH-triggered release through copolymer degradation. *Mol. Pharm.* **3,** 340–50 (2006).
42. Ostacolo, L. *et al. In vitro* anticancer activity of docetaxel-loaded micelles based on poly(ethylene oxide)-poly(epsilon-caprolactone) block copolymers: Do nanocarrier properties have a role? *J Control Release* **148,** 255–263 (2010).
43. LoPresti, C. *et al.* Controlling polymersome surface topology at the nanoscale by membrane confined polymer/polymer phase separation. *ACS Nano* **5,** 1775–1784 (2011).
44. Xin, H. *et al.* Angiopep-conjugated poly(ethylene glycol)-co-poly(epsilon-caprolactone) nanoparticles as dual-targeting drug delivery system for brain glioma. *Biomaterials* **32,** 4293–4305 (2011).
45. Conte, C. *et al.* Biodegradable core-shell nanoassemblies for the delivery of docetaxel and Zn(II)-phthalocyanine inspired by combination therapy for cancer. *J Control Release* **167,** 40–52 (2013).
46. Chernenko, T. *et al.* Label-free Raman spectral imaging of intracellular delivery and degradation of polymeric nanoparticle systems. *ACS Nano* **3,** 3552–9 (2009).
47. Chernenko, T. *et al.* Label-Free Raman Microspectral Analysis for Comparison of Cellular Uptake and Distribution between Non-Targeted and EGFR-Targeted Biodegradable Polymeric Nanoparticles. *Drug Deliv. Transl. Res.* **3,** 10.1007/s13346–013–0178–3 (2013).
48. Smart, P. L. & Laidlaw, I. M. S. An evaluation of some fluorescent dyes for water tracing. *Water Resour. Res.* **13,** 15–33 (1977).
49. Evans, N. D., Gnudi, L., Rolinski, O. J., Birch, D. J. S. & Pickup, J. C. Glucose-dependent changes in NAD(P)H-related fluorescence lifetime of adipocytes and fibroblasts *in vitro*: potential for non-invasive glucose sensing in diabetes mellitus. *J. Photochem. Photobiol. B.* **80,** 122–9 (2005).
50. Schneckenburger, H., Stock, K., Lyttek, M., Strauss, W. S. L. & Sailer, R. Fluorescence lifetime imaging (FLIM) of rhodamine 123 in living cells. *Photochem. Photobiol. Sci.* **3,** 127–31 (2004).
51. Kim, J. A., Åberg, C., Salvati, A. & Dawson, K. A. Role of cell cycle on the cellular uptake and dilution of nanoparticles in a cell population. *Nat. Nanotechnol.* **7,** 62–8 (2012).
52. Summers, H. D. *et al.* Statistical analysis of nanoparticle dosing in a dynamic cellular system. *Nature nanotechnology* **6,** 170–174 (2011).
53. Ehrlich, M. *et al.* Endocytosis by random initiation and stabilization of clathrin-coated pits. *Cell* **118,** 591–605 (2004).
54. Kulkarni, S. A. & Feng, S.-S. Effects of particle size and surface modification on cellular uptake and biodistribution of polymeric nanoparticles for drug delivery. *Pharm. Res.* **30,** 2512–22 (2013).
55. Unciti-Broceta, J. D. *et al.* Number of Nanoparticles per Cell through a Spectrophotometric Method - A key parameter to Assess Nanoparticle-based Cellular Assays. *Sci. Rep.* **5,** 10091 (2015).
56. Le Trequesser, Q. *et al.* Single cell *in situ* detection and quantification of metal oxide nanoparticles using multimodal correlative microscopy. *Anal Chem* **86,** 7311–7319 (2014).
57. Ware, M. J. *et al.* Analysis of the influence of cell heterogeneity on nanoparticle dose response. *ACS Nano* **8,** 6693–700 (2014).
58. Chang, E. H. *et al.* Nanomedicine: Past, present and future - A global perspective. *Biochem. Biophys. Res. Commun.* doi: 10.1016/j.bbrc.2015.10.136 (2015).
59. Oerlemans, C. *et al.* Polymeric Micelles in Anticancer Therapy: Targeting, Imaging and Triggered Release. *Pharm. Res.* **27,** 2569–2589 (2010).
60. Eliasof, S. *et al.* Correlating preclinical animal studies and human clinical trials of a multifunctional, polymeric nanoparticle. *Proc. Natl. Acad. Sci.* **110,** 15127–15132 (2013).
61. Thakor, A. S. & Gambhir, S. S. Nanooncology: The future of cancer diagnosis and therapy. *CA. Cancer J. Clin.* **63,** 395–418 (2013).

Acknowledgements

We gratefully acknowledge support from the Medical Research Council, U.K., (Grant number MR/J004103/1), Wessex Medical Research, UoS Research Management Committee, Nanoear FP6 (FP-6 NMP4-CT-2006), a Vice Chancellor's award from Malaya University, Malaysia, awarded to TAN, YCC, and the Institute for Life Sciences, Southampton, U.K. We also would like to thank Justin Baker for contributing to the pilot experiments, and David Johnston for technical help with confocal microscopy.

Author Contributions

T.A.N., A.H.J. and N.D.E. conceived the study. E.S., A.H.J., T.A.N. and N.D.E., designed the experiments. E.S., J.L.B. and A.H.J., performed the experiments and collected data for characterisation and microscopy uptake studies. E.S. and A.A.J., performed the experiments and collected data for the single cell analyses. N.D.E., E.S., T.A.N. and P.S.S., performed the analyses. T.A.N. and N.D.E., supervised data collection and wrote the manuscript. Y.L.W, Y.C.C., and R.O.C.O., contributed to the discussion of data and the writing of early drafts of the manuscript, with emphasis on the clinical utility and need for the study. T.A.N. and N.D.E. contributed equally to the study. All authors discussed the results and commented on the manuscript.

Additional Information

Supplementary information accompanies this paper at http://www.nature.com/srep

Competing financial interests: The authors declare no competing financial interests.

How to cite this article: Scarpa, E. *et al.* Quantification of intracellular payload release from polymersome nanoparticles. *Sci. Rep.* **6,** 29460; doi: 10.1038/srep29460 (2016).

7.6 Transient Canonical Wnt Stimulation Enriches Human Bone Marrow Mononuclear Cell Isolates for Osteoprogenitors

STEM CELLS

REGENERATIVE MEDICINE

Transient Canonical Wnt Stimulation Enriches Human Bone Marrow Mononuclear Cell Isolates for Osteoprogenitors

AGNIESZKA A. JANECZEK,[a,b,c] RAHUL S. TARE,[a,b,c] EDOARDO SCARPA,[a,b,c] INES MORENO-JIMENEZ,[a,b,c] CAROLINE A. ROWLAND,[d] DOMINIC JENNER,[d] TRACEY A. NEWMAN,[e] RICHARD O. C. OREFFO,[a,b,c] NICHOLAS D. EVANS[a,b,c]

Key Words. Wnt signaling • Marrow stromal cells/mesenchymal stem cells • Osteoprogenitors • Stem cells • Fracture healing

[a]Centre for Human Development, Stem Cells and Regeneration, [b]Bone and Joint Research Group, Human Development and Health Academic Unit, Institute for Developmental Sciences, Faculty of Medicine, [c]Institute for Life Sciences, [d]Microbiology group, Chemical, Biological and Radiological Division, Salisbury, United Kingdom; [e]Clinical and Experimental Sciences, Faculty of Medicine, Institute for Life Sciences, University of Southampton, Southampton, United Kingdom

Correspondence to: Nicholas Evans, PhD, Centre for Human Development, Stem Cells and Regeneration, University of Southampton, IDS Building, University General Hospital Campus, Tremona Road, Southampton, Hampshire SO16 6YD, United Kingdom. Telephone: 44-023-8120-3293; e-mail: n.d.evans@soton.ac.uk

Received August 17, 2015; accepted for publication October 1, 2015; first published online in STEM CELLS *EXPRESS* November 3, 2015.

1066-5099/2014/$30.00/0

http://dx.doi.org/10.1002/stem.2241

ABSTRACT

Activation of the canonical Wnt signaling pathway is an attractive anabolic therapeutic strategy for bone. Emerging data suggest that activation of the Wnt signaling pathway promotes bone mineral accrual in osteoporotic patients. The effect of Wnt stimulation in fracture healing is less clear as Wnt signaling has both stimulatory and inhibitory effects on osteogenesis. Here, we tested the hypothesis that transient Wnt stimulation promotes the expansion and osteogenesis of a Wnt-responsive stem cell population present in human bone marrow. Bone marrow mononuclear cells (BMMNCs) were isolated from patients undergoing hip arthroplasty and exposed to Wnt3A protein. The effect of Wnt pathway stimulation was determined by measuring the frequency of stem cells within the BMMNC populations by fluorescence-activated cell sorting and colony forming unit fibroblast (CFU-F) assays, before determining their osteogenic capacity in in vitro differentiation experiments. We found that putative skeletal stem cells in BMMNC isolates exhibited elevated Wnt pathway activity compared with the population as whole. Wnt stimulation resulted in an increase in the frequency of skeletal stem cells marked by the STRO-1^{bright}/Glycophorin A^{-} phenotype. Osteogenesis was elevated in stromal cell populations arising from BMMNCs transiently stimulated by Wnt3A protein, but sustained stimulation inhibited osteogenesis in a concentration-dependent manner. These results demonstrate that Wnt stimulation could be used as a therapeutic approach by transient targeting of stem cell populations during early fracture healing, but that inappropriate stimulation may prevent osteogenesis. STEM CELLS *2016;34:418–430*

SIGNIFICANCE STATEMENT

Modulation of the Wnt pathway may be an attractive therapeutic strategy for bone repair. Wnt stimulation, however, may both inhibit and promote bone differentiation of stem/progenitor cells, depending on when it is applied. Here, we show that putative skeletal stem cells have intrinsically elevated levels of Wnt pathway activation and only a controlled Wnt exposure increases their frequency. We believe this is the first study to specifically address how Wnt stimulation affects putative human skeletal stem cell populations and it provides timely evidence to suggest why novel Wnt therapeutics may be effective in osteoporosis but not in fracture healing.

INTRODUCTION

Bone injury is a major public health problem, the societal and financial implications of which are set to increase rapidly as the average age of our population rises [1, 2]. Although bone has a high regenerative capacity, in some cases fracture healing is delayed or absent (resulting in a nonunion) [3]. Therapeutic approaches to nonsevere fractures may involve strategies to fix the bones using plates, or the introduction of osteoinductive biomaterials, including allograft or autograft, to stimulate the formation of new bone. Systemic drugs offer the advantage of providing therapy without surgical intervention, but while many systemic drugs acting on a range of targets are clinically approved for stimulating bone formation in osteoporosis (e.g., parathyroid hormone [PTH]), there are little data available to suggest these agents improve fracture healing in humans [4]. Therefore, there remains a pressing need for new drugs, targets,

and treatment regimens that aim to augment the degree and rate of fracture healing.

One such target is the canonical (β-catenin-dependent) Wnt signaling pathway. The importance of Wnt signaling in bone biology is illustrated most strikingly by the corollary of mutations or genetic alterations in components of the canonical Wnt signaling pathway. In humans, genetic studies on high bone mass (HBM) diseases have shown that affected patients often have either *LRP5* gain-of-function mutations or *SOST* loss-of-function mutations [5–7]. This is also observed in animal models, where mutations that either augment or diminish Wnt signaling result in dramatic bone accrual or loss, respectively [7–9]. Such findings have led to attempts to modulate Wnt signaling for anabolic therapies for osteoporosis or for fracture healing, and there are several therapies presently undergoing clinical trials that target Wnt signaling, including humanized monoclonal antibodies directed to SOST [10] and DKK1 [11]. These therapies have been developed based on successful pre-clinical studies which found that these molecules have anabolic effects on bone formation and fracture healing [12–14]. Phase II trials of romosozumab, a humanized monoclonal Ab to SOST, have shown promising results in osteoporosis, and the drug is currently in phase III trials [15], although any positive effect on fracture healing in humans is yet to be proven.

A confounding factor for demonstrating the efficacy of drug modulation of Wnt signaling in fracture healing is the varying requirements for stimulation of this pathway during different phases of fracture healing. For example, Chen et al. found that while selective agonism of the Wnt signaling at late stages of murine fracture healing promoted bone formation, prolonged constitutive activation of β-catenin resulted in precisely the opposite effect [16]. Such in vivo data are reflected in studies on the stem and/or progenitor cells thought to be active in bone healing, marrow stromal cells (MSCs; also commonly referred to as mesenchymal stem cells). In some circumstances, Wnt stimulation inhibits the osteoblastic differentiation of MSCs [17–20], while in other studies, Wnt stimulation promotes osteogenesis [8, 21–23]. These observations may reflect differing requirements for Wnt stimulation during the lifecourse of an osteoblast—for example, several studies have found that the stimulatory effect of Wnt signaling is dependent on the stage of commitment of the progenitor cell/osteoblast [24–26]. Such data point to a complex situation where Wnt signaling may (a) promote stem/progenitor cell expansion, (b) inhibit early osteoblast differentiation, and/or (c) promote late stage osteoblast differentiation/maturation. A thorough understanding of this situation is further compounded by the lack of agreed or reliable markers for putative stem cells or progenitors that give rise to osteoblasts. In addition, in the majority of published studies, the term "mesenchymal stem cells" refers to isolates of plastic-adherent stromal cells from bone marrow mononuclear populations [18, 24, 27–30]. Such isolates are also known to contain mixed populations of cells with differing proliferative and differentiation capacities [31], and may themselves contain cells at various stages of commitment. Therefore, a more precise understanding of the effects of Wnt signaling on skeletal stem cells and the progeny at various stages of commitment to the osteogenic lineage is required to determine the optimal time window for therapeutic Wnt stimulation.

In this study, we focused on the effect of Wnt stimulation on fresh isolates of human bone marrow mononuclear cells (BMMNCs) and a population of cells with stem cell-like properties marked by the STRO-1^{bright}/Glycophorin A $(GPA)^{-}$ cell surface phenotype [32]. We tested the hypothesis that putative skeletal stem cell populations in human bone marrow samples are Wnt responsive, and that their commitment to osteogenic differentiation is influenced by Wnt signaling. Furthermore, we determined the effect of Wnt stimulation on cell populations with cell surface marker phenotypes that are known to be enriched in colony forming unit fibroblast (CFU-F) activity, and measured the effect of either an early transient Wnt stimulation or a prolonged exposure in stromal cells arising from adherent BMMNCs. Our results demonstrate that the timing of Wnt exposure in cells that contribute to fracture healing may be critical to the success of such therapies.

Materials and Methods

Reagents

Tissue culture reagents were obtained from Lonza (Basel, Switzerland, www.lonza.com) unless otherwise stated and fetal bovine serum (FBS) from Gibco (Paisley, UK, www.thermofisher.com/uk/en/home/brands/gibco.html). Biochemical reagents were obtained from Sigma-Aldrich (St. Louis, MO, www.sigmaaldrich.com) unless otherwise stated.

Cell Extraction and Culture

The bone marrow mononuclear cells (BMMNCs) used in this study were isolated from femoral bone marrow samples obtained from hematologically normal individuals undergoing hip replacement surgery at Southampton General Hospital, with the approval of the Southampton Local Research Ethics Committee (LREC 194/99). Primary cultures of human bone marrow stromal cells were established from 11 donors: seven females and four males, 57–94 years of age, mean age 75.1 years, as described previously [33, 34] (see Supporting Information Methods). Cells were maintained in basal medium (α-MEM containing 10% FBS and 100 μg/ml penicillin/streptomycin) or osteogenic medium (basal medium supplemented with 100 μM ascorbate-2-phosphate, 10 nM dexamethasone, and 5 mM β-glycerophosphate), with the exception of 24 hours exposure to Wnt3A protein (R&D Systems, Minneapolis, MN, www.rndsystems.com), where serum concentration in the media was 5%. Cells were exposed to 100 ng/ml Wnt3A protein, unless otherwise stated, either for 24 hours (short-term) or 14 days (long-term). For proliferation and apoptosis experiments, cells were exposed to 100 ng/ml Dkk1 (R&D Systems, Minneapolis, MN, www.rndsystems.com) as an additional control. Media in long-term cultures were renewed every 2–3 days. All cells were maintained at 37°C in a humidified 5% CO_2 atmosphere. All studies were conducted using cells from primary (P0) passage culture. A schematic representation of the experimental methodology is shown in Fig. 1.

Flow Cytometric Analysis and Sorting

Before staining, BMMNCs were treated with EasyLyse Erythrocyte Lysing Reagent (DAKO, Glostrup, Denmark, www.dako.com).

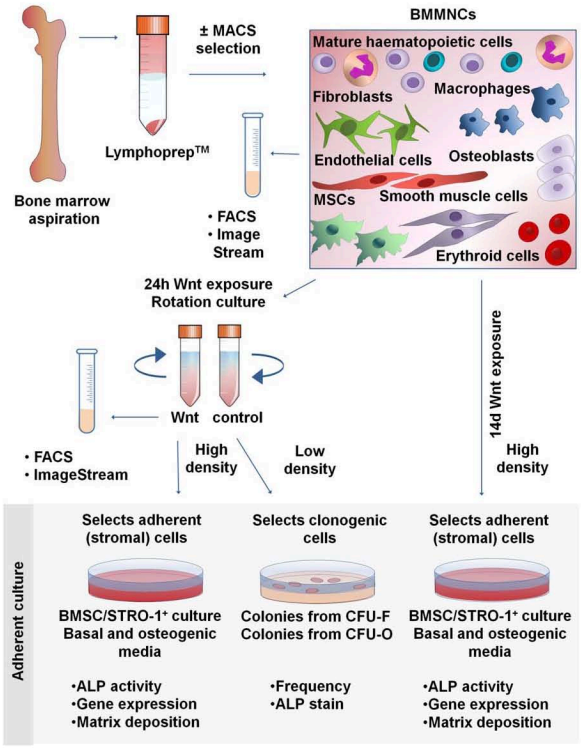

Figure 1. Experimental methodology. Bone marrow mononuclear cells (BMMNCs) were isolated from bone marrow aspirates by Lymphoprep, before further enrichment of a subset of samples by magnetic activated cell sorting selection for the STRO-1 antigen. Samples were then immediately analyzed by flow cytometry or ImageStream, or were subject to either a transient (24 hours; short-term) or prolonged (14 days; long-term) stimulation with Wnt3A. After transient stimulation, cells were analyzed by flow cytometry or ImageStream, or following 14 days of adherent culture in basal or osteogenic media, assayed for osteogenic differentiation potential (high density seeding) or CFU-F and CFU-O formation efficiency (low density seeding). Cells were also assayed after 14 days of ongoing, prolonged stimulation with Wnt (high density seeding) for their osteogenic differentiation potential. Abbreviations: ALP, alkaline phosphatase; BMMNCs, bone marrow mononuclear cells; BMSC, bone marrow stromal cell; CFU-F, colony forming unit fibroblast; CFU-O, colony formation in the presence of osteogenic medium; FACS, fluorescence-activated cell sorting; MACS, magnetic activated cell sorting; MSCs, mesenchymal stem cells.

For fluorescence-activated cell sorting (FACS) analysis, 10^6 to 10^7 cells were stained and all cells gated as positive showed a fluorescence intensity greater than that detected on 99% of the cells labeled with the isotype-matched control. Nonspecific antibody binding was blocked with phosphate-buffered saline (PBS) containing 1% bovine serum albumin (BSA), 10% human serum, and 3% sera from species in which the secondary antibodies were raised. Staining was performed at 4°C for 30 minutes, before washing (with 2 mM EDTA, 0.5% BSA in PBS). Antibodies used are listed in Supporting Information Table 1. For analysis of proliferation, a Click-iT EdU Alexa Fluor 488 Flow Cytometry Assay was used (Life Technologies, Carlsbad, CA, www.thermofisher.com) and for apoptosis/necrosis detection, Annexin V Apoptosis Detection Kit eFluor 450 (eBioscience, San Diego, CA, www.ebioscience.com). Samples were assayed on a FACS Calibur/Canto II cytometer (BD Biosciences, San Jose, CA, www.bdbiosciences.com) and analyzed using FlowJo v10 software (Ashland, OR, www.flowjo.com).

ImageStream Cytometry

Data were acquired using a dual-camera ImageStream X MkII (ISX) equipped with lasers of wavelength of 405 nm (set to 2 mW), 488 nm (set to 100 mW), 642 nm (set to 150 mW), and dedicated 785 nm (SSC, set to 10 mW). Data were collected using a 60 × objective with a numerical aperture of 0.9 and image resolution of approximately 0.33 μm/pixel. Channels

and filter information can be found in Supporting Information Table 2A. Data capture was performed with INSPIRE software v.2 (Amnis, Seattle, WA, www.emdmillipore.com), with a minimum of 1.2×10^5 and maximum of 6×10^5 in-focus (Gradient RMS M01 > 50), nucleated (Intensity Ch07 > 1×10^4) cells captured for each sample, leading to a minimum of 500 cells of the phenotype of interest ($CD45^-/GPA^-/STRO\text{-}1^+$). Single stained controls were run for each fluorochrome used and a compensation matrix was created to calculate spectral overlap (Supporting Information Table 2B). All image display properties were adjusted linearly on representative cell population images for each channel based on the pixel range of the signal and then applied to the entire data file. A data analysis template was generated from the established settings and selected gates and used for all subsequent analyses.

Colony Formation and Differentiation Assays

BMMNCs were plated at 5×10^3 to 5×10^4 cells per square centimeter due to high inter-donor variability in colony forming potential. After 14 days of culture, cells were washed with PBS, fixed with 95% ethanol, and either stained for alkaline phosphatase (ALP) or collected for ALP activity measurements. Staining was conducted using an ALP staining kit (Supporting Information Methods). Absorbance was measured using an ELx800 microplate reader (Biotek, Winooski, Vermont, www.biotek.com) at a wavelength of 415 nm. DNA content was measured using Quant-iT PicoGreen dsDNA Reagent (Life Technologies, Carlsbad, CA). Fluorescence was measured on an FLx800 fluorescence microplate reader (Biotek, Winooski, Vermont, www.biotek.com) with excitation/emission wavelengths of 480/520 nm. Two percentage of Alizarin Red S solution (pH = 4.2) was used to evaluate calcium deposition in cultured cells and the dye was subsequently extracted with 10% cetylpyridinium chloride solution. Absorbance was measured at 540 nm.

RNA Extraction and Quantitative Real-Time PCR

Total RNA was extracted with an RNeasy Mini Kit (Qiagen, Venlo, Netherlands, www.qiagen.com) or PicoPure (Life Technologies, Carlsbad, CA, www.thermofisher.com), for samples with limited cell numbers. Reverse transcription was conducted using the SuperScript VILO cDNA Synthesis Kit (Life Technologies, Carlsbad, CA, www.thermofisher.com). The ΔΔCt method of relative quantification real-time polymerase chain reaction (PCR) was performed using 7500 Real Time PCR detecting system using primers designed for genes of interest and housekeeping genes (Supporting Information Methods; Table 3).

Statistical Analysis

Statistical analysis was performed using GraphPad Prism 6 software (GraphPad, La Jolla, CA, www.graphpad.com). Differences in assays between cells exposed to Wnt protein and the control group were analyzed using a *t*-test or a paired *t*-test. For nonparametric data, Mann-Whitney or Wilcoxon's signed rank test was used. The qualitative PCR data were analyzed with the use of Kruskal-Wallis test with Tukey's post hoc correction. Data are presented as means ± SD and the significance level was set at $p = 0.05$.

Results

Putative MSCs Marked by STRO-1 Have Elevated Markers of Wnt Pathway Activation

To confirm the phenotype of $STRO\text{-}1^+$ cells, we first performed antibody staining and FACS analysis of freshly isolated BMMNCs. Populations of granulocytes, monocytes, and lymphocytes, including natural killer cells, T cells and B cells, were identified using a panel of antibodies (CD66b, CD14, CD56, CD3, and CD19, respectively) and comprised 65%, 6.63%, 2.93%, 6.37%, and 3.89%, respectively, of the BMMNCs fraction. Labeling corresponded with the known light scattering properties of these cell populations (Fig. 2A). STRO-1 marked 8.85 ± 4.66% of BMMNCs, and these cells co-localized based on light scattering properties predominantly with the monocyte population (Fig. 2B; 18.8 ± 8.21%, $n = 7$, of the monocytic fraction based on FSC *vs.* SSC). However, very few $STRO\text{-}1^+$ cells also stained with the hematopoietic surface marker CD45 or with the monocyte cell surface marker CD14 (0.88 ± 0.17%, $n = 3$) confirming the STRO-1 fraction as a distinct subpopulation (Fig. 2C, 2D, 2E), with coincidental similarities in light scattering properties.

While STRO-1-selected cells contain all the CFU-F activity, further enrichment of BMMNCS for cells with stem cell-like activity has been shown by positive selection for the highest 10% of cells expressing STRO-1 ($STRO\text{-}1^{bright}$) combined with negative selection for GPA (a marker of erythroid cells) [32]. We found that 55.81 ± 10.93% of the recovered cells were $STRO\text{-}1^+/GPA^+$ and that 6.63 ± 2.26% were $STRO^+/GPA^-$, with 0.66 ± 0.22% of the population falling into the $STRO\text{-}1^{bright}$ fraction (Fig. 2F; Supporting Information Fig. 1B). Using ImageStream cytometry, $STRO\text{-}1^+/GPA^-$ could further be distinguished from $STRO\text{-}1^+/GPA^+$ erythroid progenitors using cell morphology, as the $STRO\text{-}1^+/GPA^-$ cells exhibited both significantly greater cell area and lower cell aspect ratio (Fig. 2G; Supporting Information Fig. 1C).

As $STRO\text{-}1^+$ cells contain a multipotent population of stem cells, and considering there are data suggesting that Wnt may control the self-renewal of such cells, we reasoned that Wnt signaling may be elevated in the putative stem cell-enriched populations marked by $STRO\text{-}1^+$, $STRO\text{-}1^+/GPA^-$, and $STRO\text{-}1^{bright}$. Accordingly, we observed significant increases in the expression of several mRNA markers of Wnt pathway activation, *CCND1* and *CMYC*, in $STRO\text{-}1^{bright}$ cells compared with unsorted BMMNCs (increase in expression of 8.15 ± 5.95 and 6.48 ± 3.55, respectively, $p < 0.05$), and a similar (but nonsignificant) trend observed for *AXIN2* (Fig. 3A, 3B). It has recently been shown that *Osterix/SP7*-expressing cells can produce Wnts and respond to Wnt signaling to control bone homeostasis [35]. Therefore, we tested $STRO\text{-}1^+$ cells for the expression of *Osterix/SP7* and found that $STRO\text{-}1^{bright}$ cells expressed higher levels of *Osterix/SP7* than unsorted BMMNCs (9.69 ± 5.86 higher *vs.* control, Fig. 3C). Together, these data demonstrate that isolates of mononuclear cells from human bone marrow aspirates contain a cell population with known stem cell-like properties with intrinsically elevated levels of Wnt signaling.

Early Wnt Exposure Expands the Number of $STRO\text{-}1^+$ Osteoprogenitors in Bone Marrow Mononuclear Cell Populations

We next examined whether a transient canonical Wnt stimulus could induce an increase in the frequency of the $STRO\text{-}1^+$

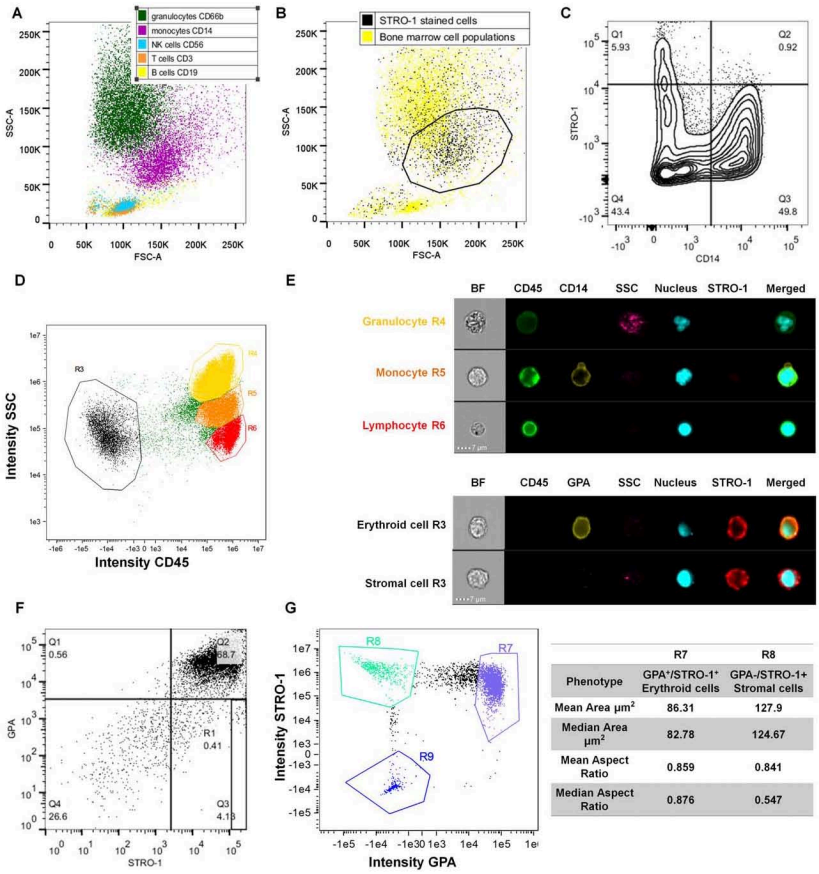

Phenotype	R7 GPA+/STRO-1+ Erythroid cells	R8 GPA-/STRO-1+ Stromal cells
Mean Area µm²	86.31	127.9
Median Area µm²	82.78	124.67
Mean Aspect Ratio	0.859	0.841
Median Aspect Ratio	0.876	0.547

Figure 2. Characterization of putative stromal stem cell populations of the bone marrow. **(A)**: Fluorescence-activated cell sorting (FACS) dot plot of bone marrow cell populations, backgated according to expression of specific markers. **(B)**: FACS dot plot overlaying STRO-1-stained cell population on the top of all bone marrow cell populations, based on FSC versus SSC. Enrichment in the "monocytic" region (marked by black polygon gate) is visible. **(C)**: FACS contour plot depicting that presence of cells double-positive for STRO-1 and CD14 (monocyte marker) within the "monocytic" gate is low (Quadrant 2, Q2). **(D)**: Image Stream dot plot and **(E)** panel showing the morphology of $CD45^+$ blood populations (granulocytes, monocytes and lymphocytes) and the lack of co-localization with STRO-1, and the two $STRO\text{-}1^+$ populations within the CD45 fraction of the bone marrow mononuclear cells (erythroid cells, mesenchymal stem cells [MSCs]). **(F)**: FACS dot plot depicting STRO-1 and Glycophorin A (GPA) co-localization (Quadrant 2, Q2). The GPA $/STRO\text{-}1^+$ fraction was located in quadrant 3 (Q3), and gate R1 demarks GPA $/STRO\text{-}1^{bright}$ population set as top 10% of the GPA $/STRO\text{-}1^+$ fraction on the day of bone marrow isolation. G) Dot plot shows the identification of STRO-1 and GPA expressing cells, and the table shows that GPA $/STRO\text{-}1^+$ cells are larger than $GPA^+/STRO\text{-}1^+$ erythroid cells. Abbreviations: BF, brightfield; FSC-A, forward scatter area; GPA, Glycophorin A; NK, natural killer; SSC-A, side scatter area.

population. Isolated BMNNCs were cultured in suspension in the presence of the canonical Wnt protein Wnt3A or a vehicle control for 24 hours, and cell surface expression of STRO-1 was measured by FACS. We first confirmed Wnt pathway activation by measuring the expression of Wnt target genes *AXIN2*, *CMYC*, and *CCND1*, in STRO-1-selected cells after Wnt3A stimulation. *AXIN2* and *CCND1* expression was significantly increased in Wnt3A-exposed cells compared with control (by factors of 2.92 ± 0.20 and 4.88 ± 2.72, respectively, $p < 0.5$), with a similar trend for *CMYC* (Fig. 4A).

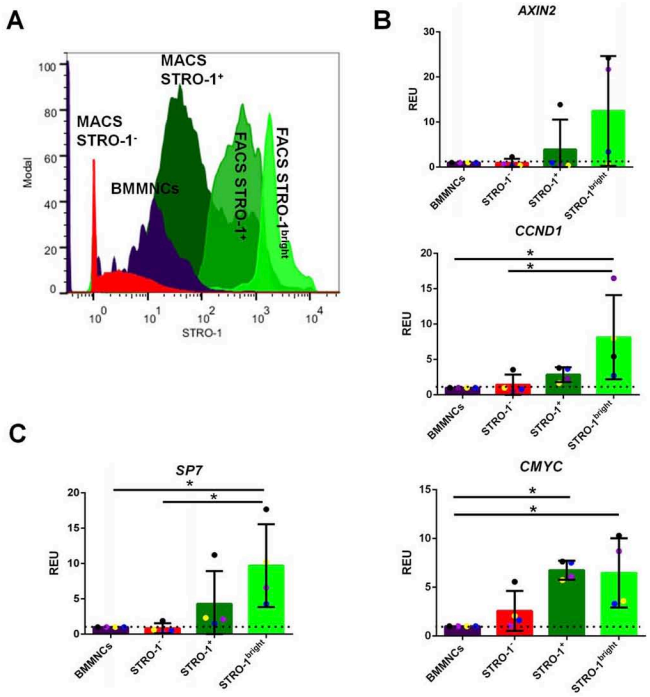

Figure 3. STRO-1$^+$ population within the bone marrow has intrinsically higher Wnt signaling than the general bone marrow population. **(A)**: Fluorescence-activated cell sorting (FACS) histogram depicting gating for FACS STRO-1-sorted samples. The STRO-1^{bright} cells are the top 10% fraction of the FACS STRO-1$^+$ cells. **(B)**: Qualitative polymerase chain reaction (qPCR) data showing Wnt signaling pathway target genes mRNA expression (*AXIN2*, *CCND1* and *CMYC*, respectively) in FACS-sorted samples (STRO-1$^-$, STRO-1$^+$, and STRO-1^{bright} cells as relative to bone marrow mononuclear cells [BMMNCs]), based on the level of STRO-1$^+$ mesenchymal stem cell [MSC] marker expression. All data have been normalized to *βACTIN* and to 1 for BMMNCs of the same marrow sample. $n = 4$; *, $p < 0.05$. **(C)**: qPCR data showing *SP7* mRNA expression in FACS-sorted samples (STRO-1$^-$, STRO-1$^+$, and STRO-1^{bright} cells as relative to BMMNCs), based on the level of STRO-1$^+$ MSC marker expression. All data have been normalized to *βACTIN* and to 1 for BMMNCs of the same marrow sample. $n = 4$; *, $p < 0.05$. Abbreviations: BMMNCs, bone marrow mononuclear cells; FACS, fluorescence-activated cell sorting; MACS, magnetic activated cell sorting; REU, relative expression units.

Following Wnt3A stimulation, we measured an increase in the BMMNC frequency of STRO-1$^+$ cells, with a greater increase measured following gating only for monocytic/stromal fractions ($p < 0.01$; Fig. 4B). There was no Wnt-dependent increase in STRO-1 expression in the granulocytic and lymphocytic fractions (Fig. 4C), supporting the notion that the increase in STRO-1 frequency was confined to cells with scattering properties comparable with monocytes, which include stromal cells. While significant inter-donor variability in STRO-1 frequency was observed (ranging from 3.32 to 17.10% in control *vs.* 5.43 to 25.3% after Wnt treatment), an increase in STRO-1 frequency was observed in every case (Supporting Information Table 4).

To further test the hypothesis that canonical Wnt stimulation enriches BMMNCs for stem cell-like populations, the effect of Wnt stimulation on the frequency of STRO-1$^+$/GPA$^-$ and STRO-1^{bright}/GPA$^-$ cells, which are known to be further enriched for stem cells, was measured. In the three separate donor BMMNCs analyzed, we measured an increase in the frequency of either STRO-1$^+$/GPA$^-$ cells (by a factor of 1.57 ± 0.16, $p < 0.01$; Fig. 4D) or STRO-1^{bright}/GPA$^-$ cells (by a factor of $1.63 \pm 0.37\%$, $p < 0.001$; Fig. 4E). Confirming these measurements, ImageStream analysis not only revealed an increased frequency in the CD45$^-$/STRO-1$^+$/GPA$^-$ population after Wnt stimulation but also an increased intensity/cell of the STRO-1 marker expression (Fig. 4F). Together, these data indicate that a short, transient exposure to a canonical Wnt ligand increases the frequency of cells with surface markers that are known to enrich BMMNC populations for stem cells.

We next considered whether canonical Wnt stimulation of mixed BMMNC populations might cause an increase in the frequency of stromal populations by nonspecific effects on

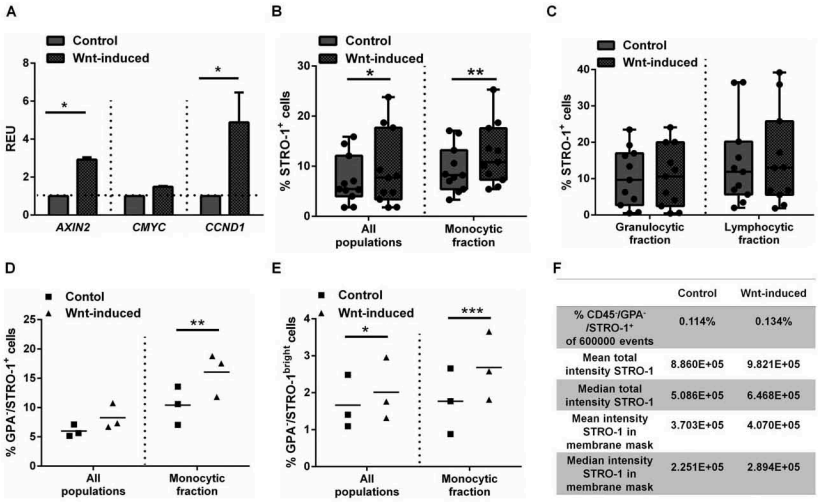

Figure 4. Wnt3A stimulation activates Wnt signaling pathway activity in stromal populations and promotes their expansion. **(A)**: Wnt target gene expression after 24 hours of suspension culture in the STRO-1-selected cells. $n = 3$, statistical significance *, $p < 0.05$. **(B)**: STRO-1 marker expression is augmented within the entire bone marrow and gate co-localizing with monocytes. ($n = 11$; *, $p < 0.05$; **, $p < 0.01$) or **(C)** unchanged within specific gates co-localizing with lymphocytes and granulocytes ($n = 11$, ns). The proportion of Glycophorin A (GPA) /STRO-1^+ cells **(D)** or GPA /STRO-1^{bright} cells **(E)** is increased following Wnt stimulation in the "monocyte" gate ($n = 3$; *, $p < 0.05$; **, $p < 0.01$; ***, $p < 0.001$. **(F)**: Image Stream analysis demonstrates an increase in cell intensity for the STRO-1 antigen staining following Wnt-induction in CD45 /GPA /STRO-1^+ population. Abbreviations: GPA, Glycophorin A; REU, relative expression units.

other cell populations. To test this, we measured cell number, cell proliferation, cell viability, DNA synthesis, apoptosis, and necrosis in whole populations and subpopulations. Following 24 hours of rotation suspension culture, we found no change in the number of viable cells, as measured by trypan blue exclusion (Fig. 5A). Wnt3A treatment resulted in a small but nonsignificant increase in the total number of cells present after incubation. Furthermore, Wnt3A treatment did not induce changes in the relative numbers of hematopoietic lineages, assessed by measurements of light scattering (Fig. 5B) or by FACS quantification of cells using markers for the hematopoietic lineages (CD3, CD19, CD56, CD14, or CD66a; Fig. 5C). These results indicate Wnt3A effects in the culture system were specific to stromal cell lineages marked by STRO-1.

We next hypothesized that Wnt3A may exert its effect by providing mitogenic or cell survival signals for stromal populations. To test this, we measured DNA synthesis, an indicator of mitosis and cell proliferation, in Wnt3A or control-exposed cell populations by EdU incorporation. Apoptotic, necrotic, and viable cells were tracked by Annexin V and 7-AAD incorporation. A Wnt3A-dependent increase in $18.70 \pm 0.75\%$ *versus* control $8.25 \pm 0.89\%$ in the number of proliferating cells in the STRO-1^+ population (with stromal cell light scattering properties) was observed (Fig. 5D). There was no evidence of a Wnt3A dependent change in cell proliferation in other cell populations, indicating that the mitogenic effect was specific to stromal populations (Fig. 5E). In addition, we measured an increase in the frequency of viable cells and a decrease in the frequency of apoptotic and necrotic cells in the STRO-1^+ subset (Fig. 5F). To try and exclude a possible indirect role for Wnt3A, for example, inducing a paracrine signal in another nonstromal cell population, we attempted to separate populations of STRO-1^+ cells to test the effect of Wnt3A exposure in the absence of hematopoietic lineages. In this system, we observed widespread death of STRO-1 cells ($62.78 \pm 15.80\%$, $p < 0.0001$) and were unable to measure any Wnt3A effects (Supporting Information Fig. 2).

It is possible the effects of Wnt3A may be evident on cells expressing other markers ascribed to mesenchymal stem cells, including CD90, CD105, and CD146. However, due to the very low frequency of these cells in BMMNCs, we were unable to measure any effects of Wnt3A on cells expressing markers of putative MSCs (Supporting Information Fig. 3A, 3B for markers in fresh isolates of BMMNCs or Fig. 3C for cultured, plastic adherent stromal cells).

Together, these data indicate that BMMNCs are responsive to stimulus with a canonical Wnt protein, that this induces an increase in frequency in the STRO-1^+ population, which is known to contain all CFU-F activity, and that this is mediated by both protection from apoptosis or necrosis and an increase in cell division, specific to stromal populations.

Early Wnt Exposure Increases the Frequency of CFU-Os but Not CFU-Fs

Since STRO-1^+ cells contain all of the multipotent CFU-F activity of BMMNCs and are enriched in Wnt-stimulated BMMNCs,

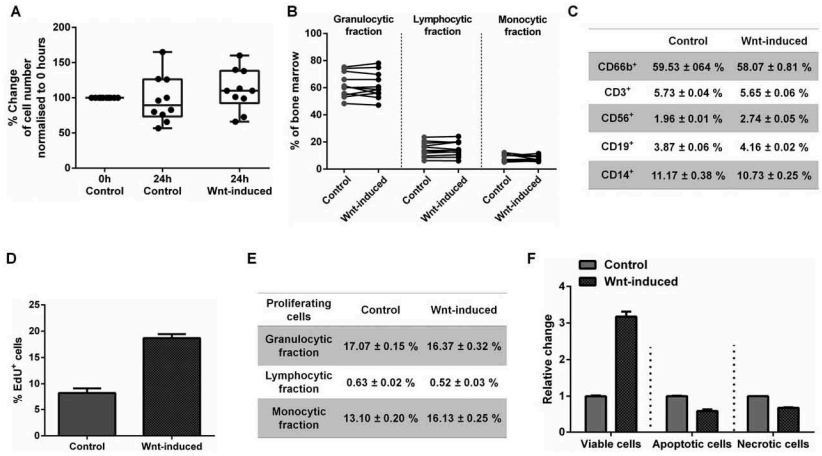

Figure 5. Wnt stimulation increases STRO-1 proliferation and protects from apoptosis and necrosis. **(A)**: Wnt3A had no effect on the total cell numbers after 24 hours of suspension culture ($n = 10$). **(B)**: Wnt stimulation had no effect on the proportion of the populations of lymphocytes, granulocytes and monocytes in bone marrow mononuclear cells (BMMNC) isolates ($n = 11$). **(C)**: Wnt has no effect on blood cell lineages. Representative figures from triplicates from one patient. **(D)**: Wnt stimulation induces an increase in the frequency of proliferating (EdU^+) cells within the STRO-1^+ population but has no effect on the proportion of EdU^+ within other populations **(E). (F)**: Wnt stimulation causes an increase in cell viability and a decrease in apoptosis and necrosis (stained with Annexin V and 7-AAD) within the STRO-1^+ population. Data in (D), (E), and (F) presented as mean ± SD, $n = 1$ donor.

we hypothesized that Wnt stimulation would increase the formation of CFU-Fs from BMMNC isolates. Surprisingly, we found no increase in the frequency of CFU-Fs (Fig. 6A). However, on staining colonies for ALP activity, we found that colonies formed from Wnt3A-stimulated cells had significantly increased ALP activity under basal medium conditions (Fig. 6B, 6C). We considered that this, combined with our measurements of elevated *SP7/Osterix* in previous experiments, was an indicator that the increase in frequency of STRO-1^+, STRO-1^+/GPA^-, and STRO-1^{bright} cells could reflect an increase in the frequency of osteoprogenitors, the growth of which might not be promoted under CFU-F culture conditions. To test this, we assayed colony formation in the presence of osteogenic medium (CFU-O assay) and observed a significant increase in the number of CFU-O recovered (Fig. 6D), and a greater proportion of ALP^+ CFU-Os compared with controls (Fig. 6E, 6F). These results suggest that Wnt3A stimulation does not increase the frequency of CFU-Fs recovered from BMMNC populations, but rather expands a subset of BMMNCs marked by STRO-1^+, STRO-1^+/GPA^-, and STRO-1^{bright} primed for osteogenesis.

Osteogenic Differentiation in BMMNCs and STRO-1 Selected Populations Is Promoted by Early Transient Wnt Exposure but Is Abrogated by Prolonged Wnt Stimulation

Due to conflicting data in the literature on the effect of canonical Wnt stimulation on the osteogenic differentiation of MSCs [18, 24, 27], we examined whether transient, early Wnt3A stimulation, or a continuous Wnt3A stimulation affected the differentiation of stromal cells arising from BMMNCs. Transient, early stimulation of BMMNCs with Wnt3A resulted in significant increases in the expression of ALP in stromal cell cultures. This was true for both cultures arising from unsorted BMMNCs and cultures from enriched stromal cells expressing STRO-1^+. Furthermore, the enhanced expression of ALP occurred regardless of whether culture medium contained osteogenic supplements, although as expected, osteogenic supplementation promoted ALP activity overall (Fig. 7A). Donor-specific differences in the magnitude of the response to Wnt3A stimulation were observed, but the trend was true for all donors and a significant effect was always measured in osteogenic media (Supporting Information Fig. 4A). In contrast, continuous incubation of stromal cells with Wnt3A, resulted in significant decreases in ALP activity. For example, in BMMNCs cultured in osteogenic media the inhibition reached a mean of 90.86 ± 3.89%, $p < 0.0001$; (Fig. 7B). This indicated a significant reduction in osteogenesis following long-term Wnt treatment, and was consistent in stromal cells from all donors under all conditions examined (Supporting Information Fig. 4B). This was not due to the concentration employed as a concentration-dependent inhibition was observed at lower Wnt3A concentrations (25 and 50 ng/ml; Supporting Information Fig. 5). No consistent effects were observed on cell proliferation in adherent cultures of stromal cells, following short- and long-term exposure to Wnt3A (Supporting Information Fig. 6).

To confirm that these ALP activity changes reflected terminal osteogenic differentiation, we performed Alizarin Red S staining to measure matrix mineralization by calcium

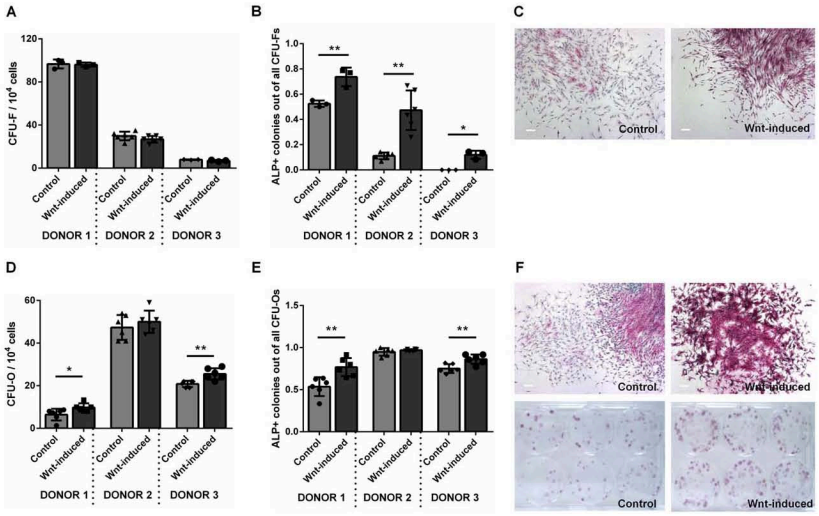

Figure 6. Early Wnt exposure increases the frequency of CFU-Os but not CFU-Fs. **(A)** Wnt stimulation of bone marrow mononuclear cells (BMMNCs) has no effect on the frequency of recovered CFU-F colonies but significantly increases the frequency of those that express ALP **(B). (C)**: ALP staining in CFU-F colonies arising in basal media. Wnt stimulation of BMMNCs significantly increased the frequency of CFU-O recovered **(D)** and expression of ALP (E and F) in 2 out of three patients tested *, $p < 0.05$; **, < 0.01. Scale bars = 200 μm. Abbreviations: ALP, alkaline phosphatase; CFU-F, colony forming unit fibroblast; CFU-O, colony formation in the presence of osteogenic medium.

deposition. Mirroring the data for ALP activity, significantly increased Ca^{2+} deposition in cultures stimulated transiently and decreased Ca^{2+} deposition in cells stimulated long term was observed (Fig. 7C, 7D). No significant differences were observed in the expression of *RUNX2* and *BGLAP* (Osteocalcin), although the trend was similar to the above (Fig. 7E).

These results indicate that transient, early Wnt stimulation augments the osteogenic potential of stromal cells derived from either unsorted or STRO-1-sorted BMMNCs, however, sustained Wnt3A activation markedly inhibits osteogenesis.

Discussion

Modulation of the Wnt signaling pathway is an attractive target for therapies that augment bone formation. Preclinical and clinical trials have indicated that drugs that elevate Wnt signaling can augment bone formation in both animal models and humans, but the target(s) of such drugs remains unresolved [10–15]. This study demonstrates that transient Wnt stimulation of BMMNCs increases the frequency of osteoprogenitors in bone marrow aspirates, but prolonged stimulation abrogates the osteogenic differentiation of the progeny of these cells. Our data show that targeted activation of Wnt signaling in stem or progenitor cells may be critical to therapeutic interventions in fracture healing.

We evaluated the effects of Wnt pathway activation in bone marrow mononuclear cells by using only freshly isolated human bone marrow aspirates, not subjected to passaging or prolonged culture. Such cell sources offer the advantage of the *ex vivo* study of the direct effects of chemical stimulation on cellular milieu found in human bone marrow, rather than on serially passaged, mixed, adherent cell populations. We first investigated a population of cells from the bone marrow, marked by the STRO-1 antigen, known to contain all of the CFU-F activity in human bone marrow [36, 37]. CFU-Fs arise from stromal populations in bone marrow isolates, and are indicative of progenitors of the nonhematopoietic lineage including skeletal stem cells, but are likely to contain cell types at different stages of commitment [38]. In agreement with other studies, we found the STRO-1 antibody labeled around 10% of BMMNCs, including cells of the blood lineages, illustrating that the STRO-1 antigen, while an enrichment marker for skeletal progenitors, is nonspecific for stromal cells in bone marrow [36]. Other studies, however, have found that further selection based on the STRO-1^{bright}/GPA^{-} phenotype enriches BMMNCs by three orders of magnitude for CFU-Fs [32]. Cells with this surface phenotype are considered to have stem-cell-like properties, exhibiting the ability to differentiate into multiple lineages in vitro and in vivo (cartilage, bone and fat), and to support the formation of hematopoietic marrow when transplanted in vivo [32]. While studying their gene expression, we found up-regulation of several genes involved in Wnt signaling in this population compared with other phenotypes. In addition, we observed Wnt pathway activation and increases in the frequency of these cells following

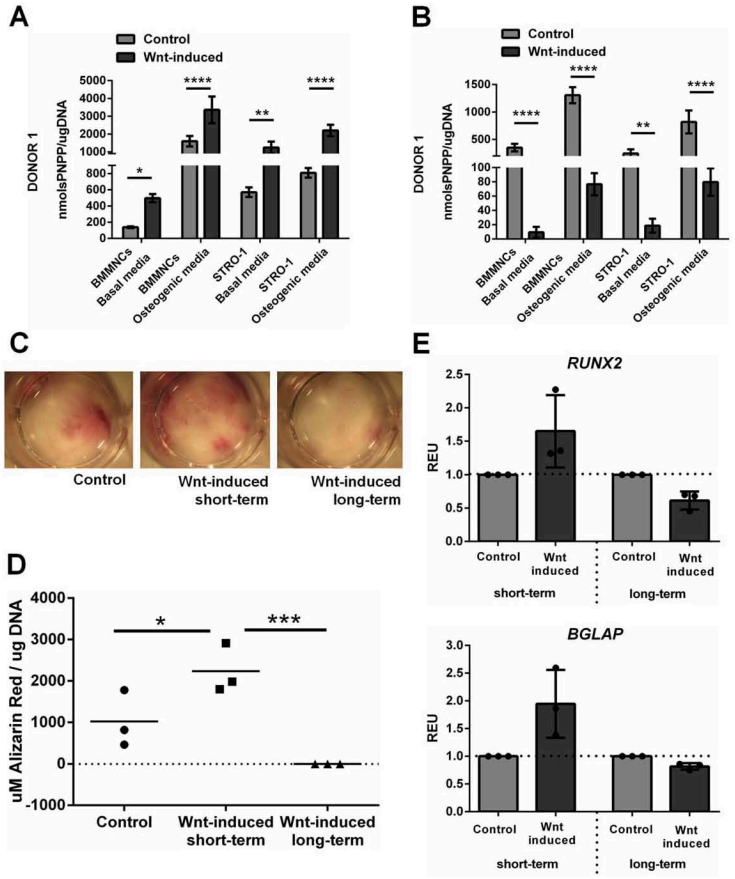

Figure 7. Osteogenic differentiation in bone marrow mononuclear cells (BMMNCs) and STRO-1-selected populations is promoted by early transient Wnt exposure but is abrogated by prolonged Wnt stimulation. **(A)**: Transient, early Wnt stimulation causes a significant increase in ALP activity in comparison with control in basal and osteogenic media in general bone marrow cell populations as well as STRO-1-selected cells while prolonged Wnt stimulation has the opposite effect **(B)**. This effect is reflected in Alizarin Red staining in cells cultured in osteogenic media **(C)** or by absorbance measurement on the extracted dye **(D)**. Gene expression analysis shows a trend towards an increase in *RUNX2* and *BGLAP* expression after short-term Wnt induction and decrease after long-term Wnt induction **(E)**. *, $p < 0.05$; **, $p < 0.01$; ***, $p < 0.001$; ****, $p < 0.0001$. Abbreviations: BMMNCs, bone marrow mononuclear cells; PNPP, p-nitrophenyl phosphate; REU, relative expression units.

exposure to a canonical Wnt ligand (Wnt3A), which was due to an increase in cell proliferation and reductions in apoptosis and necrosis. Many stem cell populations are known to be regulated by Wnt signaling [39] and although a significant body of published work has focussed on the role of Wnt signaling in cultured marrow stromal cells [18, 20, 22, 24, 28, 29, 40–43], there are comparatively little data available on the role of Wnt signaling in putative skeletal stem cells, either in their niche in vivo, or in rare populations extracted from the bone marrow [44–48]. Recently, Chan et al. demonstrated that a *de facto* skeletal stem cell population in murine marrow expressed high levels of Wnt ligands and their cognate Frizzled receptors, providing evidence that skeletal stem cell niches may be modulated by Wnts [49]. These data are further supported by work on the temporal importance of Wnt signaling in osteoprogenitor cells in development. For

example, selective removal of *Wls*, which is necessary for the secretion of Wnts, in cells expressing *Col1a1-3.6* (a marker of early osteoblastic differentiation) resulted in impairments in the maintenance of MSCs in adult animals [50]. Similar effects were measured with the removal of the canonical Wnt ligand Wnt10b [51]. In both cases, a decrease in recoverable CFU-Fs from the bone marrow of these animals was observed, and milder bone phenotypes were observed with the removal of these proteins in more committed osteoblastic cells expressing *Bglap* (*Osteocalcin*). More recently, Tan et al. [35] found that progenitor cells in bone express high levels of Wnt ligands *SP7/Osterix* and *Axin2*, the latter of which is expressed in progenitor cells lining the endosteal surfaces of bone [16]. In the data presented here, we found elevated *SP7/Osterix* transcript expression in the STRO-1^{bright} population, suggesting that this population likely contains similar osteoprogenitor cells.

Despite our observations of an increase in the frequency of STRO-1^{bright}/GPA^{-} cells in human bone marrow after Wnt treatment, we did not measure an increase in the frequency of CFU-Fs following plating at limiting dilutions, as one might expect if hypothesizing that Wnt stimulation expands a stromal, stem-like population in our bone marrow aspirates. In contrast, we did observe an increase first in the frequency of CFU-F colonies that expressed ALP, and second in the frequency of recoverable CFU-Os. It is possible that Wnt exposure primes uncommitted stromal cells in BMMNC isolates to an osteogenic fate, the clonal growth of which is favored in osteogenic medium. Despite an overall increase in the stromal cell populations, basal cell culture conditions may not be permissive for growth of these expanded cells, hence an increase in their frequency is not evident in CFU-F assays. This reasoning is supported by our observation of increased osteogenesis of marrow stromal cells derived from Wnt-stimulated BMMNCs. Taking the data together, it is therefore likely that Wnt exposure "primes" stromal cells in bone marrow aspirates to an osteogenic fate. Notably, continued Wnt exposure dramatically inhibited the osteogenic differentiation of stromal cells, supporting a series of other studies on these cells [18–20], and indicating that the timing of Wnt exposure is crucial in promoting osteogenic differentiation.

It is important to note that we were unable to access information about the medication status of our human donors, besides their sex and age. One major limitation arising from this might be the inability to assess whether the high inter-donor variability of the extent of responses to Wnt within the first 24 hours of treatment could be dependent on previous medication. On the other hand, working with samples from patients affected by bone diseases can be advantageous to the clinical relevance of the study, as bone diseases are the underlying cause of failed bone fracture healing, and we noticed positive Wnt effects regardless of the donor disease status. Future studies may seek to stratify the effects of drug intervention based on patient age, disease of medication status.

There is a pressing need to develop therapeutics that augment bone fracture healing, but it is likely that agents that function by anabolic or anti-catabolic means may fail to prove efficacious in fracture healing without due regard to the complexity of this process. Many drugs including bisphosphonates, PTH/teriparatide, and denosumab are used very successfully in the clinic to augment bone mass and prevent fracture in osteoporosis, but it remains somewhat controversial whether any has clinical benefit in fracture healing [52].

Recent phase II clinical trials on romosozumab have shown positive effects on bone formation and reduced bone resorption [15], and preclinical studies in mice have shown encouraging effects on fracture healing [53, 54]. Despite this, the cell type(s) or physiological target(s) affected by SOST inhibition remain unclear. In the case of the former trials, SOST inhibition may act by stimulating osteoblastogenesis, by inhibiting osteoclastogenesis, or by promoting or inhibiting the activity of all cell types within the basic multicellular unit (BMU) of bone, tipping the balance in favor of bone deposition; there is evidence for all these effects [55]. The situation in fracture healing is even more complex, where a coordinated series of events over a time period of many weeks ensures bone bridging. Wnt pathway activation may have effects on all these processes, some of which might be stimulatory to healing, and some of which might be inhibitory.

Several of these issues might be solved by a controlled, spatiotemporally defined delivery of drugs to fracture sites. Recently, Swami et al. demonstrated that an approved anticancer drug could be targeted specifically to metastatic bone lesions by the use of nanoparticles modified with bone-homing surface markers [56]. As the bone fracture site is characterized by both an initial hematoma, and a later prolonged period of inflammation, these periods during fracture healing may represent attractive windows when drug targeting might be achieved. Knowledge concerning the times at which cells of the osteoblast lineage are most conducive to stimulation by Wnt signaling, such as data presented in this study, will also inform these approaches.

Conclusions

In summary, we have demonstrated that transient canonical Wnt stimulation enriches human bone marrow samples for cells expressing known markers of stem/progenitor cells, and leads to a subsequent increase in osteogenesis, which is abrogated if Wnt stimulation is sustained. These results emphasize that therapeutic approaches to modulate Wnt signaling in fracture healing should consider the complexity of Wnt signaling requirements for successful differentiation of osteoblasts from progenitors present at injury sites.

Acknowledgments

We thank Dr. Kam Hussain for help with the hematopoietic panel FACS staining, the orthopaedic surgeons at Southampton General Hospital for provision of bone marrow samples, and Dr. Janos Kanczler for critical feedback on the manuscript. This work was supported by the Medical Research Council, U.K., (Grant number MR/J004103/1), Wessex Medical Research, UoS Research Management Committee, and the Institute for Life Sciences, Southampton, U.K.

Author Contributions

A.A.J.: conception and design, collection and/or assembly of data, data analysis and interpretation, manuscript writing, final approval of manuscript; R.S.T. and T.A.N.: conception and design, data analysis and interpretation, final approval of

manuscript; E.S. and D.J.: collection and/or assembly of data, data analysis and interpretation, final approval of manuscript; I.M.-J.: collection and/or assembly of data; C.R.: data analysis and interpretation, final approval of manuscript; R.O.C.O.: conception and design, data analysis and interpretation, financial support, final approval of manuscript; N.D.E.: conception and design, financial support, data analysis and interpretation, manuscript writing, final approval of manuscript.

Disclosure of Potential Conflicts of Interest

The authors indicate no potential conflicts of interest.

References

1 Burge R, Dawson-Hughes B, Solomon DH et al. Incidence and economic burden of osteoporosis-related fractures in the United States, 2005-2025. J Bone Miner Res 2007; 22:465–475.

2 Burge R, Worley D, Johansen A et al. The cost of osteoporotic fractures in the UK: Projections for 2000–2020. J Med Econ 2001; 4:51–62.

3 Rodriguez-Merchan EC, Forriol F. Nonunion: General principles and experimental data. Clin Orthop Relat Res 2004;419:4–12.

4 Aspenberg P. Annotation: Parathyroid hormone and fracture healing. Acta Orthop 2013;84:4–6.

5 Balemans W, Ebeling M, Patel N et al. Increased bone density in sclerosteosis is due to the deficiency of a novel secreted protein (SOST). Hum Mol Genet 2001;10:537–543.

6 Boyden LM, Mao J, Belsky J et al. High bone density due to a mutation in LDL-receptor-related protein 5. N Engl J Med 2002;346:1513–1521.

7 Gong Y, Slee RB, Fukai N et al. LDL receptor-related protein 5 (LRP5) affects bone accrual and eye development. Cell 2001;107:513–523.

8 Babij P, Zhao W, Small C et al. High bone mass in mice expressing a mutant LRP5 gene. J Bone Miner Res 2003;18:960–974.

9 Kato M, Patel MS, Levasseur R et al. Cbfa1-independent decrease in osteoblast proliferation, osteopenia, and persistent embryonic eye vascularization in mice deficient in Lrp5, a Wnt coreceptor. J Cell Biol 2002;157:303–314.

10 Padhi D, Jang G, Stouch B et al. Single-dose, placebo-controlled, randomized study of AMG 785, a sclerostin monoclonal antibody. J Bone Miner Res 2011;26:19–26.

11 Iyer SP, Beck JT, Stewart AK et al. A Phase IB multicentre dose-determination study of BHQ880 in combination with anti-myeloma therapy and zoledronic acid in patients with relapsed or refractory multiple myeloma and prior skeletal-related events. Br J Haematol 2014;167:366–375.

12 Jin H, Wang B, Li J et al. Anti-DKK1 antibody promotes bone fracture healing through activation of beta-catenin signaling. Bone 2015;71:63–75.

13 Ominsky MS, Vlasseros F, Jolette J et al. Two doses of sclerostin antibody in cynomolgus monkeys increases bone formation, bone mineral density, and bone strength. J Bone Miner Res 2010;25:948–959.

14 Li X, Grisanti M, Fan W et al. Dickkopf-1 regulates bone formation in young growing rodents and upon traumatic injury. J Bone Miner Res 2011;26:2610–2621.

15 McClung MR, Grauer A, Boonen S et al. Romosozumab in postmenopausal women with low bone mineral density. N Engl J Med 2014;370:412–420.

16 Chen Y, Whetstone HC, Lin AC et al. Beta-catenin signaling plays a disparate role in different phases of fracture repair: Implications for therapy to improve bone healing. PLoS Med 2007;4:e249.

17 Ling L, Nurcombe V, Cool SM. Wnt signaling controls the fate of mesenchymal stem cells. Gene 2009;433:1–7.

18 Boland GM, Perkins G, Hall DJ et al. Wnt 3a promotes proliferation and suppresses osteogenic differentiation of adult human mesenchymal stem cells. J Cell Biochem 2004;93:1210–1230.

19 Cho HH, Kim YJ, Kim SJ et al. Endogenous Wnt signaling promotes proliferation and suppresses osteogenic differentiation in human adipose derived stromal cells. Tissue Eng 2006;12:111–121.

20 de Boer J, Siddappa R, Gaspar C et al. Wnt signaling inhibits osteogenic differentiation of human mesenchymal stem cells. Bone 2004;34:818–826.

21 Minear S, Leucht P, Jiang J et al. Wnt proteins promote bone regeneration. Sci Transl Med 2010;2:29ra30.

22 Gregory CA, Gunn WG, Reyes E et al. How Wnt signaling affects bone repair by mesenchymal stem cells from the bone marrow. Ann N Y Acad Sci 2005;1049:97–106.

23 Bennett CN, Longo KA, Wright WS et al. Regulation of osteoblastogenesis and bone mass by Wnt10b. Proc Natl Acad Sci U S A 2005;102:3324–3329.

24 Liu G, Vijayakumar S, Grumolato L et al. Canonical Wnts function as potent regulators of osteogenesis by human mesenchymal stem cells. J Cell Biol 2009;185:67–75.

25 Cook DA, Fellgett SW, Pownall ME et al. Wnt-dependent osteogenic commitment of bone marrow stromal cells using a novel GSK3beta inhibitor. Stem Cell Res 2014;12: 415–427.

26 Quarto N, Behr B, Longaker MT. Opposite spectrum of activity of canonical Wnt signaling in the osteogenic context of undifferentiated and differentiated mesenchymal cells: Implications for tissue engineering. Tissue Eng Part A 2010;16:3185–3197.

27 De Boer J, Wang HJ, Van Blitterswijk C. Effects of Wnt signaling on proliferation and differentiation of human mesenchymal stem cells. Tissue Eng 2004;10:393–401.

28 Baksh D, Boland GM, Tuan RS. Cross-talk between Wnt signaling pathways in human mesenchymal stem cells leads to functional antagonism during osteogenic differentiation. J Cell Biochem 2007;101:1109–1124.

29 Krause U, Harris S, Green A et al. Pharmaceutical modulation of canonical Wnt signaling in multipotent stromal cells for improved osteoinductive therapy. Proc Natl Acad Sci U S A 2010;107:4147–4152.

30 Centola M, Tonnarelli B, Scharen S et al. Priming 3D Cultures of Human Mesenchymal Stromal Cells Toward Cartilage Formation Via Developmental Pathways. Stem Cells Dev 2013;22:2849–2858.

31 Sengers BG, Dawson JI, Oreffo RO. Characterisation of human bone marrow stromal cell heterogeneity for skeletal regeneration strategies using a two-stage colony assay and computational modelling. Bone 2010;46:496–503.

32 Zannettino AC, Paton S, Kortesidis A et al. Human mulipotential mesenchymal/stromal stem cells are derived from a discrete subpopulation of STRO-1bright/CD34 / CD45(-)/glycophorin-A-bone marrow cells. Haematologica 2007;92:1707–1708.

33 Gothard D, Greenhough J, Ralph E et al. Prospective isolation of human bone marrow stromal cell subsets: A comparative study between Stro-1-, CD146- and CD105-enriched populations. J Tissue Eng 2014;5: 2041731414551763.

34 Howard D, Partridge K, Yang X et al. Immunoselection and adenoviral genetic modulation of human osteoprogenitors: In vivo bone formation on PLA scaffold. Biochem Biophys Res Commun 2002;299:208–215.

35 Tan SH, Senarath-Yapa K, Chung MT et al. Wnts produced by Osterix-expressing osteolineage cells regulate their proliferation and differentiation. Proc Natl Acad Sci U S A 2014;111:E5262–E5271.

36 Simmons PJ, Torok-Storb B. Identification of stromal cell precursors in human bone marrow by a novel monoclonal antibody, STRO-1. Blood 1991;78:55–62.

37 Gronthos S, Graves SE, Ohta S et al. The STRO-1 + fraction of adult human bone marrow contains the osteogenic precursors. Blood 1994;84:4164–4173.

38 Russell KC, Phinney DG, Lacey MR et al. In vitro high-capacity assay to quantify the clonal heterogeneity in trilineage potential of mesenchymal stem cells reveals a complex hierarchy of lineage commitment. Stem Cells 2010;28:788–798.

39 Clevers H, Loh KM, Nusse R. Stem cell signaling. An integral program for tissue renewal and regeneration: Wnt signaling and stem cell control. Science 2014;346:1248012.

40 Baksh D, Tuan RS. Canonical and non-canonical Wnts differentially affect the development potential of primary isolate of human bone marrow mesenchymal stem cells. J Cell Physiol 2007;212:817–826.

41 Shen L, Glowacki J, Zhou S. Inhibition of adipocytogenesis by canonical WNT signaling in human mesenchymal stem cells. Exp Cell Res 2011;317:1796–1803.

42 Qiu W, Chen L, Kassem M. Activation of non-canonical Wnt/JNK pathway by Wnt3a is associated with differentiation fate determi-

nation of human bone marrow stromal (mesenchymal) stem cells. Biochem Biophys Res Commun 2011;413:98–104.
43 Saraswati S, Deskins DL, Holt GE et al. Pyrvinium, a potent small molecule Wnt inhibitor, increases engraftment and inhibits lineage commitment of mesenchymal stem cells (MSCs). Wound Repair Regen 2012;20:185–193.
44 Mendez-Ferrer S, Michurina TV, Ferraro F et al. Mesenchymal and haematopoietic stem cells form a unique bone marrow niche. Nature 2010;466:829–834.
45 Worthley DL, Churchill M, Compton JT et al. Gremlin 1 identifies a skeletal stem cell with bone, cartilage, and reticular stromal potential. Cell 2015;160:269–284.
46 Park D, Spencer JA, Koh BI et al. Endogenous bone marrow MSCs are dynamic, fate-restricted participants in bone maintenance and regeneration. Cell Stem Cell 2012;10:259–272.
47 Sacchetti B, Funari A, Michienzi S et al. Self-renewing osteoprogenitors in bone marrow sinusoids can organize a hematopoietic microenvironment. Cell 2007;131:324–336.
48 Zhou BO, Yue R, Murphy MM et al. Leptin-receptor-expressing mesenchymal stromal cells represent the main source of bone formed by adult bone marrow. Cell Stem Cell 2014;15:154–268.
49 Chan CK, Seo EY, Chen JY et al. Identification and specification of the mouse skeletal stem cell. Cell 2015;160:285–298.
50 Wan Y, Lu C, Cao J et al. Osteoblastic Wnts differentially regulate bone remodeling and the maintenance of bone marrow mesenchymal stem cells. Bone 2013;55:258–267.
51 Stevens JR, Miranda-Carboni GA, Singer MA et al. Wnt10b deficiency results in age-dependent loss of bone mass and progressive reduction of mesenchymal progenitor cells. J Bone Miner Res 2010;25:2138–2147.
52 Goldhahn J, Feron JM, Kanis J et al. Implications for fracture healing of current and new osteoporosis treatments: An ESCEO consensus paper. Calcif Tissue Int 2012;90:343–353.
53 Ominsky MS, Li C, Li X et al. Inhibition of sclerostin by monoclonal antibody enhances bone healing and improves bone density and strength of nonfractured bones. J Bone Miner Res 2011;26:1012–1021.
54 Suen PK, He YX, Chow DH et al. Sclerostin monoclonal antibody enhanced bone fracture healing in an open osteotomy model in rats. J Orthop Res 2014;32:997–1005.
55 Baron R, Kneissel M. WNT signaling in bone homeostasis and disease: From human mutations to treatments. Nat Med 2013;19:179–192.
56 Swami A, Reagan MR, Basto P et al. Engineered nanomedicine for myeloma and bone microenvironment targeting. Proc Natl Acad Sci U S A 2014;111:10287–10292.


See www.StemCells.com for supporting information available online.